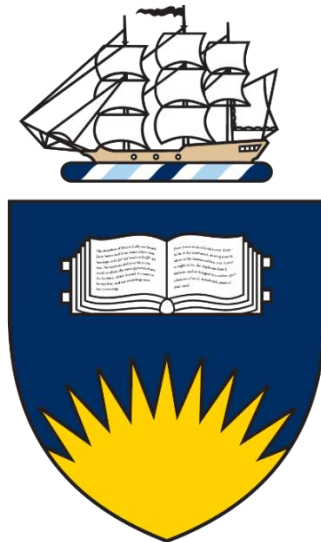


# Investigations into the effects of birnessite-like material structures on their effectiveness for metal dissolution

Jennie Bartle

BSc (Hons) Enhanced Program for High Achievers

A thesis submitted for the fulfilment of the degree of  
Doctor of Philosophy



**Flinders**  
UNIVERSITY

College of Science and Engineering  
July 2020

## Declaration

“I certify that this thesis does not incorporate without acknowledgement any material previously submitted for a degree or diploma in any university, and that to the best of my knowledge and belief does not contain any material previously published or written by another person except where due to reference is made in text.”

Jennie Bartle

on 06/04/2020

## Acknowledgements

A PhD is never completed in isolation, it takes a dedicated team of individuals to make a project a success, to that end, I would like to extend my sincerest thanks and appreciation to my supervisory team. To Claire, thank you for all the care, support, advice and encouragement throughout our time working together, all the way from back when I was a fledgling undergraduate to now. To Allan, thank you for your wise words, advice and interesting stories throughout the struggles of this project, I hope we've delved a little deeper into the black box that is this "predicament". And last but not least, to Frank, thank you for teaching me to appreciate the joy of science, and for teaching me to welcome everyone's opinions. I hope you would be proud of how this project turned out.

A special thank you to Dr Jeffery Post for welcoming my visit to the Smithsonian National Museum of Natural History. My visit to learn from you was a tremendous help and was a highlight of my PhD. To Dr Gabriela Farfan, thank you for taking me under your wing throughout my visit to D.C., your help and advice was greatly appreciated.

To the staff of Flinders Analytical both old and new, thank you for the aid and advice with using the ICP-MS throughout this project. To the members of the analytical research group both past and current, thank you for the support and advice over the years. To all my friends in the PhD cohort, thank you for sharing these interesting yet stressful times. Good luck with completing your own projects and trust me, it does end.

A special shout-out to Dr Tristan Kilmartin, Shaun Johns, and Connor Retallick for the tremendous levels of support, encouragement and belief in my abilities.

I would like to acknowledge and thank the Australian Government for funding me throughout my PhD under an Australian Government Research Training Program Scholarship.

To my parents and family, thank you for being supportive throughout my tertiary education, even if you don't understand a word I say sometimes. Thank you for still asking me about my project, how my day went and allowing me to ramble to you.

Thank you to the members of my Friday night boardgames group, Adam, Connor, Nathan and Dr Ruby. Your company, laughter, compassion and advice have been welcome distractions throughout my PhD, it's been a great help to end the work week with you all.

And finally, my biggest thanks go to my fiancé Dr Tim Solheim, thank you for putting up with me throughout this process, the seemingly endless edits, discussions and advice have helped me greatly. Thank you for your endless consideration, love and support. We both made it to the end of our PhDs, and I'll be forever grateful.

## Summary

Birnessite-like manganese oxides (BLMOs) are useful in a wide variety of applications, including in the oxidation of organic molecules and heavy metal cations. However, many of the application studies utilise poorly characterised materials, creating difficulties for researchers wishing to expand on prior research. There is also significant variation in the materials prepared for these applications.

This study synthesised BLMO materials utilising a variety of methods, and the resulting materials were characterised using x-ray diffraction and subsequent Rietveld refinements, scanning electron microscopy, and determination of the average manganese oxidation state. It was found that the materials prepared had different unit cell parameters, levels of stacking order and morphologies. Further investigations into the reproducibility of material synthesis between batches showed that even when conducting the synthesis identically, slight differences in the purity and unit cell parameters occur.

This thesis demonstrates, for the first time, that BLMO materials are able to oxidise elemental vanadium (V(0)), gold (Au(0)) and other metals when the materials are placed in an acidic saline solution. The conditions utilised are significantly less hazardous than most existing metal dissolution methodologies. Triclinic BLMO materials oxidised V(0) inconsistently and hexagonal BLMO materials had greater consistency. The variability observed in the triclinic BLMO materials was found to be caused by the stabilising effect of K<sup>+</sup> cations on the layered structure of triclinic BLMOs. It was shown that the dissolved V can be incorporated into the interlayer space and octahedral sheets of BLMO. Long term experiments observed the formation of the manganese vanadate mineral ansermetite, which is likely formed from the coprecipitation of the dissolved Mn<sup>2+</sup> and V<sup>5+</sup> generated by this reaction system.

The study was extended to tunnel structured manganese oxide materials in the form of cryptomelane (2x2), todorokite (3x3) and pyrolusite (1x1). It was found that the reactivity of these tunnelled materials towards oxidation of V followed the trend of 1x1>2x2>3x3. The variability found in the oxidation of V led to a preliminary investigation into the oxidation of elemental Au by a selection of layered and tunnelled manganese oxide materials. A general trend where a material that achieved high levels of oxidised V also resulted in high levels of oxidised Au. There were two exceptions to this trend, pyrolusite and a disordered BLMO material, which could be due to surface passivation and a greater affinity for absorption, however, further investigations into this area are required.

Further investigations showed that BLMOs can oxidise elemental palladium (Pd), in addition to vanadium and gold at higher levels than an acidic saline control. Contrastingly, copper, lead, nickel and iron were generated at higher amounts in the acidic controls than the BLMO test, suggesting that the BLMO materials inhibits the oxidation of these metals. The trend observed with the metals able to be oxidised by BLMOs follows the trend observed by the corresponding metal chloride salt solubility, with a more soluble chloride salt resulting in more metal oxidised. This work led to a preliminary investigation into assessing the ability of BLMO materials to recover metals from electronic waste. It was found that this system can oxidise metals from CPUs and RAM pins however further work is required to adapt this reaction system for the efficient extraction of metals.

*Dedicated to*

*Nana*

*and*

*Dr Frank Reith*

*Not all those who wander are lost.*

*-J.R.R. Tolkien*

## Contents

Declaration.....	ii
Acknowledgements.....	iii
Summary.....	v
Figures.....	xii
Tables.....	xx
List of Acronyms.....	xxii
Chapter 1 Introduction .....	1
1.1 Manganese Oxide Materials .....	1
1.1.1 Birnessite and birnessite-like manganese oxide materials .....	1
1.1.2 Tunnelled manganese oxide materials .....	10
1.2 Metal oxidation and extraction.....	14
1.2.1 Transition Metal Extraction .....	14
1.2.2 Gold.....	17
1.2.3 Vanadium .....	22
1.3 E-Waste .....	23
1.4 Instrumentation .....	25
1.4.1 X-Ray Diffraction .....	25
1.4.2 Rietveld Refinement .....	27
1.4.3 Scanning Electron Microscopy.....	28
1.4.4 Raman Spectroscopy.....	31
1.4.5 Inductively Coupled Plasma Mass Spectrometry .....	32
1.5 Project aims.....	33
Chapter 2 General Methods .....	34
2.1 X-Ray Diffraction Analysis .....	34
2.2 Rietveld Refinement.....	35
2.3 Scanning Electron Microscopy/Energy Dispersive Spectroscopy .....	35
2.4 Raman Spectroscopy.....	35
2.5 Average Manganese Oxidation State Determination .....	36
2.6 Standard Oxidation Reaction Conditions .....	37
2.7 Inductively Coupled Plasma Mass Spectrometry.....	37

2.7.1	Vanadium analysis .....	38
2.7.2	Gold analysis .....	39
2.7.3	Multielement analysis.....	39
2.8	General reagents .....	40
Chapter 3	Synthesis and Characterisation of Birnessite-Like Manganese Oxides .....	42
3.1	Introduction.....	42
3.2	Materials and Methods .....	45
3.2.1	BLMO Synthesis Methods .....	45
3.2.2	Characterisation of BLMO materials.....	47
3.2.3	Post-synthesis treatments .....	47
3.3	Results and Discussion .....	48
3.3.1	Different literature synthesis methods.....	48
3.3.2	Effect XRD Source on Rietveld Refinements.....	56
3.3.3	Changing crystallinity via potassium chloride treatment .....	58
3.3.4	Changing the interlayer cation.....	63
3.3.5	Synthesis reproducibility.....	68
3.3.6	Static Ageing .....	72
3.3.7	Stirring Rate .....	75
3.3.8	Reagent Age .....	77
3.3.9	Reagent Concentration .....	77
3.3.10	Synthesis NaOH Concentration.....	81
3.3.11	Variability in BLMO parameters.....	81
3.4	Conclusion .....	86
Chapter 4	Reactivity of birnessite-like manganese oxide materials .....	87
4.1	Introduction.....	87
4.2	Materials and Methods .....	90
4.2.1	Reaction Conditions .....	90
4.2.2	BLMO Reactivity Experiments.....	91
4.2.3	Effect of Reaction Solution on BLMO Structure .....	92
4.3	Results and Discussion .....	92
4.3.1	Reaction Conditions .....	92

4.3.2	Effect of Structural Order on Reactivity.....	95
4.3.3	Finding a correlation between BLMO structure and vanadium oxidation .....	103
4.3.4	Confirming the role of potassium .....	111
4.3.5	Effect of Interlayer Cation.....	113
4.3.6	Changes to BLMO material .....	114
4.3.7	Long term reaction.....	119
4.4	Conclusion .....	121
Chapter 5	Tunnel Structured Manganese Oxide Materials.....	122
5.1	Introduction.....	122
5.2	Materials and Methods .....	123
5.2.1	Synthesis of Cryptomelane (2x2 TSMO) .....	124
5.2.2	Reactivity of Other Manganese Oxide Materials.....	125
5.3	Results and Discussion .....	126
5.3.1	Structural analysis of tunnel structured manganese oxide materials .....	126
5.3.2	Oxidation of V(0) with TSMOs .....	132
5.3.3	Comparison of Manganese Oxide Reactivity for Vanadium and Gold .....	137
5.4	Conclusion .....	141
Chapter 6	Electronic Waste Applications .....	142
6.1	Introduction.....	142
6.2	Materials and Methods.....	144
6.2.1	Preliminary Metal Oxidations .....	144
6.2.2	First Electronic Waste Oxidations .....	144
6.2.3	Second Electronic Waste Oxidations .....	144
6.2.4	Aqua Regia Digest Controls.....	145
6.3	Results and Discussion .....	145
6.3.1	Preliminary Metal Oxidations .....	145
6.3.2	Electronic Waste Applications .....	148
6.4	Conclusion .....	155
Chapter 7	Conclusion and Future Work .....	156
7.1	Conclusions.....	156
7.2	Future Work .....	159

7.2.1	Expansion of manganese oxide materials .....	159
7.2.2	Stabilisation effect of $K^+$ on cryptomelane materials .....	159
7.2.3	Confirming the production of chlorine .....	160
7.2.4	Determinations of reaction rates for different metals .....	160
7.2.5	Further exploration into metal recovery from electronic waste.....	161
Chapter 8	References .....	162

## Figures

Figure 1-1: Layered crystal structure of a) triclinic BLMO and b) hexagonal BLMO, images made using CrystalMaker from CIF structural files <sup>6</sup> .....	2
Figure 1-2: CoK $\alpha$ diffraction pattern of triclinic BLMO materials synthesised in an alkaline environment, showing the expected peaks for BLMO, hausmannite, and feitknechtite. ....	5
Figure 1-3: BLMO crystal structure showing the triclinic unit cell.....	5
Figure 1-4: SEM images of a) nanoflower, c) nanowire, and e) nanosheet BLMO morphologies and TEM images of b) nanoflower, d) nanowire and f) nanosheet BLMO morphologies, taken from Hou <i>et al.</i> <sup>32</sup> .....	6
Figure 1-5: a) XPS spectra of hexagonal BLMO from Ilton <i>et al.</i> <sup>37</sup> b) XANES spectra of various manganese oxides from Manceau <i>et al.</i> <sup>38</sup> .....	8
Figure 1-6: Diagrams showing the crystal structure of pyrolusite (top left), cryptomelane (top right), and todorokite (bottom). Structures were recreated using CrystalMaker from CIF structure files from structure determination papers <sup>86-88</sup> .....	11
Figure 1-7: CoK $\alpha$ diffraction patterns and the expected peaks for a) pyrolusite, b) cryptomelane, and c) todorokite, black= experimental diffraction pattern, red=expected diffraction pattern.....	12
Figure 1-8: Unit cell diagrams of TMOs a) pyrolusite, b) cryptomelane, and b) todorokite. ...	13
Figure 1-9: a) A diagram showing the diffraction of x-rays through a sample, indicating that the angle of incidence is the same as the angle of diffraction. b) CuK $\alpha$ diffraction pattern of NaCl <sup>179</sup> .....	26
Figure 1-10: Diagram showing the two common geometries utilised in X-ray diffraction, a) Bragg-Brentano and b) Debye-Scherrer. Images modified from Modern Diffraction Methods <sup>177</sup> .....	27
Figure 1-11: A diagram showing some of the outputs caused by the interaction of an electron beam with a sample <sup>186</sup> .....	29
Figure 1-12: Schematic of the atomic events that produces characteristic x-rays for EDX <sup>188</sup> ..	30
Figure 1-13: A schematic of the instrumentation involved in an SEM <sup>187</sup> .....	31
Figure 1-14: Schematic diagram of an ICP-MS <sup>193</sup> .....	32

Figure 2-1: SEM image showing the morphology and size of the vanadium powder used throughout this work .....	40
Figure 2-2: SEM image showing the morphology and size of the gold powder used throughout this work.....	40
Figure 3-1: View of common birnessite crystal structures along the [100] direction, a) Triclinic birnessite, b) Hexagonal birnessite, where the white octahedra signify Mn vacancies. ....	44
Figure 3-2: SEM images of synthesized BLMO material taken at 20,000x magnification with a beam voltage of 10 kV. a) Method A, b) Method B, c) Method C, and d) Method D. ....	49
Figure 3-3: EDXS spectra of untreated birnessite synthesized using method C, showing the presence of both Na and K present in the birnessite sample. ....	51
Figure 3-4: MoK $\alpha$ X-ray diffraction patterns of the BLMO resulting from the four different synthesis methods and the modified materials of method c and d. Patterns are offset for ease of clarity. ....	51
Figure 3-5: EDXS of BLMO prepared using Method B, showing the presence of K <sup>+</sup> in the structure.....	53
Figure 3-6: Raman spectra of the BLMO material prepared by method B (blue), a sample of hexagonal BLMO (red) and a sample of triclinic BLMO (black) for comparison.....	53
Figure 3-7: Rietveld refinements (green) on experimental XRD data (blue) and difference curves (teal) using the MoK $\alpha$ patterns for a-c and e-g and CoK $\alpha$ for d of the six BLMO materials prepared using four literature methods. Reflections of manganese oxide phases are shown below the patterns.....	54
Figure 3-8: X-ray diffraction patterns collected using Cu, Co, and Mo radiation for a) a crystalline sample of BLMO synthesised via Method C and b) a poorly crystalline sample of BLMO synthesised via Method A. The diffractograms have been converted to CoK $\alpha$ $^{\circ}2\theta$ values for comparison. Top: CoK $\alpha$ , Middle: CuK $\alpha$ and Bottom: MoK $\alpha$ . ....	57
Figure 3-9: CoK $\alpha$ X-ray diffraction patterns of synthetic birnessite material treated with H <sub>2</sub> O for 2 hours, and 1 M KCl for 1, 2, 5, 8 and 24 hrs. Patterns are y-offset for clarity. ....	60
Figure 3-10: SEM images of the potassium chloride treatments a) untreated, b) H <sub>2</sub> O treatment, c) 2 hr treatment and d) 24 hr treatment .....	61

Figure 3-11: Rietveld refinements and difference curves for the birnessite materials treated with KCl for different time intervals. Refinement a and b were conducted using CoK $\alpha$ diffraction patterns and c-g were conducted on patterns collected by MoK $\alpha$ . .....	62
Figure 3-12: CoK $\alpha$ X-ray diffraction patterns of birnessite material treated with different 1 M cation solutions (H $^+$ , Li $^+$ , K $^+$ , Na $^+$ Mg $^{2+}$ and Ca $^{2+}$ , H $^+$ then K $^+$ and H $^+$ and K $^+$ ). Patterns are y-offset for clarity.....	64
Figure 3-13: SEM images of the different BLMOs prepared in the cation exchange study. a) H $^+$ , b) H $^+$ then K $^+$ , c) Li $^+$ , d) Na $^+$ , e) K $^+$ (KCl), f) K $^+$ (KBr), g) Mg $^{2+}$ and h) Ca $^{2+}$ .....	65
Figure 3-14: Rietveld refinement and difference plots for the cation BLMOs formed from the cation treatment study. a) H $^+$ , b) H $^+$ then K $^+$ , c) H $^+$ + K $^+$ , d) Li $^+$ , e) Na $^+$ , f) K $^+$ (KBr), g) K $^+$ (KCl), h) Mg $^{2+}$ and i) Ca $^{2+}$ . The refinements for H $^+$ (a) and (h) Mg $^{2+}$ were conducted using diffraction patterns collected by CoK $\alpha$ whereas the others were collected by MoK $\alpha$ . .....	66
Figure 3-15: CoK $\alpha$ XRD patterns for the nine replicate materials synthesised using method C. Patterns are y-offset for clarity.....	69
Figure 3-16: Rietveld refinements and difference curves for the nine replicate birnessite materials conducted on diffraction patterns collected by CoK $\alpha$ . .....	71
Figure 3-17: CoK $\alpha$ XRD patterns for the BLMO materials prepared while investigating the effect of static ageing time synthesised using method C. Patterns are y-offset for clarity. ...	73
Figure 3-18: Rietveld refinements and difference curves for the static ageing BLMO materials conducted on diffraction patterns collected by CoK $\alpha$ . a) 0 days, b) 1 day, c) 2 days, d) 5 days and e) 7 days. ....	74
Figure 3-19: CoK $\alpha$ diffraction patterns collected for BLMO samples prepared with various stirring conditions. Patterns are y-offset for clarity. ....	75
Figure 3-20: Rietveld refinements and difference curves of birnessites prepared with various stirring rates a) no stirring, b) slow stirring, and c) fast stirring. Diffraction patterns were collected by CoK $\alpha$ . ....	76
Figure 3-21: CoK $\alpha$ diffraction patterns collected for BLMO samples prepared with fresh and two-month aged stock solutions. Patterns are y-offset for clarity.....	78
Figure 3-22: Rietveld refinements and difference curves of birnessite prepared with a) fresh stock solutions and b) two-month-old stock solutions. Diffraction patterns were collected by CoK $\alpha$ . .....	78

Figure 3-23: CoK $\alpha$ diffraction patterns collected for BLMO samples prepared using concentrated and diluted stock solutions. Patterns are y-offset for clarity.....	79
Figure 3-24: Rietveld refinements and difference curves of birnessites prepared with different concentrations of stock solutions a) 1 in 10 dilution, b) 1 in 2 dilutions, and c) concentrated stock solutions. Diffraction patterns were collected by CoK $\alpha$ . .....	80
Figure 3-25: CoK $\alpha$ diffraction patterns of BLMOs prepared with varying sodium hydroxide content.....	82
Figure 3-26: Rietveld refinements and difference curves of birnessites prepared with different amounts of sodium hydroxide a) 3 g, b) 6 g, c) 9 g, and d) 12 g. Diffraction patterns were collected by CoK $\alpha$ . .....	83
Figure 3-27: Scatter plots showing the variation in structural parameters refined for the BLMO materials synthesized in this chapter. The parameters shown here are a) average manganese oxidation state, b) Scheerer crystallite size, c) % birnessite phase present in the refinement, d) the a unit cell parameter, e) the b unit cell parameter, f) the c unit cell parameter, g) the $\alpha$ unit cell parameter, h) the $\beta$ unite cell parameter, i) the $\gamma$ unit cell parameter, j) the unit cell volume, and k) the average Mn-O bond length in the manganese oxide octahedra. ....	85
Figure 4-1: Three individual trials attempting to use BLMO material to oxidise gold powder. Error bars represent one standard deviation $n=2$ . .....	93
Figure 4-2: Effect of rotational speed on the amount of vanadium dissolved by a BLMO material. Error bars represent one standard deviation $n=3$ .....	94
Figure 4-3: Effect of BLMO aggregate size on the amount of vanadium dissolved by a BLMO material. Error bars represent one standard deviation $n=3$ .....	95
Figure 4-4: Vanadium dissolution achieved by six synthetic BLMOs prepared via six literature methods. Error bars represent one standard deviation $n=3$ .....	97
Figure 4-5: Structural order plots comparing the amount of vanadium oxidised and the FWHM of six BLMO materials prepared by different synthesis methods. Error bars represent one standard deviation $n=3$ . .....	97
Figure 4-6: Vanadium oxidation reproducibility study using replicate BLMO samples synthesised by method C. Error bars represent one standard deviation $n=3$ .....	99

Figure 4-7: Structural order plots comparing the amount of vanadium oxidised and the FWHM of six replicate BLMO materials prepared by method C. Error bars represent one standard deviation $n=3$ . .....	99
Figure 4-8: Structural order plots comparing the amount of vanadium oxidised and the FWHM of the BLMO materials modified by different static aging times. Error bars represent one standard deviation $n=3$ . .....	101
Figure 4-9: Effect of BLMO age time in synthesis solution on the oxidation of vanadium powder. Error bars represent one standard deviation $n=3$ . .....	101
Figure 4-10: Effect of BLMO crystallinity on the oxidation of vanadium powder. Error bars represent one standard deviation $n=3$ . .....	102
Figure 4-11: Structural order plots comparing the amount of vanadium oxidised and the FWHM of the BLMO materials modified by different KCl treatment times. Error bars represent one standard deviation $n=3$ . .....	103
Figure 4-12: Plot showing the variation in reactivity of 35 BLMO materials and errors bars are a standard deviation of 3 oxidation replicates. ....	104
Figure 4-13: Variance plots produced for hexagonal and triclinic BLMOs using all oxidation experiment replicates. ....	105
Figure 4-14: Correlation plots comparing the amount of vanadium dissolved to various structural and chemical properties, with samples reacted for 4 days in red and samples reacted for 3 days in black. a) $a$ , b) $b$ , c) $c$ , d) $\alpha$ , e) $\beta$ , f) $\gamma$ , g) volume, h) average Mn-O bond length, i) average manganese oxidation state, j) scheerer crystallite size, and k) weight percentage of birnessite phase.....	107
Figure 4-15: CoK $\alpha$ diffraction patterns of the untreated BLMOs exposed to pH 2 0.05M NaCl solution for various time intervals, showing 26-32 $^{\circ}2\theta$ . .....	109
Figure 4-16: CoK $\alpha$ diffraction patterns of the Na treated BLMOs exposed to an acidic saline solution for various time intervals, showing 26-32 $^{\circ}2\theta$ . .....	110
Figure 4-17: CoK $\alpha$ diffraction patterns of the water treated BLMOs exposed to an acidic saline solution for various time intervals, showing 26-32 $^{\circ}2\theta$ . .....	110
Figure 4-18: CoK $\alpha$ diffraction patterns of the K treated BLMOs exposed to an acidic saline solution for various time intervals, showing 26-32 $^{\circ}2\theta$ . .....	111
Figure 4-19: Raman spectra of standards of Na-BLMO, K-BLMO and six BLMO materials. .	112

Figure 4-20: Comparison plot showing the reactivity of six BLMO materials separated by the presence of sodium in the crystal structure determined by Raman spectroscopy. Error bars represent one standard deviation $n=3$ . .....	112
Figure 4-21: Effect of the interlayer cation present in BLMO materials on the oxidation of vanadium powder. Error bars represent one standard deviation $n=3$ . .....	114
Figure 4-22: CoK $\alpha$ diffraction patterns of BLMO materials, a) BLMO material before exposure, b) BLMO material after utilisation of V(0) oxidation for 3 days, and c) BLMO material after exposure in acidic saline solution without V(0) for 3 days. ....	116
Figure 4-23: Rietveld refinement and difference plots for the BLMOs formed after exposure to different reaction solutions a) acidic saline solution without V(0) for 3 days , b) an acidic saline reaction solution utilised for the oxidation of V(0) . The refinements were conducted on diffraction patterns collected via CoK $\alpha$ . ....	117
Figure 4-24: SEM image of the BLMO material after utilisation for the oxidation of V(0), showing two different morphologies and the locations analysed via EDXS. ....	118
Figure 4-25: EDXS spectra of the left hand EDXS spot on Figure 4-24 of the BLMO material utilised to oxidise V(0), showing the presence of V and Mn present in the BLMO. ....	118
Figure 4-26: EDXS spectra of the right hand EDXS spot on Figure 4-24 of the BLMO material utilised to oxidise V(0), showing the presence of V and Mn present in the BLMO. ....	118
Figure 4-27: a) spindle clusters of red crystals found in the resulting reaction solution after storage for several months, b) multiple small crystals forming. ....	119
Figure 4-28: CoK $\alpha$ diffraction patterns of the red crystals found in the reaction solution after several months and the starting BLMO material for comparison .....	120
Figure 4-29: Crystal structure of ansermetite, a manganese vanadate mineral, structure created using CrystalMaker and the structure file provided with Brugger <i>et al.</i> <sup>230</sup> . ....	120
Figure 5-1: Diagrams showing the crystal structure of pyrolusite (top left), cryptomelane (top right) and todorokite (bottom). Structures were recreated using CrystalMaker from CIF structure files from structure determination papers <sup>86-88</sup> . ....	122
Figure 5-2: MoK $\alpha$ diffraction patterns of five synthetic cryptomelane samples. ....	127
Figure 5-3: CoK $\alpha$ diffraction patterns of synthetic todorokite and commercial pyrolusite. .	127
Figure 5-4: SEM images of four TSMO materials , a) cryptomelane method A-3, b) cryptomelane method C, c) todorokite, and d) pyrolusite. ....	129

Figure 5-5: Rietveld refinement and difference plots for the TSMO materials presented. a) cryptomelane A-1, b) cryptomelane A-2, c) cryptomelane A-3, d) cryptomelane B, e) cryptomelane C, f) todorokite, and g) pyrolusite. ....	130
Figure 5-6: Reactivity plots for other manganese oxide materials, with a hexagonal and the best and worst triclinic BLMO as a reference comparison. Error bars represent one standard deviation $n=3$ . ....	133
Figure 5-7: Variability plots showing different refined parameters for the tunnel structure manganese oxide minerals, a) $c$ unit cell parameter, b) $\alpha$ and $\gamma$ unit cell parameter, c) average manganese oxidation state, d) $a$ unit cell parameter, e) unit cell volume and f) the average Mn-O bond length.....	134
Figure 5-8: Comparison of the average manganese oxidation state and the amount of V oxidised by the five cryptomelane samples. ....	136
Figure 5-9: Crystal structure of bixbyite (left) showing the random point-sharing and edge-sharing $MnO_6$ octahedra, and hausmannite (right).....	136
Figure 5-10: $CoK\alpha$ diffraction patterns of cryptomelane method A-2 before and after oxidising vanadium and stored in the reaction solution for two years. *cryptomelane, +BLMO.....	137
Figure 5-11: Comparison plot of the reactivities of nine manganese oxide materials for the oxidation of gold and vanadium. Red-BLMO, Black-TSMO. Error bars represent one standard deviation $n=3$ . ....	139
Figure 5-12: SEM image of the pyrolusite powder after submersion in 100 ppm $Au^{3+}$ for three days. ....	140
Figure 5-13: EDXS spectra of pyrolusite powder collected after submersion in 100 ppm $Au^{3+}$ solution for 3 days.....	140
Figure 5-14: $CoK\alpha$ diffraction patterns collected for the pyrolusite powder before and after submersion in a 100 ppm $Au^{3+}$ solution for 3 days.....	141
Figure 6-1: Preliminary trials for BLMO oxidation of nine transition metals .....	146
Figure 6-2: Reaction of copper metal with different combinations of halide salts and acids .....	148
Figure 6-3: Preliminary concentration results from the first attempt to oxidise the metals in CPUs with our reaction system. *concentrations were determined from the solutions at a later date than the other elements. Error bars represent one standard deviation $n=2$ . ....	150

Figure 6-4: Preliminary concentration results from the first attempt to oxidise the metals in RAM pins with our reaction system. \* concentration were determined from the solutions at a later date than the other elements. Error bars represent one standard deviation  $n=2$ .....150

Figure 6-5: Concentration results from a second attempt at oxidising the metals in CPUs with our reaction system. Error bars represent one standard deviation  $n=2$ .....152

Figure 6-6: Concentration results from a second attempt at oxidising the metals in RAM pins with our reaction system. Error bars represent one standard deviation  $n=2$ .....152

Figure 6-7: CoK $\alpha$  diffraction pattern of green precipitate found in RAM card samples after the second oxidation trial. +BLMO, \*atacamite, #paratacamite .....153

Figure 6-8: Efficiency plots for the metals extracted from CPUs from both BLMO trials. ....154

Figure 6-9: Efficiency plots for the metals extracted from RAM pins from both BLMO trials. ....154

## Tables

Table 2-1: ICP-MS instrumental operating conditions.....	38
Table 2-2: Minimum criteria for ICP-MS analysis .....	38
Table 2-3: The chemicals used throughout this study.....	41
Table 3-1: Average manganese oxidation state for the six synthesised materials using four literature methods. Errors are standard deviation of triplicate analysis ( $n=3$ ). .....	49
Table 3-2: Rietveld refinement results for the four synthesis methods, shown are the final refined cell parameters, $R(F^2)$ and the residual ( $R_{wp}$ ). .....	55
Table 3-3: Results of the Rietveld refinements conducted using various radiation sources on a crystalline sample (Method C), shown are the final refined cell parameters, $R(F^2)$ and the residual ( $R_{wp}$ ). .....	58
Table 3-4: Average manganese oxidation state of the potassium chloride treatment. Errors are standard deviation of triplicate analysis ( $n=3$ ). .....	60
Table 3-5: Rietveld refinement results for the KCl treatment study. Shown are the final refined cell parameters, the $R(F^2)$ and $R_{wp}$ values.....	63
Table 3-6: Average manganese oxidation state for different cation BLMOs. Errors are standard deviation of triplicate analysis ( $n=3$ ). .....	64
Table 3-7: Rietveld refinement results for different cation treatments, shown are the final refined cell parameters, the $R(F^2)$ and $R_{wp}$ values. ....	67
Table 3-8: Average manganese oxidation states for nine replicates of synthesis method C. Errors are standard deviation of triplicate analysis ( $n=3$ ). .....	68
Table 3-9: Rietveld refinement results for the nine replicate BLMO materials, shown are the final refined cell parameters, $R(F^2)$ and the residual ( $R_{wp}$ ). .....	70
Table 3-10: Average manganese oxidation state of BLMO prepared while investigating the effect of static ageing. Errors are standard deviation of triplicate analysis ( $n=3$ ). .....	72
Table 3-11: Rietveld refinement results for BLMO materials prepared while investigating the effect of static ageing, shown are the final refined cell parameters, $R(F^2)$ and the residual ( $R_{wp}$ ). .....	73
Table 3-12: Rietveld refinement results for BLMOs prepared with different stirring rates, shown are the final refined cell parameters, the $R(F^2)$ and $R_{wp}$ values. ....	76

Table 3-13: Rietveld refinement results for birnessite prepared with fresh and two-month-old stock solutions, shown are the final refined cell parameters, the $R(F^2)$ and $R_{wp}$ values. ....	79
Table 3-14: Rietveld refinement results for BLMOs prepared with different stock concentrations, shown are the final refined cell parameters, the $R(F^2)$ and $R_{wp}$ values. ....	80
Table 3-15: Rietveld refinement results for BLMOs prepared with different sodium hydroxide concentrations, shown are the final refined cell parameters, the $R(F^2)$ and $R_{wp}$ values. ....	82
Table 4-1: Summary of the experimental conditions used for the oxidation of metals by BLMO materials in literature. ....	88
Table 4-2: FWHM for the primary XRD peak and corresponding assigned structural ordering values for the different BLMO synthesis methods. ....	96
Table 4-3: FWHM for the primary XRD peak and corresponding assigned structural ordering values for the synthesis replicates of method C. ....	98
Table 4-4: FWHM for the primary XRD peak and corresponding assigned structural ordering values for the alteration of the static aging time. ....	100
Table 4-5: FWHM for the primary XRD peak and corresponding assigned structural ordering values for the post synthesis treatment with KCl. ....	102
Table 4-6: Rietveld refinement results for different cation treatments, shown are the final refined cell parameters, the $R(F^2)$ and $R_{wp}$ values. ....	117
Table 5-1: Average manganese oxidation state for TSMO materials. Errors are standard deviation of triplicate analysis ( $n=3$ ). ....	128
Table 5-2: Rietveld refinement results for the TSMO materials prepared, shown are the final refined cell parameters, the $R(F^2)$ and $R_{wp}$ values. ....	131

## List of Acronyms

AAS	Atomic Absorption Spectroscopy
AOS	Average Oxidation State
BLMO	Birnessite-Like Manganese Oxides
CPU	Computer Processing Unit
EDXSS	Energy Dispersive X-Ray Spectroscopy
E-waste	Electronic waste
FWHM	Full Width Half Maximum
GSAS II	General Structure Analysis System II
I.D.	Internal Diameter
ICP-MS	Inductively Coupled Plasma-Mass Spectrometry
KED	Kinetic Energy Discrimination
MO	Manganese Oxide
PCBs	Printed Circuit Boards
ppb	Parts Per Billion
ppm	Parts Per Million
PVDF	Polyvinylidene Difluoride
QID	Quadrupole Ion Deflector
RAM Pins	Random Access Memory Pins
SEM	Scanning Electron Microscopy
TEM	Transmission Electron Microscopy
TSMO	Tunnel Structured Manganese Oxides
XANES	X-ray Absorption Near Edge Structure
XPS	X-Ray Photoelectron Spectroscopy
XRD	X-Ray Diffraction

# Chapter 1 Introduction

## 1.1 Manganese Oxide Materials

Manganese (Mn) is commonly found in the environment in the form of oxide/hydroxide minerals. There are over 30 structural forms with varying crystal structures and Mn oxidation state combinations<sup>1</sup>. This variety in crystal structure and oxidation state leads to differences in the minerals crystallinity, morphology, and chemical reactivity<sup>1</sup>. The manganese oxide crystal structure is typically composed of  $\text{MnO}_6$  octahedra arranged in different orientations. This results in several overarching structural groups: layer structures, tunnel structures, and framework structures, of which the first two are investigated in this project. This chapter will give a detailed introduction into the crystal structure, characterisation and applications of both layered manganese oxides and tunnelled manganese oxides. This is followed by a discussion of metal extractions and the chemistry around the oxidation and dissolutions of metals such as gold and vanadium, and subsequent information about the extraction of metals from electronic waste. Then finally, background information about the instrumental techniques is presented.

### 1.1.1 Birnessite and birnessite-like manganese oxide materials

#### 1.1.1.1 Structure

Birnessite ( $\text{Na}_x\text{MnO}_2 \cdot y\text{H}_2\text{O}$ ) is one of the more prevalent manganese dioxide minerals found in the environment<sup>2</sup> and was first discovered in 1956 by Jones and Milne<sup>3</sup>. Birnessite and its altered forms, termed birnessite-like manganese oxides (BLMOs,  $\text{A}_x\text{MnO}_2 \cdot y\text{H}_2\text{O}$ , where A is a cation other than  $\text{Na}^+$ ), have gained the interest of the scientific community due to their chemical reactivity<sup>1, 4</sup>. BLMOs are comprised of layered sheets of edge-sharing manganese oxide octahedra ( $\text{Mn}^{4+, 3+}\text{O}_6$ ) interleaved by hydrated cations to charge balance the negatively

charged layers<sup>5</sup>. BLMOs have two crystal forms, triclinic and hexagonal (Figure 1-1). Triclinic BLMOs are described by a non-standard face centred  $C-1$  space group<sup>6</sup> and hexagonal BLMOs adopt a hexagonal unit cell in space group  $P-3$ <sup>7</sup>. Triclinic BLMO materials have a more ordered crystal structure, with neatly packed layered octahedra with hydrated cations (e.g.  $\text{Na}^+$ ,  $\text{K}^+$  etc.) held in the interlayer space. In contrast, the hexagonal form consists of hydrated  $\text{Mn}^{2+/3+}$  from the octahedral layers acting as the interlayer cations, resulting in the formation of vacancies within the octahedral layers<sup>8</sup>. The difference in the ratio of  $\text{Mn}^{3+}$  to  $\text{Mn}^{4+}$  in both crystal structures and the particle size is thought to influence the minerals reactivity<sup>9-10</sup>. Modelling by Lucht and Mendoza-Cortes<sup>11</sup> suggests that changing the internal cation in the structure may change the  $\text{Mn}^{3+}/\text{Mn}^{4+}$  ratio which can lead to different reactivity and properties, which consequently means that BLMO materials can be tuneable.

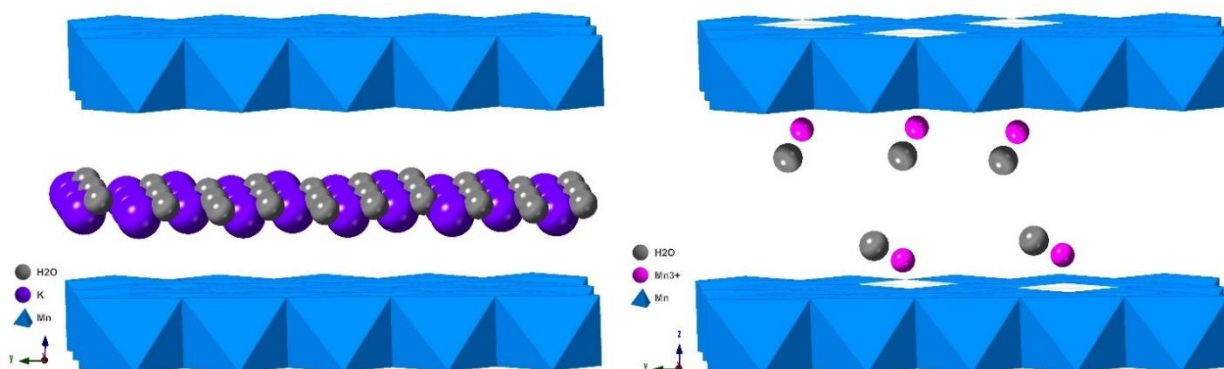


**Figure 1-1: Layered crystal structure of a) triclinic BLMO and b) hexagonal BLMO, images made using CrystalMaker from CIF structural files<sup>6</sup>.**

Naturally occurring birnessites are typically fine grained, amorphous, and are difficult to isolate from bulk soils<sup>1</sup>. They are also usually contaminated with silicates, iron oxides, and other metal species<sup>2</sup>. Consequently, experiments examining birnessite reactivity are usually undertaken using synthetically prepared BLMOs.

Synthesis of BLMOs typically involves either the reduction of  $\text{Mn}^{7+}$  or the oxidation of  $\text{Mn}^{2+}$ . The synthesis of manganese minerals has been undertaken since the 1940s and these methods were reviewed by McKenzie in 1971<sup>12</sup>. The methods outlined by McKenzie form the basis of methodology used today to prepare synthetic BLMOs. These methods predominately use either hydrothermal synthesis<sup>13</sup> or sol-gel synthesis<sup>14</sup>. Hydrothermal methods typically involve homogenizing a solution of potassium permanganate with a reductant, such as manganese chloride or potassium persulfate<sup>15</sup>. The resulting mixture is subsequently placed into an autoclave for several hours. The morphology of BLMOs produced using hydrothermal synthesis mostly consists of spheres of crystallites (70 - 90 nm) or rods (20 - 500 nm) with broad peaks in XRD spectra due to the small crystallite size<sup>15-17</sup>. Sol-gel synthesis uses a similar chemistry, whereby either aqueous solutions of  $\text{Mn}^{2+}$  are oxidized or aqueous solutions of  $\text{Mn}^{7+}$  are reduced. However, the sol-gel synthesis method has mixed success in producing crystalline BLMO because accurate control of the molar ratio of reactants is required<sup>18</sup>. Here, the solutions are slowly combined at room temperature to form a BLMO suspension. Alternate reductants include glucose<sup>14</sup>, ethanol<sup>19</sup>, sodium lactate<sup>20</sup> and manganese chloride<sup>21</sup>. The main benefit of this approach, apart from its simplicity, is the ability to achieve greater control of particle size and shape<sup>14, 22</sup>.

#### 1.1.1.2 Characterisation

The methodologies used by researchers to prepare BLMO materials varies greatly, and as such there is great variation in the structure, morphology, and structural order of the resulting materials<sup>23</sup>. There are several techniques utilised to characterise BLMO materials. These include imaging techniques such as Scanning Electron Microscopy (SEM) and Transmission Electron Microscopy (TEM), along with elemental spectroscopic techniques such as X-ray Photoelectron Spectroscopy (XPS) and X-ray Absorption Near Edge Spectroscopy (XANES),

with the most predominantly used technique being X-ray Diffraction (XRD). BLMO materials typically have major diffraction peaks at  $\sim 7$  and  $\sim 3.5 \text{ \AA}^{24}$ , which correspond to the interlayer distance, further diffraction peaks can be observed at  $\sim 2.5$ ,  $\sim 2.2$ , and  $\sim 1.9 \text{ \AA}^{24}$ , which correspond to the  $\text{MnO}_6$  layers. However, the quality of diffraction patterns can be influenced by the long-range structural order of the material, the x-ray source utilised and the length of analysis<sup>5</sup>. The more disordered a sample is, the greater peak broadening and potential peak collapse. The purity of the prepared material is dependent on the method of synthesis; for example, alkaline synthesis methods have been reported to contain hausmannite ( $4.86, 3.05, 2.74, 2.47, 2.3, 2.02 \text{ \AA}$ )<sup>25</sup> and feiknechtite ( $4.62, 2.63, 2.36, 1.96 \text{ \AA}$ )<sup>26</sup> as minor impurities<sup>27-28</sup>. An example diffraction pattern of a synthetic BLMO can be seen in Figure 1-2, which shows the presence of BLMO, hausmannite, feiknechtite, and the expected peak locations of the three phases.

XRD patterns that contain defined peaks and no impurities can be further analysed via Rietveld refinement, which results in an approximation of the unit cell substructure of the materials. The unit cell for triclinic BLMO can be seen in Figure 1-3, showing the a, b and c unit cell parameters, which correspond to the spacings between manganese atoms in the layer structure (a and b) and the distance between the layers (c)<sup>5</sup>.

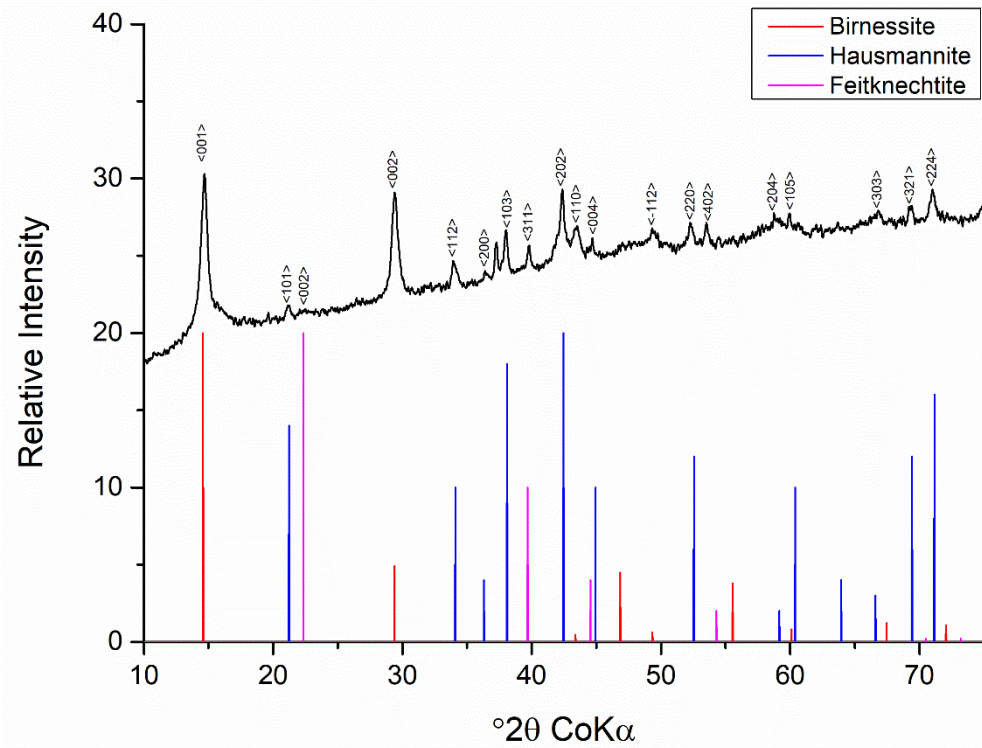


Figure 1-2: CoK $\alpha$  diffraction pattern of triclinic BLMO materials synthesised in an alkaline environment, showing the expected peaks for BLMO, hausmannite, and feitknechtite.

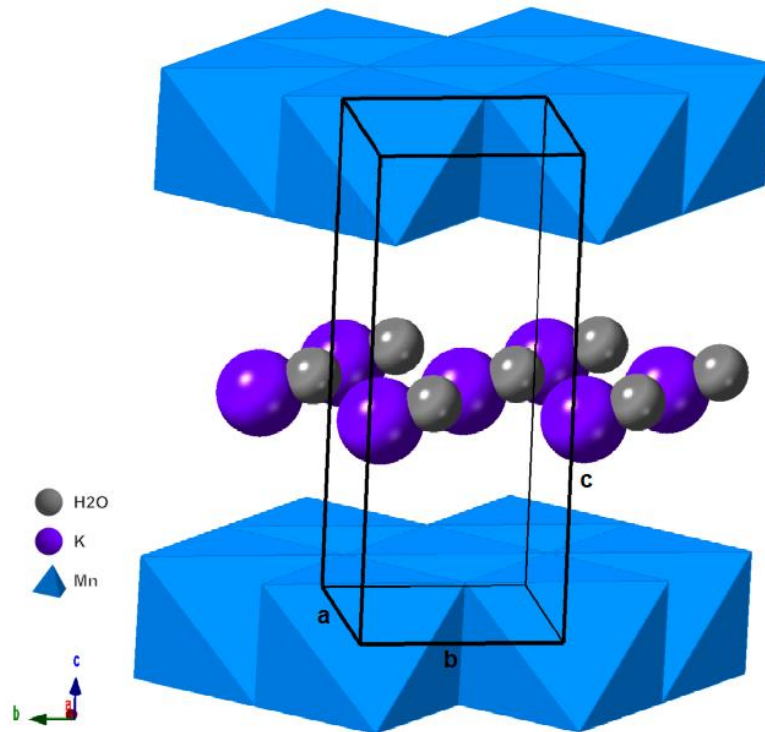


Figure 1-3: BLMO crystal structure showing the triclinic unit cell

Morphology determination is also a common characterisation method utilised for BLMOs, with either Scanning Electron Microscopy or Transmission Electron Microscopy being conducted by researchers<sup>29-31</sup>. Typically, synthesised BLMO structures have a plate-like morphology<sup>5</sup> (Figure 1-4e), however, the morphologies can consist of spherical clusters, nanoflowers (Figure 1-4a), and wires (Figure 1-4c) depending on the preparation method<sup>32</sup>.

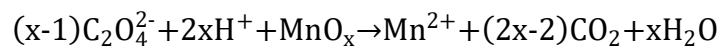
Figure 1-4 has been removed due to Copyright restrictions.

**Figure 1-4: SEM images of a) nanoflower, c) nanowire, and e) nanosheet BLMO morphologies and TEM images of b) nanoflower, d) nanowire and f) nanosheet BLMO morphologies, taken from Hou *et al.*<sup>32</sup>**

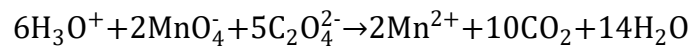
The final piece of information commonly reported while characterising a BLMO material is the oxidation state of the manganese present in the materials. This is reported into two ways, either as the average oxidation state or as a percentage breakdown of  $\text{Mn}^{2+}/\text{Mn}^{3+}/\text{Mn}^{4+}$ <sup>33-35</sup>.

The average oxidation state is typically determined using a two-step process. The first step involves wet chemistry such as the oxalate/oxalic acid-permanganate back titration to determine the levels of high valent Mn. Here, a sample of MO is reacted with excess oxalate to reduce  $Mn^{3+/4+}$  to  $Mn^{2+}$  (Equation 1-1)<sup>34</sup>, followed by a titration of the remaining oxalate with  $KMnO_4$  to determine the amount of oxalate reacted (Equation 1-2)<sup>36</sup>. This is followed by the second step which is used to determine the total quantity of Mn present, and is determined either by a colorimetric test, Atomic Absorption Spectroscopy (AAS), or Inductive Coupled Plasma techniques (ICP)<sup>34</sup>.

**Equation 1-1**



**Equation 1-2**



To determine the exact quantities of  $Mn^{2+}/Mn^{3+}/Mn^{4+}$  a technique that can distinguish between the different oxidation states is required. Two techniques that have been utilised to achieve this are X-ray Photoelectron Spectroscopy (XPS)<sup>37</sup> and X-ray Absorption Near Edge Structure (XANES)<sup>38</sup>. XPS uses x-rays to eject electrons from the surface of a material, and subsequent analysis of the energy of the electrons provides information on the source element and the binding energy of the electron<sup>39</sup>. The resulting spectra can be analysed using peak fitting to determine the oxidation states of metals, Ilton *et al.*<sup>37</sup> developed a XPS fitting method for the determination of Mn oxidation state ratios using the Mn3p and Mn3s absorption lines (Figure 1-5a). In contrast, XANES involves the excitation of electrons to higher energy states, which provides information about the unoccupied electron states<sup>40</sup>. Manceau *et al.*<sup>38</sup> demonstrated the use of XANES for the determination of Mn oxidation state in several manganese oxides (Figure 1-5b).

Figure 1-5 has been removed due to Copyright restrictions.

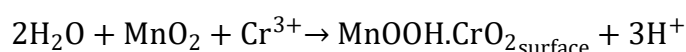
**Figure 1-5: a) XPS spectra of hexagonal BLMO from Ilton *et al.*<sup>37</sup> b) XANES spectra of various manganese oxides from Manceau *et al.*<sup>38</sup>**

#### 1.1.1.3 Uses in literature

BLMOs have been reported to have a wide variety of uses from catalysis<sup>41-42</sup>, semiconductors/supercapacitors<sup>16, 43-44</sup>, batteries<sup>22, 45-47</sup>, to the adsorption of heavy metal ions<sup>48</sup>. Interest in the oxidative properties of manganese minerals has resulted in a large body of research being conducted worldwide, mainly focusing on the oxidation of organic molecules such as formaldehyde<sup>49-59</sup>, ethyl acetate<sup>60-63</sup>, as well as various substituted aromatics<sup>60, 64-74</sup>. BLMOs have demonstrated an ability to oxidise chromium (III) in solution<sup>75-78</sup>. Through XPS analysis of the surface of the minerals, it was proposed by Banerjee *et al.*<sup>75</sup> that Cr<sup>3+</sup> binds to the surface of the BLMO and undergoes multiple one step electron transfers

until Cr<sup>5+</sup> and Mn<sup>2+</sup> are formed and released into the solution (Equation 1-3, Equation 1-4 and Equation 1-5 respectively)<sup>75</sup>. Intermediate oxidation states of Mn<sup>3+</sup> and Cr<sup>4+</sup> were observed to occur on the surface as well as in the solution, suggesting that the pathway can be interrupted. A similar process has been suggested for the oxidation of arsenic, where manganese oxides were shown to oxidise As<sup>3+</sup> to As<sup>5+</sup> <sup>79-81</sup>.

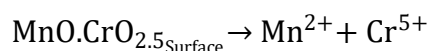
**Equation 1-3**



**Equation 1-4**



**Equation 1-5**



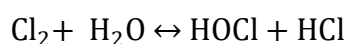
All the metal oxidation cases presented so far have involved the oxidation of aqueous metal complexes. Studies conducted by Ta *et al.*<sup>82</sup> and Bartle *et al.*<sup>83</sup> have demonstrated that BLMO suspensions in acidified saline solutions are able to oxidise Au<sup>0</sup> to Au<sup>3+</sup>. Bartle achieved a dissolved gold concentration of 114 ppm after 7 days of Au(0) exposure to an acidic 0.1M sodium chloride solution containing BLMO at 20 °C<sup>83</sup>. A proposed mechanism for the dissolution of gold via manganese oxide was put forward by Emmons<sup>84</sup> and Boyle<sup>85</sup>. They proposed that dissolved chlorine gas is produced by the reaction of MnO<sub>2</sub> with acidic sodium chloride (Equation 1-6). This is the mechanism hypothesised for the work of Ta and Bartle<sup>82-83</sup>, where the acidic saline solution when combined with BLMO results in the slow production of dissolved chlorine, which subsequently dissociates in acidic aqueous solutions to hypochlorous acid and hydrochloric acid (Equation 1-7). It is likely that it is the dissolved

chlorine and hypochlorous acid that are the reactive agents that proceed to oxidise and dissolve elemental metal.

**Equation 1-6**



**Equation 1-7**



### 1.1.2 Tunnelled manganese oxide materials

#### 1.1.2.1 Structure

Tunnelled manganese oxides (TSMOs) are comprised of chains of edge sharing  $\text{MnO}_6$  octahedra, where neighbouring chains are linked at the corners to form square/rectangular cross-sections, which form 'tunnels'<sup>1</sup>. The number of octahedra joined in this manner can vary, resulting in a wide variety of crystal structures such as 1x1 (pyrolusite), 2x1 (ramsdellite), 2x2 (hollandite-type), and 3x3 structures (todorokite) (Equation 1-4)<sup>1</sup>, (where 1 represents 1 octahedra in the chain). Much like layered manganese oxides, these tunnel spaces can contain cations, water molecules or remain empty. The most common type of tunnel structure reported in application literature are cryptomelane structures (2x2 tunnels containing  $\text{K}^+$ ).

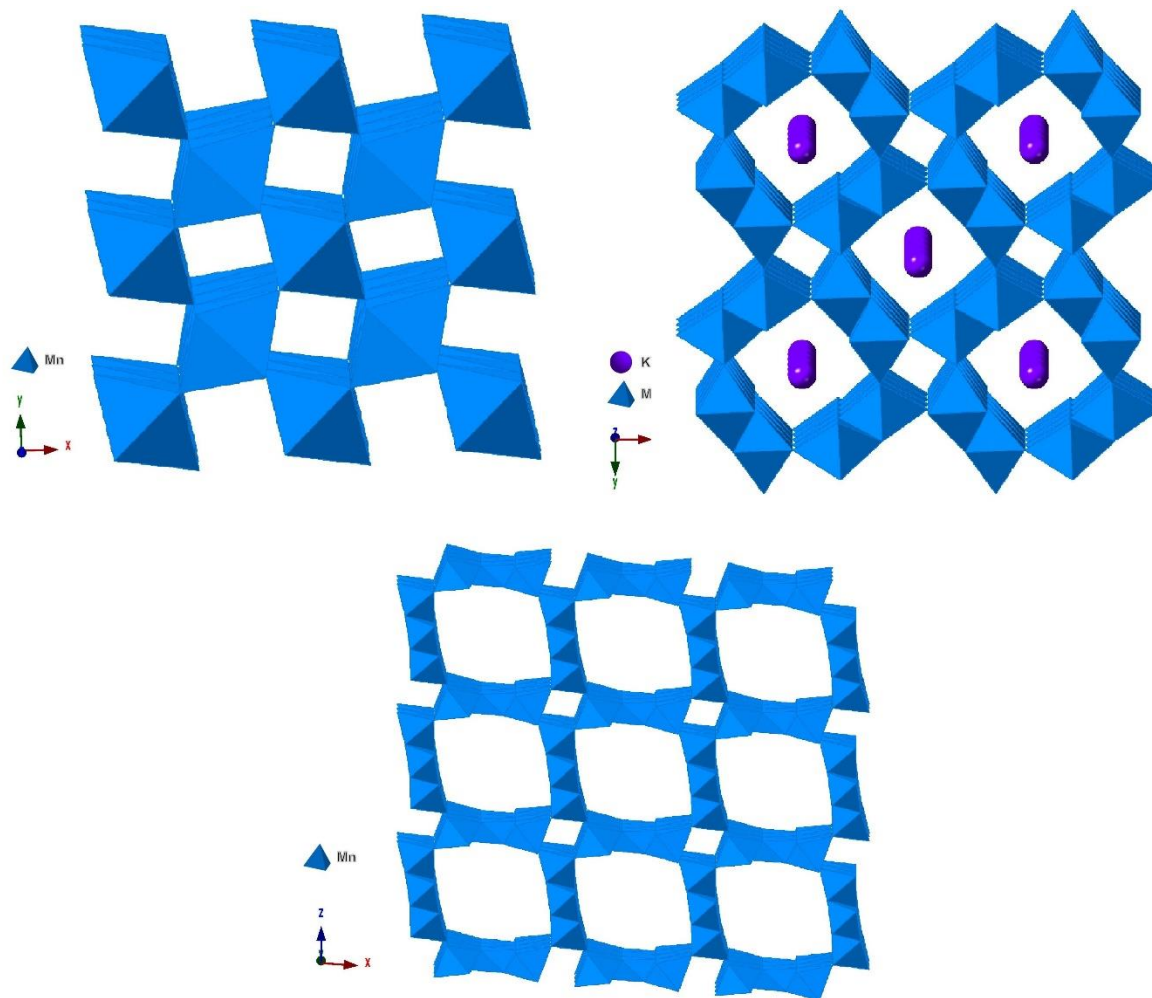


Figure 1-6: Diagrams showing the crystal structure of pyrolusite (top left), cryptomelane (top right), and todorokite (bottom). Structures were recreated using CrystalMaker from CIF structure files from structure determination papers<sup>86-88</sup>.

### 1.1.2.2 Characterisation

The main characterisation techniques for BLMOs are also utilised for TSMOs. Pyrolusite is the simplest TSMO and as such it produces a simple diffraction pattern with the major diffraction peak found at  $\sim 3.1 \text{ \AA}$ <sup>89</sup> (Figure 1-7a), which corresponds to an integer of the distance between diagonally opposite  $\text{MnO}_6$  octahedra through the unit cell. Cryptomelane has several major diffraction peaks at 6.91 and 3.09  $\text{\AA}$ <sup>90</sup> that correspond to the diffractions along diagonally opposite  $\text{MnO}_6$  octahedra. It also diffracts at 2.39 and 1.82  $\text{\AA}$ <sup>90</sup> due to diffraction through adjacent tunnels, as well as at 4.89  $\text{\AA}$ <sup>90</sup> which is a result of a diffraction off a plane that passes

through a single tunnel. Whereas, the diffraction patterns of todorokite diffraction patterns will typically have major peaks at 9.7, 4.8, 2.39, 1.4 and 1.3 Å<sup>91</sup>. Unit cell diagrams for the three TSMOs are shown in Figure 1-8, where it can be seen that the unit cell distances correspond to different distances within the tunnels.

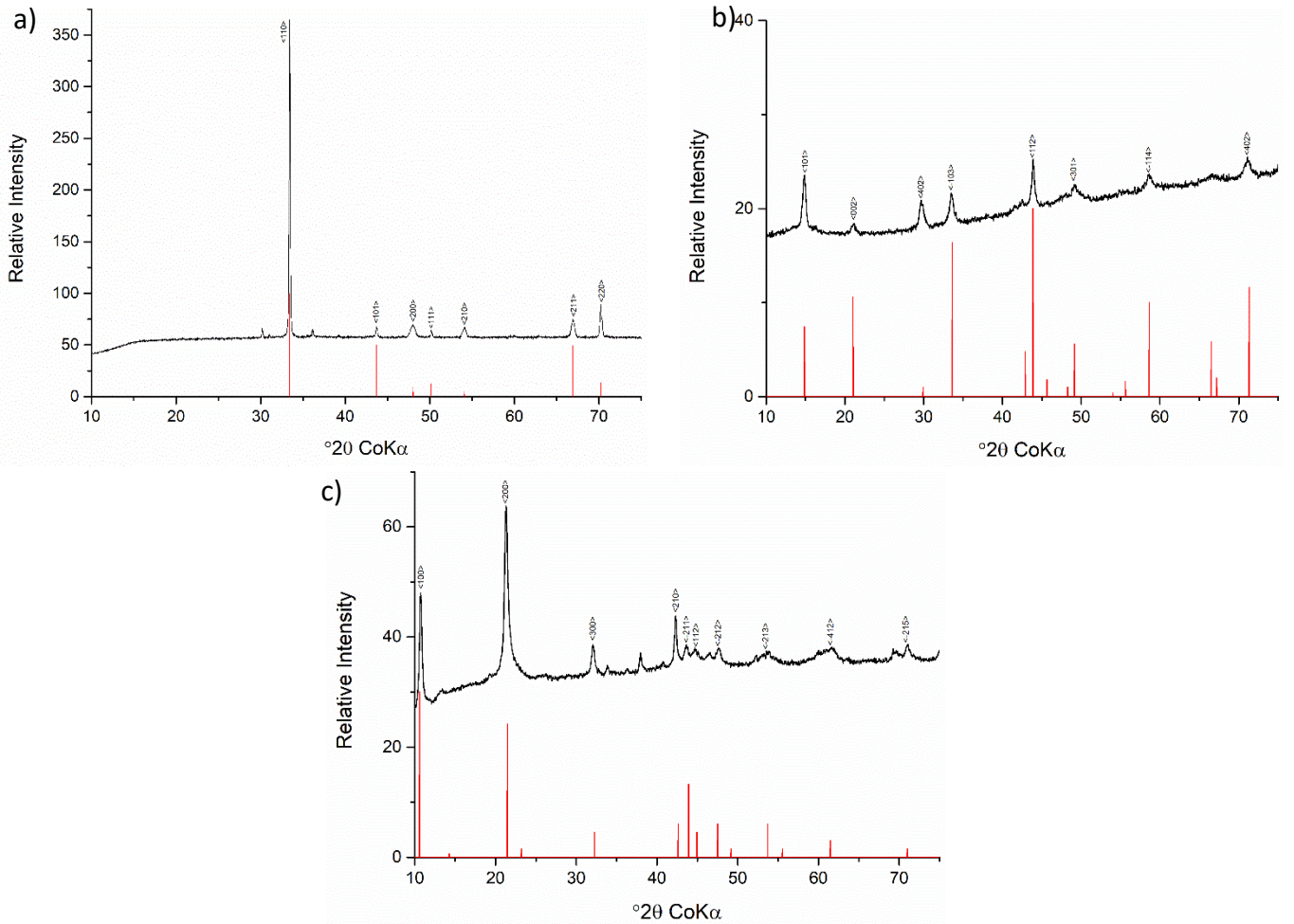


Figure 1-7: CoK $\alpha$  diffraction patterns and the expected peaks for a) pyrolusite, b) cryptomelane, and c) todorokite, black= experimental diffraction pattern, red=expected diffraction pattern.

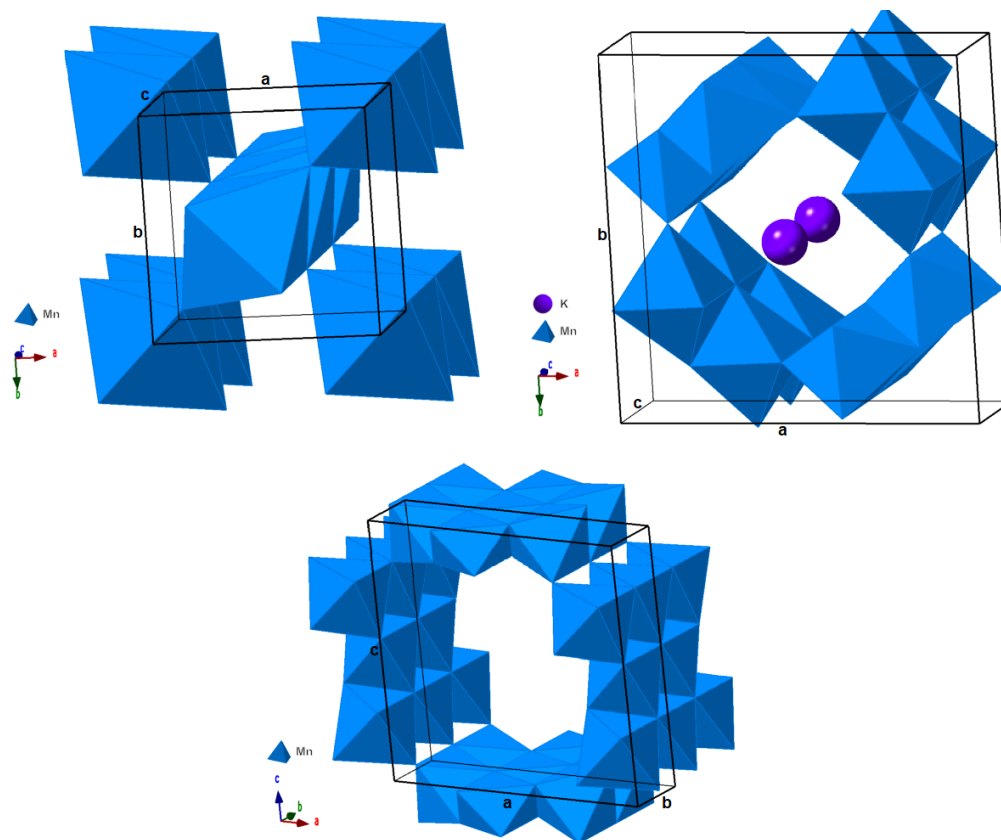


Figure 1-8: Unit cell diagrams of TMOs a) pyrolusite, b) cryptomelane, and b) todorokite.

### 1.1.2.3 Uses in literature

Research utilising TSMOs primarily focuses on the oxidation and degradation of organic compounds. In these cases, the manganese oxide typically acts as a catalyst rather than a direct oxidant. For example, Opembe *et al.*<sup>92</sup> utilised cryptomelane materials to catalyse the selective oxidation of vaporised benzyl alcohol to benzaldehyde using oxygen, while Genuino *et al.*<sup>93</sup> used similar conditions to achieve the oxidation of benzene, toluene, and xylenes to CO<sub>2</sub> and H<sub>2</sub>O. Son *et al.*<sup>94</sup> achieved the conversion of various benzylic and allylic alcohols in a toluene liquid phase with cryptomelane. TSMOs have been also been combined with peroxymonosulfate in aqueous solutions to achieved the degradation of organic dyes such as acid orange, methylene blue, and rhodamine B<sup>95</sup>. Unlike layered manganese oxides, the use of tunnel structured manganese oxides to oxidise metals has not been as extensively

researched with only two papers found showing the oxidation of  $\text{As}^{3+}$  to  $\text{As}^{6+}$  <sup>96-97</sup> by tunnel structured manganese oxides.

## 1.2 Metal oxidation and extraction

### 1.2.1 Transition Metal Extraction

One potential application of manganese oxide-based oxidations is the extraction of transition metals from ores or other metal sources such as electronic waste. Transition metals are found in groups 3 - 12 of the periodic table and have partially filled d and f subshells<sup>98</sup>. This group includes some of the most commonly used metals, including metals with high abundance (e.g. iron and copper) and very low abundance (e.g. gold and palladium)<sup>99</sup>. Transition metals have a variety of interesting physical and chemical properties; they are high density metals, durable, can easily form alloys with each other, and typically have variable electron valence<sup>98</sup>. The partially filled d and f subshells allow transition metals to exist in various oxidation states and therefore transition metals are very good electrical conductors<sup>98</sup>. The uses of transition metals are varied; iron and copper are used in structural and building applications<sup>100</sup>, whereas the more unreactive and rare metals such as gold, platinum and palladium are used for jewellery, electrical circuitry and catalysts<sup>100</sup>. A summary of some of the natural abundances and common oxidation states of various transition metals can be seen in Table 1.

**Table 1: Summary of percentage abundances and common oxidation states of a selection of common and rare transition metals<sup>99</sup>**

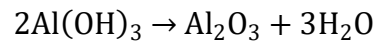
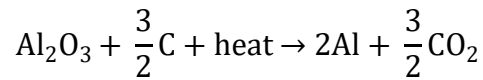
Transition Metal Element	Natural Abundance in the Earth's Surface (%)	Common Oxidation States
Au	$4 \times 10^{-7}$	0, +1, +3
Ag	$8 \times 10^{-6}$	0, +1
Cu	0.0068	0, +3, +2
Fe	6.2	0, +2, +3
V	0.0136	0, +2, +3, +4, +5
Ni	0.0099	0, +2, +3
Zn	0.0076	0, +2
Pd	$1.5 \times 10^{-6}$	0, +2
Pt	$1 \times 10^{-6}$	0, +2, +4
Rh	$1 \times 10^{-8}$	0, +3

Transition metals are extracted from ores and minerals that are mined from ore deposits all around the world. These mined ores are generally mixtures of metals in complex mineral structures<sup>101</sup>. This leads to a range of complex processes to separate the different elements from the ore. The simplest metal extraction is that of reactive metals such as iron and zinc, which involves the reduction of the metal oxides to metallic metal by reaction with carbon at very high temperatures (Equation 1-8)<sup>102</sup>.

**Equation 1-8**



An example of complex mining processing is that of aluminium which is mined as the ore bauxite (which contains various aluminium oxide minerals and several iron oxide minerals). Here, bauxite is converted to gibbsite and then refined to alumina ( $\text{Al}_2\text{O}_3$ ) using the lengthy Bayer refining process<sup>103</sup> (Equation 1-9) and is then smelted through the molten electrolysis of the alumina to form metallic aluminium (Equation 1-10)<sup>104</sup>.

**Equation 1-9****Equation 1-10**

These extraction procedures are not 100% efficient and do not work well with unreactive metals such as gold, silver and platinum. As a result, chemical leaching methods are used to concentrate and recover the remaining metal in mine waste and to extract and purify metals such as gold and silver.

The chemical extraction of metals is typically based on the aqueous oxidation of metals in the presence of a stabilising ligand. A chemical oxidant is used to increase the oxidation state of the metal (Equation 1-11) and a ligand is used to stabilise the charged metal species so that it remains in solution (Equation 1-12).

**Equation 1-11****Equation 1-12**

## 1.2.2 Gold

Gold is a precious metal typically found in its elemental oxidation state, due to its lack of reactivity towards air and most acids<sup>98, 105</sup>. Various oxidants and ligands have been investigated for gold oxidation and extraction from ore materials over the years, such as mercury, cyanide, thiosulfate and chlorine. Several reviews of each process have been conducted<sup>106-111</sup>.

### 1.2.2.1 Extraction using mercury

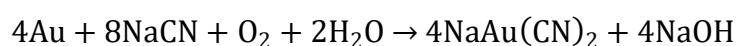
Mercury amalgamation was the original method for gold and silver extraction and is thought to have been in use as early as 50 AD<sup>112</sup>. Throughout history there have been periods of increased mercury use for extraction, from the Romans in 77 AD to Spanish Mexico during the 1600s<sup>105</sup>. The main benefit of mercury amalgamation is that it is a simple process, with little training or chemical knowledge required for its successful use. The process involves covering crushed ore containing gold with mercury, which adsorbs to the surface of the gold particles and forms an amalgam. The amalgam is removed either by panning or gravity, and the mercury is then burned off to leave the impure gold which is purified by smelting<sup>113</sup>. The drawback of this method is that there are a number of ways mercury can be released into the environment, including in a soluble form in tailing solutions after panning and in an airborne form after the burning of mercury during the removal of mercury and the smelting process<sup>113</sup>. The latest United Nations Global Mercury Assessment conducted in 2010 estimated that between 410-1040 tonnes per year of mercury is released into the atmosphere by artisanal and small-scale gold mining<sup>114</sup>. The effects of mercury exposure depend on the form of mercury, with the lethal doses of mercury (II) chloride in water and mercury vapour being 7.15 mg/kg and 1429 mg/kg respectively<sup>115</sup>. Most progressive mining companies have replaced mercury amalgamation with cyanidation. However, there are a large number of

mining companies/sites in developing countries and China that still use mercury because it is cheap<sup>113</sup>.

#### 1.2.2.2 Oxidation of gold using cyanidation

In 1783, Carl Wilhelm Scheele discovered that combining gold with aqueous solutions of cyanide resulted in the dissolution of gold<sup>116</sup>. Nearly a century later in 1887, John MacArthur, Robert Forrest and William Forest developed the MacArthur-Forrest process to utilise cyanide solutions to extract gold and silver from ores<sup>117</sup>, providing an alternative to mercury. The cyanidation of gold occurs via the reaction outlined in Equation 1-13, and typically involves placing the crushed ore in a leach heap and mixing with an alkaline solution containing high levels of cyanide<sup>118</sup>.

#### Equation 1-13



The metal is oxidised over time to form a metal cyanide complex, these complexes are soluble and are removed from the solid rock through filtration. Although the cyanidation process is simple and efficient, the chemicals required are toxic and hazardous to worker health. Ingestion of cyanide salts causes dizziness, vomiting and increased heart rate, and when a lethal dose is ingested convulsions and death generally occur within minutes<sup>119</sup>. The lethal dose of hydrogen cyanide has been stated to be anywhere between 0.54 mg/kg to 3 mg/kg<sup>120</sup>. Cyanide leaching is also used for reprocessing mine tailings (waste that has come from mining processes), this causes more opportunity for health risks as there can be more incidents where the cyanide is accidentally released into the environment. Despite this, cyanide leaching is still in use worldwide although its use is significantly more controlled because of its effectiveness at leaching metals into solution.

Efforts towards increasing the efficiency of the cyanidation first involved the manipulation of the reaction (Equation 1-13). This was achieved by increasing the concentration of NaCN and O<sub>2</sub>, to increase the rate of reaction<sup>121</sup>. However, this approach was found to be problematic when the ores contained sulfide minerals as these would react with oxygen from the system before it could participate in the cyanidation reaction<sup>122</sup>. Subsequently, the addition of lead nitrate to the reaction vats was found to increase the dissolution of gold even when sulfide minerals were present<sup>123</sup>. Pre-oxidation of the gold in sulfide ores by hydrogen peroxide has also been found to increase the rate of cyanidation from ores that contain high levels of sulfur<sup>124-125</sup>. Current mining processes contain ways to monitor and control the concentration of oxygen and cyanide<sup>122</sup>. This 'chemical' cyanidation process has an extraction efficiency of 50-90%<sup>126</sup> and depending on the grade of ore uses, between 200-600 mg/L of cyanide<sup>127</sup>.

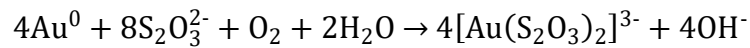
Another improvement to the cyanidation process is the addition of treatment methods, where the free cyanide in solution is converted into less toxic forms such as thiocyanate, ammonia, nitric acid and carbonate<sup>128</sup>. This has been achieved through several chemical and microbial processes<sup>128</sup>, enabling the cyanide levels to be reduced back to manageable levels when they become too high. Although several alternatives to cyanidation are known, they do not compete with cyanidation in terms of economics and efficiency in all ore applications<sup>129</sup>. Two of the most promising ligands/reactions for gold solubilisation are thiosulfate and chloride.

#### 1.2.2.3 Oxidation of gold using thiosulfate

Thiosulfates were originally found to dissolve gold in the early 1900s<sup>130</sup>, but had minimal incorporation into mining process in Mexico and South America and did not become widespread due to issues with extraction from copper-based ores<sup>106</sup>. This persisted until the development of an improved method utilising ammoniacal thiosulfate<sup>131-132</sup>, which overcame

the issues with copper-based ores. The thiosulfate reaction involves several different reagents and is a complex process when compared to the cyanidation reaction<sup>129</sup>, the net reaction can be seen in Equation 1-14 below<sup>107</sup>.

**Equation 1-14**

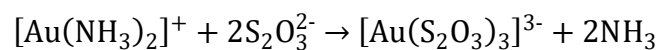


This complex reaction is the result of three reactions that involve gold in its elemental state, a copper ammonium complex, thiosulfate, and oxygen. The first step consists of the initial oxidation of Au(0) by copper(II) tetraamine which forms the kinetically favoured diaminoaurate(I) complex (Equation 1-15)<sup>107</sup>. A ligand exchange then occurs between the ammonium and thiosulfate ligands to form the thermodynamically favoured aurothiosulfate(I) complex (Equation 1-16)<sup>107</sup>. While this ligand transfer is occurring the copper (II) tetraamine complex is regenerated via oxidation with dissolved oxygen (Equation 1-17)<sup>107</sup>.

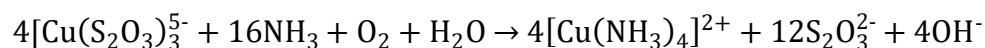
**Equation 1-15**



**Equation 1-16**



**Equation 1-17**



A problem presented by using thiosulfate in leaching processes is the decomposition of thiosulfate and the build-up of sulfur coatings on the surface of the gold, which cause the leaching process to slow and eventually stop. The presence of ammonia in the solutions

prevents this build-up of sulfur by preferentially binding to the gold surface, it also stabilises the copper (II) species<sup>106</sup>. The presence of copper acts as a catalyst in the dissolution of gold by replacing oxygen as the oxidant and increases the dissolution by a factor of ~20<sup>133</sup>, but the copper also catalyses the decomposition of thiosulfate. Extraction efficiencies of ~80%<sup>134</sup> are achieved in the absence of sulfur bearing ores and this decreases when sulfur ores are present<sup>135</sup>. The complexity of the process combined with the variability in ore compositions and the high reagent consumption of the thiosulfate reaction (14.5 kg/ton) when compared to the cyanide reaction (0.15 kg/ton)<sup>136</sup> hinders the widespread use of ammoniacal thiosulfate as a leaching method, due to the variability in ore compositions.

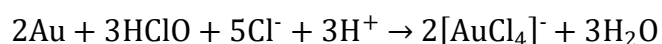
#### 1.2.2.4 Oxidation of gold using chlorine

The extraction of gold using chlorine has been known since the late 1848, when Karl Plattner achieved the dissolution of gold using chlorine gas and chlorine water<sup>137</sup>, and was utilised in Australia and North America until it was replaced by the more economical cyanidation methodology<sup>111</sup>. However, now that more is known about the health effects of cyanide, processes utilising chlorine are re-emerging<sup>138</sup>. Chlorination processes use chloride with various oxidising agents, the two main chloride reactions involve either chlorine gas as the oxidant (Equation 1-18) or hypochlorous acid (Equation 1-19)<sup>138</sup>. Both reactions have been theorised to form a gold(I) chloride intermediate at the surface of the gold and then subsequent oxidation to gold(III) tetrachloride occurs once it moves into solution<sup>139</sup>.

##### Equation 1-18



##### Equation 1-19



Extraction efficiencies of these reactions can range from 60-100%<sup>138, 140-141</sup>, but like thiosulfate leaching they also have the disadvantage of increased reagent consumption and decrease in dissolution rate when using chlorine gas on sulfur-bearing ores<sup>138</sup>. Since chloride is the preferred ligand for gold due to an increased rate of dissolution for  $\text{AuCl}_4^-$  over  $\text{Au}(\text{CN})_2^-$ <sup>142</sup>, research has focused on finding different oxidants such as ozone<sup>143</sup> and hydrogen peroxide<sup>144</sup>. The problem with  $\text{AuCl}_4^-$  is that it is an unstable gold complex<sup>145</sup> and is only stable in solutions of high chloride ion concentration and a pH of less than 2.

The use of chloride as a complexing agent for the chemical leaching of gold is one of the most promising, because it has a quicker rate of dissolution than cyanide complexes, is less toxic than other ligands, and is easily available. The main issue with the chloride system is the lack of an appropriate oxidant and the potential for exposure to chlorine gas in certain systems.

### 1.2.3 Vanadium

Vanadium is a metal rarely found in its elemental oxidation state<sup>146</sup> due to its reactivity at elevated temperatures towards oxygen, nitrogen and carbon, resulting in a variety of vanadium minerals<sup>98</sup>. However, it is a metal that is resistant to oxidation and corrosion by air, water, alkali, and non-oxidising acids except  $\text{HF}$ <sup>98</sup>. This chemical resistance combined with its tensile strength and shock resistance has resulted in its inclusion into iron alloys<sup>147</sup>. The use of vanadium in ferrous and non-ferrous alloys is expected to increase, as the demand for improved materials increases and because vanadium has also gained increasing interest in battery applications due to its wide range of oxidation states.

Extraction of vanadium from its various ores was originally achieved via a roast-leach-precipitation process, where the ore is combined with sodium chloride and heated to high temperatures, to form sodium metavanadate<sup>147</sup>. This intermediate compound is then exposed to sulfuric acid, which causes the conversion to and subsequent precipitation of

vanadium pentoxide as the final form of vanadium<sup>147</sup>. However, the roasting of sodium chloride can cause the release of chlorine gas and hydrochloric acid gas, which forced the development of a new extraction method<sup>148</sup>. This method involves chemical leaching in concentrated sulphuric acid either at atmospheric pressure or at high pressure. The extraction rates of vanadium using this process are ~75%<sup>148</sup>, however, the highly acidic conditions result in the extraction of other elements commonly found in the ores (Fe, K, Mg). These impurities have led to difficulty in purifying the final leachate solutions, causing an increase in research investigating the separation of these elements. Successful separation has been achieved using ionic liquids<sup>149</sup>, ion exchange resins<sup>150-152</sup> and solvent extractions<sup>153-154</sup>.

### 1.3 E-Waste

The rapid advancement of technology over the past few decades has increased the amount of electronic waste produced globally. Electronic waste is a term that covers a broad range of items from monitors and IT equipment to larger equipment such as washing machines and solar panels<sup>155</sup>. In 2010, 33.8 million tonnes<sup>156</sup> of electronic waste was generated worldwide, while only 6 years later this value increased to 44.7 million tonnes<sup>155</sup>. Current projections estimate the e-waste production for 2020 at ~51 million tonnes<sup>155</sup>. As of 2016, only 20% of e-waste was recycled<sup>155</sup>, with the rest either incinerated or dumped into landfills. A specific component of e-waste is printed circuit boards (PCBs), found in computers, phones and other electronic devices. PCBs have a high metal content, which ranges from common metals such as Cu, Sn, Pb, and Ni<sup>157</sup> to rarer metals such as Au, Ag and Pd<sup>158</sup>. Interest in the recovery of metals from PCBs has increased due to the economic value of recovering precious metals from secondary sources and the cost of mining diminishing deposits of precious metals<sup>159-160</sup>. Current industrial recycling processes generally involves grinding of the PCBs, followed by pyrometallurgical processes<sup>161</sup>. The pyrometallurgical process employed at Aurubis involves

using the Kayser Recycling System to separate the copper from the iron, zinc, tin and lead present in the PCBs<sup>162</sup>. This 95% pure copper smelt is then cast into anodes and electrowinned to both separate the precious metals such as gold and silver, and remove nickel as an electrolyte by-product<sup>162</sup>.

Research into metal extraction from PCBs is mostly focused on improving the separation stage of metal recovery. This is split into three methodologies: 1) pyrometallurgical, 2) hydrometallurgical, and 3) biometallurgical. Pyrometallurgical extraction of metals is the traditional route employed<sup>163</sup>, which involves the incineration/smelting and electrolysis of the ground e-waste. This is currently the preferred method due to its ability to recover metals from any type of electronic scrap, but has disadvantages in the lack of metal selectivity, energy cost and the released pollutants<sup>163</sup>. Current pyrometallurgical research is focused on investigating ways to limit the toxicity of incineration by-products through the use of filters<sup>164</sup> and alkaline molten salts<sup>165</sup>. Hydrometallurgical extraction processes typically employ acidic or alkaline medium to achieve the dissolution of metals from ground<sup>166</sup> or chemically pre-treated<sup>163</sup> PCBs. This process is safer, has a lower overhead cost, and is more selective than pyrometallurgical processes. Current hydrometallurgical research is focus on the development of greener, more sustainable extraction techniques such as ionic liquids<sup>167-168</sup>, glycine<sup>169-170</sup> and supercritical CO<sub>2</sub><sup>171-172</sup>. Another avenue of research is looking for more effective pre-treatments<sup>166, 173</sup> and the addition of multistep processes<sup>174</sup>.

## 1.4 Instrumentation

### 1.4.1 X-Ray Diffraction

X-ray Diffraction (XRD) is a technique used to determine the structure and composition of crystalline materials and is typically used for the analysis of minerals. Diffraction of x-rays was first observed in 1912 when Max van Laue observed that crystalline samples can act as three-dimensional diffraction gratings<sup>175</sup>. Combined with Bragg's diffraction Law ( $n\lambda=2d\sin\theta$ )<sup>176</sup> (where  $n$  is an integer,  $\lambda$  is the wavelength of incident x-rays,  $d$  is the distance between atoms and  $\theta$  is the angle of incidence/diffraction), XRD allows for the determination of the spacing between atoms and as a result allows the determination of the crystal structure of materials<sup>177</sup>.

X-ray generation is achieved through the interaction of an electron beam with a metal target, where the wavelength of the x-rays is determined by the metal composition of the target, common targets include tungsten ( $0.21 \text{ \AA}$ )<sup>178</sup>, copper ( $1.54 \text{ \AA}$ )<sup>178</sup> and iron ( $1.93 \text{ \AA}$ )<sup>178</sup>. Using the appropriate x-ray wavelengths is important because wavelengths that are close to the excitation bands of certain materials can cause fluorescence, which causes difficulty in the interpretation of the diffractogram<sup>177</sup>. The x-rays are monochromated through a filter before interacting with the sample of interest<sup>175</sup>.

Sample interaction with x-rays can result in two outcomes i) absorption of the x-rays or, ii) scattering of the x-rays. Absorption of the x-rays by the atoms results in the ejection of an electron from the sample<sup>176</sup> and scattering produces various diffracted x-rays that can cause destructive or constructive interference as determined by Bragg's Law. Constructive interference occurs when the x-rays travel a path that is a whole integer value of the incident wavelength (Figure 1-9a). For Bragg diffraction, the x-rays are considered as reflecting from

sets of parallel planes of atoms in the structure, therefore Bragg diffraction only occurs in materials with a regular 3D arrangement of atoms (i.e. crystalline materials).

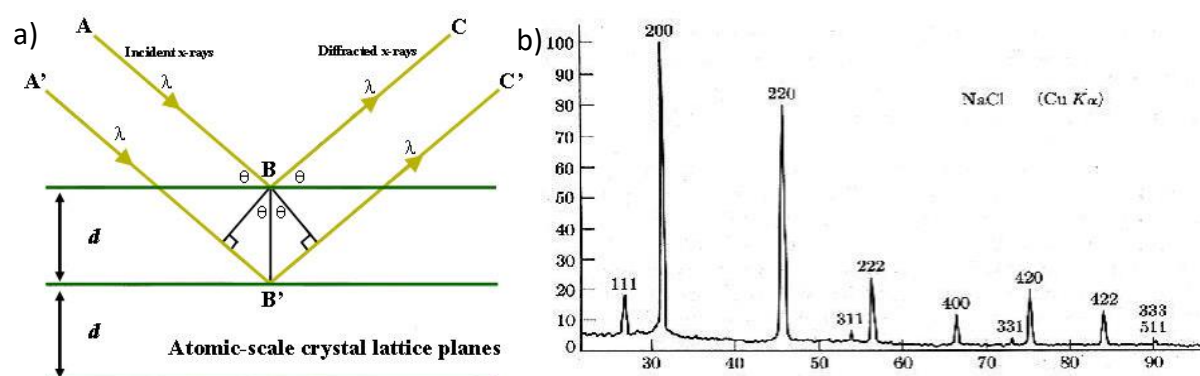


Figure 1-9: a) A diagram showing the diffraction of x-rays through a sample, indicating that the angle of incidence is the same as the angle of diffraction. b) CuK $\alpha$  diffraction pattern of NaCl<sup>179</sup>.

When constructive interference occurs, the resulting diffracted x-rays travel out of the sample and are collimated into a detector which records the intensity of the diffracted X-rays; where no diffraction has occurred, no signal is recorded<sup>175</sup>. The angle of incidence is varied throughout the analysis so that all the possible values of  $\theta$  are explored for a powdered sample. This results in a signal vs angle of incidence ( $2\theta$ ) plot, which forms a diffractogram (Figure 1-9b). A diffractogram can be used to calculate the spacing between the atoms of the crystal and to determine the spacing of crystal lattices. These features are unique to each mineral and therefore XRD is an excellent technique for mineral structure identification.

Two commonly used diffraction geometries exist for instrument orientation, i) Bragg-Brentano and ii) Debye-Scherrer. Bragg-Brentano is the most common geometry utilised in the laboratory setting, due to avoiding the need for monochromatisation and the resulting loss in beam intensity<sup>180</sup>. This geometry involves keeping the angle of x-ray incidence equal to the angle of detection, with the ability to vary these angles during analysis, the sample is placed in the centre of rotation of the tube and detector (Figure 1-10a)<sup>177</sup>. Contrastingly, Debye-Scherrer geometries involves centring the sample in a system where the sample is surrounded by a photographic plate (Figure 1-10b). This allows for analysis of all diffraction

angles, reduces the effect of preferred orientation of diffraction patterns and requires a small amount of sample<sup>177</sup>. The Debye-Scherrer orientation is preferred for conducting Rietveld analysis on samples due to reducing the effect of peak-shape distortion and sample preferred orientation<sup>177</sup>.

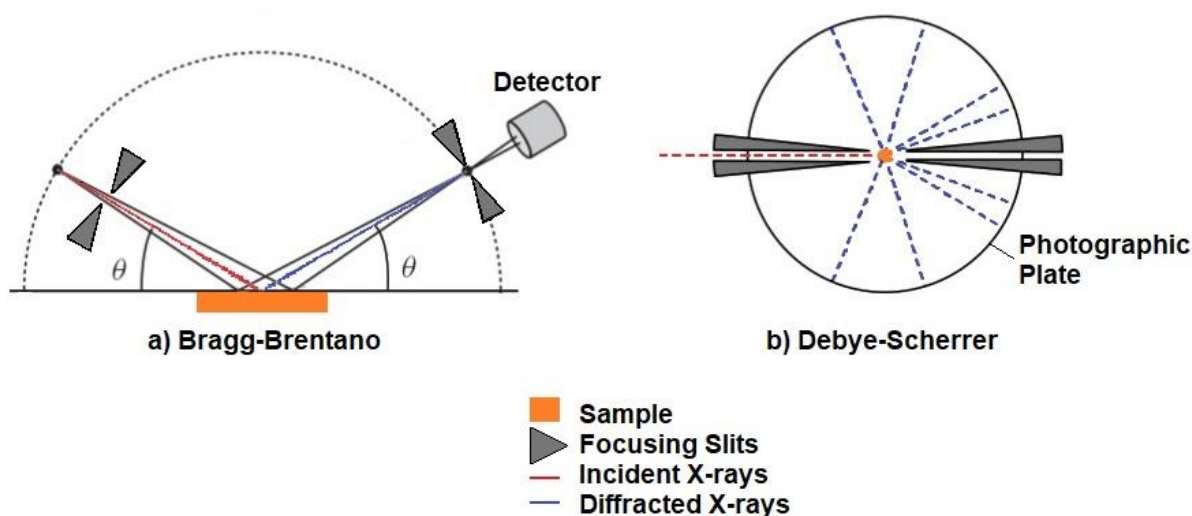


Figure 1-10: Diagram showing the two common geometries utilised in X-ray diffraction, a) Bragg-Brentano and b) Debye-Scherrer. Images modified from Modern Diffraction Methods<sup>177</sup>.

#### 1.4.2 Rietveld Refinement

Rietveld refinement is a data analysis technique developed by Hugo Rietveld in 1969<sup>181</sup> that can be conducted on powder x-ray diffraction data of crystalline materials to elucidate its crystal structure. This procedure takes starting structure information from a material that has an analogous structure to the material of interest and then overlays a theoretical diffraction pattern with the experimentally determined diffraction pattern. Structural parameters (atom positions, occupancy factors, and temperature), unit cell parameters, background coefficients and profile parameters (peak shape and instrumental considerations) are varied using the least squares method to refine this theoretical model until it best matches the observed diffraction pattern. This results in a refined crystal structure that would cause the experimental diffraction pattern. The structural information refined for BLMOs and TSMOs can be useful in determining any structural variances between samples which could result in

differences in effectiveness for application purposes, for example, unit cell and octahedra distortions due to differences in interlayer species.

### 1.4.3 Scanning Electron Microscopy

Scanning Electron Microscopy (SEM) is an imaging technique that is similar to an optical microscope; however, instead of using light to generate an image it utilises a beam of electrons. The first image produced via the interaction of an object with a beam of electrons was produced by Max Knoll in 1935<sup>182</sup>, followed by the development of the first dedicated SEM instrument by Manfred von Ardenne in 1937<sup>183</sup>. It then took 30 years for the first commercial SEM to be produced by a Cambridge research group headed by Charles Oatley<sup>184</sup>. SEM is based on the interaction of an electron beam with a sample, these interactions can vary and result in unique outputs that can be detected (Figure 1-11). The most common of these are secondary electrons, which are formed when the incident electrons release loosely bound electrons on the surface of the sample through inelastic scattering. These secondary electrons have an energy of approximately 2-50 eV<sup>185</sup>, which allows for the easy detection of secondary electrons through a simple positively charged collector grid that diverts in the electrons towards a photomultiplier tube<sup>185</sup>. Due to these electrons being emitted from the first few nanometres of the sample, it results in the production of an image that gives surface and topological information about the sample.

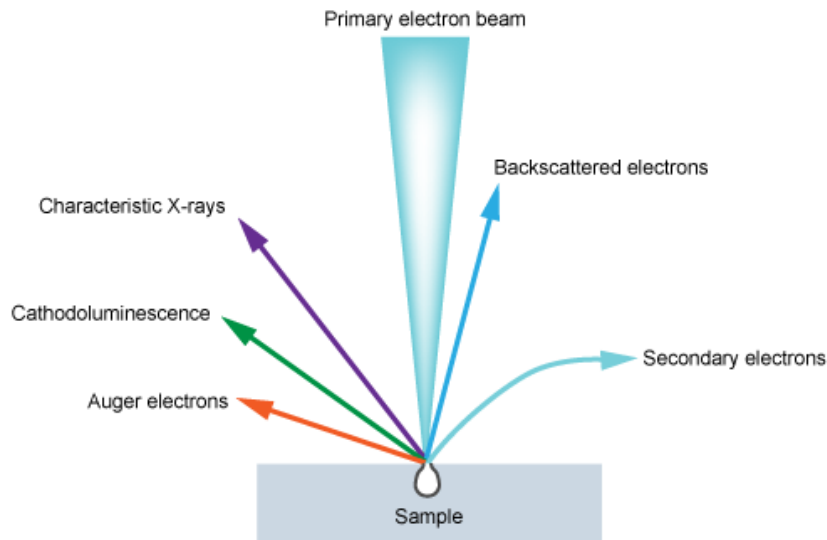


**Figure 1-11: A diagram showing some of the outputs caused by the interaction of an electron beam with a sample<sup>186</sup>.**

Another output utilised by researchers are backscattered electrons, which occur when the incident electrons are elastically scattered by the sample which results in a trajectory change of more than  $90^\circ$ <sup>187</sup>. These scattered electrons are from deeper in the sample, and the quantity of backscattered electrons produced is dependent on the atomic number of elements, the higher the average atomic number of the sample, the more backscattered electrons will be produced and the lighter those sections of the image will be<sup>187</sup>. Therefore, backscattered electrons are useful in determining the elemental composition of the sample and producing images showing the compositional variation in a sample. Backscattered electrons have energies in the keV range which is dependent on the power of the electron beam<sup>185</sup>. This high energy means that the electrons' trajectory cannot be altered as easily as secondary electrons, therefore a large detector is present next to the aperture of the electron beam to collect the backscattered electrons.

The last output of interest in this work is the production of characteristic x-rays. These are formed by the incident electrons interacting with a tightly bound electron in the sample, which causing the ejection of an electron from the inner electron shells of interacting atom. This ejection results in the shifting of an electron from a higher energy electron shell into the

lower energy electron shell, causing the release of the excess energy as an x-ray<sup>187</sup> (Figure 1-12). The energy gaps between electron shells are unique to each element and therefore the emitted x-rays have unique energies and can be used to identify the emitting atom. The x-rays emitted in a SEM are collected using a lithium drifted silicon detector and used to identify the atoms present in the sample analysed, this analysis technique is called Energy Dispersive X-ray Spectroscopy (EDXS).

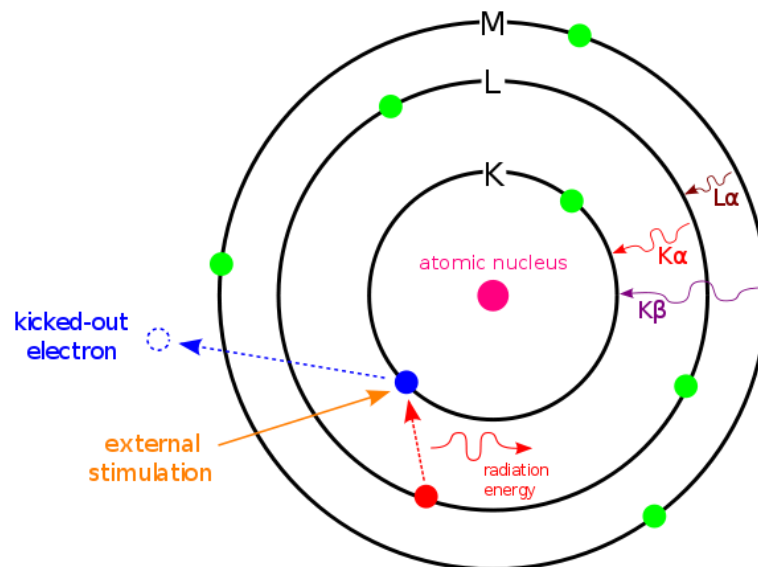


**Figure 1-12: Schematic of the atomic events that produces characteristic x-rays for EDX<sup>188</sup>.**

SEM is a technique favoured by nanotechnologists and is useful to other research fields, due to the wide variety of information that can be gained. The high resolution (~10 nm) and magnification that can be achieved with SEM allows for the imaging of minute samples that are on the order of nanometres to micrometres. The SEM has various instrumental components which can be seen in Figure 1-13, the most important being the electron gun/column and detectors<sup>187</sup>. The electron gun produces electrons from a tungsten target and the electrons are accelerated down the electron column towards the sample at a set energy (0.1-30 keV). The electron column is composed of electromagnetic lenses that decrease the electron beam diameter to a set size. This focused beam can then be rastered

across the surface of the sample with the aid of tuneable scan coils to produce the interaction outputs that are collected by various detectors.

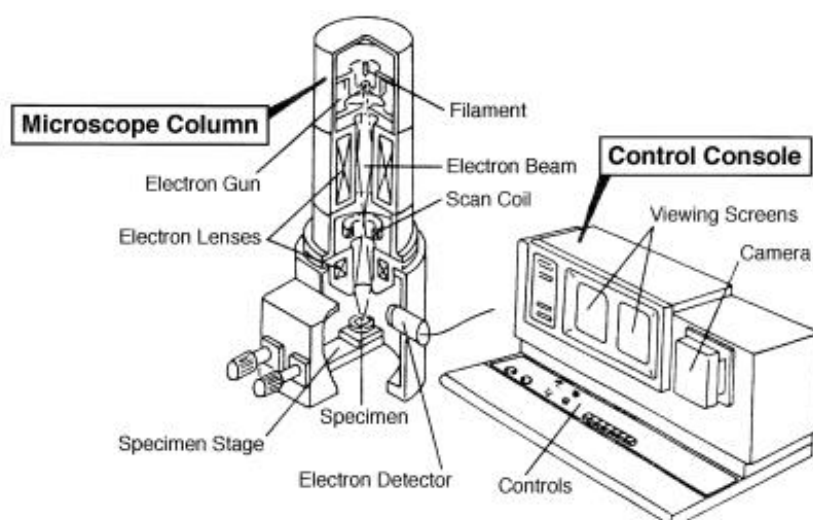


**Figure 1-13: A schematic of the instrumentation involved in an SEM<sup>187</sup>.**

#### 1.4.4 Raman Spectroscopy

Raman spectroscopy is a technique used to characterise materials based on the interaction of monochromatic laser light with molecules. It utilises the phenomena discovered in 1928 by Raman and Krishnan, who found that monochromatic light is scattered inelastically by molecules, where the emitted photons are at lower (Stokes) or higher energies (Anti-Stokes) than the incident light<sup>39</sup>. This difference in photon energy can be analysed to give information about the vibrational modes present in the molecule, which in turn is used to identify the structural bonds and atoms in the molecules. Manganese oxide materials have been found to exhibit unique Raman shifts based on their crystal structure<sup>189</sup>, and unlike XRD, Raman spectroscopy can provide structural information about amorphous and crystalline materials<sup>190</sup>. Dr Jeffrey Post has also shown that the Raman shifts present in Raman spectra of layered and tunnelled structured manganese oxides has the potential to be used to distinguish between different cations and different Mn oxidation states present in BLMO materials<sup>191</sup>. Therefore, Raman spectroscopy has potential to become routinely used in the analysis of manganese oxides materials,

### 1.4.5 Inductively Coupled Plasma Mass Spectrometry

Inductively Coupled Plasma Mass Spectrometry (ICP-MS) is a mass spectrometry technique that utilises a plasma to ionise samples of interest, a schematic is shown in Figure 1-14. Aqueous samples are aerosolised by a nebuliser before being introduced via a spray chamber to a hot argon plasma (~6500 K), which subsequently atomises and ionises the sample<sup>192</sup>. Upon ionisation, the charged sample is passed through an interface and focused by an ion lens which filters any neutral or negatively charged atoms<sup>192</sup>. If required the ion beam can then be passed through a reaction chamber, where interactions between the ion stream and a gas (typically He) can occur, these interactions result in the removal of doubly charged or polyatomic ions that may cause interferences when analysing for certain elements. Once this has occurred, the ion stream is focused into a quadrupole to separate the remaining ions based on their mass and charge by applying alternating currents between the rods of a quadrupole<sup>192</sup>. This allows for the detection of specific elements based on their molecular weight<sup>192</sup>, and has therefore found much interest in the field of trace metal analysis in aqueous systems.

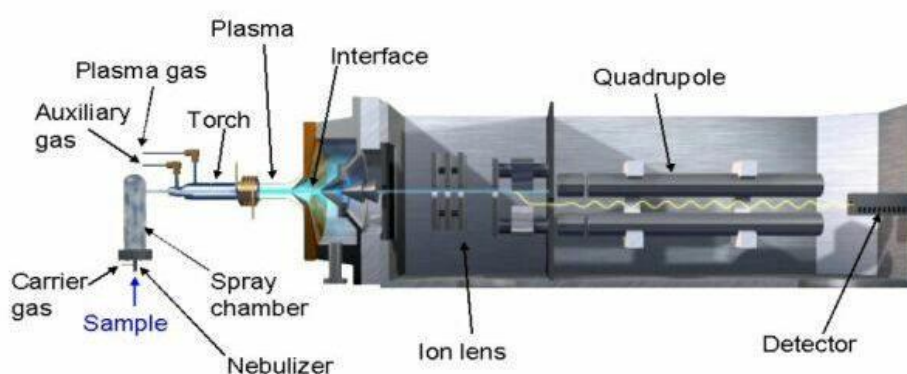


Figure 1-14: Schematic diagram of an ICP-MS <sup>193</sup>.

## 1.5 Project aims

There are a limited number of studies that investigate multiple BLMO materials for their chosen application, and with the wide variety of synthesis methods used it is difficult to compare the studies in literature. This lack of a comprehensive selection of materials used for an individual application and the variability observed in the results reported demonstrates the need for a systematic study into the effect of BLMO structure on its application effectiveness. The minimal research into utilising BLMO materials for the oxidation and subsequent dissolution of elemental metals provides a new application to focus this systematic study on. There is also a lack of research into extending BLMOs oxidative abilities to develop greener, less harsh methodologies for the recovery of metals from ore and electronic waste. This project aimed to address this knowledge gap by the following sub aims:

1. Investigate the effect of BLMO synthesis method and post synthesis modifications on the unit cell structure of the resulting BLMO materials (Chapter 3).
2. Investigate the effectiveness of each BLMO for oxidising V(0) in acidic saline solutions, with subsequent investigation into the structural factors causing a variability in effectiveness (Chapter 4).
3. Extend the structural and application study to several TSMO materials, and also conducted a preliminary comparison into the effectiveness of these BLMO and TSMO structures for oxidising Au(0) (Chapter 5).
4. Investigate the feasibility of utilising BLMO materials in an acidic saline solution for the extraction and recovery of metals from electronic waste (Chapter 6).

## Chapter 2 General Methods

### 2.1 X-Ray Diffraction Analysis

The identities and phase purity of the manganese oxide samples prepared during this project were determined using powder X-ray Diffraction (XRD) using three different instruments.

The main instrument used was a D8 Eco Diffractometer (Bruker, USA) equipped with  $\text{CoK}\alpha$  radiation and utilised Bragg-Brentano geometry (Flinders University). Samples were disaggregated with a mortar and pestle before analysis and were distributed evenly on powder diffraction disks with the aid of acetone. The diffraction patterns were collected with x-rays generated at 35 kV and 28 mA, with the sample spun on phi ( $10^\circ/\text{s}$ ), over the angle range of  $10\text{-}75^\circ 2\theta$  over a 43-minute run time.

The second XRD instrument used was a Rigaku II D/MAX-RAPID microdiffractometer (Rigaku, Japan) equipped with  $\text{MoK}\alpha$  radiation, a graphite monochromator, a 0.3mm collimator and utilised Debye-Scherrer geometry (Smithsonian Institution, Department of Mineral Sciences). Small single clumps ( $\sim 1$  mm) of sample were mounted onto glass fibres and were spun on phi ( $1^\circ/\text{s}$ ). The x-rays used to collect these diffraction patterns were 50 kV and 40 mA and were analysed over the angle range of  $3\text{-}45^\circ 2\theta$  over a 5-minute run time.

The third instrument used for several samples was a Rigaku 9 kW SmartLab Diffractometer (Rigaku, Japan) with a fixed slit of  $0.1^\circ$ , utilising  $\text{CuK}\alpha$  radiation and Bragg-Brentano geometry (CSIRO Land and Water). The diffraction patterns were collected with x-rays generated at 45 kV and 200 mA, over the range of  $10\text{-}78^\circ 2\theta$  over 106 hours.

## 2.2 Rietveld Refinement

Rietveld refinements<sup>181</sup> were performed for all prepared samples using the General Structure Analysis System-II (GSAS-II) software<sup>194</sup>. Calibrations for instrumental peak broadening profile parameters were conducted using diffraction data generated from a corundum standard. The background intensities were fitted with a Chebyshev function using 7 terms. A two-step refinement process was undertaken. Firstly, Mn-O bond lengths were constrained to 1.92 Å and the background parameters, scale factor, unit-cell parameters, peak profile coefficients and atomic parameters were allowed to vary. Upon completion of this refinement, the bond lengths were set as unconstrained and atomic positions were allowed to vary.

## 2.3 Scanning Electron Microscopy/Energy Dispersive Spectroscopy

Scanning Electron Microscopy (SEM) images were captured on samples adhered to aluminium stubs with carbon tape and were imaging was conducted on an Inspect FEI F50 SEM (FEI, Thermo Fisher Scientific, USA). Beam parameters consisted of a spot size of 4, beam voltage of 10 kV and a typical image collection time of 30 μs. Elemental composition was investigated via Energy-Dispersive X-ray Spectroscopy (EDXS) using an Ametek EDAX system (Ametek, USA) coupled with TEAM software. A SEM image of the areas of interest were collected and EDXS spectra were captured via spot spectra, the EDXS spectra were collected using a spot size of 4, 10 kV and an acquisition time of 30 seconds.

## 2.4 Raman Spectroscopy

Raman spectra for the manganese oxide samples were collected using a HORIBA LabRam HR Evolution (Horiba, Japan) equipped with deep-depleted thermoelectrically cooled charge coupled device array detector and an optical microscope (Smithsonian Institution, Department of Mineral Sciences). All measurements were made at 25 °C. All powders were

lightly pressed onto glass discs for Raman analysis. Sample areas were analysed using an Olympus 100× objective, an integration time of 30 s, and at a spectral resolution of  $2\text{ cm}^{-1}$  using a 784 nm solid state laser. Two to four acquisitions per spot were set to improve the signal-to-noise ratio. Low laser power was used to minimize sample alteration by heating; the laser power on the sample was measured to be  $\sim 300\text{ }\mu\text{W}$ . The spectrometer was fitted with a holographic notch filter and 300 g/mm grating and was controlled using the Horiba LaBSPEC6 software.

## 2.5 Average Manganese Oxidation State Determination

Average manganese oxidation state of each material prepared was determined using modified methods outlined by Zhu *et al.*<sup>34</sup>.

Firstly, the total number of moles of  $\text{Mn}^{3+}$  and  $\text{Mn}^{4+}$  (combined) was determined by oxalate back titration with  $\text{KMnO}_4$ <sup>195</sup>. Here, 0.1 g of synthetic manganese oxide was completely reacted with excess sodium oxalate in an acidic aqueous solution ( $\text{Na}_2\text{C}_2\text{O}_4$ , 10 mL, 0.26 M) and sulfuric acid ( $\text{H}_2\text{SO}_4$ , 10 mL, 1 M), the remaining oxalate was then titrated at 80 °C with aqueous  $\text{KMnO}_4$  (75 mM). Secondly, the total number of moles Mn was determined by a formaldoxime colorimetric test<sup>196</sup>, where 0.01 g of synthetic manganese oxide was dissolved in aqueous hydroxylamine ( $\text{NH}_2\text{OH}\cdot\text{HCl}$ , 50 mL, 0.01 M) to reduce the high valent Mn to  $\text{Mn}^{2+}$  and diluted by a factor of 10 in water. A 10% formaldoxime solution was prepared by dissolving hydroxylamine hydrochloride (5 g) in formaldehyde (5 g, 30% v/v), diluted to 100 mL, and then basified to pH 10 with NaOH. For analysis 2 mL of the diluted sample was combined with 2 mL of the formaldoxime solution, allowed to react for 15 min and then analysed via UV-vis at 450 nm. Mn concentrations were determined by comparison to calibration curve (1-18 ppm  $\text{Mn}^{2+}$ ).  $\text{Mn}^{2+}$  standards were prepared by aqueous dilution of a 1000 ppm standard.

## 2.6 Standard Oxidation Reaction Conditions

Unless otherwise specified, oxidation experiments consist of an acidified aqueous solution of sodium chloride (pH 2, 0.05 M NaCl, 100 mL), containing 20 mg of elemental metal and 200 mg of solid manganese oxide material, that has been manually sieved to a size range of <125 µm. Oxidation solutions are kept in polypropylene containers (250 mL, Sarstedt Australia), and the temperature and rotation were kept constant using various orbital incubators. After the reaction time has elapsed, solutions are either diluted and analysed immediately or were frozen at -20 °C.

## 2.7 Inductively Coupled Plasma Mass Spectrometry

The concentration of dissolved metals was determined using Inductively Coupled Plasma Mass Spectrometry (ICP-MS, PerkinElmer NexION 350D). The standard ICP-MS operating conditions used during analysis can be seen in Table 2-1. The plasma was allowed to stabilise for 20 minutes before a daily tune and performance check was conducted with a tuning analyte solution (100 ppb Be, Ce, Fe, In, Li, Mg, Pb, and U), the minimum count values for a successful tune can be seen in

Table 2-2. Daily tuning was conducted by the optimisation of the torch alignment, nebulizer gas flow, and the quadrupole ion deflector (QID), followed optimisation of the QID for kinetic energy discrimination (KED) analysis mode. After tuning was completed, an internal standard was introduced via a T piece and allowed to stabilise until the counts of the internal standard became consistent over a three-and-a-half-minute period with a relative standard deviation of <3%. Once the internal standard was stable, samples were analysed. The preparation method for the samples was dependent on the element/s to be analysed and are outlined below.

**Table 2-1: ICP-MS instrumental operating conditions**

<b>Component/Parameter</b>	<b>Type/Value/Mode</b>
Nebulizer	Quartz, Meinhard 0.5 mm I.D.
Spray Chamber	Quartz glass cyclonic w/Peltier cooler
Injector	Sapphire 1.8 mm
Torch	High Matrix demountable quartz
Triple cone interface material	Nickel
Plasma gas flow	18 L/min
Auxiliary gas flow	1.2 L/min
Nebulizer gas flow	0.86-0.96 L/min
RF Power	1,600 W
Sweeps per reading/replicates per sample	10 sweeps/3 replicates

**Table 2-2: Minimum criteria for ICP-MS analysis**

<b>Analyte Element</b>	<b>Target</b>
Be 9	>2,000 counts
In 114	>40,000 counts
U 238	>30,000 counts
CeO 156/Ce 140	<0.015
Ce <sup>2+</sup> 70/Ce 140	<0.3

### 2.7.1 Vanadium analysis

For the determination of dissolved V content, samples were analysed in a nitric acid matrix (2%, Choice Analytical, Australia), where samples were diluted by a factor of 500 to ensure a concentration within the calibration range. Particulate BLMO material was removed from the diluted solutions via syringe filtering (PVDF, 0.45 µm, Kinesis Australia). Calibration standards were prepared fresh for each analysis via dilution from a 1000 ppm V stock solution (ACR Elemental Standard) to concentrations of 50 ppb, 100 ppb, 150 ppb and 200 ppb. A 5% HNO<sub>3</sub> rinse/wash solution was utilised between samples to ensure no carryover occurred with a wash time of 75 seconds.

### 2.7.2 Gold analysis

The concentration of dissolved Au was determined in a similar manner to vanadium, but a reverse aqua regia matrix (2%, 3:1 HNO<sub>3</sub>:HCl, Choice Analytical, Australia) was used for these samples, and samples were diluted by a factor of 2000 to ensure a concentration within the calibration range. Particulate BLMO material was removed from the diluted solutions via syringe filtering (PVDF, 0.45 µm, Kinesis Australia). Calibration standards were prepared fresh for each analysis via dilution from a 1000 ppm Au stock solution (High Purity Standards) to concentrations of 5 ppb, 10 ppb, 25 ppb, and 50 ppb. A 5% reverse aqua regia rinse/wash solution was utilised between samples to ensure no carryover occurred with a wash time of 120 seconds.

### 2.7.3 Multielement analysis

The concentration of dissolved metals was determined in a similar manner to vanadium and gold, however, an aqua regia matrix (2%, 1:3 HNO<sub>3</sub>:HCl, Choice Analytical, Australia) was used for these samples, and samples were diluted by a factor of 1000 to ensure concentrations within the calibration range. Particulate BLMO material was removed from the diluted solutions via syringe filtering (PVDF, 0.45 µm, Kinesis Australia). Calibration standards were prepared fresh for each analysis via dilution of 100 ppm multielement quality control stock solution (High Purity Standards, Ag, Al, As, B, Ba, Be, Ca, Cd, Co, Cr, Cu, Fe, K, Mg, Mn, Mo, Na, Ni, Pb, Sb, Se, Si, Sr, Ti, Tl, V, and Zn) to concentrations of 1 ppt, 0.1 ppb, 1 ppb, 10 ppb and 100 ppb. Additional Sn, Ni and Cu were added to the standard solutions to achieve higher standard concentrations of 0.5 ppb, 5.5 ppb, 55 ppb, 550 ppb, and 5500 ppb, and Au was also added to the stock solution to achieve concentrations of 1 ppt, 0.1 ppb, 1 ppb, 10 ppb, and 100 ppb. A 5% aqua regia rinse/wash solution was utilised between samples to ensure no carryover occurred with a wash time of 60 seconds.

## 2.8 General reagents

The chemicals used in this study can be found listed in Table 2-3, where aqueous solutions were required, high-purity water (MilliQ, 18.2 M $\Omega$ ) was used. The vanadium powder was determined via SEM to have a wire-like morphology and had a typical diameter of 20 nm and various lengths (Figure 2-1), whereas the gold utilised was spherical with diameters ranging from 1  $\mu\text{m}$  to  $\sim 7.5 \mu\text{m}$  (Figure 2-2).

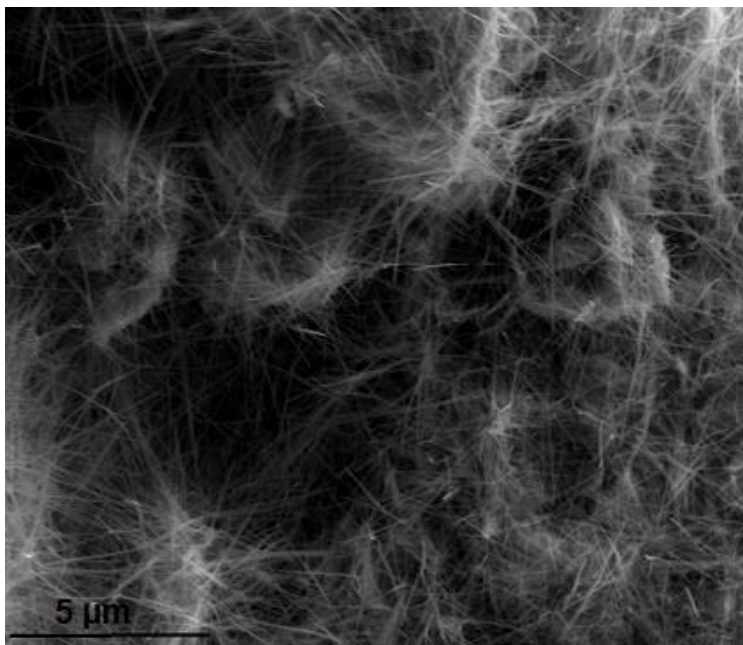


Figure 2-1: SEM image showing the morphology and size of the vanadium powder used throughout this work

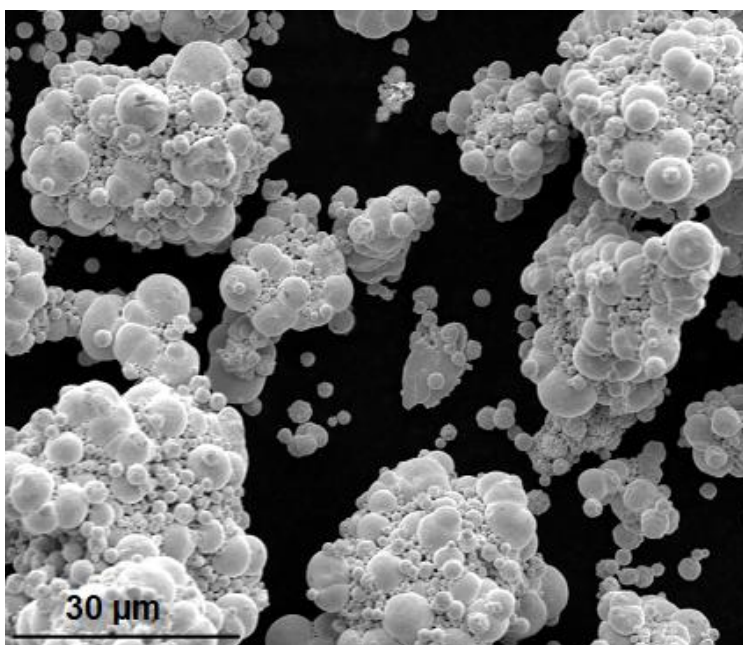


Figure 2-2: SEM image showing the morphology and size of the gold powder used throughout this work

**Table 2-3: The chemicals used throughout this study**

Chemical	Supplier	Grade	Purity/Concentration
27 Element Quality Control Standard	High Purity Standards	Analytical	100 µg/L
Acetic acid	RCI Labscan	Analytical	99.90%
Acetone	Chem-supply	Reagent	99%
Au Powder	Alfa Aesar	Reagent	99.60%
Au Standard	High Purity Standards	Analytical	1000 mg/L
Calcium chloride	Sigma Aldrich	Reagent	99%
Citric acid	Chem-supply	Reagent	Not Stated
Copper filings	Chem-supply	Reagent	99.90%
Copper Standard	High Purity Standards	Analytical	1000 mg/L
Ethanol	Chem-supply	Reagent	99%
Formaldehyde	Chem-supply	Reagent	37%
Hydrobromic acid	Sigma Aldrich	Reagent	48%
Hydrochloric acid	Sharlau	Analytical	34.70%
Hydrochloric acid	Choice Analytical	Analytical	37%
Hydroxylamine hydrochloride	Sigma Aldrich	Reagent	99%
ICP-MS tuning solution	Perkin Elmer	Analytical	1 µg/L
Iron filings	Chem-supply	Reagent	Not Stated
Lead filings	Chem-supply	Reagent	99.90%
Lithium chloride	Sigma Aldrich	Reagent	99%
Magnesium chloride	Merck	Analytical	98.50%
Manganese acetate	Sigma Aldrich	Reagent	99%
Manganese Chloride tetrahydrate	Sigma Aldrich	Reagent	99%
Mn Standard	BDH Chemicals	Analytical	1000 mg/L
MnO <sub>2</sub>	Chem-supply	Reagent	97%
Nickel powder	Hopkins and Williams	Reagent	Not Stated
Nickel Standard	ACR Elemental Standard	Analytical	1000 mg/L
Nitric acid	Choice Analytical	Analytical	67-69%
Palladium powder	Strem Chemicals	Reagent	99.95%
Platinum powder	Strem Chemicals	Reagent	99.90%
Potassium acetate	M&B Ltd	Laboratory	99%
Potassium bromide	Ajax Chemicals	Analytical	98.50%
Potassium chloride	Chem-supply	Analytical	99%
Potassium Permanganate	Sigma Aldrich	Reagent	99%
Rhodium powder	Strem Chemicals	Reagent	99.95%
Sn Standard	ACR Elemental Standard	Analytical	1000 mg/L
Sodium bromide	Sharlau	Reagent	99.50%
Sodium chloride	Chem-supply	Analytical	99.70%
Sodium chloride	Merck	HPLC	Not Stated
Sodium hydroxide	Chem-supply	Analytical	98%
Sodium lactate	Sigma Aldrich	Not Stated	90%
Sodium oxalate	BDH Chemicals	Reagent	99.90%
Sulphuric acid	Merck	Analytical	95-97%
V Powder	Hopkins and Williams	Reagent	Not Stated
V Standard	ACR Elemental Standard	Analytical	1000 mg/L

## Chapter 3 Synthesis and Characterisation of Birnessite-Like

### Manganese Oxides

#### 3.1 Introduction

Birnessite ( $\text{Na}_x\text{MnO}_2 \cdot y\text{H}_2\text{O}$ ) and birnessite-like manganese oxide materials (BLMOs,  $\text{A}_x\text{MnO}_2 \cdot y\text{H}_2\text{O}$ , where A is a cation other than  $\text{Na}^+$ ) have been reported to have important oxidative<sup>77, 197</sup>, catalytic<sup>71</sup> and semiconducting properties<sup>198</sup>. For example, they have been shown to either directly oxidize or catalyse the oxidation of various organic molecules including formaldehyde<sup>58, 199</sup>, benzene<sup>73</sup>, 1,2-diols<sup>200</sup>, and antibiotics<sup>201</sup> along with oxidizing dissolved heavy metal cations such as  $\text{Cr}^{3+}$ ,  $\text{As}^{3+}$ , and  $\text{Au}^+$  in solution<sup>32, 75, 77-78, 82, 197, 202</sup>. They have also been reported to be a suitable electrode materials in rechargeable batteries<sup>198, 203-204</sup> and to be able to adsorb toxic heavy metal ions such as Pb, As, Sb, and Tl<sup>30, 48, 81, 205-206</sup>. Natural samples of birnessite ( $\text{Na}_x\text{MnO}_2 \cdot y\text{H}_2\text{O}$ ), are typically i) fine grained, ii) poorly crystalline, and iii) contain various impurities<sup>1</sup>, and thus synthetic BLMOs are used in most research applications.

Synthetic BLMOs are highly variable in terms of preparation method, structure, crystallite size, and purity<sup>18, 33, 44, 64, 207-208</sup>. Indeed, a family of BLMOs can be synthesized with differing interlayer cations. Recently, Sabri *et al.*<sup>23</sup> showed that the structural topology and layer stacking disorder can be critical factors that affect the reactivity of the synthesized material. Their research showed that more ordered materials were better catalysts whilst more disordered materials were better oxidants. Application results can be quite variable, for example, Ghodbane *et al.*<sup>198</sup> reports a value of  $225 \text{ Fg}^{-1}$  for the specific capacitance of BLMOs, whereas Zhou *et al.*<sup>209</sup> report a value of  $158 \text{ Fg}^{-1}$ . Whilst some research groups take great pains to ensure that the materials utilised are identical, a large amount of the research

published does not go to the same lengths. Indeed, numerous papers are published each year where the authors simply assume that a method works exactly the same each time. Few researchers do report on the crystallinity of the material, they are often broadly classifying the material using XRD peak locations. Many researchers neglect to process the XRD pattern using Rietveld refinement or other structural analysis techniques. Without more detailed knowledge of the BLMO structure, application results are difficult or almost impossible to directly compare. This creates significant challenges for researchers attempting to replicate and expand upon the prior research.

BLMO materials have distinctive crystal structures comprised of layered sheets of edge-sharing manganese oxide octahedra ( $\text{Mn}^{4+,3+}\text{O}_6$ ) interleaved by hydrated cations to charge balance the negatively charged layers<sup>5</sup>. There are two crystal forms, triclinic and hexagonal. Triclinic BLMO materials are generally described by a non-standard face centred  $C-1$  space group<sup>6</sup> (Figure 3-1a). Hexagonal BLMO materials on the other hand adopt a hexagonal unit cell in space group  $P-3$ <sup>7</sup> (Figure 3-1b). Triclinic BLMO materials have a more ordered crystal structure, with neatly packed layered octahedra with hydrated cations (e.g.  $\text{Na}^+$ ,  $\text{K}^+$  etc.) held in the interlayer space. In contrast, the hexagonal form consists of hydrated  $\text{Mn}^{2+/3+}$  from the octahedral layers acting as the interlayer cations, resulting in the formation of Mn vacancies in the octahedral layers<sup>8</sup>. In literature it is common to see the term 'birnessite' used to describe any layered manganese dioxide material. However, these materials should be denoted BLMOs, as birnessite is a soil mineral with a very specific chemical composition.

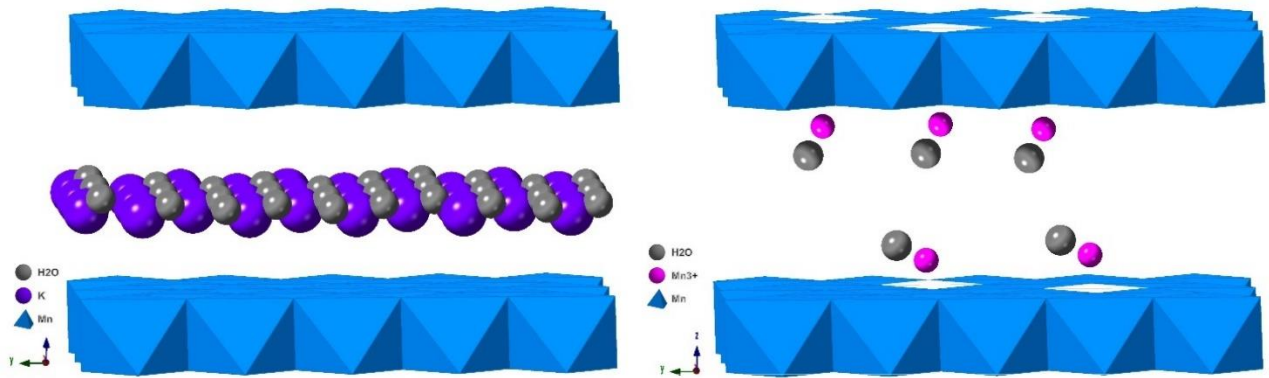


**Figure 3-1: View of common birnessite crystal structures along the [100] direction, a) Triclinic birnessite, b) Hexagonal birnessite, where the white octahedra signify Mn vacancies.**

The crystal structures (and crystallite size and morphology) of BLMO materials are dependent on the method of synthesis. Numerous papers have been published reporting the preparation of BLMOs, however, despite this body of work, the reproducible preparation of single-phase crystalline BLMOs remains challenging. A variety of methods have been reported that predominately use either hydrothermal synthesis<sup>13</sup> or sol-gel synthesis<sup>14</sup>. Hydrothermal methods typically involve homogenizing a solution of potassium permanganate with a reductant, such as manganese chloride or potassium persulfate<sup>15</sup>. The resulting mixture is subsequently placed into an autoclave for several hours. The morphology of the BLMO produced using hydrothermal synthesis mostly consists of spheres of crystallites (70 - 90 nm) or rods (20 - 500 nm) with broad peaks in XRD spectra due to the small crystallite size<sup>15-17</sup>. Sol-gel synthesis uses a similar chemistry, whereby either  $Mn^{2+}$  is oxidized or  $Mn^{7+}$  is reduced, however, in this case the reagent solutions are prepared separately. The solutions are then slowly combined at room temperature to form a BLMO suspension. The sol-gel synthesis method has mixed successes in producing crystalline BLMO because accurate control of the molar ratio of reactants is required<sup>18</sup>. The main benefit of this approach, apart from its simplicity, is the ability to achieve greater control of particle size and shape<sup>14,22</sup>. To date, there has been no detailed study into the effect of BLMO synthesis methods on the resulting material structure and order.

## 3.2 Materials and Methods

All reagents were reagent grade or higher and purchased from Sigma Aldrich, USA unless otherwise stated below. NaOH and NaCl were purchased from Chem Supply, Australia, HCl was sourced from Sharlau, Spain and KBr was obtained from Ajax Chemicals, Australia. High purity water (MilliQ, 18.2 M $\Omega$ ) was used throughout.

### 3.2.1 BLMO Synthesis Methods

Synthetic BLMO samples were prepared from aqueous solutions via sol-gel processes according to six differing procedures, detailed below. These procedures were selected due to the practical simplicity and to avoid the need to use specialised equipment such as autoclaves, pressure microwaves and freeze driers.

**Method A** followed the procedure described by Handel *et al.*, 2013<sup>20</sup>. Aqueous sodium lactate (NaC<sub>3</sub>H<sub>5</sub>O<sub>3</sub>, 12 mL, 50% v/v, 7.12x10<sup>-5</sup> moles) was added dropwise at a rate of 1 mL/min to a stirred solution of aqueous KMnO<sub>4</sub> (600 mL, 0.03798 moles, 0.063 M) at room temperature and pressure. Stirring was continued for 30 minutes post completion of the addition of the reductant. The resulting precipitate was left to age unstirred at room temperature in the uncovered reaction solution for two days. The precipitate was then filtered (Whatman, cellulose, 11  $\mu$ m), washed with MilliQ water and air-dried at room temperature.

**Method B** was according to McKenzie, 1971<sup>12</sup>. Here, concentrated HCl (16.5 mL, 2 moles, 37% w/w) was added dropwise at a rate of 2 mL/min to a boiling stirred solution of aqueous KMnO<sub>4</sub> (250 mL, 1 mole, 0.4 M). The resulting suspension was allowed to cool (with stirring) for approximately 1hr post addition of the reductant. The resulting precipitate was left to age unstirred at room temperature in the uncovered reaction solution for two days. The precipitate was then filtered (Whatman, cellulose, 11  $\mu$ m), washed with MilliQ water and air-dried at room temperature.

**Method C** added aqueous manganese chloride tetrahydrate ( $\text{MnCl}_2 \cdot 4\text{H}_2\text{O}$ , 400 mL, 0.112 moles, 0.28 M) dropwise (4 mL/min) to a stirred strongly alkaline solution of aqueous  $\text{KMnO}_4$  (400 mL, 0.04 moles, 0.1 M), as described by Shen *et al.* 2005<sup>21</sup>. Sodium hydroxide (NaOH, 1.2 moles, 48 g) was used to basify the solution. Stirring was continued for 30 minutes post completion of the addition of the reductant. The resulting precipitate was left to age unstirred at room temperature in the uncovered reaction solution for two days. The precipitate was then filtered (Whatman, cellulose, 11  $\mu\text{m}$ ), washed with MilliQ water, and air-dried at room temperature.

**Method C-M** was a modified sample of the BLMO prepared by method C. The modification was achieved by taking 2 g of dried BLMO synthesised by method C and soaked in 1 M potassium chloride for 2 hrs. The BLMO powder was then collected via filtration, washed with MilliQ water, and air dried at room temperature.

**Method D** samples were provided by Dr Jeffrey Post at the Smithsonian Institution and were prepared following the synthesis for Na-birnessite outlined in Lopano *et al.* <sup>210</sup>, based on the synthesis procedures described by Golden *et al.*<sup>207</sup>. Sodium hydroxide (NaOH, 250 mL, 5.5 M) and manganese dichloride tetrahydrate ( $\text{MnCl}_2 \cdot 4\text{H}_2\text{O}$ , 200 mL, 0.5 M) were chilled overnight at 4 °C. The Na-birnessite precipitate was formed by stirring the NaOH and  $\text{MnCl}_2 \cdot 4\text{H}_2\text{O}$  solutions at room temperature and then bubbling oxygen into the mixture with a Pyrex™ coarse porosity fritted cylinder (pore size = 40-60  $\mu\text{m}$ ) for five hours. Analytical grade chemicals and deionized water were used for the synthesis. The precipitate was centrifuged in conical polypropylene centrifuge tubes (capacity = 50 mL) and rinsed five times with 40 mL of deionized water. The sample was then left to air-dry on a watch glass at room temperature overnight. After 24 hours, the sample was dried at 30 °C for 5 minutes to effect a complete transformation from Na-buserite to Na-birnessite.

**Method D-M** samples was also provided by Dr Jeffrey Post and follows the same procedure as outlined in method D except potassium hydroxide was used in place of sodium hydroxide.

### 3.2.2 Characterisation of BLMO materials.

All BLMO materials prepared were characterised through X-ray Diffraction as described in section 2.1, and the average manganese oxidation state was determined via the procedure outlined in section 2.5. A selection of the materials were examined via SEM, EDXS and Raman spectroscopy, the procedures for which can be found in section 2.3, section 2.3, and section 2.4 respectively.

### 3.2.3 Post-synthesis treatments

**Potassium Chloride Treatment:** Dried BLMO synthesized by method C was disaggregated using a mortar and pestle. Subsamples (1.5 g) of the powdered material were placed into aqueous KCl (1 M, 60 mL) and the resulting mixtures were stirred for 1, 2, 5, 8, and 24 h, respectively. The BLMO powder was then collected via filtration, washed with MilliQ water, and air dried at room temperature.

**Cation Exchange:** Dried BLMO synthesized by method C was disaggregated using a mortar and pestle. Subsamples (1.5 g) were placed into individual solutions of  $H^+$ ,  $Li^+$ ,  $Na^+$ ,  $K^+$ ,  $Ca^{2+}$ , and  $Mg^{2+}$  chloride salts (all 1 M, 60 mL) and the mixtures stirred for 2 hours. The BLMO powder was then collected via filtration, washed with MilliQ water, and air dried at room temperature. To examine the effect of the anion, an additional  $K^+$  solution (1 M, 60 mL) was formed from KBr.

**Static Aging:** BLMO materials were synthesised according to method C above with smaller volumes of reagents (100 mL each, instead of 400 mL) and the static aging time was varied to 0, 1, 2, 5, and 7 days.

**Stirring Rate:** BLMO materials were synthesised according to method C above using smaller volumes of reagents and the stirring rate was altered to either no stirring, medium stirring or fully maxed stirring using stirring hot plates.

**Reagent Concentration:** BLMO materials were synthesised according to method C above, except that different reagent concentrations were used. Stock solutions were made for the reagents (Stock 1:  $\text{KMnO}_4$ : 9.48 g, 600 mL and NaOH: 72 g, Stock 2:  $\text{MnCl}_2 \cdot 4\text{H}_2\text{O}$ : 33.3729 g, 600 mL), which were then diluted by a factor of two and ten before synthesis.

**Reagent Age:** BLMO materials were synthesised according to method C above and used smaller volumes of reagents, the reagent solutions used were 2 months old and were from the remaining stock solutions prepared in the section above.

**Synthesis NaOH Concentration:** BLMO materials were synthesised according to method C above and used smaller volumes. Here, the amount of NaOH used in the synthesis was varied to values of 0 g, 3 g, 6 g, 9 g, and 12 g.

### 3.3 Results and Discussion

#### 3.3.1 Different literature synthesis methods

Synthesis methods A, C, and D produced dark-grey/black BLMO that was found to have distinctly micaceous morphology through SEM (Figure 3-2a,c,d). In contrast, method B produced a brown material that exhibited spherical clusters (Figure 3-2b). The average Mn oxidation state for the synthetic BLMOs are shown in Table 3-1. The highest oxidation state ( $3.96 \pm 0.05$ ) was observed for the spherical morphology material formed using method B, whereas materials with micaceous morphology had similar oxidation states ( $\sim 3.5$ ). The difference in oxidation state between method B compared to the others implies a difference in stoichiometry, which is expected due to the use of different reductants, as hydrochloric acid is known to remove  $\text{Mn}^{3+}$  from the crystal structure of BLMO<sup>33</sup>. In keeping with the

observation of Ling *et al.*<sup>33</sup> higher Mn<sup>3+</sup> (lower average oxidation state) content materials tended to have lower values for  $\alpha$  and  $\beta$  cell angles and are more triclinic in nature.

**Table 3-1: Average manganese oxidation state for the six synthesised materials using four literature methods. Errors are standard deviation of triplicate analysis ( $n=3$ ).**

BLMO Material	Average Manganese Oxidation State
Method A	3.31 ± 0.06
Method B	3.96 ± 0.05
Method C	3.33 ± 0.10
Method C-M	3.40 ± 0.07
Method D	3.37 ± 0.12
Method D-M	3.79 ± 0.18

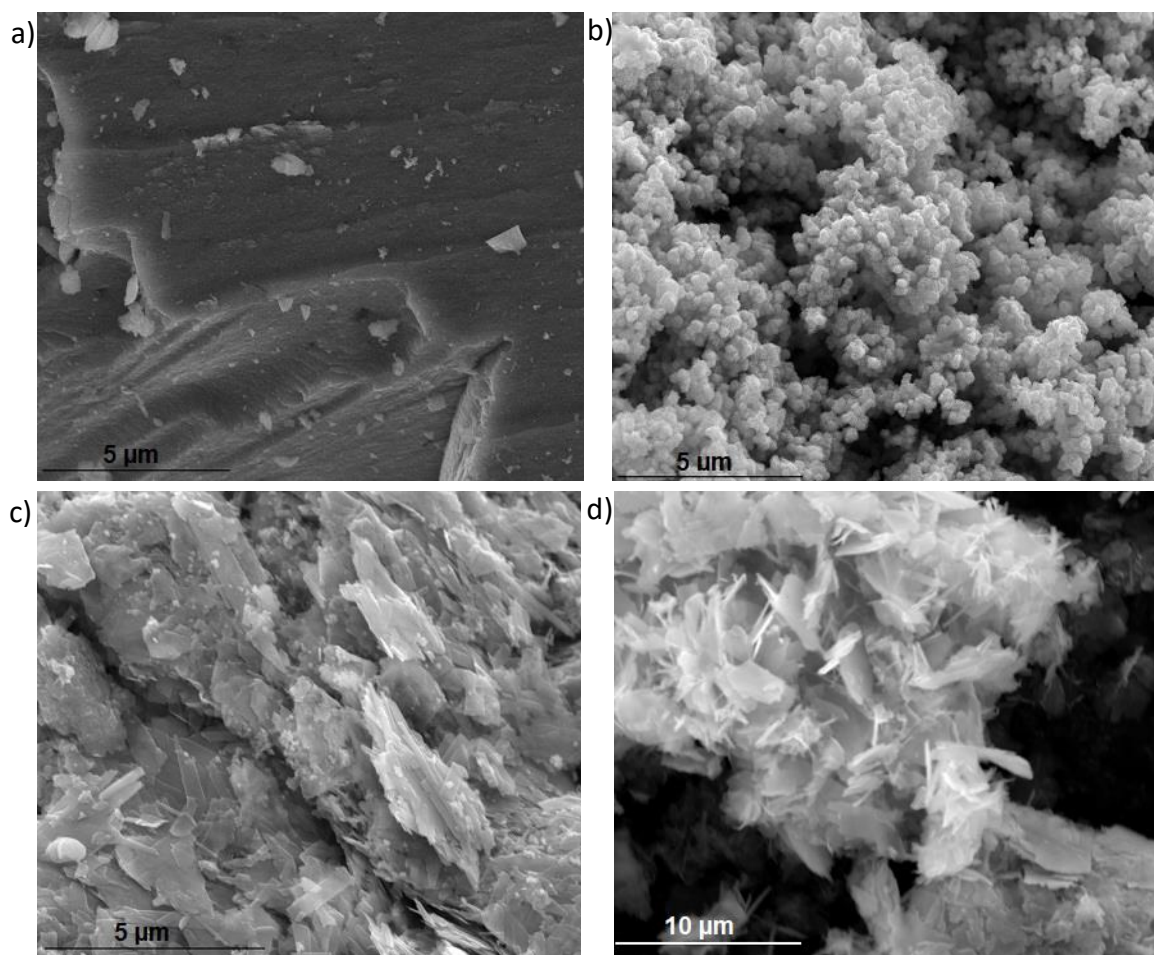


**Figure 3-2: SEM images of synthesized BLMO material taken at 20,000x magnification with a beam voltage of 10 kV. a) Method A, b) Method B, c) Method C, and d) Method D.**

The XRD patterns of the resulting precipitates collected using Mo radiation are shown in Figure 3-4. The BLMO synthesized by Method A had a largely featureless XRD pattern that contains extremely broad ‘peaks’ at the expected locations for the 001 and 100 reflections of

BLMOs. The lack of strong reflections in the XRD pattern could be due to the small crystallite sizes or a more amorphous nature of the bulk material. It must be noted that the peaks in the original paper are not indicative of a highly crystalline material when compared to BLMO's prepared by other methods. . The material prepared using method B had very broad peaks with d-spacings of 7.17, 3.63, and 2.44 Å corresponding to the 001, 002, and 100 reflections in the BLMO crystal structure. The broad nature of the peaks indicates either tiny crystallites or increased stacking disorder. The SEM (Figure 3-2b) exhibits small plated spheres (~0.2 µm) indicating that the broadening is likely to be due to tiny crystallites. The BLMO prepared using Method C exhibited two sharp peaks at 7.06 and 3.53 Å, along with sharp peaks of smaller intensity at 5.28, 4.8, 2.74, 2.47, and 2.36 Å. The peaks at 7.06 and 3.53 Å corresponded to the 001 and 002 reflections of BLMO and are typical of a mostly crystalline sample, which was expected due to the plate like structure of BLMO observed in the SEM. However, the d-spacings are between the values expected for Na-BLMO and K-BLMO, suggesting the presence of both Na<sup>+</sup> and K<sup>+</sup> ions in the interlayer space, as both are present in the synthesis solution. Energy Dispersive Spectroscopy of the BLMO synthesized by method C confirmed the presence of both Na<sup>+</sup> and K<sup>+</sup> in the final BLMO product (Figure 3-3). Whilst the BLMO synthesized using this method is the most crystalline of the four methods tried, there are a number of impurities in the final sample. The peaks at 5.28, 2.74, 2.47, and 2.36 Å indicate the presence of hausmannite (Mn<sub>3</sub>O<sub>4</sub>) and the peak at 4.8 Å indicates the presence of feitknechtite (MnO(OH)). It has been reported that the presence of hausmannite and feitknechtite impurities is common when alkaline synthesis of BLMO is undertaken<sup>27-28</sup>.

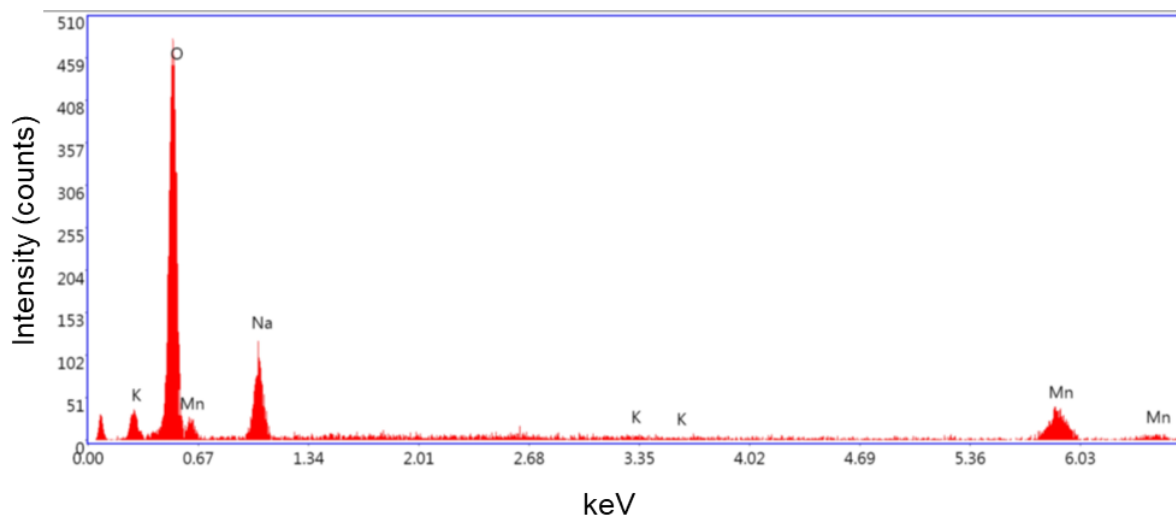


Figure 3-3: EDXS spectra of untreated birnessite synthesized using method C, showing the presence of both Na and K present in the birnessite sample.

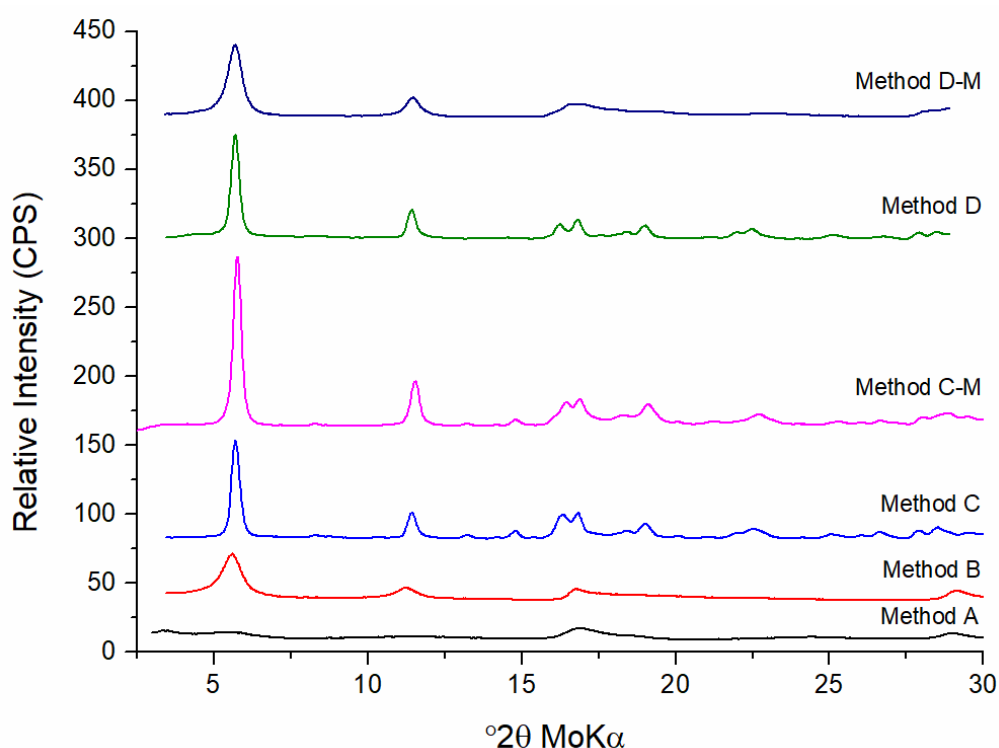


Figure 3-4: MoK $\alpha$  X-ray diffraction patterns of the BLMO resulting from the four different synthesis methods and the modified materials of method c and d. Patterns are offset for ease of clarity.

Rietveld analysis for patterns collected using Mo radiation (Table 3-2, Figure 3-7a-e) confirmed that the materials shown in Figure 3-4 were triclinic BLMOs with differing levels of stacking disorder within the crystal structure. The level of disorder was estimated by examining the extent of broadening of the main BLMO peak at approximately 7 Å. The sodium lactate method resulted in the most disordered and the KCl treated material being the most

ordered, with the order increasing from  $A < B < D - M < C = D < C - M$ . The pattern collected for the lactate sample (Figure 3-7a) is a difficult pattern to conduct a reliable refinement on due to the low diffraction intensity and the broad features present, but the main features of triclinic BLMO can still be observed. Prior work has suggested that the hydrochloric acid synthesis method produces hexagonal BLMO due to the use of acid<sup>48, 79</sup>, but here we have conducted Rietveld refinements using a triclinic model (Figure 3-7b) and a hexagonal model (Figure 3-7c) and found that the triclinic model was a better fit than the hexagonal model (Table 3-2). This preference for a triclinic structure could be due to the presence of  $K^+$  in the material shown by EDXS (Figure 3-5), which could create sections of the BLMO that are distorted from the simple hexagonal parent structure to the triclinic form. Raman spectroscopy was conducted on this sample and the resulting spectra can be seen in Figure 3-6. Two major Raman peaks were observed at 570 and 637  $\text{cm}^{-1}$ , with a small peak visible just above the noise at 507  $\text{cm}^{-1}$ . These peaks are shifted from those reported by Julien and co-workers<sup>190</sup> for hexagonal H-BLMO (506, 575 and 646  $\text{cm}^{-1}$ ) and triclinic Li-BLMO (510, 585 and 625  $\text{cm}^{-1}$ ), although a direct comparison cannot be made. Our work used a laser power of  $\sim 300 \mu\text{W}$  and Julien's work used 10 mW, this higher laser power may well have degraded the sample<sup>211</sup>. Additionally, when compared to Raman spectra of known triclinic and hexagonal samples (Figure 3-6), the Raman spectra of BLMO prepared using HCl shares features with both triclinic and hexagonal samples. These results provide further evidence that the BLMO produced by method B may be a mixture of the two forms or may be a single-phase intermediate between the hexagonal and triclinic end member structures.

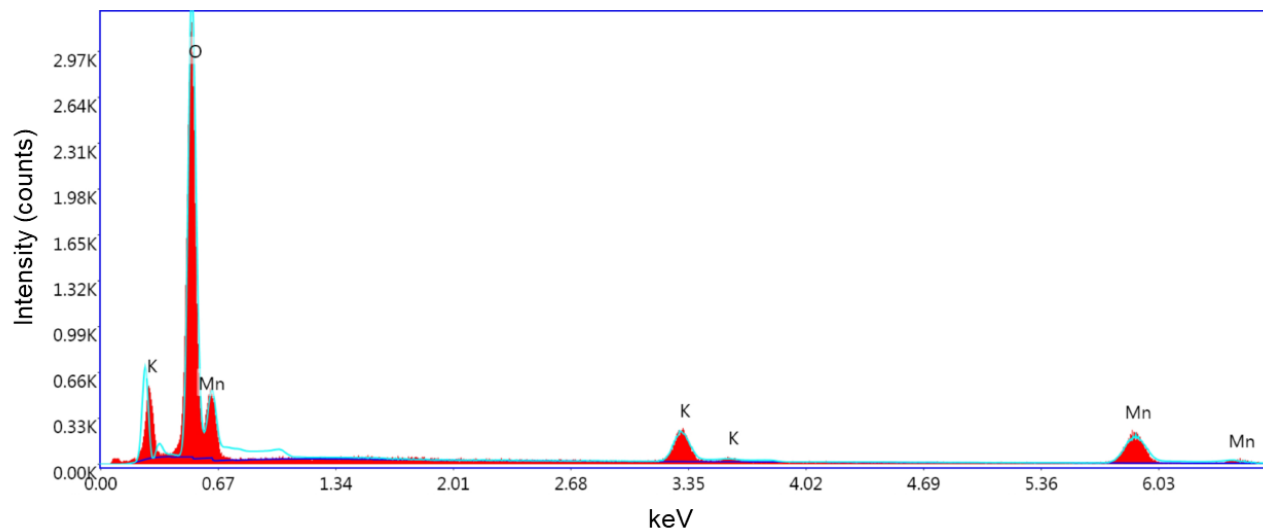


Figure 3-5: EDXS of BLMO prepared using Method B, showing the presence of  $K^+$  in the structure.

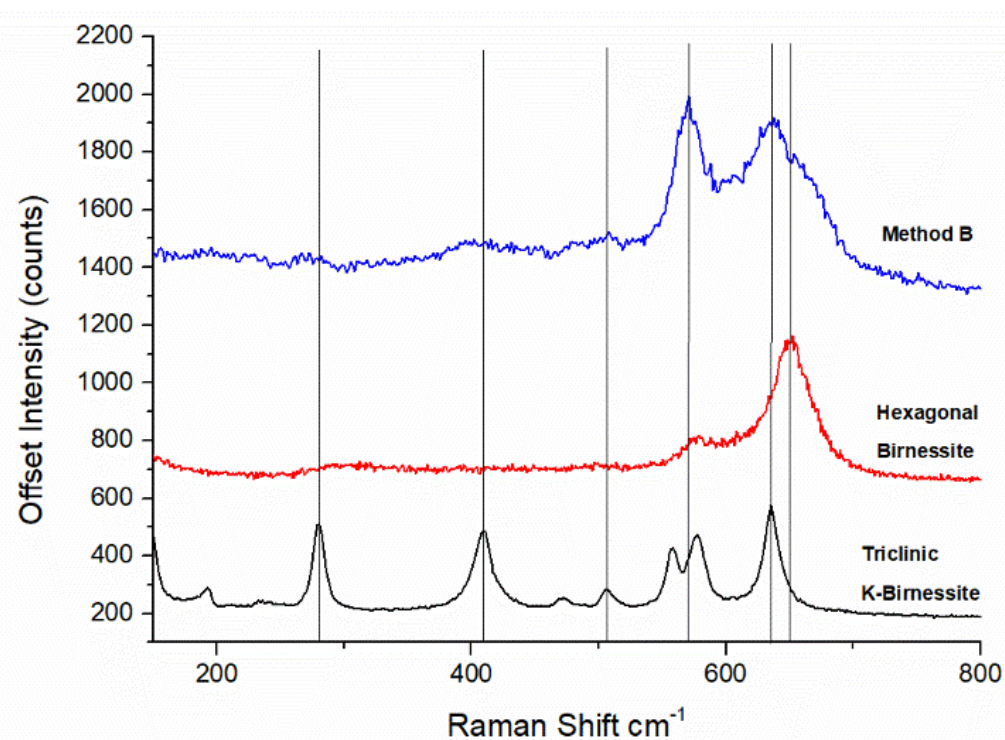
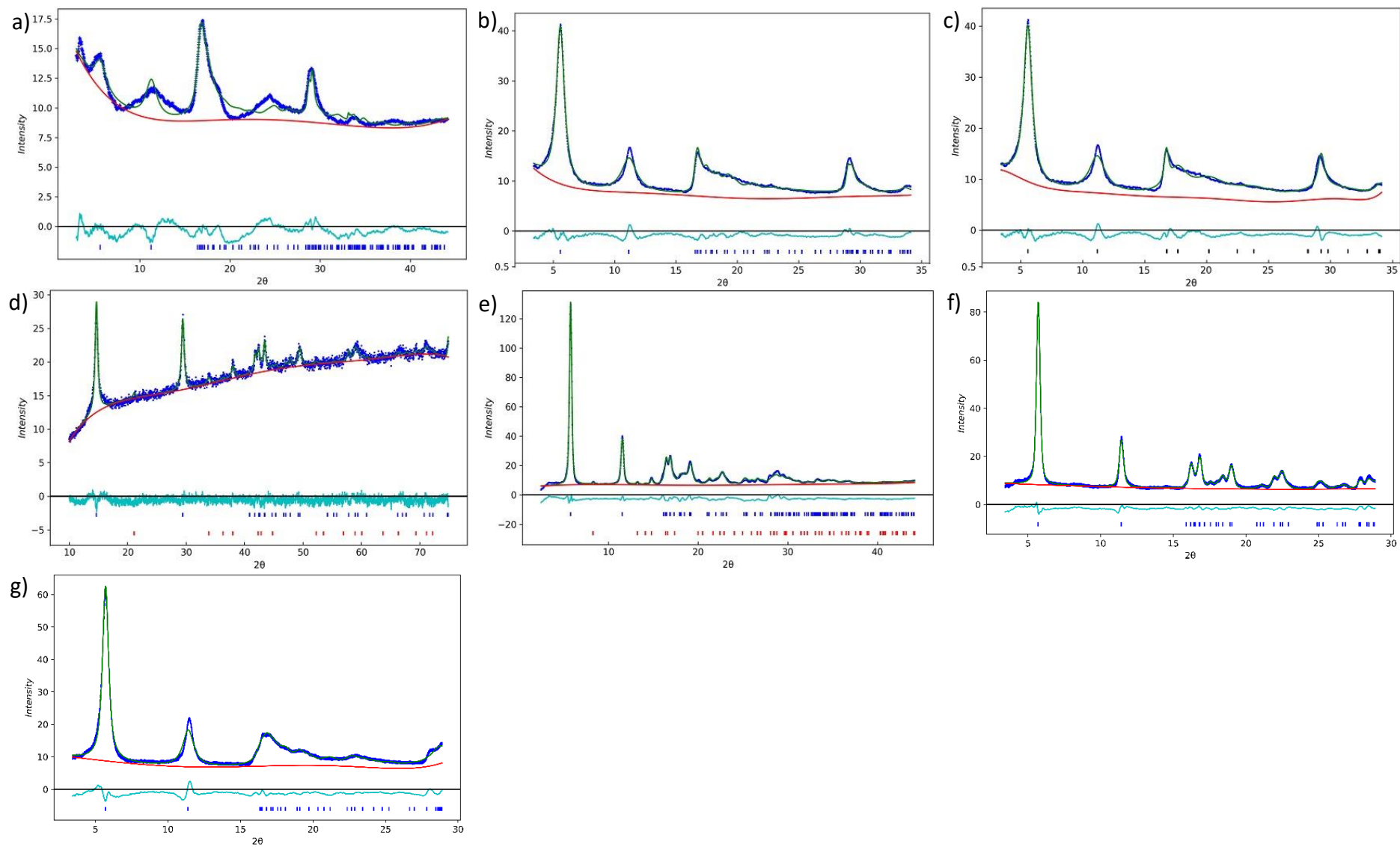


Figure 3-6: Raman spectra of the BLMO material prepared by method B (blue), a sample of hexagonal BLMO (red) and a sample of triclinic BLMO (black) for comparison.



**Figure 3-7: Rietveld refinements (green) on experimental XRD data (blue) and difference curves (teal) using the MoK $\alpha$  patterns for a-c and e-g and CoK $\alpha$  for d of the six BLMO materials prepared using four literature methods. Reflections of manganese oxide phases are shown below the patterns.**

**Table 3-2: Rietveld refinement results for the four synthesis methods, shown are the final refined cell parameters,  $R(F^2)$  and the residual ( $R_{wp}$ ).**

	Method A	Method B	Method B	Method C	Method C-M	Method D	Method D-M
Space Group	<i>C</i> -1	<i>C</i> -1	<i>P</i> -3	<i>C</i> -1	<i>C</i> -1	<i>C</i> -1	<i>C</i> -1
Radiation Source	Mo						
Unit Cell							
a (Å)	4.90(6)	4.909(8)	2.8098(14)	5.165(4)	5.102(7)	5.171(4)	4.983(12)
b (Å)	2.877(8)	2.8351(25)	2.8098(14)	2.8463(8)	2.8526(13)	2.8473(8)	2.885(7)
c (Å)	7.88(15)	7.357(19)	7.2810(28)	7.321(9)	7.231(15)	7.335(8)	7.21(3)
$\alpha$ (°)	95.5(13)	91.69(4)	90	90.56(6)	90.54(8)	90.50(8)	91.93(29)
$\beta$ (°)	112.92(22)	97.17(10)	90	103.229(26)	102.19(5)	103.23(25)	96.86(16)
$\gamma$ (°)	89.60(11)	89.16(6)	120	90.177(20)	90.03(3)	90.212(25)	89.33(11)
Vol (Å <sup>3</sup> )	101.77(17)	101.53(7)	49.78(4)	104.780(26)	102.85(6)	105.117(28)	102.86(23)
Refinement							
No. of Observations	2060	1536	1536	2037	2085	1275	1275
No. of Reflections	114	63	25	125	120	36	35
Diffraction Range (°2 $\theta$ )	3 - 44	3.5 - 34	3.5 - 34	8 - 44	3.5 - 44	3.5 - 29	3.5 - 29
$R(F^2)$	0.20781	0.0586	0.00891	0.10018	0.10111	0.05598	0.03065
$R_{wp}$	0.04424	0.03785	0.04007	0.04539	0.06496	0.04356	0.05023

### 3.3.2 Effect XRD Source on Rietveld Refinements

XRD analysis can be difficult for manganese oxide materials due to the different interactions of Mn with the different incident wavelengths. The common XRD sources of Co, Cu, and Fe, cause Mn fluorescence and have low signal intensity for Mn, whereas this is not an issue for Mo and synchrotron sources don't have this issue. However, Mo sources are not as common due to the reduced wavelength producing low resolution and compacted diffraction patterns. Not all researchers have access to a Mo or a synchrotron radiation source to collect well defined diffraction patterns for manganese dioxide materials, but many have access to XRD instruments with Co and Cu radiation sources. We undertook a comparison of the structural information that could be refined using the Rietveld method on diffraction patterns collected with Mo, Co and Cu sources on three different XRD instruments. The Mo XRD instrument utilised in this work was optimised for Mn oxides and has a Debye-Scherrer geometry with an imaging plate detector and the full set of diffraction rings were integrated to get improved diffraction intensities and reduce orientation effects. In contrast, the Cu and Co instruments utilized the more common Bragg-Brentano geometries and were used under standard instrument conditions that were not optimized for Mn oxides.

Despite the differences in instrumental set-up, all the x-ray patterns collected for the crystalline sample (Figure 3-8a) show the expected features of BLMO with the Mo providing the best diffraction pattern due to the greater detail in the higher angle reflections caused by the greater peak to background ratio and diffraction intensities. These reflections are still visible with the Cu and Co patterns, but are less defined, due to the fluorescence in the case of Cu and the lower x-ray intensity in Co. Rietveld analysis on these three patterns (Table 3-3) show that the cell parameters refined for the crystalline sample are similar between the difference sources, with Co being slightly different due to the larger x-ray wavelength and

lower number of reflections. This suggests that although Co and Cu sources result in spectra with lower peak intensity and signal to noise ratios, along with less defined peaks, they can still be reliably used to define basic structural information for a crystalline BLMO.

However, the low signal obtained using Co and Cu radiation causes difficulty in interpreting and analysing the XRD patterns for poorly crystalline BLMO materials, as demonstrated by the sample prepared by method A. This sample was determined to be amorphous  $\text{MnO}_2$  when using XRD data obtained from Co and Cu sources (Figure 3-8b) but was determined to be a disordered triclinic BLMO when interrogated using an optimised Mo instrument. This indicates that whilst data can be collected using any of the sources (Mo, Co, and Cu) and configurations, care needs to be taken in analysing the resulting spectra. Ideally for structural refinements, the instrument conditions should be optimized so that data is collected under conditions that maximize the peak to background ratio and diffraction intensity. Importantly, Cu and Co radiation can still provide patterns that might be useful for identification and limited structure refinement.

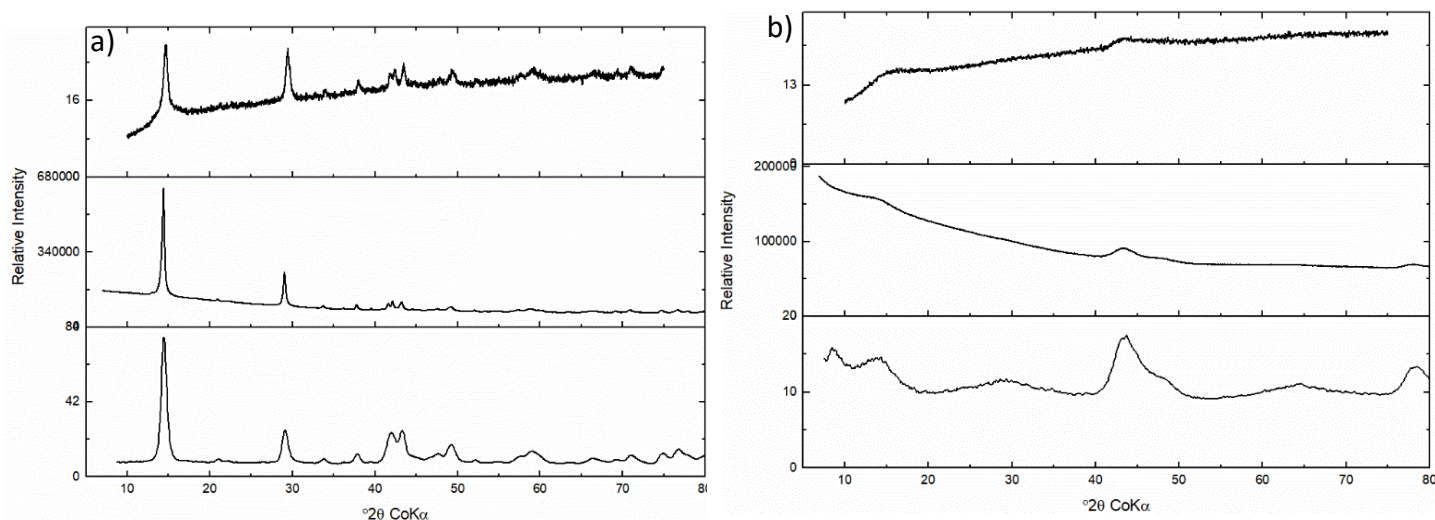


**Figure 3-8: X-ray diffraction patterns collected using Cu, Co, and Mo radiation for a) a crystalline sample of BLMO synthesised via Method C and b) a poorly crystalline sample of BLMO synthesised via Method A. The diffractograms have been converted to  $\text{CoK}\alpha$   $2\theta$  values for comparison. Top:  $\text{CoK}\alpha$ , Middle:  $\text{CuK}\alpha$  and Bottom:  $\text{MoK}\alpha$ .**

**Table 3-3: Results of the Rietveld refinements conducted using various radiation sources on a crystalline sample (Method C), shown are the final refined cell parameters,  $R(F^2)$  and the residual ( $R_{wp}$ ).**

Crystalline Sample (Method C)			
Radiation Source	Mo	Co	Cu
Space Group	C -1	C -1	C -1
<b>Unit Cell</b>			
a (Å)	5.165(4)	5.160(8)	5.172(4)
b (Å)	2.8463(8)	2.8373(18)	2.8531(5)
c (Å)	7.321(9)	7.233(15)	7.338(7)
$\alpha$ (°)	90.56(6)	90.50(10)	90.330(25)
$\beta$ (°)	103.229(26)	103.6(4)	103.125(22)
$\gamma$ (°)	90.177(20)	89.926(26)	90.048(15)
Vol (Å <sup>3</sup> )	104.780(26)	102.92(6)	105.44(14)
<b>Refinement</b>			
No. of Observations	2037	2985	7501
No. of Reflections	125	30	67
Diffraction Range (°2 $\theta$ )	10 - 75	10 - 75	5 - 80
$R(F^2)$	0.10018	0.14694	0.07059
$R_{wp}$	0.04539	0.02523	0.06022

### 3.3.3 Changing crystallinity via potassium chloride treatment

To improve crystallinity, the mixed cation BLMO material synthesized by method C was soaked in a 1 M KCl solution for 2 hours, in an attempt to form a pure K-BLMO (Method C-M). The d-spacings for the 001 reflection shifted from 6.86 Å to 7.02 Å, and the 002 reflection shifted from 3.46 Å to 3.51 Å. These spacings, within errors, match the pure K-BLMO d-spacings given by Post and Veblen<sup>5</sup>, indicating that the cation exchange was successful. As can be seen, there was an associated increase in peak sharpness after the cation exchange process. This increased sharpness indicates that cation exchange to a pure K-BLMO results in increased crystallinity of the material (Figure 3-4). Furthermore, peaks at 5.28, 4.8, 2.74, 2.47, and 2.36 Å were reduced indicating that the treatment also decreased the amount of hausmannite and feitknechtite in the material. This reduction is likely due to the disproportionation of hausmannite into a disordered layered octahedral structure, which transforms into ordered BLMO material<sup>212</sup>. The average oxidation state of the manganese present in the materials was found to increase slightly from  $3.34 \pm 0.17$  for the unwashed

sample to  $3.73 \pm 0.01$  after 5 hours of KCl treatment, with there being no significant differences between oxidation state (Table 3-4). Increasing the duration of the KCl immersion times resulted in further increases in peak intensity along with decreasing peak widths at half height of the 001 and 002 reflections (Figure 3-9). The d-spacings change from 7.06 Å for untreated BLMO to 7.00 Å after 24 hours of KCl treatment, closer to the literature values of K-BLMO<sup>5</sup>. SEM images (Figure 3-10) show that the untreated BLMO contain granular clumps of material and NaCl crystals that formed during the synthesis of the BLMO. The water and KCl treatments all have similar micaceous morphology and increasing the treatment time has no effect on the morphology. Rietveld analysis (Figure 3-11, Table 3-5) showed a gradual decrease in all cell parameters over time, suggesting that the crystal structure of the BLMO becomes more ordered and compact with longer exposures. These results are in contrast with previously reported timed in-situ synchrotron investigations that have shown that the level of order during cation exchange decreases to a steady state crystallinity<sup>210</sup>. In that work, the decrease in crystallinity was attributed to the uptake of water molecules between the octahedral layers<sup>210</sup>. However, our study examined dried end-member material only. Our results suggest we may have a more crystalline product, however it is difficult to make a direct comparison as i) the material used in the previous study was prepared using a different synthesis method, and ii) the prior study did not report an XRD of the dried material.

Table 3-4: Average manganese oxidation state of the potassium chloride treatment. Errors are standard deviation of triplicate analysis ( $n=3$ ).

BLMO Material	Average Manganese Oxidation State
Unwashed	$3.34 \pm 0.17$
Washed H <sub>2</sub> O	$3.45 \pm 0.03$
1 hr KCl	$3.45 \pm 0.08$
2 hr KCl	$3.61 \pm 0.09$
5 hr KCl	$3.73 \pm 0.01$
8 hr KCl	$3.83 \pm 0.31$
24 hr KCl	$3.41 \pm 0.05$

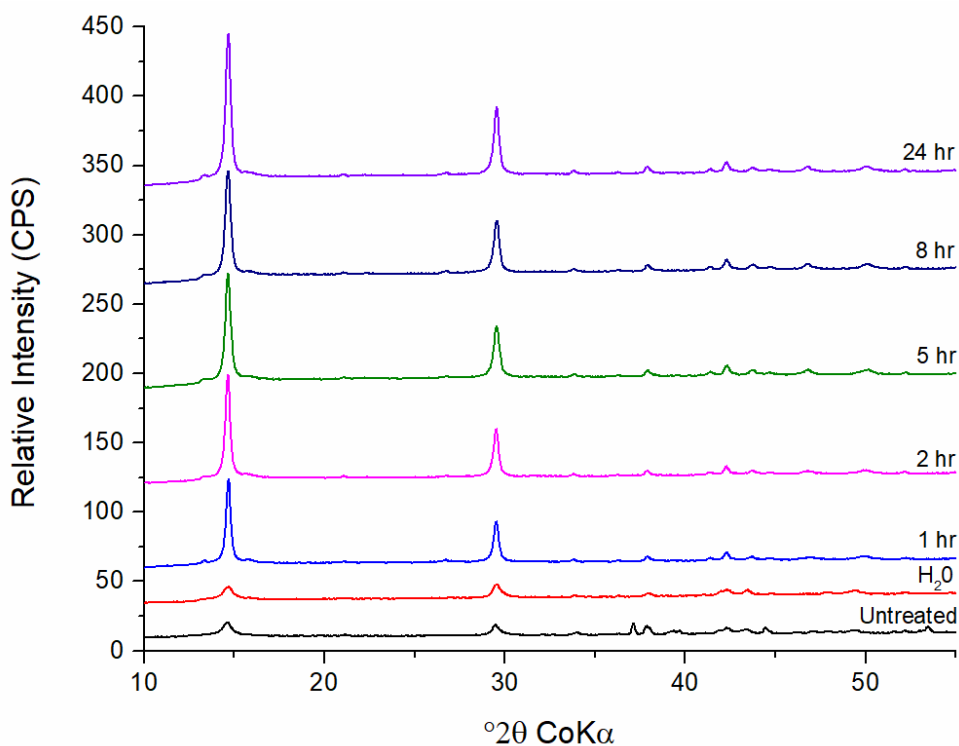


Figure 3-9:  $\text{CoK}\alpha$  X-ray diffraction patterns of synthetic birnessite material treated with H<sub>2</sub>O for 2 hours, and 1 M KCl for 1, 2, 5, 8 and 24 hrs. Patterns are  $\gamma$ -offset for clarity.

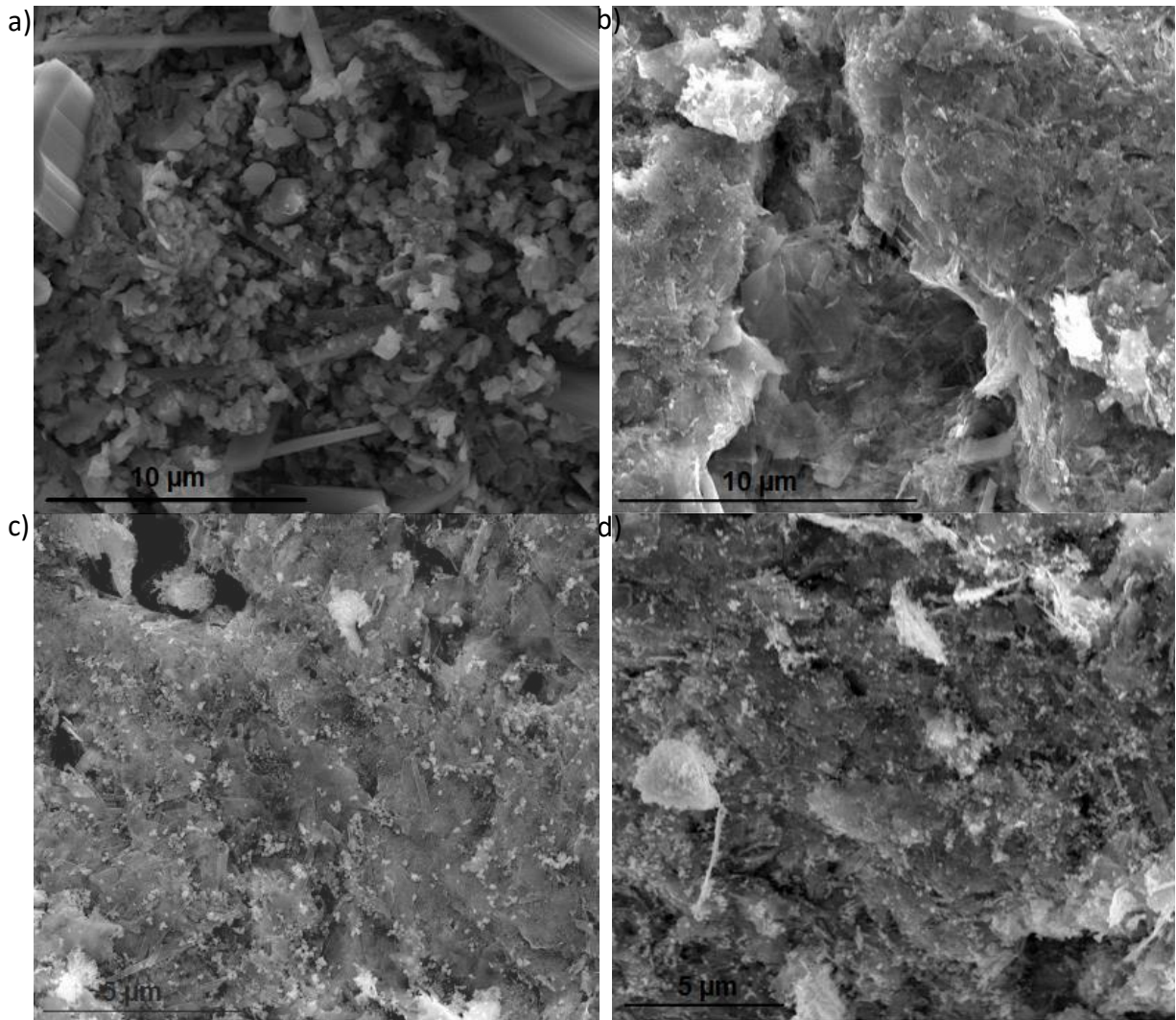


Figure 3-10: SEM images of the potassium chloride treatments a) untreated, b) H<sub>2</sub>O treatment, c) 2 hr treatment and d) 24 hr treatment

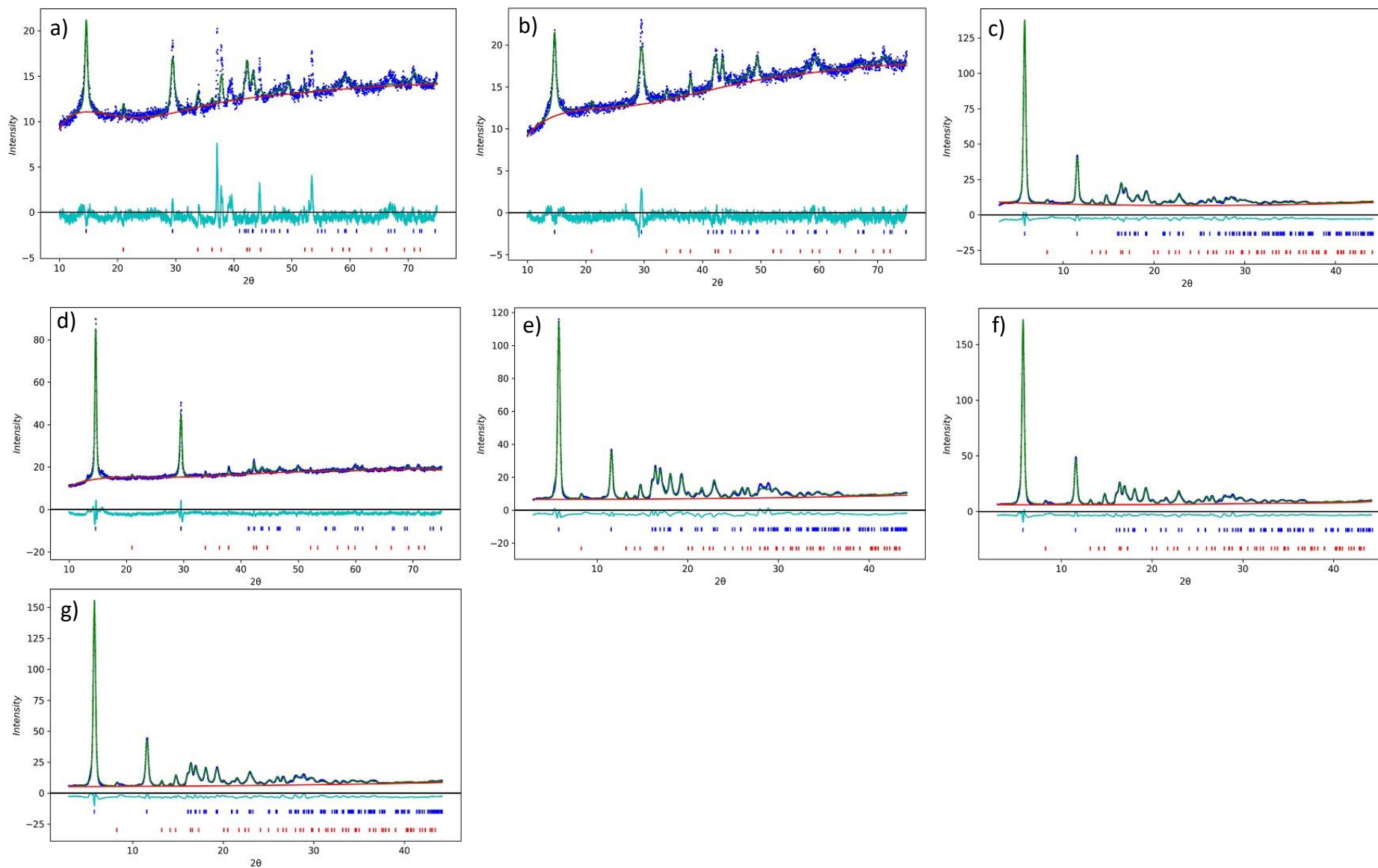


Figure 3-11: Rietveld refinements and difference curves for the birnessite materials treated with KCl for different time intervals. Refinement a and b were conducted using CoK $\alpha$  diffraction patterns and c-g were conducted on patterns collected by MoK $\alpha$ .

**Table 3-5: Rietveld refinement results for the KCl treatment study. Shown are the final refined cell parameters, the R(F<sup>2</sup>) and R<sub>wp</sub> values.**

	Unwashed	H <sub>2</sub> O	1 hr KCl	2 hr KCl	5 hr KCl	8 hr KCl	24 hr KCl
Space Group	C -1	C -1	C -1	C -1	C -1	C -1	C -1
Radiation Source	Co	Co	Mo	Mo	Mo	Mo	Mo
Unit Cell							
a (Å)	5.151(25)	5.153(10)	5.153(5)	5.152(12)	5.148(4)	5.149(4)	5.145(4)
b (Å)	2.850(4)	2.8436(15)	2.8479(12)	2.8433(28)	2.8455(9)	2.8450(9)	2.8473(12)
c (Å)	7.23(5)	7.219(20)	7.199(11)	7.150(24)	7.152(8)	7.145(8)	7.143(9)
α (°)	89.70(29)	90.20(10)	89.61(12)	90.34(13)	89.49(7)	89.93(10)	90.38(9)
β (°)	103.47(18)	103.58(6)	101.79(4)	100.72(9)	100.28(3)	100.29(3)	100.17(4)
γ (°)	89.61(9)	89.86(4)	90.10(4)	89.73(5)	89.773(26)	89.98(4)	89.78(3)
Vol (Å <sup>3</sup> )	103.30(13)	102.83(5)	103.41(5)	102.91(10)	103.077(30)	102.981(30)	102.99(3)
Refinement							
No. of Observations	2985	2985	2060	2985	2060	2060	2060
No. of Reflections	29	29	125	29	125	124	125
Diffraction Range (°2θ)	10 - 75	10 - 75	10 - 75	10 - 75	10 - 75	10 - 75	10 - 75
R(F <sup>2</sup> )	0.29667	0.15886	0.09861	0.15675	0.14647	0.04861	0.07514
R <sub>wp</sub>	0.0486	0.02845	0.05274	0.03471	0.06301	0.05539	0.05845

### 3.3.4 Changing the interlayer cation

The cation exchange with monovalent cations (H<sup>+</sup>, Li<sup>+</sup>, Na<sup>+</sup>, K<sup>+</sup>) resulted in more ordered BLMO structures (Figure 3-12, Figure 3-14, Table 3-7), with d-spacings proportional to the radius of the hydrated cation. The Li<sup>+</sup>, Na<sup>+</sup> and K<sup>+</sup> treated BLMOs maintained their triclinic form, however the H<sup>+</sup> treated BLMO converted to the hexagonal form, as has been observed by many researchers<sup>8, 33, 213</sup>. Exchanging the cation with Ca<sup>2+</sup> and Mg<sup>2+</sup> resulted in the increase in d-spacings from 7.01 Å to ~9 Å. This is due to the formation of Ca-buserite (Ca<sub>2</sub>Mn<sub>14</sub>O<sub>27</sub>·21H<sub>2</sub>O) and Mg-buserite (Mg<sub>2</sub>Mn<sub>14</sub>O<sub>27</sub>·21H<sub>2</sub>O), which is a layered manganese oxide mineral that contains a double hydration layer between the manganese oxide sheets. The BLMO materials retained their sheet-like morphology independent of what cation was used (Figure 3-13), however the H<sup>+</sup> treated BLMOs appear to have thinner flakier sheets.

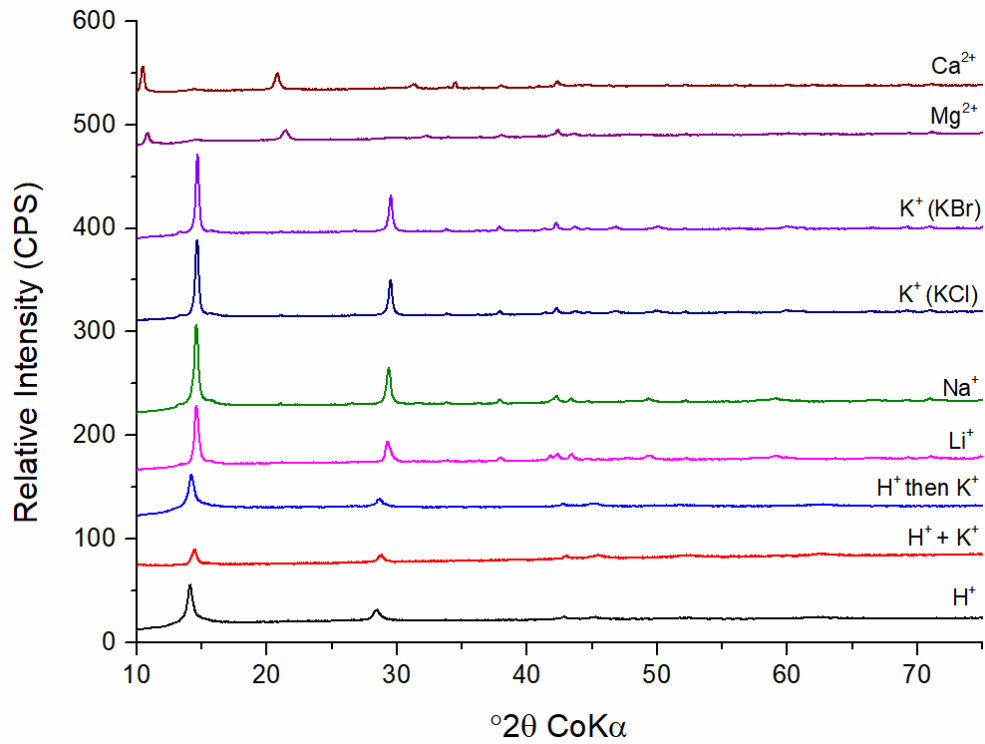


Figure 3-12: CoK $\alpha$  X-ray diffraction patterns of birnessite material treated with different 1 M cation solutions (H<sup>+</sup>, Li<sup>+</sup>, K<sup>+</sup>, Na<sup>+</sup>, Mg<sup>2+</sup> and Ca<sup>2+</sup>, H<sup>+</sup> then K<sup>+</sup> and H<sup>+</sup> and K<sup>+</sup>). Patterns are y-offset for clarity.

Table 3-6: Average manganese oxidation state for different cation BLMOs. Errors are standard deviation of triplicate analysis ( $n=3$ ).

BLMO Material	Average Manganese Oxidation State
H <sup>+</sup>	3.48 $\pm$ N/A
H <sup>+</sup> then K <sup>+</sup>	3.57 $\pm$ 0.15
H <sup>+</sup> + K <sup>+</sup>	3.11 $\pm$ 0.51
Li <sup>+</sup>	3.22 $\pm$ 0.11
Na <sup>+</sup>	3.52 $\pm$ 0.17
K <sup>+</sup> (KCl)	3.61 $\pm$ 0.10
K <sup>+</sup> (KBr)	3.41 $\pm$ 0.08
Mg <sup>2+</sup>	3.50 $\pm$ 0.09
Ca <sup>2+</sup>	3.45 $\pm$ 0.05

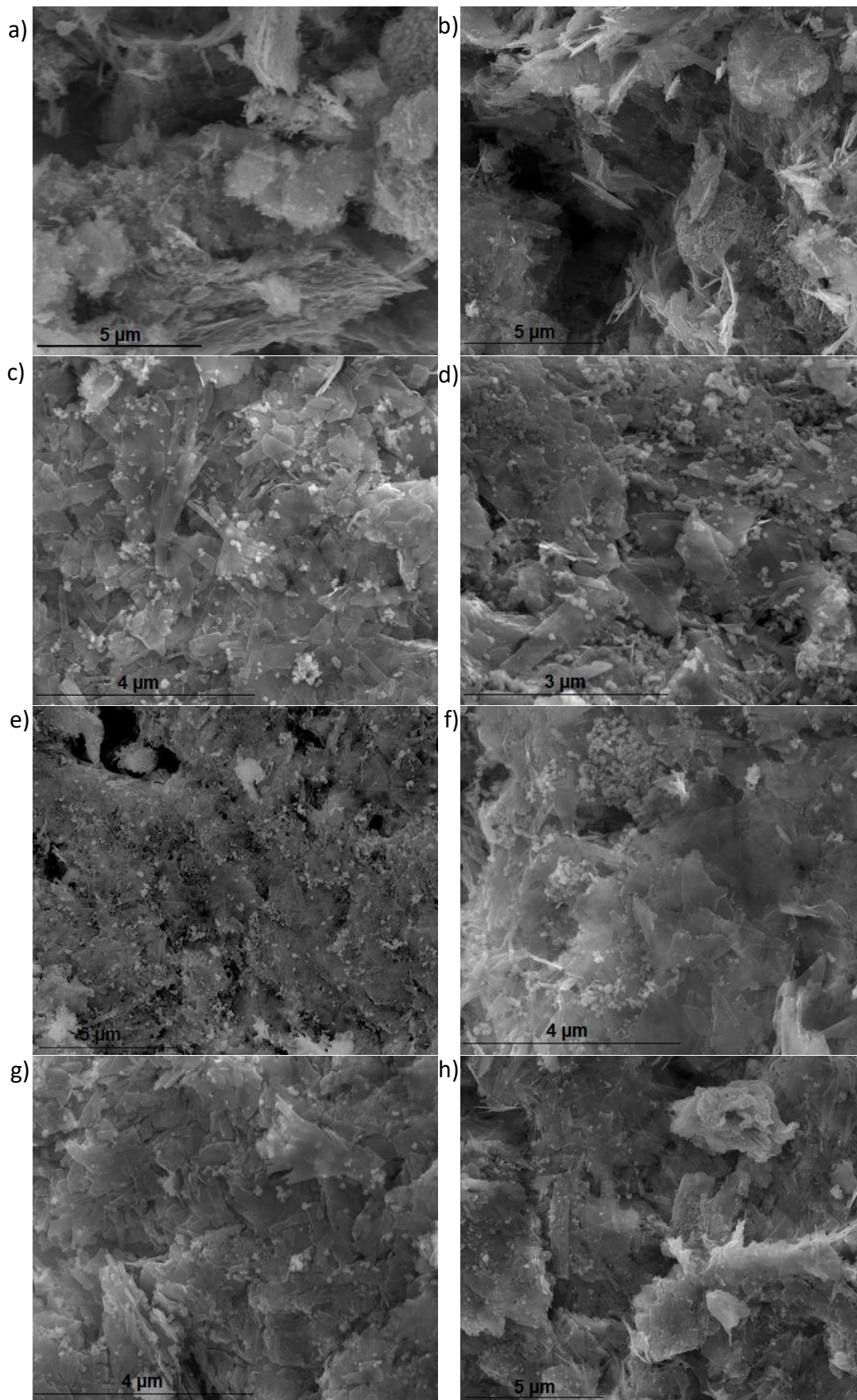


Figure 3-13: SEM images of the different BLMOs prepared in the cation exchange study. a)  $H^+$ , b)  $H^+$  then  $K^+$ , c)  $Li^+$ , d)  $Na^+$ , e)  $K^+$  (KCl), f)  $K^+$  (KBr), g)  $Mg^{2+}$  and h)  $Ca^{2+}$

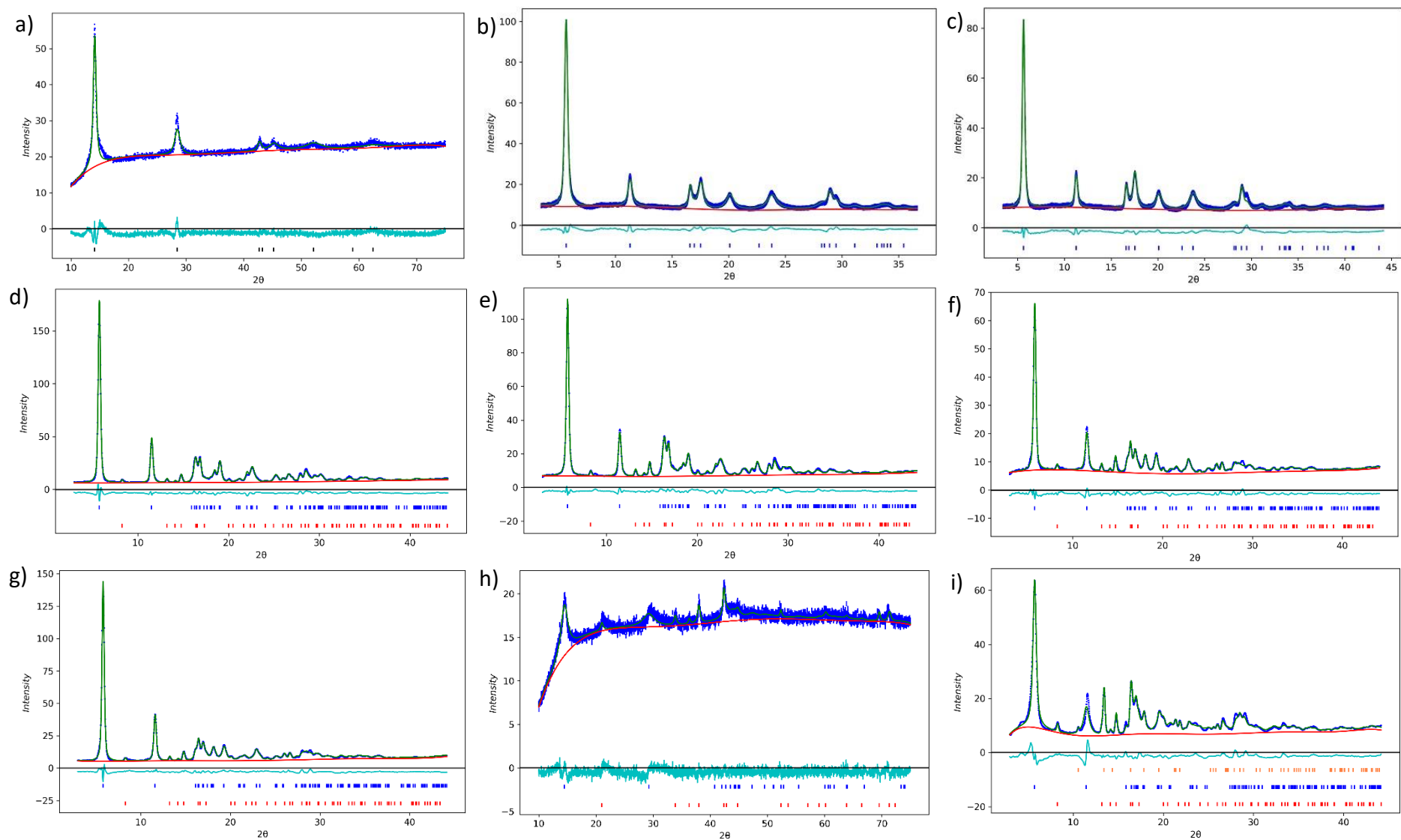


Figure 3-14: Rietveld refinement and difference plots for the cation BLMOs formed from the cation treatment study. a)  $\text{H}^+$ , b)  $\text{H}^+$  then  $\text{K}^+$ , c)  $\text{H}^+$  +  $\text{K}^+$ , d)  $\text{Li}^+$ , e)  $\text{Na}^+$ , f)  $\text{K}^+$  (KBr), g)  $\text{K}^+$  (KCl), h)  $\text{Mg}^{2+}$  and i)  $\text{Ca}^{2+}$ . The refinements for  $\text{H}^+$  (a) and (h)  $\text{Mg}^{2+}$  were conducted using diffraction patterns collected by  $\text{CoK}\alpha$  whereas the others were collected by  $\text{MoK}\alpha$ .

**Table 3-7: Rietveld refinement results for different cation treatments, shown are the final refined cell parameters, the R(F<sup>2</sup>) and R<sub>wp</sub> values.**

	H <sup>+</sup>	H <sup>+</sup> then K <sup>+</sup>	H <sup>+</sup> and K <sup>+</sup>	Li <sup>+</sup>	Na <sup>+</sup>	K <sup>+</sup> (KBr)	K <sup>+</sup> (KCl)	Mg <sup>2+</sup>	Ca <sup>2+</sup>
Space Group	<i>P</i> -1	<i>P</i> -1	<i>P</i> -1	<i>C</i> -1	<i>C</i> -1	<i>C</i> -1	<i>C</i> -1	<i>C</i> -1	<i>C</i> -1
Radiation Source	Co	Mo	Mo	Mo	Mo	Mo	Mo	Co	Mo
Unit Cell									
a (Å)	2.8357(25)	2.8421(6)	2.8398(6)	5.1604(27)	5.158(3)	5.145(5)	5.146(5)	4.844(31)	4.964(6)
b (Å)	2.8357(25)	2.8421(6)	2.8398(6)	2.8465(5)	2.8465(5)	2.8451(9)	2.8499(10)	2.974(17)	2.935(3)
c (Å)	7.2787(10)	7.2197(7)	7.2452(8)	7.271(5)	7.300(7)	7.155(9)	7.162(10)	7.11(8)	7.131(12)
α (°)	90	90	90	90.44(5)	89.55(5)	89.76(8)	89.50(6)	90.9(11)	93.04(8)
β (°)	90	90	90	103.209(17)	103.289(20)	100.58(4)	100.32(4)	94.8(6)	93.26(9)
γ (°)	120	120	120	90.049(17)	89.961(18)	89.71(4)	89.54(4)	88.2(4)	92.35(6)
Vol (Å <sup>3</sup> )	50.69(5)	50.504(14)	50.601(13)	103.971(19)	104.307(20)	102.96(3)	103.328(31)	102.1(7)	103.46(10)
Refinement									
No. of Observations	2985	1663	2037	2060	2060	2060	2060	2985	2060
No. of Reflections	11	29	42	124	124	124	124	28	125
Diffraction Range (°2θ)	10 - 75	3 - 45	3 - 45	3 - 45	3 - 45	3 - 45	3 - 45	10 - 75	3 - 45
R(F <sup>2</sup> )	0.20245	0.03473	0.08188	0.09304	0.09079	0.07754	0.06613	0.1006	0.06851
R <sub>wp</sub>	0.02764	0.03751	0.04107	0.04878	0.04544	0.05002	0.03925	0.02333	0.06596

### 3.3.5 Synthesis reproducibility

Due to method C-M resulting in the most well ordered BLMO, it was decided to investigate the reproducibility of BLMO synthesis using this method. Synthesis in triplicate was conducted on three different days to investigate the inter-day variation and the day to day variation of BLMO synthesis. The resulting materials were characterised through XRD using a Co K $\alpha$  source and Rietveld analysis. The XRD patterns collected for the materials can be seen in Figure 3-15, where peaks for BLMO ( $\sim 7.0$  and  $\sim 3.5$  Å) and hausmannite (approximately 5.28, 2.74, 2.47, and 2.36 Å) are observed. From the XRD patterns, the BLMO inter-day variation between the samples is usually minimal, however, there is a larger day to day variation in the material prepared. Discrepancies in all the cell parameters refined (Table 3-9, Figure 3-16) are observed between the nine replicates, with the most dissimilarity found in the  $b$ ,  $\alpha$ , and  $\beta$  parameters. Even with the uncertainty within the refinement system this shows that there can be slight changes to BLMO crystallite structure between different batches prepared using the same synthesis method.

**Table 3-8: Average manganese oxidation states for nine replicates of synthesis method C. Errors are standard deviation of triplicate analysis ( $n=3$ ).**

BLMO Material	Average Manganese Oxidation State
Set 1 Rep1	3.33 $\pm$ 0.10
Set 1 Rep 2	3.47 $\pm$ 0.07
Set 1 Rep 3	3.54 $\pm$ 0.02
Set 2 Rep1	3.14 $\pm$ 0.21
Set 2 Rep 2	3.26 $\pm$ 0.09
Set 2 Rep 3	3.78 $\pm$ 0.18
Set 3 Rep 1	3.17 $\pm$ 0.46
Set 3 Rep 2	3.50 $\pm$ 0.14
Set 3 Rep 3	3.53 $\pm$ 0.02

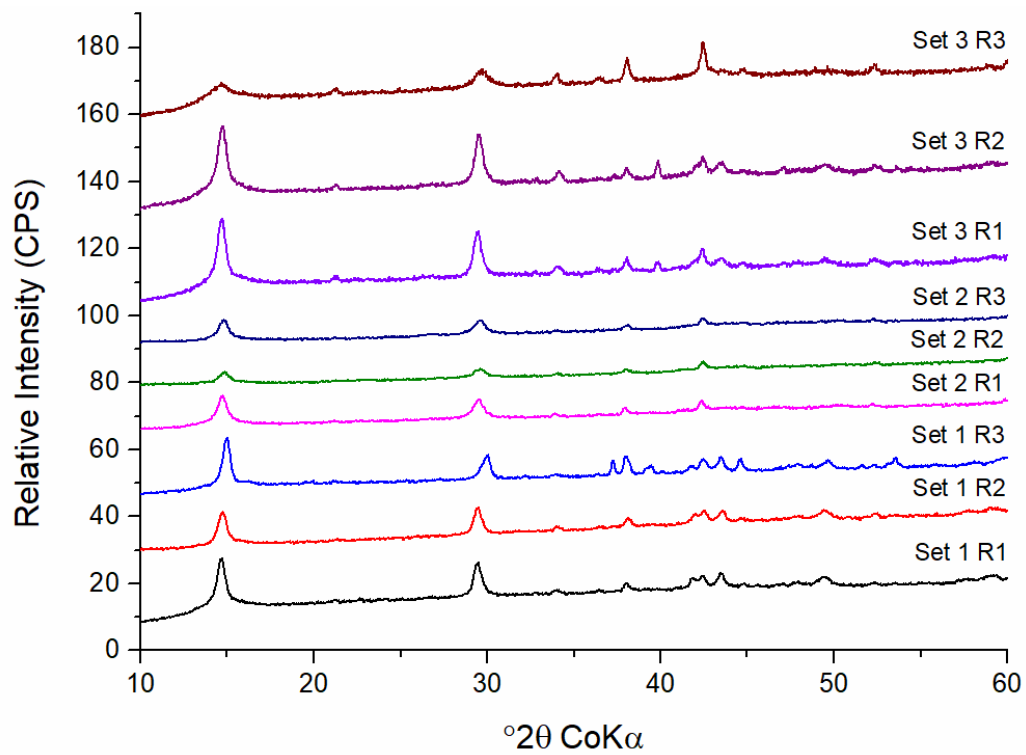


Figure 3-15:  $\text{CoK}\alpha$  XRD patterns for the nine replicate materials synthesised using method C. Patterns are y-offset for clarity.

**Table 3-9: Rietveld refinement results for the nine replicate BLMO materials, shown are the final refined cell parameters,  $R(F^2)$  and the residual ( $R_{wp}$ ).**

	Set1 R1	Set1 R2	Set1 R3	Set2 R1	Set2 R2	Set2 R3	Set3 R1	Set3 R2	Set 3 R3
Space Group	C -1	C -1	C -1	C -1					
Radiation Source	Co	Co	Co	Co	Co	Co	Co	Co	Co
Unit Cell									
a (Å)	5.160(8)	5.167(9)	5.195(30)	5.176(18)	5.128(27)	5.068(16)	5.09(13)	5.152(14)	5.138(22)
b (Å)	2.8373(18)	2.8464(14)	2.836(5)	2.813(6)	2.821(11)	2.941(10)	2.88(3)	2.8454(23)	2.838(6)
c (Å)	7.233(15)	7.293(17)	7.12(6)	7.16(4)	7.25(6)	7.15(4)	7.18(24)	7.258(30)	7.22(6)
$\alpha$ (°)	90.50(10)	89.52(14)	89.5(4)	90.9(3)	88.2(4)	92.24(28)	87.8(9)	89.54(17)	90.4(4)
$\beta$ (°)	103.6(4)	103.37(6)	104.11(19)	101.49(12)	101.42(15)	97.62(14)	102.8(8)	103.51(9)	103.17(17)
$\gamma$ (°)	89.926(26)	89.59(3)	89.44(9)	89.41(8)	87.53(10)	93.68(11)	87.1(4)	89.69(5)	90.2(7)
Vol (Å <sup>3</sup> )	102.92(6)	104.3(5)	101.69(18)	102.16(22)	102.62(29)	105.36(32)	102.3(6)	103.45(8)	102.47(17)
Refinement									
No. of Observations	2985	2985	2985	2985	2985	2985	2985	2985	2985
No. of Reflections	30	29	30	29	30	30	29	30	28
Diffraction Range (°2 $\theta$ )	10 - 75	10 - 75	10 - 75	10 - 75	10 - 75	10 - 75	10 - 75	10 - 75	10 - 75
$R(F^2)$	0.14694	0.15257	0.32718	0.0686	0.03568	0.04777	0.08447	0.16245	0.0902
$R_{wp}$	0.02523	0.02607	0.04283	0.02144	0.01738	0.01885	0.02732	0.0308	0.03135

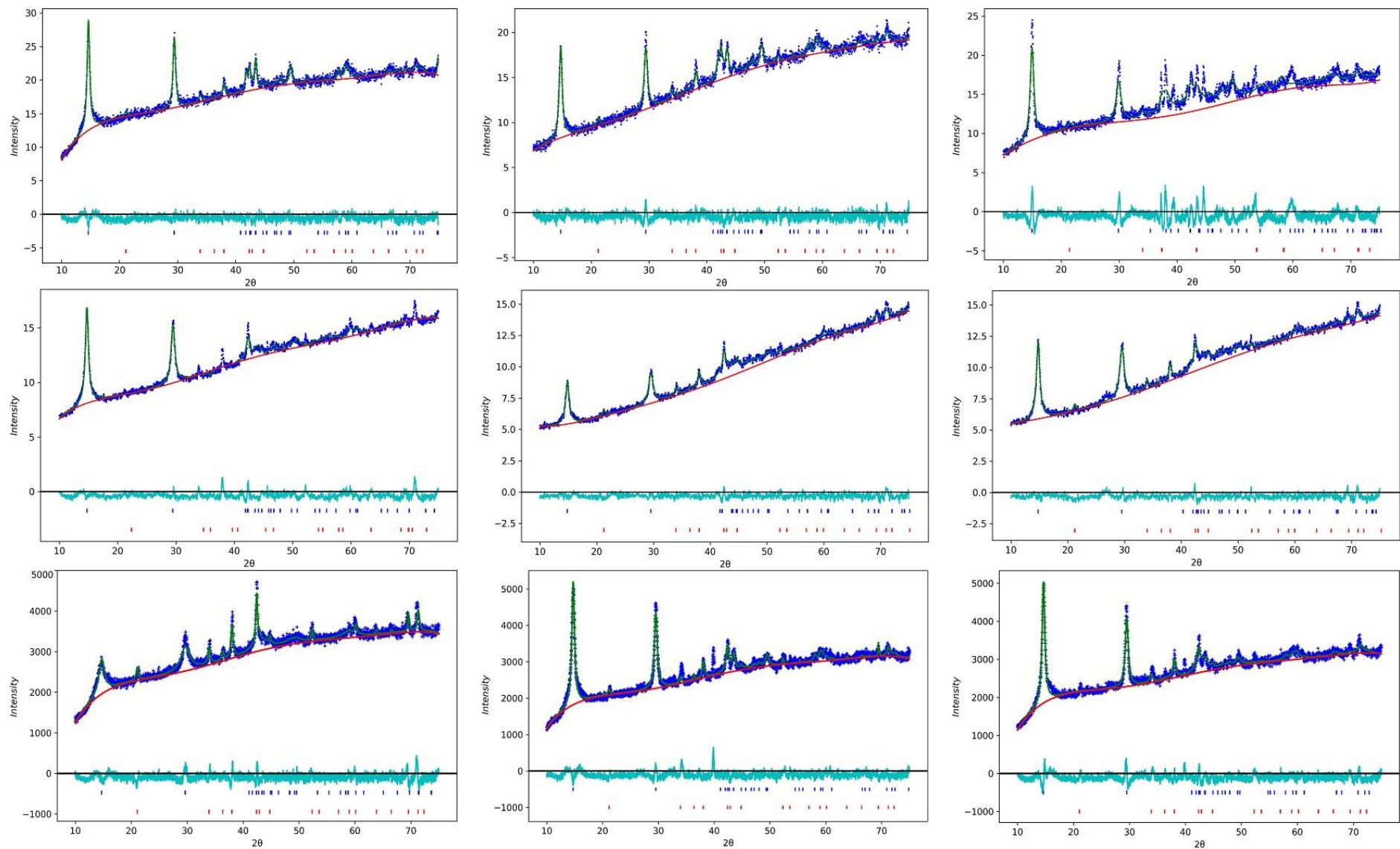


Figure 3-16: Rietveld refinements and difference curves for the nine replicate birnessite materials conducted on diffraction patterns collected by CoK $\alpha$ .

### 3.3.6 Static Ageing

The variation in synthesis reproducibility of BLMO materials presents concerns for the reactivity and application reproducibility of BLMOs. Here, we investigate what effect changing the time allowed to age in solution has on the crystal structure of the BLMO prepared using method C. The CoK $\alpha$  XRD patterns (Figure 3-17) collected show that the crystalline BLMO structure is formed after two days, and that increasing the time further doesn't does not have an increased positive effect. It was found that the sample allowed to age for 7 days contained more hausmannite impurities than the other time points. The average manganese oxidation state takes a day to increase from  $\sim 3$  to the expected value of with errors  $\sim 3.5$  (Table 3-10). This suggests that there is a slow change in oxidation state that over time results in an increase in crystallinity of the BLMO material. Rietveld refinements (Table 3-11, Figure 3-18) support this change in structure as the cell parameters change slowly towards the values expected for Na-BLMO with the closest values being for the two day sample. There is some uncertainty in these refinement values due to using a CoK $\alpha$  source.

**Table 3-10: Average manganese oxidation state of BLMO prepared while investigating the effect of static ageing. Errors are standard deviation of triplicate analysis ( $n=3$ ).**

BLMO Material	Average Manganese Oxidation State
0 Days	$3.06 \pm 0.09$
1 Day	$3.96 \pm 0.24$
2 Days	$3.99 \pm 0.49$
5 Days	$3.72 \pm 0.46$
7 Days	$4.37 \pm 0.30$

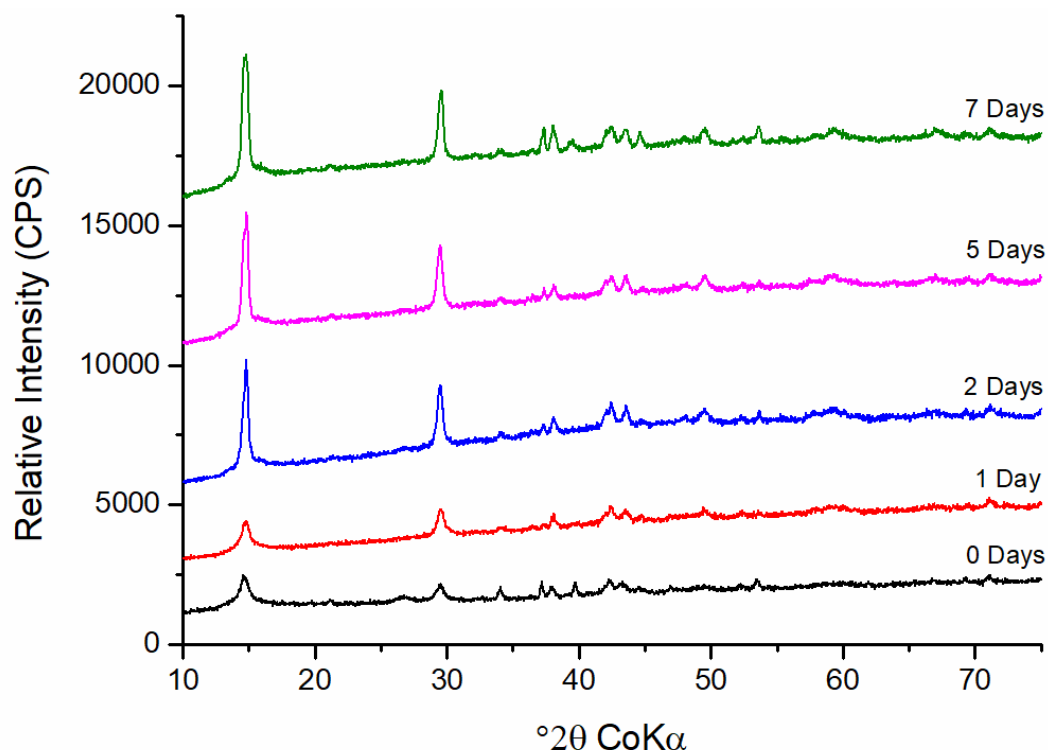
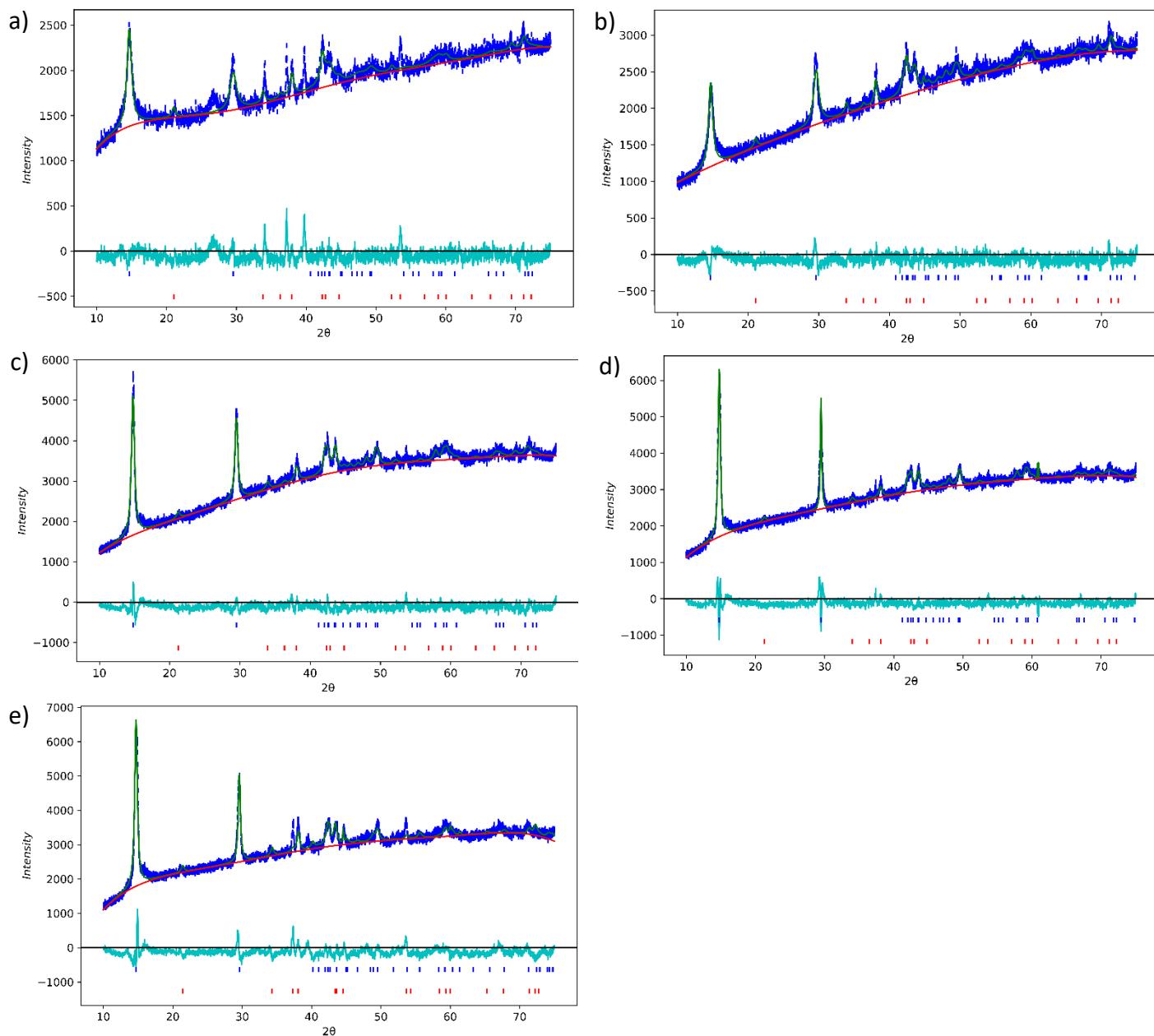


Figure 3-17: CoK $\alpha$  XRD patterns for the BLMO materials prepared while investigating the effect of static ageing time synthesised using method C. Patterns are  $\gamma$ -offset for clarity.

Table 3-11: Rietveld refinement results for BLMO materials prepared while investigating the effect of static ageing, shown are the final refined cell parameters,  $R(F^2)$  and the residual ( $R_{wp}$ ).

	0 Days	1 Day	2 Days	5 Days	7 Days
Space Group	C-1	C-1	C-1	C-1	C-1
Radiation Source	Co	Co	Co	Co	Co
Unit Cell					
a (Å)	5.19(9)	5.16(14)	5.16(8)	5.158(11)	5.137(18)
b (Å)	2.838(12)	2.8361(31)	2.8484(161)	2.8486(18)	2.966(25)
c (Å)	7.24(16)	7.201(27)	7.295(16)	7.293(22)	7.63(15)
$\alpha$ (°)	89.5(9)	90.41(17)	90.44(11)	89.60(19)	107.45(20)
$\beta$ (°)	104.2(5)	103.70(8)	103.34(5)	103.26(7)	105.17(12)
$\gamma$ (°)	89.47(31)	89.68(5)	90.011(27)	89.64(4)	87.80(6)
Vol (Å <sup>3</sup> )	103.3(6)	102.39(11)	104.33(6)	104.30(6)	106.82(11)
Refinement					
No. of Observations	2985	2985	2985	2985	2985
No. of Reflections	28	29	28	29	32
Diffraction Range (°2 $\theta$ )	10 - 75	10 - 75	10 - 75	10 - 75	10 - 75
$R(F^2)$	0.19335	0.15274	0.11379	0.19663	0.25776
$R_{wp}$	0.03571	0.02847	0.02601	0.0327	0.03922



**Figure 3-18: Rietveld refinements and difference curves for the static ageing BLMO materials conducted on diffraction patterns collected by  $\text{CoK}\alpha$ . a) 0 days, b) 1 day, c) 2 days, d) 5 days and e) 7 days.**

### 3.3.7 Stirring Rate

Another synthesis factor that may result in different BLMO materials is stirring rate. We found that decreasing the stirring rate resulted in a decrease in the peak height of the BLMO peaks, along with an increase in the hausmannite peaks in the XRD patterns (Figure 3-19). Consistent with this, the cell parameters (Table 3-12, Figure 3-20) were dependent on the stirring rate. The greatest effect on the cell parameters was observed for the unstirred reaction mixture. When compared to the stirred mixture, the unstirred mixture resulted in lower unit cell volumes,  $a$  and  $\beta$  values, along with larger  $b$ ,  $\alpha$  and  $\gamma$  values. Minor differences in the cell parameters were observed for the slow and fast stirring speeds, but these were within refinement errors. However, the level of hausmannite peaks was observed to increase in the slow stirring sample. This indicates that fast stirring is essential for achieving high crystallinity and reduced impurities.

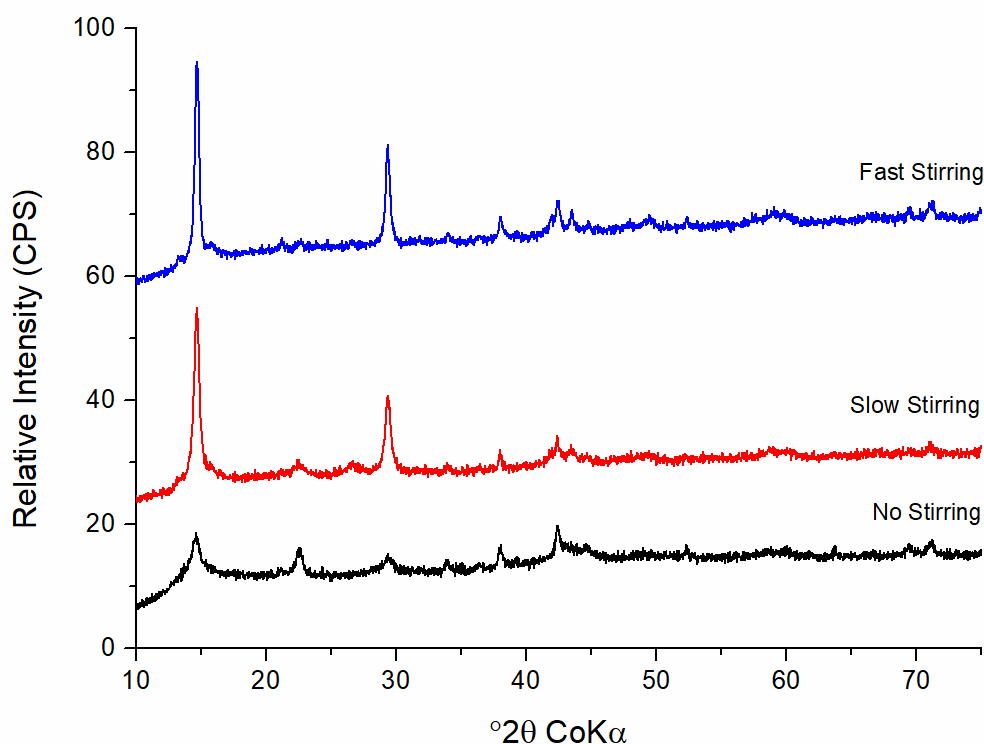
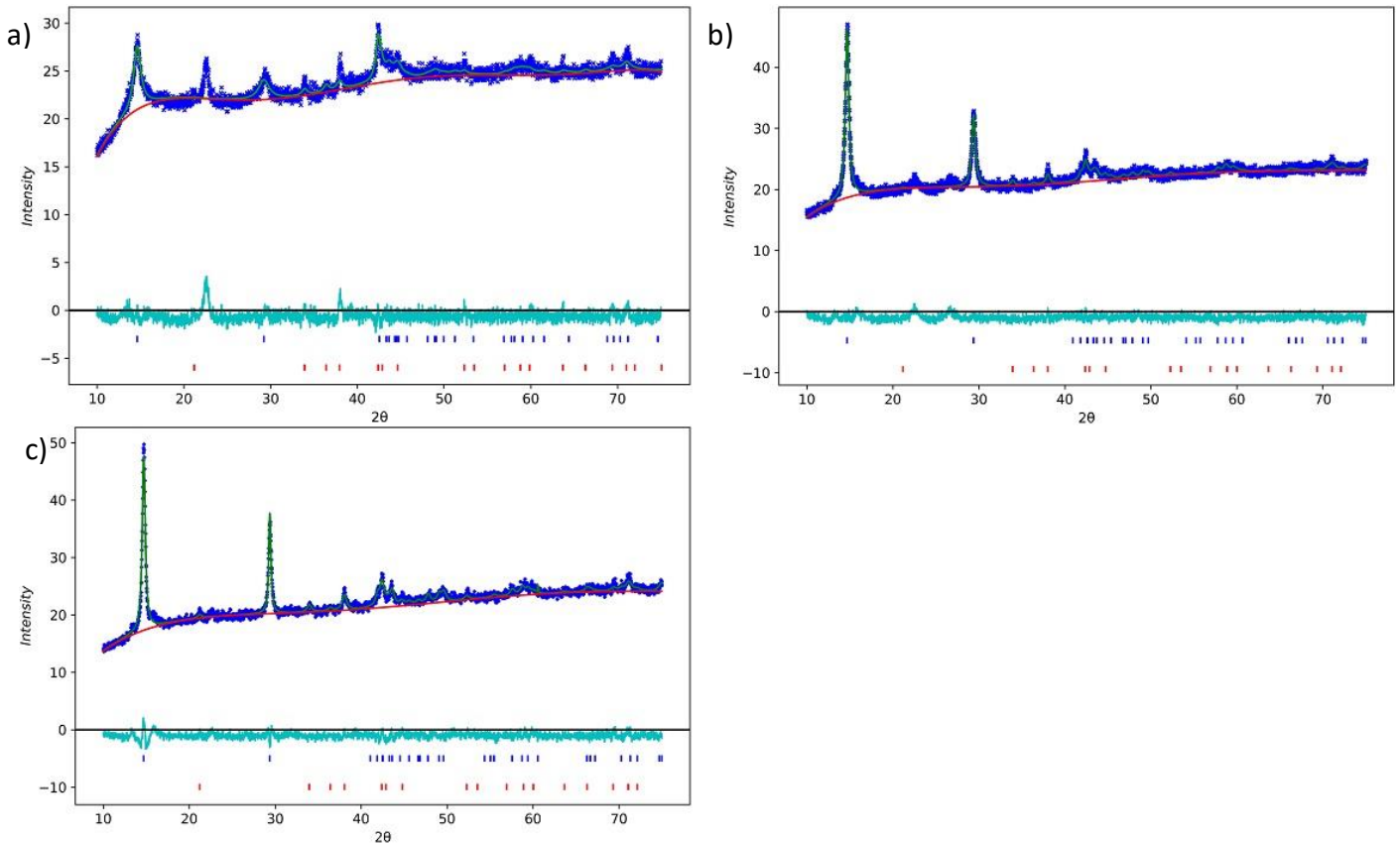


Figure 3-19:  $\text{CoK}\alpha$  diffraction patterns collected for BLMO samples prepared with various stirring conditions. Patterns are y-offset for clarity.

**Table 3-12: Rietveld refinement results for BLMOs prepared with different stirring rates, shown are the final refined cell parameters, the  $R(F^2)$  and  $R_{wp}$  values.**

	No Stirring	Slow Stirring	Fast Stirring
Space Group	C -1	C -1	C -1
Radiation Source	Co	Co	Co
Unit Cell			
a (Å)	4.805(30)	5.183(13)	5.173(8)
b (Å)	2.883(12)	2.839(3)	2.85535(22)
c (Å)	7.29(8)	7.313(27)	7.318(18)
$\alpha$ (°)	93.6(4)	90.79(17)	90.62(11)
$\beta$ (°)	100.64(27)	103.64(8)	103.23(5)
$\gamma$ (°)	90.47(16)	89.77(4)	89.784(20)
Vol (Å <sup>3</sup> )	99.04(30)	104.58(12)	105.15(8)
Refinement			
No. of Observations	2985	2060	2060
No. of Reflections	30	30	30
Diffraction Range (°2 $\theta$ )	10 – 75	10 - 75	10 - 75
$R(F^2)$	0.11564	0.13482	0.0666
$R_{wp}$	0.023	0.02084	0.02205



**Figure 3-20: Rietveld refinements and difference curves of birnessites prepared with various stirring rates a) no stirring, b) slow stirring, and c) fast stirring. Diffraction patterns were collected by CoK $\alpha$ .**

### 3.3.8 Reagent Age

In order to examine the effect of reagent age, the synthesis of BLMO was undertaken with both fresh stock solutions and solutions kept covered at 4 °C for two months. When analysing the diffraction patterns (Figure 3-21), it can be seen that the BLMO peaks remain similar between the two batches but there is an increased intensity of the hausmannite peaks when using the aged reagent, suggesting an increase in impurities. This is reflected in the cell parameters refined for both the fresh and aged samples (Table 3-13, Figure 3-22), which remain similar within errors. These results suggest that reagent age doesn't does not affect the crystal structure of BLMO materials, but that it affects the synthesis of by-products.

### 3.3.9 Reagent Concentration

To investigate the subtle differences in BLMO crystal structures that could be due to the slight differences in concentration of the reactant solutions, BLMOs were prepared using stock solutions of  $\text{KMnO}_4/\text{NaOH}$  and  $\text{MnCl}_2$  that were used in the concentrated and diluted forms (10% and 50%). It can be seen in the diffraction patterns (Figure 3-23) that there is some difference in the peak shapes and only minor differences in the hausmannite peaks shapes between the usual concentration and the 50% sample, whereas the 10% shows minimal BLMO features. The refined cell parameters for these samples (Table 3-14, Figure 3-24), show that the cell parameters transform from distorted unit cell values for the 10%, to only minorly distorted values in the 50% test, to the expected values for the concentrated values.

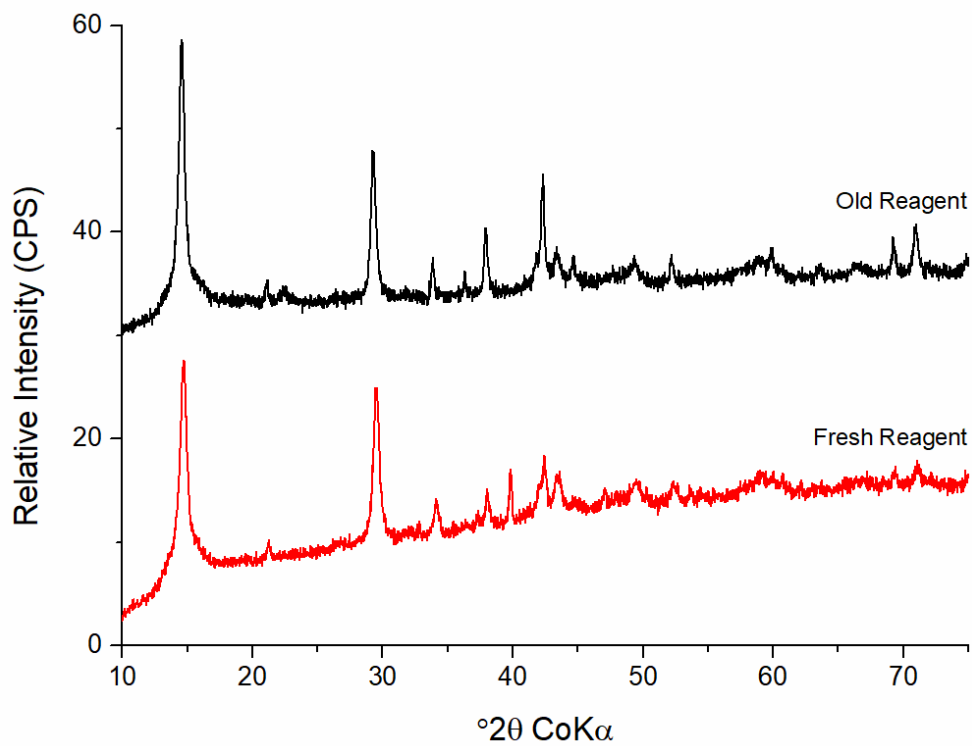


Figure 3-21: CoK $\alpha$  diffraction patterns collected for BLMO samples prepared with fresh and two-month aged stock solutions. Patterns are y-offset for clarity.

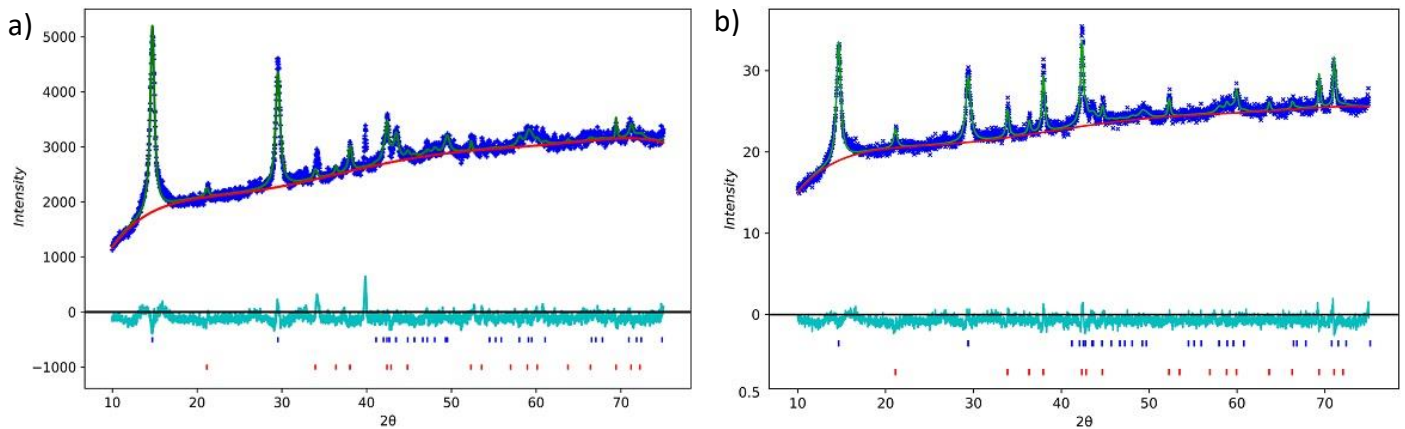
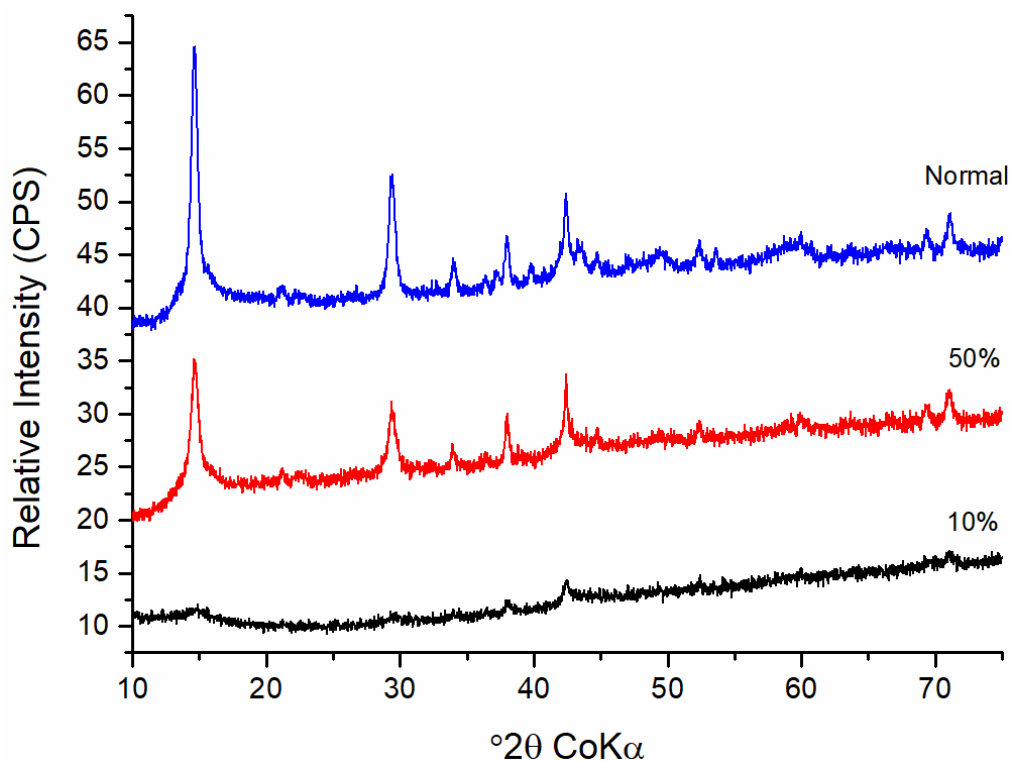


Figure 3-22: Rietveld refinements and difference curves of birnessite prepared with a) fresh stock solutions and b) two-month-old stock solutions. Diffraction patterns were collected by CoK $\alpha$ .

**Table 3-13: Rietveld refinement results for birnessite prepared with fresh and two-month-old stock solutions, shown are the final refined cell parameters, the  $R(F^2)$  and  $R_{wp}$  values.**

	Fresh Reagent	Old Reagent
Space Group	C -1	C -1
Radiation Source	Co	Co
Unit Cell		
a (Å)	5.152(14)	5.14(22)
b (Å)	2.8454(23)	2.839(8)
c (Å)	7.258(30)	7.29(5)
$\alpha$ (°)	89.54(17)	90.7(5)
$\beta$ (°)	103.51(9)	103.42(14)
$\gamma$ (°)	89.69(5)	90.17(8)
Vol (Å <sup>3</sup> )	103.45(8)	103.41(24)
Refinement		
No. of Observations	2985	2060
No. of Reflections	30	30
Diffraction Range (°2 $\theta$ )	10 - 75	10 - 75
$R(F^2)$	0.16245	0.21048
$R_{wp}$	0.0308	0.02079



**Figure 3-23: CoK $\alpha$  diffraction patterns collected for BLMO samples prepared using concentrated and diluted stock solutions. Patterns are y-offset for clarity.**

**Table 3-14: Rietveld refinement results for BLMOs prepared with different stock concentrations, shown are the final refined cell parameters, the  $R(F^2)$  and  $R_{wp}$  values.**

	10% Dilution	50% Dilution	Concentrated
Space Group	C -1	C -1	C -1
Radiation Source	Co	Co	Co
Unit Cell			
a (Å)	4.967(24)	5.02(7)	5.158(23)
b (Å)	2.930(6)	2.912(25)	2.837(7)
c (Å)	7.11(4)	7.21(18)	7.24(5)
$\alpha$ (°)	91.26(17)	91.6(12)	90.5(3)
$\beta$ (°)	100.53(15)	100.1(5)	103.56(15)
$\gamma$ (°)	93(10)	90.68(19)	89.61(7)
Vol (Å <sup>3</sup> )	101.55(18)	103.7(7)	102.98(23)
Refinement			
No. of Observations	2985	2985	2985
No. of Reflections	29	28	30
Diffraction Range (°2 $\theta$ )	10 - 75	10 - 75	10 - 75
$R(F^2)$	0.4889	0.18111	0.10986
$R_{wp}$	0.02483	0.02032	0.02946

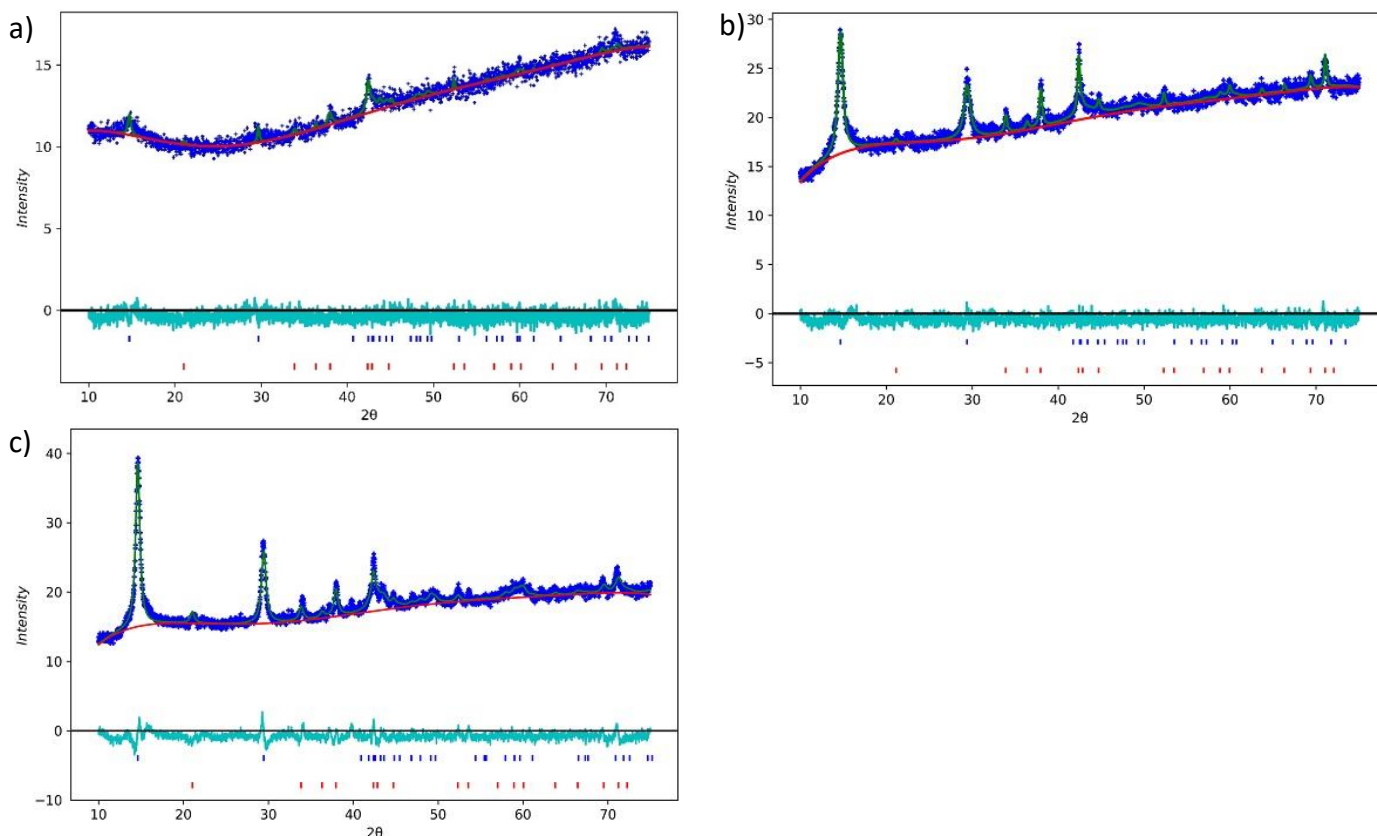


**Figure 3-24: Rietveld refinements and difference curves of birnessites prepared with different concentrations of stock solutions a) 1 in 10 dilution, b) 1 in 2 dilutions, and c) concentrated stock solutions. Diffraction patterns were collected by CoK $\alpha$ .**

### 3.3.10 Synthesis NaOH Concentration

As reagent concentration was determined to have a significant effect on the structure of BLMOs prepared by method C, an investigation was conducted into the effect of NaOH concentration independent of other reagents. We observed that a 25% reduction in the NaOH amount causes a significant decrease in the peak sharpness of the BLMO materials (Figure 3-25) and continued to decrease as the amount was decreased. Rietveld Refinements (Figure 3-26, Table 3-15) show that the BLMO crystal structure becomes extremely distorted as the NaOH concentration is decrease, which the 0 g NaOH material being unable to be refined. The 9 g and 6 g materials contained an increased amount of hausmannite, and sodium chloride as by-products of the synthesis. These results suggest that for this synthesis method, NaOH plays an important role in the BLMO structure.

### 3.3.11 Variability in BLMO parameters

The large number of BLMO materials prepared and characterised in this work have shown the variability in BLMO structure, even when using the same synthesis method. Variation plots for many structural properties can be seen in Figure 3-27 and clearly show the variability present in synthetic BLMO materials. As the reactivity of BLMO is known to be dependent on its structure, the slight variability in structure imparted by the synthesis method could cause some variations in the materials reactivity. The effect of this structural variability on the reactivity of these materials is investigated in Chapter 4.

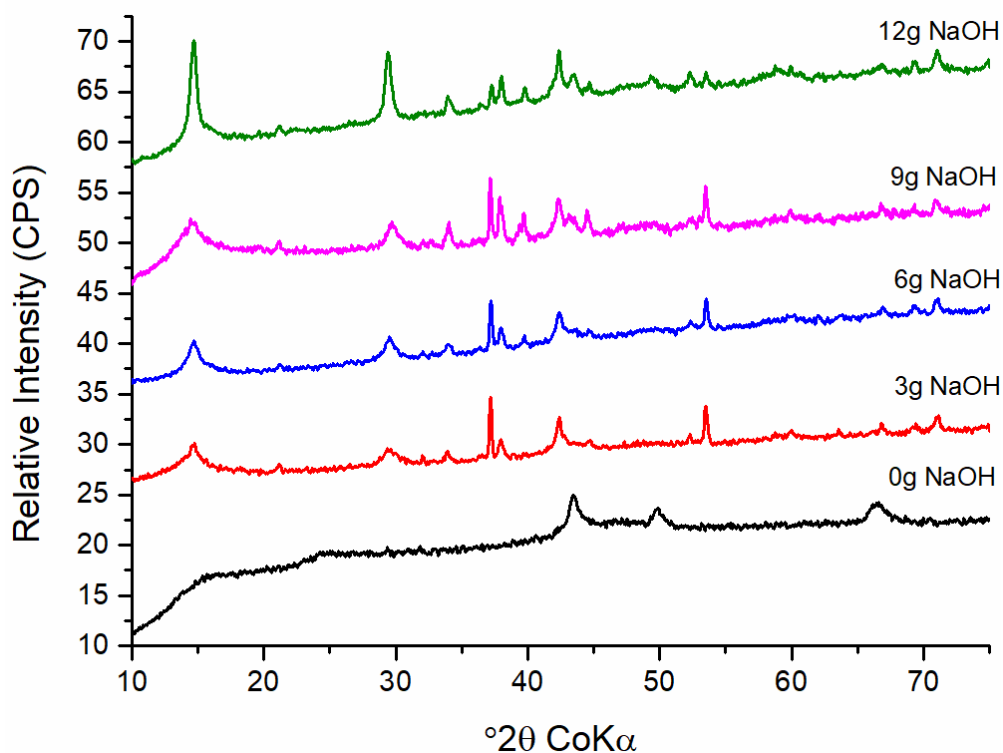
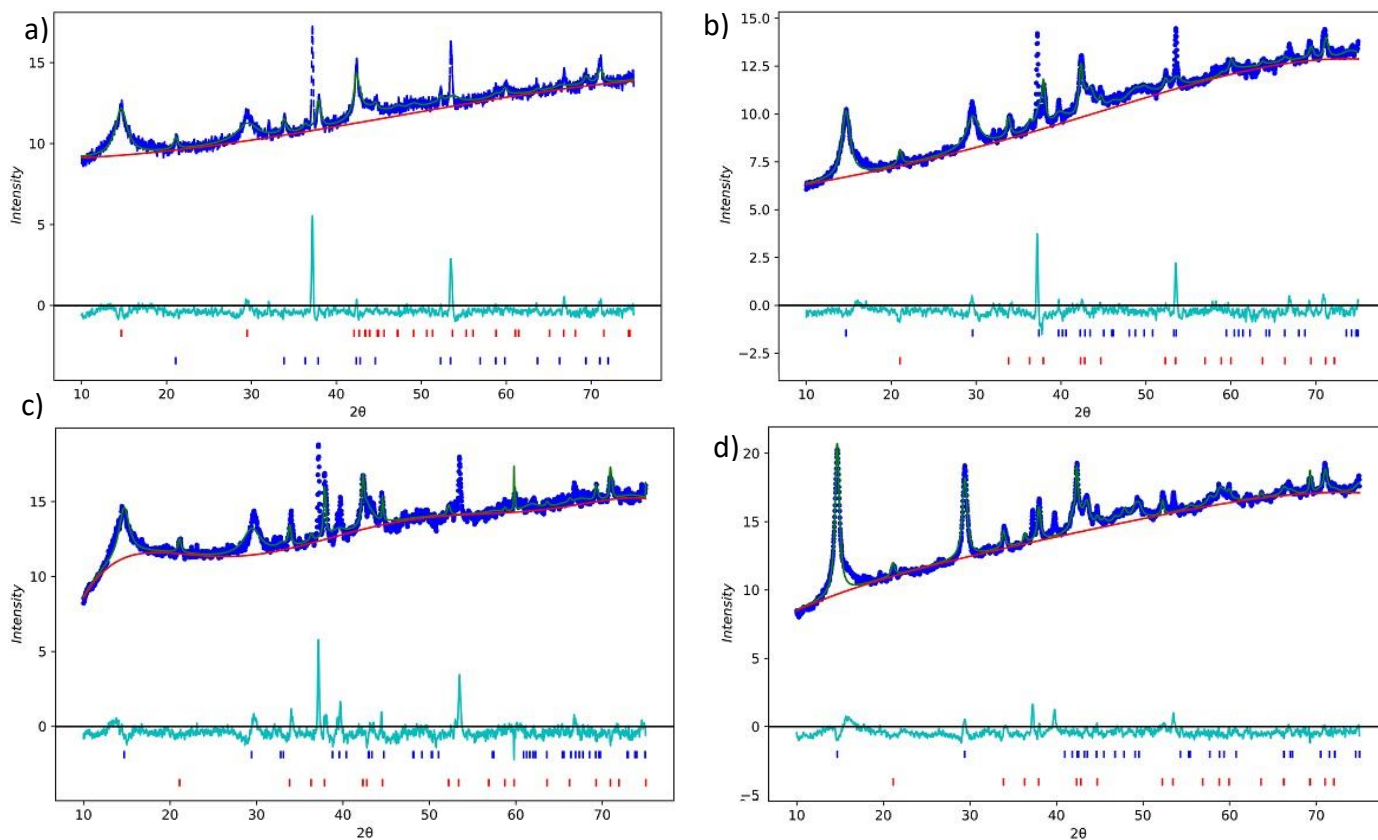


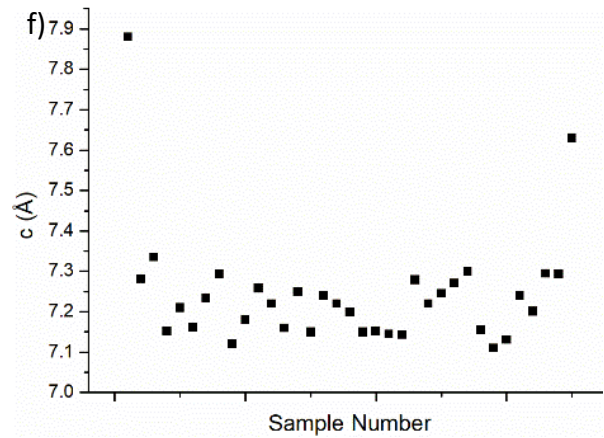
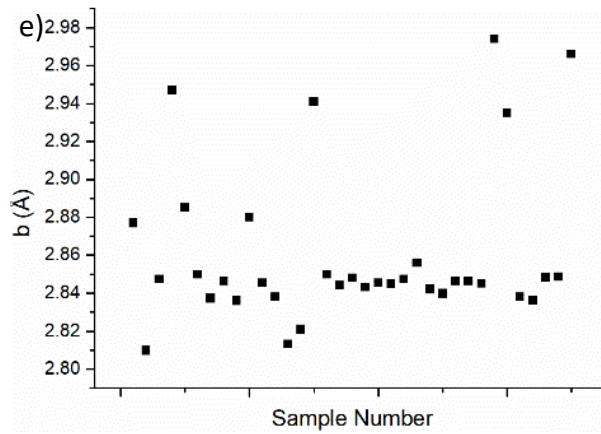
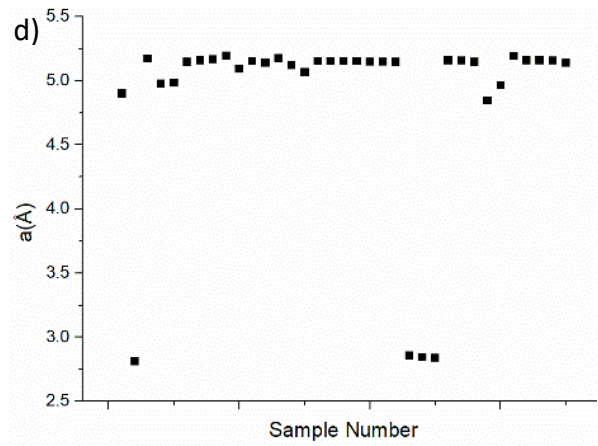
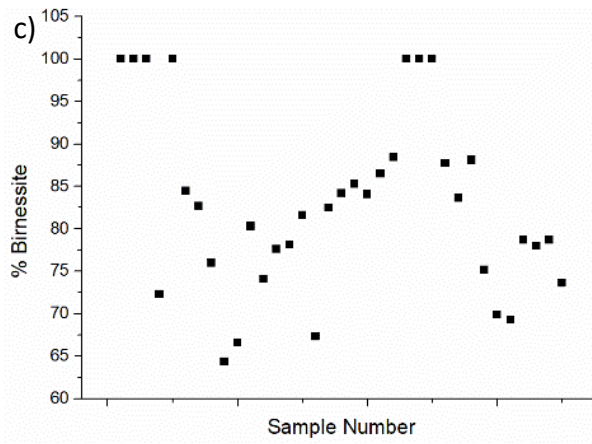
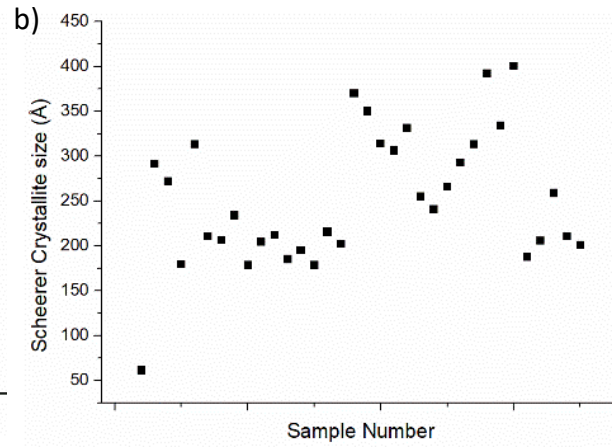
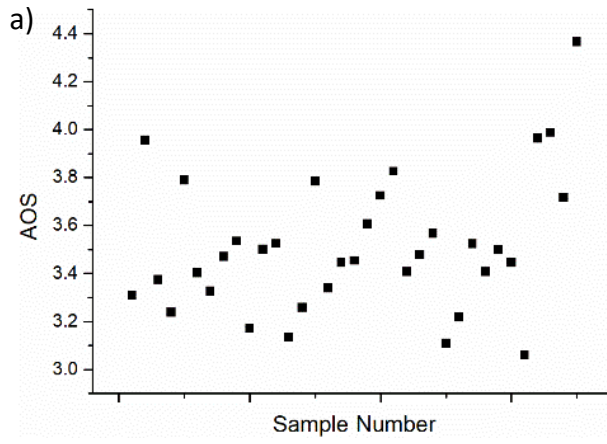
Figure 3-25: CoK $\alpha$  diffraction patterns of BLMOs prepared with varying sodium hydroxide content.

Table 3-15: Rietveld refinement results for BLMOs prepared with different sodium hydroxide concentrations, shown are the final refined cell parameters, the  $R(F^2)$  and  $R_{wp}$  values.

	3g	6g	9g	12g
Space Group	C -1	C -1	C -1	C -1
Radiation Source	Co	Co	Co	Co
Unit Cell				
a (Å)	4.855(22)	4.846(13)	6.52(27)	5.173(11)
b (Å)	2.904(24)	3.276(11)	2.766(19)	2.8498(22)
c (Å)	7.12(13)	7.008(10)	8.7(5)	7.291(22)
$\alpha$ (°)	96.3(4)	88.84(21)	83.1(5)	90.44(14)
$\beta$ (°)	94.2(5)	90.23(17)	125.5(6)	103.44(7)
$\gamma$ (°)	90.41(17)	86.45(13)	93.6(4)	89.68(4)
Vol (Å <sup>3</sup> )	99.4(5)	111.02(19)	127.3(5)	104.54(8)
Refinement				
No. of Observations	2985	2985	2985	2985
No. of Reflections	17	34	42	30
Diffraction Range (°2 $\theta$ )	10 - 75	10 - 75	10 - 75	10 - 75
$R(F^2)$	0.12644	0.12223	0.16092	0.12658
$R_{wp}$	0.03009	0.02814	0.03377	0.02203



**Figure 3-26: Rietveld refinements and difference curves of birnessites prepared with different amounts of sodium hydroxide a) 3 g, b) 6 g, c) 9 g, and d) 12 g. Diffraction patterns were collected by  $\text{CoK}\alpha$ .**



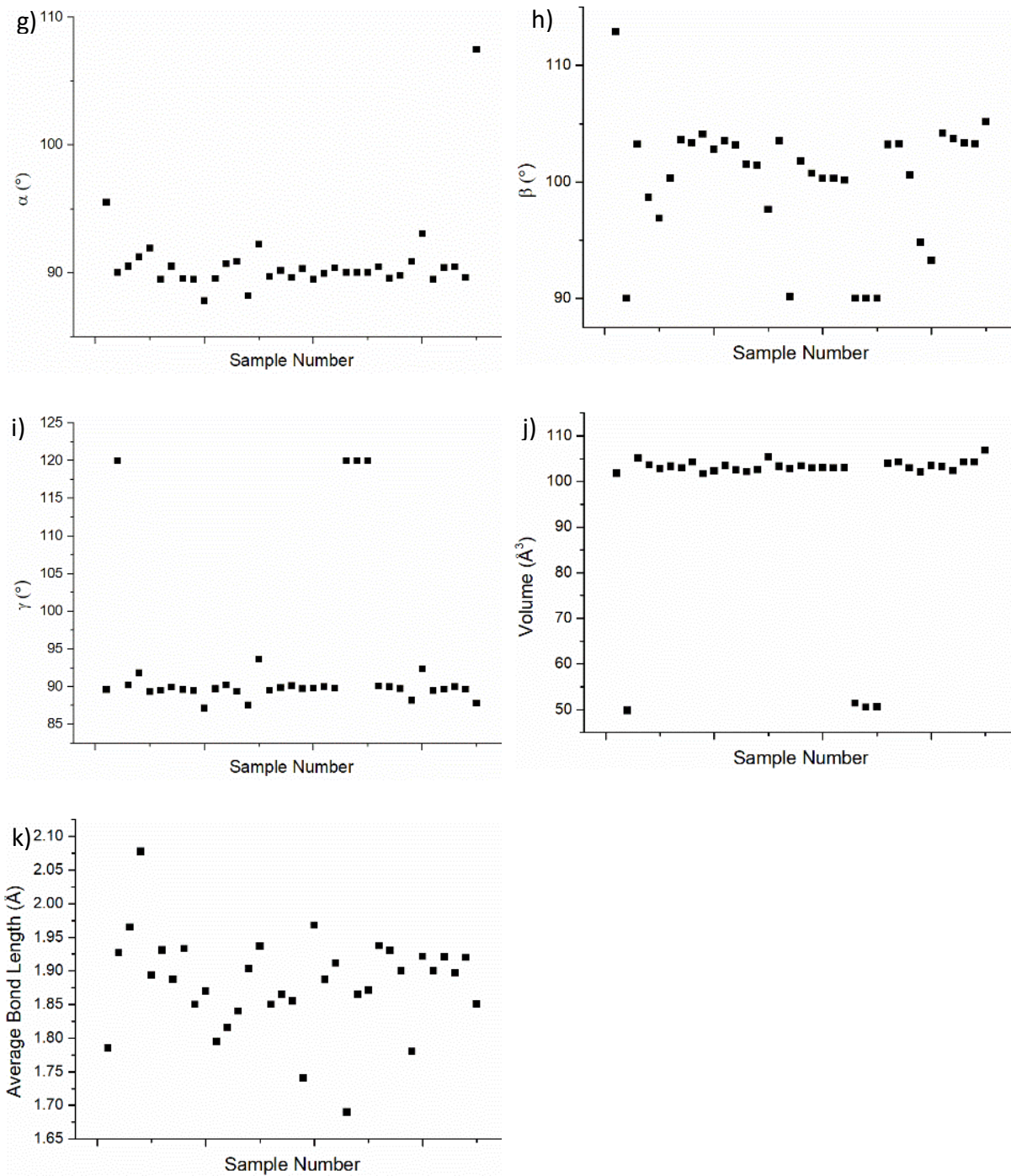


**Figure 3-27: Scatter plots showing the variation in structural parameters refined for the BLMO materials synthesized in this chapter. The parameters shown here are a) average manganese oxidation state, b) Scheerer crystallite size, c) % birnessite phase present in the refinement, d) the a unit cell parameter, e) the b unit cell parameter, f) the c unit cell parameter, g) the  $\alpha$  unit cell parameter, h) the  $\beta$  unit cell parameter, i) the  $\gamma$  unit cell parameter, j) the unit cell volume, and k) the average Mn-O bond length in the manganese oxide octahedra.**

### 3.4 Conclusion

The structure and morphology of synthetic BLMO is greatly dependent on the preparation method and post synthesis treatments. Furthermore, even when using the same synthesis method, batch to batch variations can be observed. Thus, careful characterization (SEM, XRD and Rietveld refinements) of synthetic BLMO is crucial to enable the comparison of any applications utilizing this material. We show that fit for purpose Rietveld refinements can be achieved for crystalline BLMO samples using Mo, Co and Cu x-ray sources, demonstrating that XRD data from more common x-ray sources such as Co and Cu can be used to provide useful structural information. Investigations into the effect of simple changes to the synthesis of BLMOs found that reagent concentration, stirring rate, and the length of aging time were factors that had a large effect on the resulting BLMOs crystallinity and purity. The optimal synthesis procedure for preparing well crystallized homogenous BLMO materials using an alkaline reduction of  $Mn^{7+}$  with  $Mn^{2+}$  involves the rapid stirring of highly concentrated reagents followed by an aging time of two days. These parameters could also influence the quality of BLMO materials prepared using other synthesis methods, but further investigation is needed.

## Chapter 4 Reactivity of birnessite-like manganese oxide materials

### 4.1 Introduction

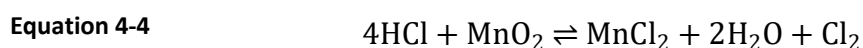
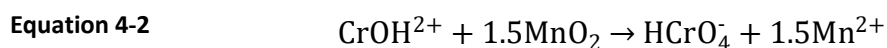
Layered manganese oxide materials such as birnessite ( $\text{Na}_x\text{MnO}_2 \cdot y\text{H}_2\text{O}$ ) and birnessite-like manganese oxides (BLMOs,  $\text{A}_x\text{MnO}_2 \cdot y\text{H}_2\text{O}$ , where A is a cation other than  $\text{Na}^+$ ) have been reported to have a wide range of applications that range from the oxidation of organic molecules<sup>49, 53, 66, 73, 214</sup>, to their use in supercapacitors<sup>209, 215</sup>. A number of studies have reported the ability of BLMOs to oxidise dissolved metal species such as  $\text{As}^{3+}$  to  $\text{As}^{6+}$ <sup>29, 80-81, 216-217</sup>,  $\text{Au}^+$  to  $\text{Au}^{3+}$ <sup>82</sup>,  $\text{Cr}^{3+}$  to  $\text{Cr}^{6+}$ <sup>77, 218-219</sup> and  $\text{Co}^{2+}$  to  $\text{Co}^{3+}$ <sup>220-222</sup>. In 2019, a study by Manning *et al.*<sup>223</sup> demonstrated that aqueous suspensions of BLMOs have the ability to oxidise silver nanoparticles from their elemental oxidation state of Ag to  $\text{Ag}^+$ .

Experimental conditions reported for the oxidation of metals by BLMO materials in aqueous conditions vary widely. Reactions have been undertaken using differing metal concentrations, pH's, and in the presence or absence of NaCl (Table 4-1). To further complicate matters, researchers utilize different BLMO synthesis methods, resulting in different BLMO materials being used. These factors make it difficult to directly compare the reported reactivity of BLMOs towards metal oxidation.

**Table 4-1: Summary of the experimental conditions used for the oxidation of metals by BLMO materials in literature.**

Study	Element Oxidised	Initial Concentration of Metal	pH	NaCl	Birnessite/BLMO Utilised
Gude <i>et al.</i> 2017 <sup>216</sup>	As <sup>3+</sup>	20 µg/L	7	N/A	Birnessite, mixed MnO <sub>2</sub>
Villalobos <i>et al.</i> 2014 <sup>29</sup>	As <sup>3+</sup>	300 µM	4.5, 6	Yes	Acid birnessite, triclinic birnessite
Fischel <i>et al.</i> 2015 <sup>217</sup>	As <sup>3+</sup>	100 µM	4.5, 7.2, 9	Yes	Acid birnessite, random stacked birnessite, biogenic Mn-Oxide, hexagonal birnessite
Lafferty <i>et al.</i> 2010 <sup>80</sup>	As <sup>3+</sup>	100 µM	7.2	Yes	Hexagonal birnessite
Wang <i>et al.</i> 2013 <sup>81</sup>	As <sup>3+</sup>	1 mg/L	6	No	Unknown
Ta <i>et al.</i> 2015 <sup>82</sup>	Au <sup>+</sup>	1 mg/L	2	Yes	Unknown
Kim <i>et al.</i> 2002 <sup>77</sup>	Cr <sup>3+</sup>	200 µM, 400 µM	4, 7	KCl	Natural birnessite
Kong <i>et al.</i> 2019 <sup>218</sup>	Cr <sup>3+</sup>	1 mM	2-5	No	Triclinic birnessite
Landrot <i>et al.</i> 2012 <sup>219</sup>	Cr <sup>3+</sup>	50 mM	2.5, 3, 3.5	KCl	Acid birnessite, random stacked birnessite, amorphous birnessite
Crowther <i>et al.</i> 1983 <sup>220</sup>	Co <sup>2+</sup>	0.01 M	4,6,8, 10	No	Unknown
Manceau <i>et al.</i> 1997 <sup>221</sup>	Co <sup>2+</sup>	unknown	4	No	unknown
Simanova <i>et al.</i> 2015 <sup>222</sup>	Co <sup>2+</sup>	unknown	6.5	Yes	Hexagonal
Manning <i>et al.</i> 2019 <sup>223</sup>	Ag(0)	15 mg/L	Unkn own	No	Acid birnessite

These differing reaction conditions are likely to influence the reaction mechanism and kinetics. Two mechanisms of metal oxidation have been reported in the literature. The oxidations of As<sup>3+</sup>, Cr<sup>3+</sup>, and Ag(0) were reported to occur via the direct redox reaction between the manganese dioxide material and the metal (Equation 4-1, Equation 4-2, Equation 4-3). In contrast, the oxidation of Au<sup>+</sup> was not observed in the absence of acid and sodium chloride. Here, the oxidation of Au<sup>+</sup> was hypothesized to occur via a two-step mechanism<sup>82</sup>, where the first step involved the generation of aqueous Cl<sub>2</sub>, due to the reaction of manganese oxides with acid in a sodium chloride solution (Equation 4-4)<sup>84-85</sup>. The second step via the well-researched oxidation of gold by chlorine (Equation 4-5)<sup>138, 140, 142, 145</sup>.



Chapter 3 shows that the structure, crystallite size, and purity of synthetic BLMOs are highly variable, even when prepared using the same conditions. This variability has the potential to have significant impacts on their resulting applications in catalysis, oxidation and environmental remediation. Indeed, Sabri *et al.*<sup>23</sup> showed that the structural topology and layer stacking disorder can be critical factors that affect the reactivity of the synthesized material. Their research indicated that disordered BLMOs were better oxidants. This is in contrast with the results of using BLMOs for metal oxidation, by Landrot *et al.*<sup>219</sup> and Fischel *et al.*<sup>217</sup>, who found that the more ordered acid BLMO materials oxidized more Cr<sup>3+</sup> and As<sup>3+</sup> than the disordered BLMO tested. This suggests that other factors control the ability of BLMOs to oxidise metals.

This chapter examines factors influencing the ability of BLMO's to oxidise vanadium (0) in acidic saline solutions. Our results indicate that hexagonal BLMOs are more suitable for the oxidation of vanadium and that the reactivity of triclinic BLMOs are extremely variable. We explore the underlying causes of this variability.

## 4.2 Materials and Methods

### 4.2.1 Reaction Conditions

**Preliminary Gold Oxidations:** Pilot Au oxidation was conducted in duplicate in an acidic saline solution (pH 2, 0.001 M NaCl), where 216 mg of BLMO synthesised by method C and 20 mg of Au powder (3.0-3.5  $\mu\text{m}$ , Alfa Aesar, USA) were combined and kept constant at 20 °C and 180 rpm in an orbital incubator (Labec Shaking Incubator, Australia). Samples were taken for ICP-MS analysis as described in section 2.7.2 after seven days. Preliminary PhD Au oxidations were conducted in duplicate in an acidic saline solution (pH 2, 0.05 M NaCl), where 216 mg of BLMO synthesised by method C and 20 mg of Au powder (3.0-3.5  $\mu\text{m}$ , Alfa Aesar, USA) were combined and kept constant at 25 °C and 120 rpm in a different orbital incubator (OM15, Ratek, Australia). Samples were taken for ICP-MS analysis as described in section 2.7.2 after seven days.

**Incubator Rotational Speed:** The effect of rotational speed was investigated in triplicate in an acidic saline solution (pH 2, 0.05 M NaCl), where 200 mg of BLMO synthesised by method C and 20 mg of V powder (Hopkins & Williams Limited, Wales) were combined and kept constant at 25 °C in an orbital incubator (MaxQ6000, Thermo Scientific, USA). The rotational speed of the orbital incubator was varied to values of 0, 50, 100, 150 and 200 rpm. Samples were taken for ICP-MS analysis as described in section 2.7.1 after three days.

**BLMO Aggregate Particle size:** BLMO aggregate particle size was investigated in triplicate in an acidic saline solution (pH 2, 0.05 M NaCl), where 200 mg of BLMO synthesised by method C and 20 mg of V powder (Hopkins & Williams Limited, Wales) were combined and kept constant at 25 °C and 150 rpm in an orbital incubator (MaxQ6000, Thermo Scientific, USA). Various aggregate size ranges were created using a mortar and pestle and separated using sieves, the ranges investigated were <125  $\mu\text{m}$ , 125  $\mu\text{m}$ -250  $\mu\text{m}$ , 250  $\mu\text{m}$ -500  $\mu\text{m}$ , >1 mm, and

single grain particles. Samples were taken for ICP-MS analysis as described in section 2.7.1 after four days.

#### 4.2.2 BLMO Reactivity Experiments

**Synthesis Methods:** These oxidation experiments were conducted according to the method outlined in section 2.6 utilising V powder (Hopkins & Williams Limited, Wales). The BLMO samples investigated in this section were the samples presented and characterised in section 3.3.1. These samples were allowed to react for four days before taken for analysis via ICP-MS using the methodology described in section 2.7.1.

**Effect of crystallinity:** These oxidation experiments were conducted according to the method outlined in section 2.6 utilising V powder (Hopkins & Williams Limited, Wales). The BLMO samples investigated in this section were the samples presented and characterised in section 3.3.3. These samples were allowed to react for three days before taken for analysis via ICP-MS using the methodology described in section 2.7.1.

**Effect of Interlayer Cation:** These oxidation experiments were conducted according to the method outlined in section 2.6 utilising V powder (Hopkins & Williams Limited, Wales). The BLMO samples investigated in this section were the samples presented and characterised in section 3.3.4. These samples were allowed to react for three days and after the reaction time elapsed the solutions were analysed via ICP-MS using the methodology described in section 2.7.1.

**Synthesis Reproducibility:** These oxidation experiments were conducted according to the method outlined in section 2.6 utilising V powder (Hopkins & Williams Limited, Wales). The BLMO samples investigated in this section were the samples presented and characterised in section 3.3.5. These samples were allowed to react for three days before taken for analysis via ICP-MS using the methodology described in section 2.7.1.

**Effect of Static Aging:** These oxidation experiments were conducted according to the method outlined in section 2.6 utilising V powder (Hopkins & Williams Limited, Wales). The BLMO samples investigated in this section were the samples presented and characterised in section 3.3.6. These samples were allowed to react for three days before taken for analysis via ICP-MS using the methodology described in section 2.7.1.

#### 4.2.3 Effect of Reaction Solution on BLMO Structure

A large batch of BLMO synthesised by method C was split into four sub samples consisting of 4.8 g of BLMO and then exposed to four different pre-treatments. One was soaked in milli Q water (200 mL) for 4 hours, one was soaked in a KCl solution (1 M, 200 mL) for 4 hours, the third was soaked in a NaCl solution (1 M, 200 mL) for 4 hours and the final subsample was left untreated. Further subsamples of these four BLMO materials (200 mg) were then exposed to stirring acidic saline solutions (pH 2, 0.05 M NaCl) for different amounts of time 0.25, 0.5, 1, 2, 4, 24, 48, and 72 hours. After the exposure the BLMO powders were collected via filtration, dried at room temperature and then analysed via XRD utilising a Co source as outlined in section 2.1.

### 4.3 Results and Discussion

#### 4.3.1 Reaction Conditions

A pilot study conducted using BLMO and acidic saline solutions showed that this reaction system was able to oxidised Au(0) to Au(III) and determined that pH and NaCl concentration are factors that affect the amount of gold dissolved by BLMO materials<sup>83</sup>. Where a higher NaCl concentration and lower pH results in more gold dissolved. Preliminary PhD oxidation experiments showed that there was a decrease in the amount of gold dissolved using the same BLMO (Figure 4-1), which was unexpected due to the increased salt concentration used, which should have resulted in an increase in the levels of dissolved Au.

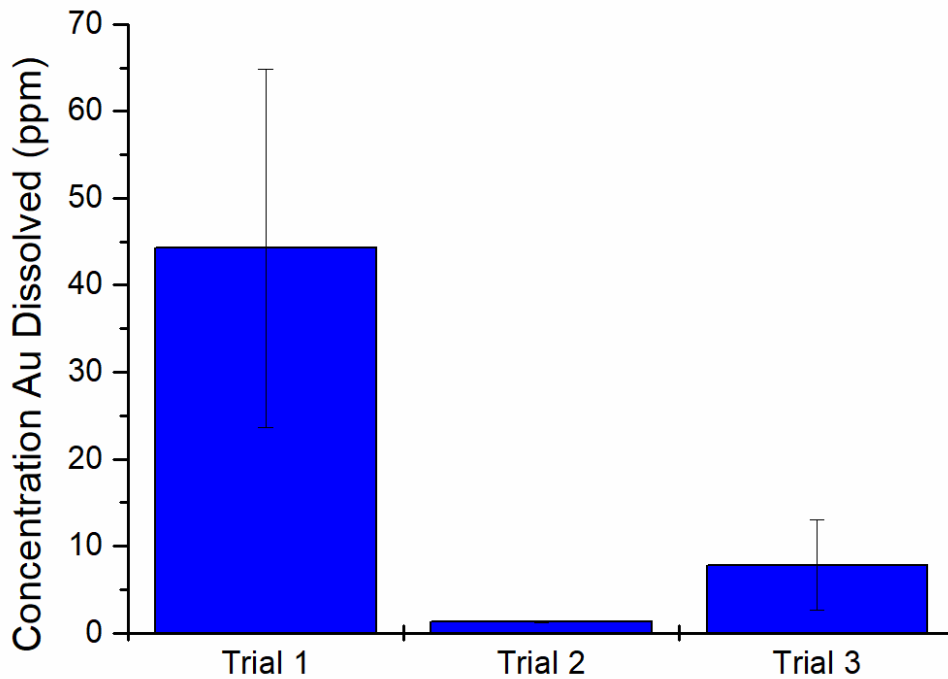


**Figure 4-1: Three individual trials attempting to use BLMO material to oxidise gold powder. Error bars represent one standard deviation  $n=2$ .**

This variation in dissolution suggest that there are some unknown factors beyond NaCl concentration and pH that affects the oxidation of metals by BLMOs. Therefore, new factors were tested to determine their effect on the reactivity of BLMO materials using the oxidation of vanadium powder instead of gold powder due to the expense. The two factors tested were rotational speed due to the observed differences in incubator rotation speed and aggregate particle size. For these experiments the salt concentration, pH, mass of V and mass of BLMO were kept constant at 0.05 M, pH 2, 20 mg V and 200 mg BLMO in 100 mL of MilliQ water. Rotational speed was varied from 0-200 rpm and the concentration of oxidised V was determined after three days via ICP-MS. Upon completion of the reaction time, it was seen that the previously colourless solutions had become yellow, which indicates the presence of  $V^{5+}$  in solution. It was observed that the amount of V oxidised was consistent within errors at ~59 ppm until the speed was increased to 150 rpm (Figure 4-2), where the amount of V in solution increased to 94 ppm. This shows that agitation increases the rate of reaction by increasing the interaction of reactants because of collision theory and mass transfer between

solid and liquid interfaces. It also shows that there is a range of rotational speeds (0-100 rpm) where the addition of agitation does not improve the effect of natural diffusion forces on metal dissolution.

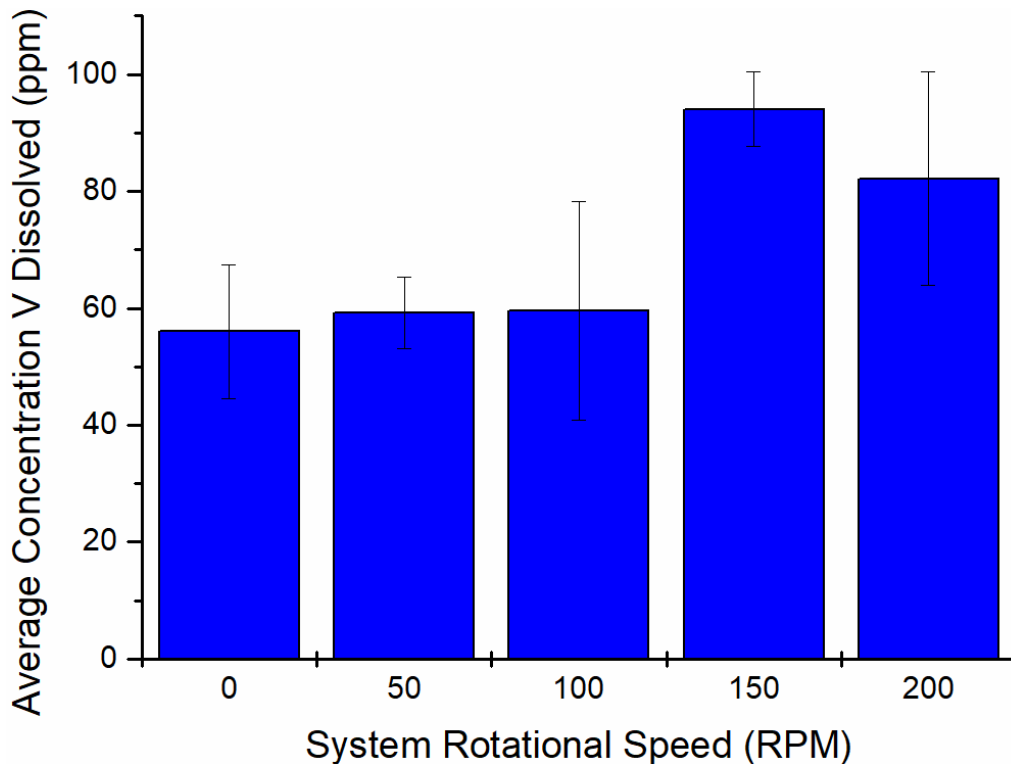


Figure 4-2: Effect of rotational speed on the amount of vanadium dissolved by a BLMO material. Error bars represent one standard deviation  $n=3$ .

Due to surface area to volume ratios affecting the rate of reaction for reactions occurring in a solid-liquid interface, BLMO aggregate size was also investigated in the same manner as above. A distribution of physical aggregates of dried BLMO material was achieved by manually grinding and sieving the dried BLMO into different size ranges. It was observed that as the BLMO size decreased from a single grain to a fine powder of  $<125 \mu\text{m}$ , the amount of V increased from 27 ppm to 112 ppm (Figure 4-3), this equates to 12-51% of the original V present. This shows that control of the aggregate size and rotational speed needs to be implemented to ensure accurate comparisons can be made between different BLMO materials in further studies. The standard conditions used for the reactivity tests in the rest

of this chapter were pH 2 (HCl), 0.05 M NaCl, 150 rpm, an aggregate particle size of <125  $\mu\text{m}$ , 25  $^{\circ}\text{C}$ , 200 mg BLMO, 20 mg vanadium powder and a final volume of 100 mL.

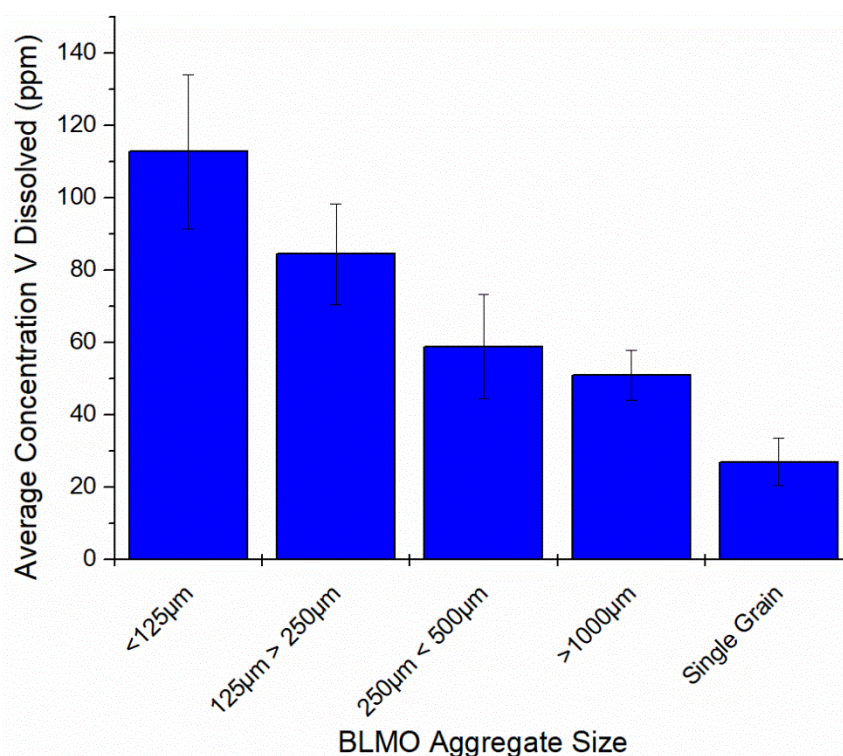


Figure 4-3: Effect of BLMO aggregate size on the amount of vanadium dissolved by a BLMO material. Error bars represent one standard deviation  $n=3$ .

#### 4.3.2 Effect of Structural Order on Reactivity

Six BLMOs with different unit cell structures were synthesized using six different literature methods. BLMO's prepared by Methods A, B, C, and C-M were all from the reduction of  $\text{Mn}^{7+}$ , whilst Methods D and D-M were prepared by oxidation of  $\text{Mn}^{2+}$ . All six BLMOs were shown by XRD with Rietveld refinement in Chapter 3 to be triclinic BLMOs, with varying levels of structural order (Table 4-2). The structural order of the BLMOs was assigned by determining the full width at half maximum (FWHM) of the 001 diffraction peak, where sharper peaks give smaller FWHM values. The FWHM values for each set of BLMO materials were then compared and ranked based on the sharpness of the peaks, giving an order value for each BLMO. The six BLMOs and powdered  $\text{V}(0)$  were placed in an acidic saline solution and allowed to react at 25  $^{\circ}\text{C}$ , with agitation (150 rpm) for 3-4 days. The resulting mixture was then filtered and the

concentration of dissolved V in the filtrate was determined using ICP-MS. As shown in Figure 4-4, the amount of V oxidized by the system ranged from 0.018 mgV/mgBLMO to 0.082 mgV/mgBLMO. This equates to 19 to 81% of the original V metal being oxidized, which are significantly higher than the 5% oxidized by the acidic saline control after seven days. These results show the increased oxidation action of BLMO materials for V oxidation in acidic saline solutions.

**Table 4-2: FWHM for the primary XRD peak and corresponding assigned structural ordering values for the different BLMO synthesis methods.**

<b>BLMO Name</b>	<b>FWHM Primary XRD Peak</b>	<b>Structural Order Value</b>
Method A	1.164	6
Method B	0.679	5
Method C	0.311	3
Method C-M	0.302	1
Method D	0.307	2
Method D-M	0.539	4

It is clear from these results that the synthesis method can have a large impact on the BLMO activity. It was thought that this may be related to variation in structural order within the BLMOs. Under the conditions used, there was no correlation between level of structural order and BLMO reactivity towards V oxidation (Figure 4-5). Method D and D-M produced ordered and slightly disordered triclinic birnessites, respectively. These were observed to yield the highest concentrations of V under the conditions used. The BLMO formed using the HCl and  $MnCl_2 \cdot 4H_2O$  methods (methods B and C respectively) produced a disordered triclinic and an ordered triclinic birnessite respectively but were found to have similar reactivity (Figure 4-4). The most ordered birnessite (Method C-M) was found to oxidize less vanadium than the other ordered structures (B, C and D). This suggests a more compact and ordered crystal structure reduces the reactivity of BLMOs. The lactate synthesis method (method A) produced a disordered triclinic (almost amorphous) material, which was found to have the lowest

reactivity towards the oxidation of vanadium. These results show that the synthesis methods used to prepare BLMOs can influence the final reactivity of the materials.

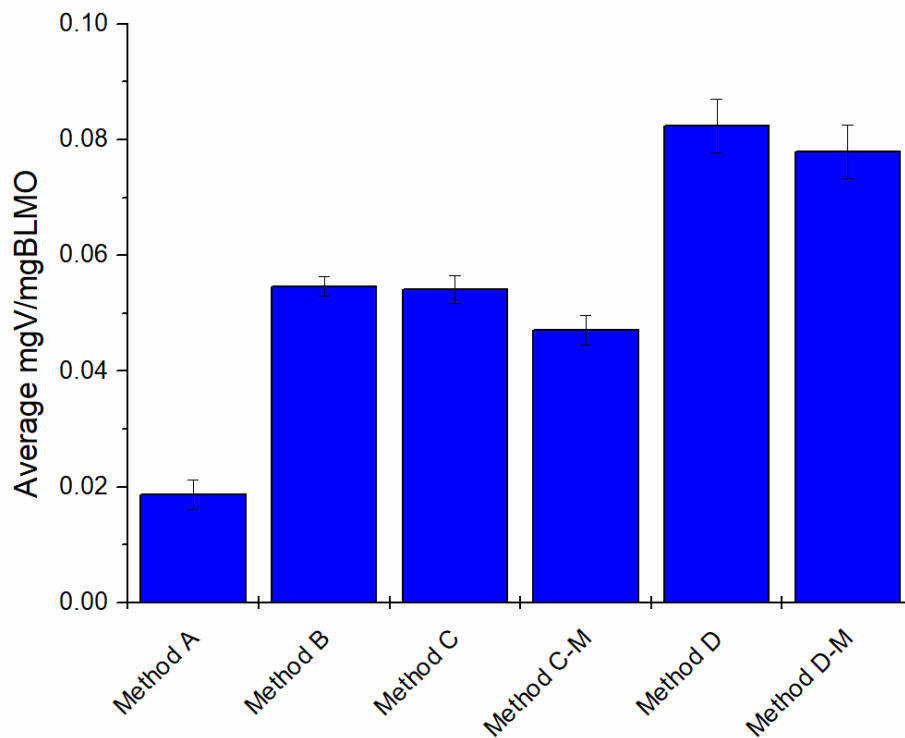


Figure 4-4: Vanadium dissolution achieved by six synthetic BLMOs prepared via six literature methods. Error bars represent one standard deviation  $n=3$ .

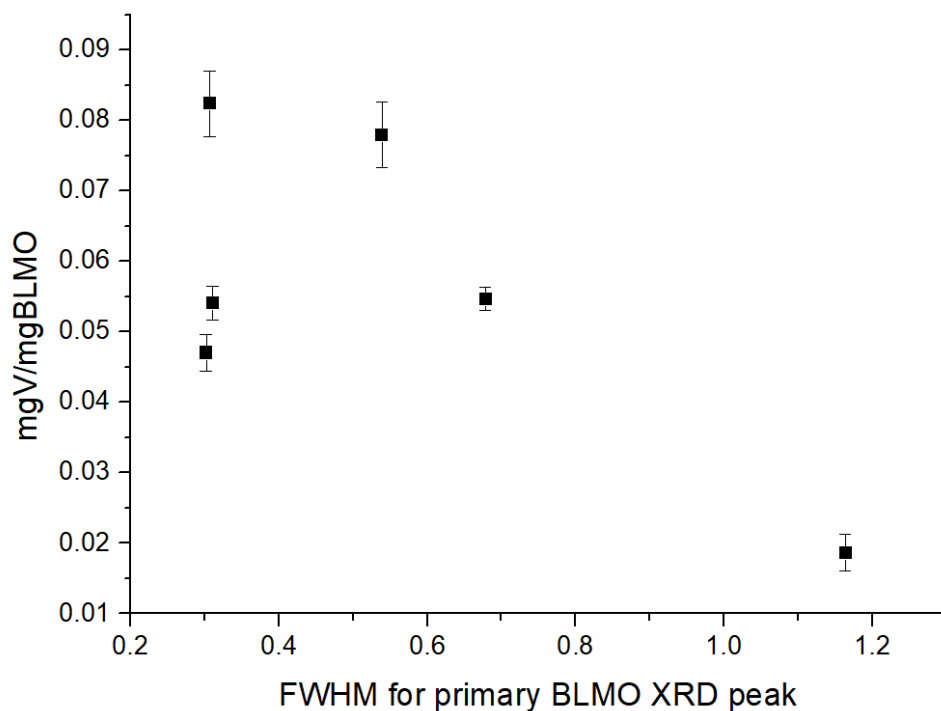


Figure 4-5: Structural order plots comparing the amount of vanadium oxidised and the FWHM of six BLMO materials prepared by different synthesis methods. Error bars represent one standard deviation  $n=3$ .

The characterisation work in Chapter 3 showed that not only can the fine structure of BLMOs can vary between synthesis methods, it can also vary between synthetic replicates prepared using the same methodology. In order to see if this structural variability influenced the reaction with V, six replicate BLMOs were prepared using the alkaline synthesis (Method C) and subjected to reaction with V as described earlier. These six materials were all determined to be triclinic BLMOs with varying levels of impurities and structural order (Table 4-3). The average amount of vanadium oxidized by these six BLMOs is  $0.049 \pm 0.15$  mgV/mgBLMO (Figure 4-6), which is on average 49% of the original material, and is consistent with the results found when comparing methods (presented in Figure 4-4). However, the BLMO materials reactivity towards V was highly variable (ranges from 0.032 mgV/mgBLMO to 0.074 mgV/mgBLMO, this corresponds to 31% to 84% of the initial metal to be oxidized) and no correlation between structural order and reactivity was observed (Figure 4-7).

**Table 4-3: FWHM for the primary XRD peak and corresponding assigned structural ordering values for the synthesis replicates of method C.**

<b>BLMO Name</b>	<b>FWHM Primary XRD Peak</b>	<b>Structural Order Value</b>
Batch 1	0.526	3
Batch 2	0.56	4
Batch 3	0.585	5
Batch 4	0.894	6
Batch 5	0.507	2
Batch 6	0.505	1

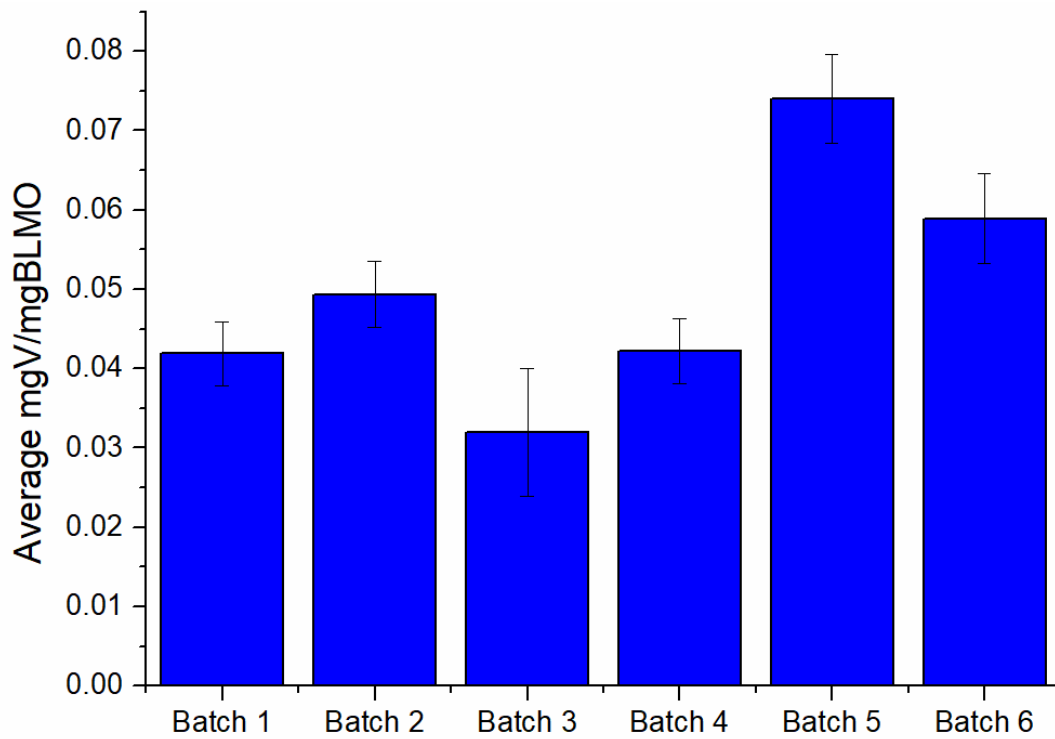


Figure 4-6: Vanadium oxidation reproducibility study using replicate BLMO samples synthesised by method C. Error bars represent one standard deviation  $n=3$ .

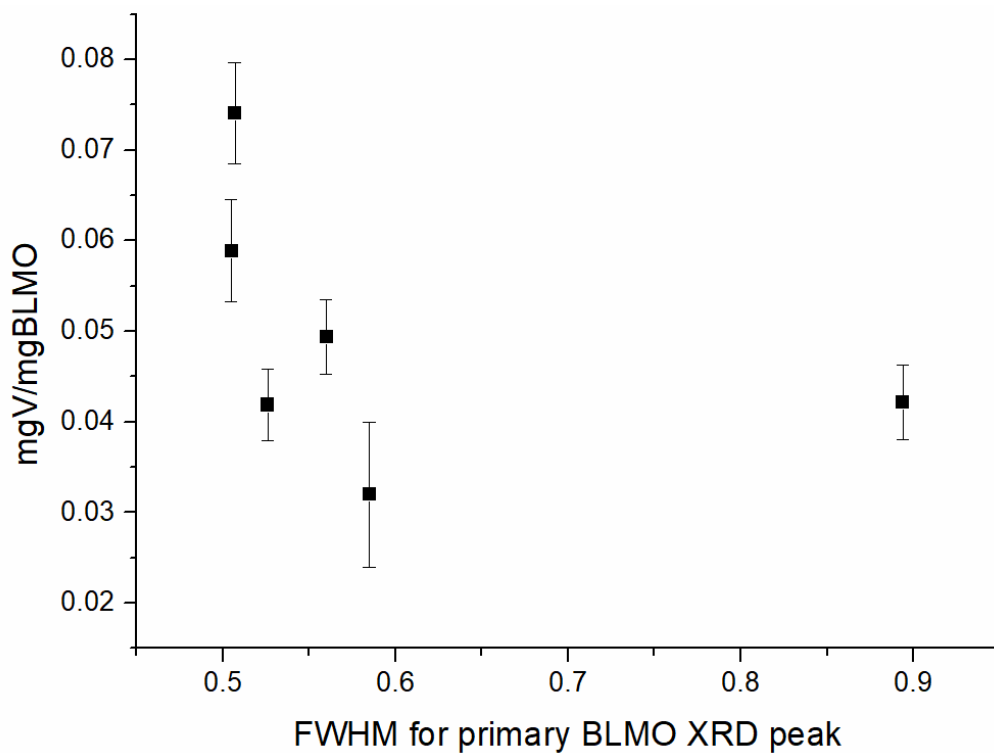


Figure 4-7: Structural order plots comparing the amount of vanadium oxidised and the FWHM of six replicate BLMO materials prepared by method C. Error bars represent one standard deviation  $n=3$ .

Two studies were undertaken to further confirm that structural order of triclinic BLMOs does not influence their reactivity towards the oxidation of V. Firstly, the altering the static aging time of the reaction mixture was varied from 0-7 days to improve structural order. Here subsamples of the reaction mixture were taken at various times across the 7-day period and worked up to collect the BLMO. Secondly, a batch of BLMO was subjected to post-synthesis treatments with a KCl solution. Increasing the static aging time did not change the triclinic base structure, however, the structural order varied with time (Table 4-4). These BLMOs were reacted with V in the same manner as before and, as with previous experiments, there was no correlation between the reactivity and changes in structural order (Figure 4-8). The amount of V oxidized ranged from 0.045 mgV/mgBLMO to 0.063 mgV/mgBLMO, which corresponds to oxidizing 41-45% of the original V material (Figure 4-9). Similarly, post synthesis treatment with 1 M KCl over time resulted in triclinic BLMOs with improved structural order (Table 4-5). Once again, when these samples were reacted with V, it was found that there was variation in the amount of vanadium dissolved (Figure 4-10), with values ranging from 0.037 mgV/mgBLMO to 0.057 mgV/mgBLMO. These results did not correlate with structural order (Figure 4-11). These results comprehensively confirm that the structural order of BLMO materials is not driving the observed variation in the amount of V oxidized. Therefore, some other variable is driving the variation.

**Table 4-4: FWHM for the primary XRD peak and corresponding assigned structural ordering values for the alteration of the static aging time.**

<b>BLMO Name</b>	<b>FWHM Primary XRD Peak</b>	<b>Structural Order Value</b>
0 Days	0.653	5
1 Day	0.592	4
2 Days	0.413	1
5 Days	0.501	2
7 Days	0.523	3

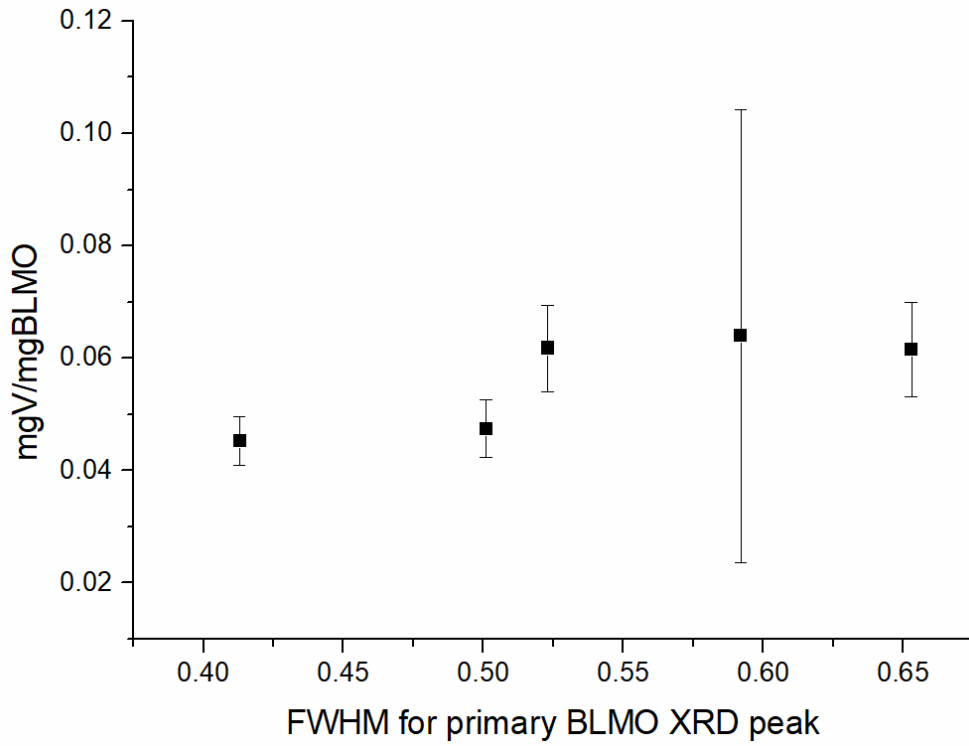


Figure 4-8: Structural order plots comparing the amount of vanadium oxidised and the FWHM of the BLMO materials modified by different static aging times. Error bars represent one standard deviation  $n=3$ .

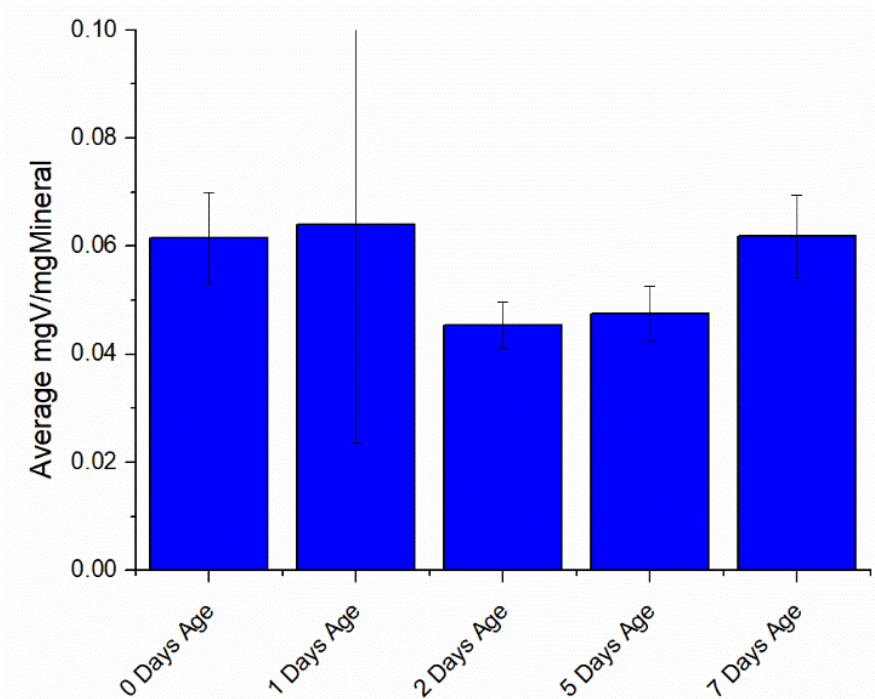
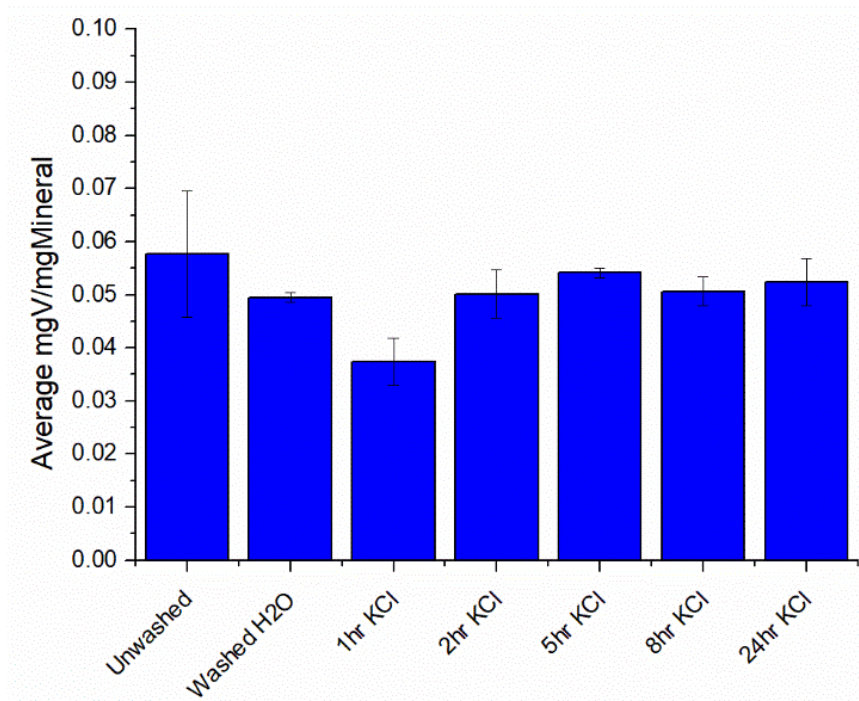


Figure 4-9: Effect of BLMO age time in synthesis solution on the oxidation of vanadium powder. Error bars represent one standard deviation  $n=3$ .

**Table 4-5: FWHM for the primary XRD peak and corresponding assigned structural ordering values for the post synthesis treatment with KCl.**

<b>BLMO Name</b>	<b>FWHM Primary XRD Peak</b>	<b>Structural Order Value</b>
Unwashed	0.519	7
H2O Treated	0.492	6
1hr KCl Treatment	0.285	1
2 Hr KCl Treatment	0.3	2
5 hr KCl Treatment	0.334	4
8 hr KCl Treatment	0.346	5
24hr KCl Treatment	0.317	3



**Figure 4-10: Effect of BLMO crystallinity on the oxidation of vanadium powder. Error bars represent one standard deviation  $n=3$ .**

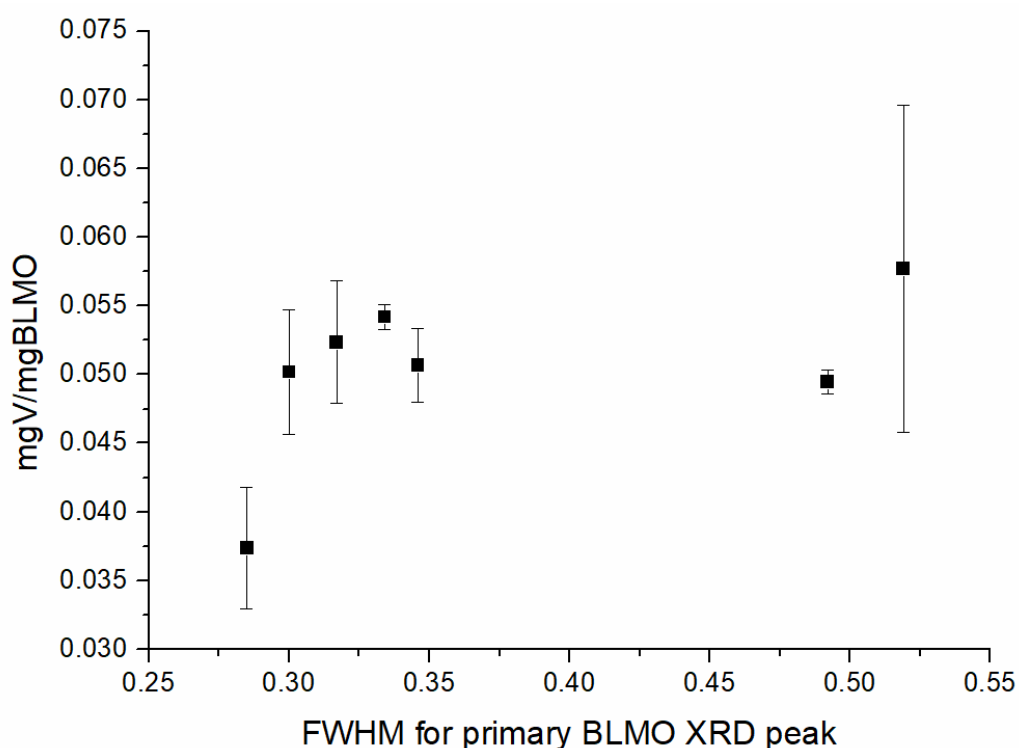


**Figure 4-11: Structural order plots comparing the amount of vanadium oxidised and the FWHM of the BLMO materials modified by different KCl treatment times. Error bars represent one standard deviation  $n=3$ .**

#### 4.3.3 Finding a correlation between BLMO structure and vanadium oxidation

A larger study was undertaken to investigate the underlying reason/s behind the variation in the amount of V oxidised by triclinic BLMO materials. Thirty-five BLMO materials were prepared and reacted with powdered V(0) as described earlier (Figure 4-12). Two sets of results are presented, one where the reaction with V was allowed to proceed for three days, and another set where the reaction was allowed to proceed for four days. These have been identified in the Figure 4-12. As shown, the amount of V oxidized by the system ranged somewhat from 0.018 mgV/mgBLMO to 0.082 mgV/mgBLMO. The measured levels of V were consistent across both days, indicating that the reaction may be mostly complete within three days. When looking at the entire dataset, the five samples that generated the most V in solution were split between different reaction times (two for 3 days and three for 4 days). Similarly, the samples that oxidized the least V were spread across both reaction times. This indicates that the BLMO is more important than reaction time under the conditions studied.

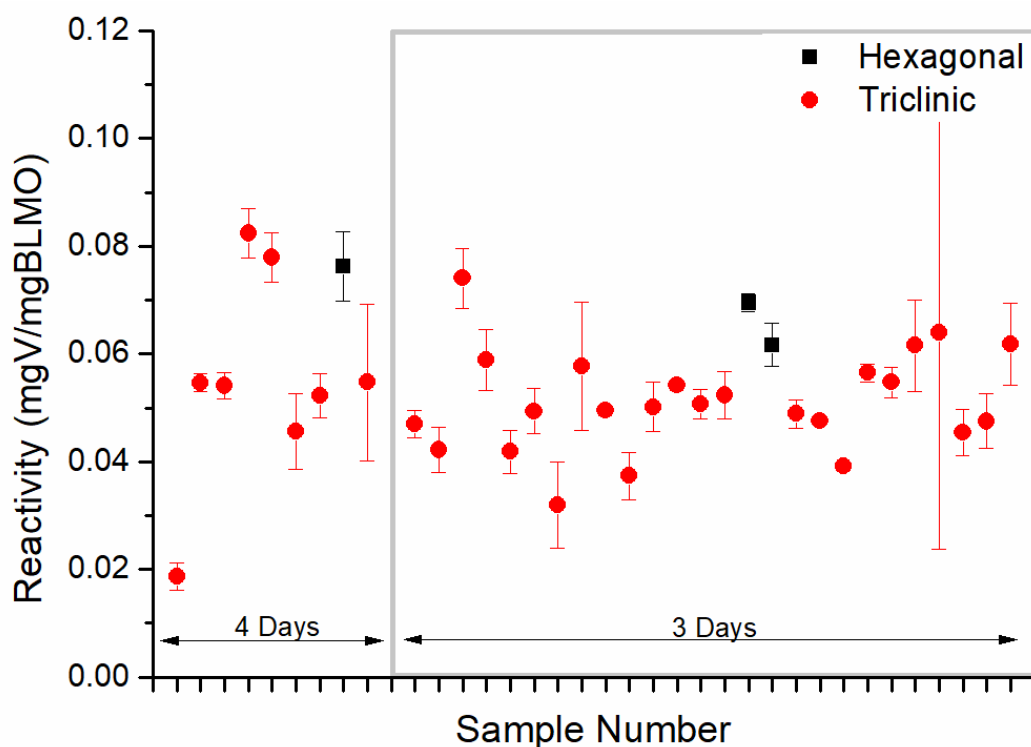


Figure 4-12: Plot showing the variation in reactivity of 35 BLMO materials and errors bars are a standard deviation of 3 oxidation replicates.

XRD analysis with Rietveld refinement showed that three of the BLMO materials tested have a hexagonal structure and the remaining thirty-two have triclinic structures. When comparing the reactivity of the structure types (Figure 4-12), it can be seen that two of the most reactive samples are hexagonal, and three are triclinic. Neither form of BLMO is substantially more reactive than the other. The limited data set may suggest that the hexagonal form results in higher yields of oxidized V and lower variability with replicates (Figure 4-13), but further analysis of additional hexagonal BLMO would be required to substantiate this.

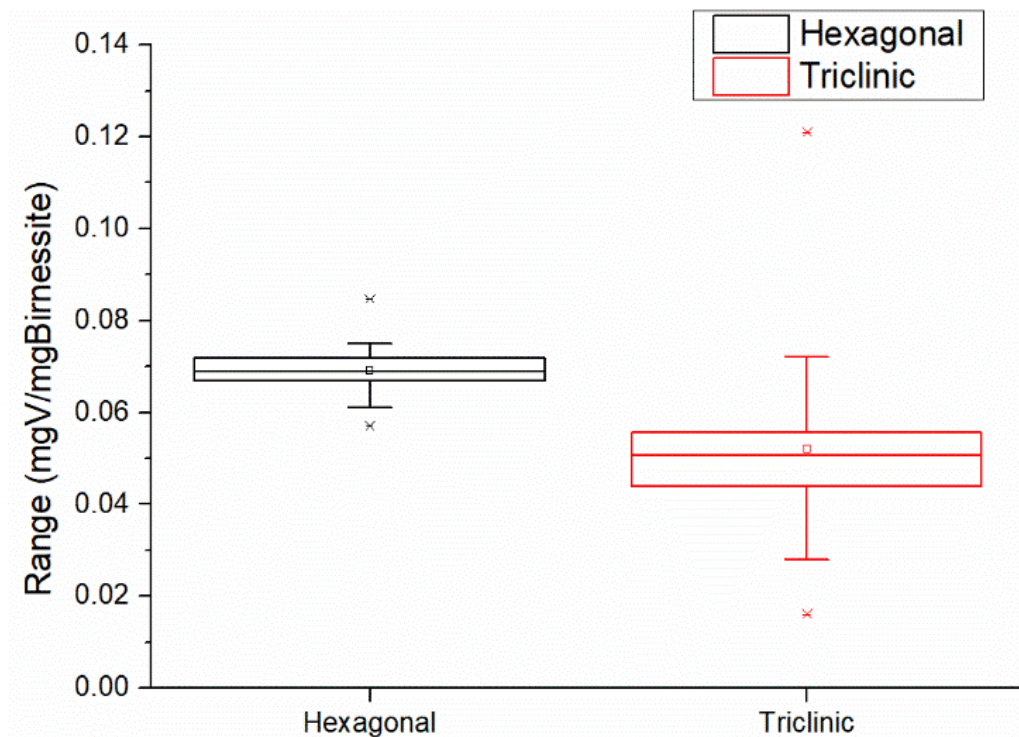
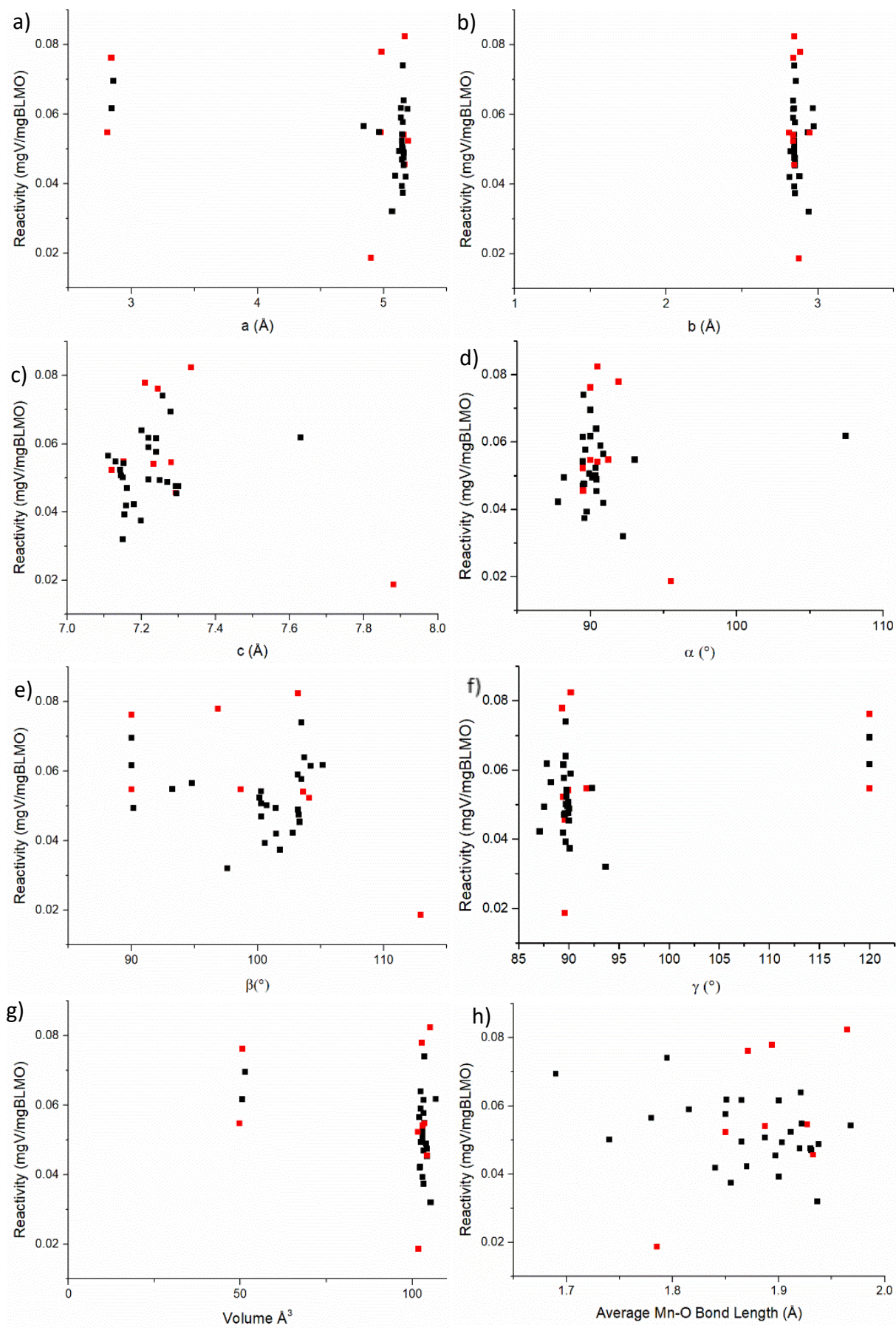
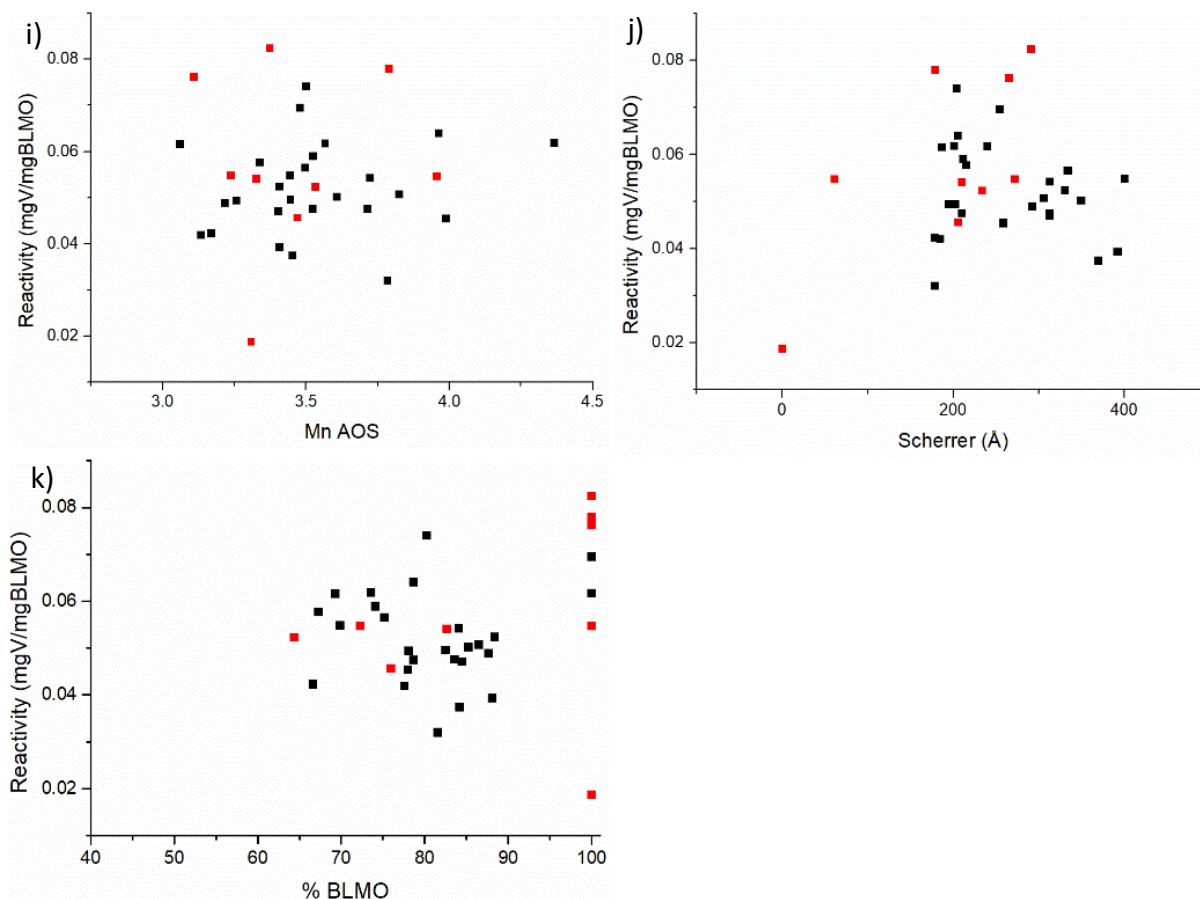


Figure 4-13: Variance plots produced for hexagonal and triclinic BLMOs using all oxidation experiment replicates.

Detailed structural information for the BLMO samples was obtained by XRD and Rietveld refinement and compared with the reactivity towards V. Physical and chemical parameters were plotted against reactivity for vanadium oxidation to determine if there were any correlations that could assist in explaining the variability (Figure 4-14). Eight parameters describing the unit cell (the lengths and angles of the unit cell, volume and average Mn-O octahedral bond length) are compared with the V reactivity in Figure 4-14a-h. Visual inspection of these plots shows no observed trend, which further confirms that the variability in the fine structure of the BLMO materials is not the driving force for the variability. The average manganese oxidation state, crystallite size and weight percentage of birnessite seen in Figure 4-14i-k, and were also found to not have a correlation with the reactivity variability of triclinic birnessite.





**Figure 4-14: Correlation plots comparing the amount of vanadium dissolved to various structural and chemical properties, with samples reacted for 4 days in red and samples reacted for 3 days in black. a)  $\alpha$ , b)  $\beta$ , c)  $\gamma$ , d)  $\alpha$ , e)  $\beta$ , f)  $\gamma$ , g) volume, h) average Mn-O bond length, i) average manganese oxidation state, j) scherrer crystallite size, and k) weight percentage of birnessite phase**

A remaining avenue of investigation is the potential difference in interlayer cation within the BLMO structure. The amount of  $\text{Na}^+$  and/or  $\text{K}^+$  (or other cations) within the triclinic crystal lattice may vary depending on the synthesis method, crystallization conditions and the reagents used. True hexagonal BLMOs lack an interlayer cation, and would not be influenced by this, but any triclinic impurities in the hexagonal material would also likely have variable cation levels. In addition to this, acidic solutions are known to cause the conversion of triclinic BLMOs into hexagonal BLMOs<sup>33</sup>. As our reaction system uses an acidic solution (pH 2) this may also play a role. Figure 4-13 indicates that the hexagonal birnessites were more reactive (and somewhat less variable) than the triclinic BLMOs, suggesting that the interlayer cation may be playing a role in driving the reaction. It has been reported that some cations (e.g.  $\text{Cu}^{2+}$ ,

Mg<sup>2+</sup>, and Ca<sup>2+</sup>) are known to have a stabilizing effect on layered BLMO structure<sup>224</sup>. Thus, it was hypothesized that the interlayer cation was influencing the conversion of triclinic BLMOs into hexagonal BLMOs, and thus causing the variability in the reactivity of the BLMOs towards V.

In order to test this, three BLMOs were prepared from the same batch of starting material, with differing post synthesis treatments alongside an untreated control. One mixed Na/K-BLMOs, one Na-BLMO and one K-BLMO were all prepared by post synthesis cation exchange. Subsamples of these four BLMO materials were then exposed to an acidic saline solution (pH 2, 0.05 M NaCl) and allowed to react for different time intervals. The remaining BLMO was subsequently collected. XRD analysis of the BLMO materials show that the triclinic starting materials convert to hexagonal BLMOs over time. The peak position of the 002 diffraction peak for layered BLMO on a Co source shifts from ~29.5 °2θ for triclinic to ~28.5 °2θ for hexagonal. The untreated triclinic and sodium treated BLMO materials converted to hexagonal peak positions after 2 hours and remained constant throughout the rest of the time points (Figure 4-15 and Figure 4-16). Whereas the water treated BLMO (Figure 4-17) also took two hours to completely convert, but a shift was observed towards higher °2θ values over the course of the study. The potassium treated BLMO (Figure 4-18) took the longest to convert to hexagonal with a conversion time of 4 hours and a more pronounced shift to higher °2θ values was observed. Differences in the time taken to convert and the presence of further shifting in two samples can be explained by the different rates of cation exchange (Na<sup>+</sup>/K<sup>+</sup> for H<sup>+</sup>). Lopano *et al.*<sup>210</sup> observed that during cation exchange, the internal cation undergoes atomic repositioning within the interlayer space and is followed by small adjustments to the atomic position upon completion of the exchange. These adjustments can cause a slight relaxation of the structure achieved through contractions that cause a small shift to higher

$^{\circ}2\theta$  values. The results of these experiments show that  $K^{+}$  ions increase the time required to convert to hexagonal BLMO and that the structure undergoes structural relaxation afterwards. This suggests that potassium cations could have a stabilising effect on the conversion of triclinic BLMOs to hexagonal BLMOs and subsequently could affect their ability to oxidise vanadium.

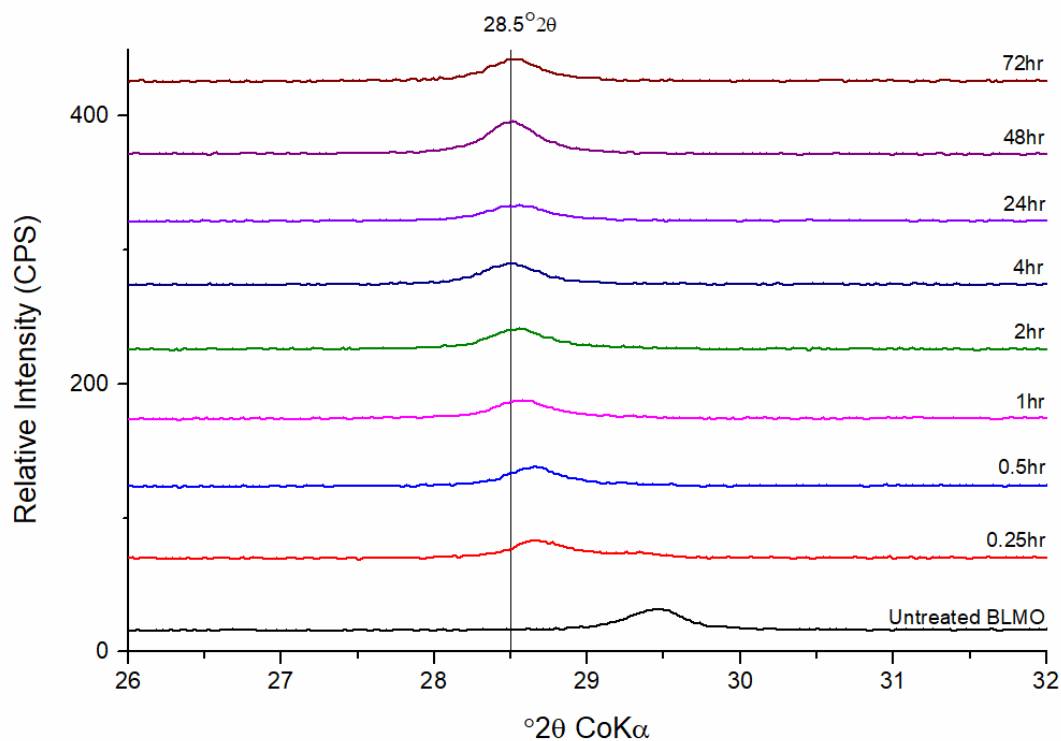


Figure 4-15: CoK $\alpha$  diffraction patterns of the untreated BLMOs exposed to pH 2 0.05M NaCl solution for various time intervals, showing 26-32  $^{\circ}2\theta$ .

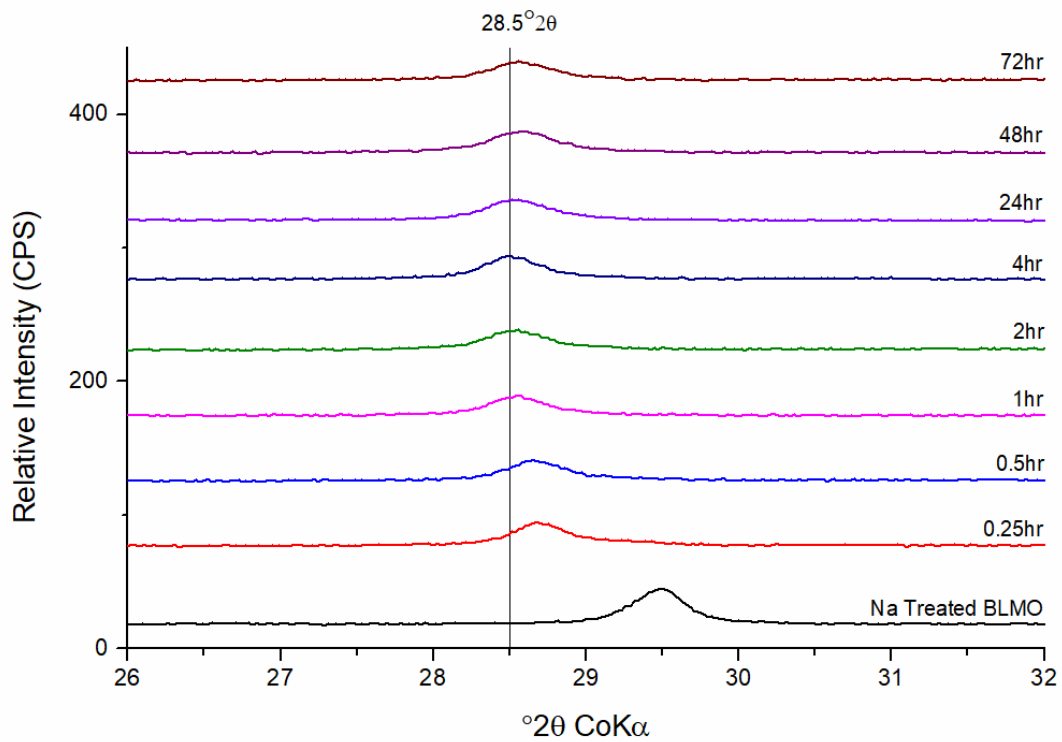


Figure 4-16:  $\text{CoK}\alpha$  diffraction patterns of the Na treated BLMOs exposed to an acidic saline solution for various time intervals, showing 26-32  $^\circ 2\theta$ .

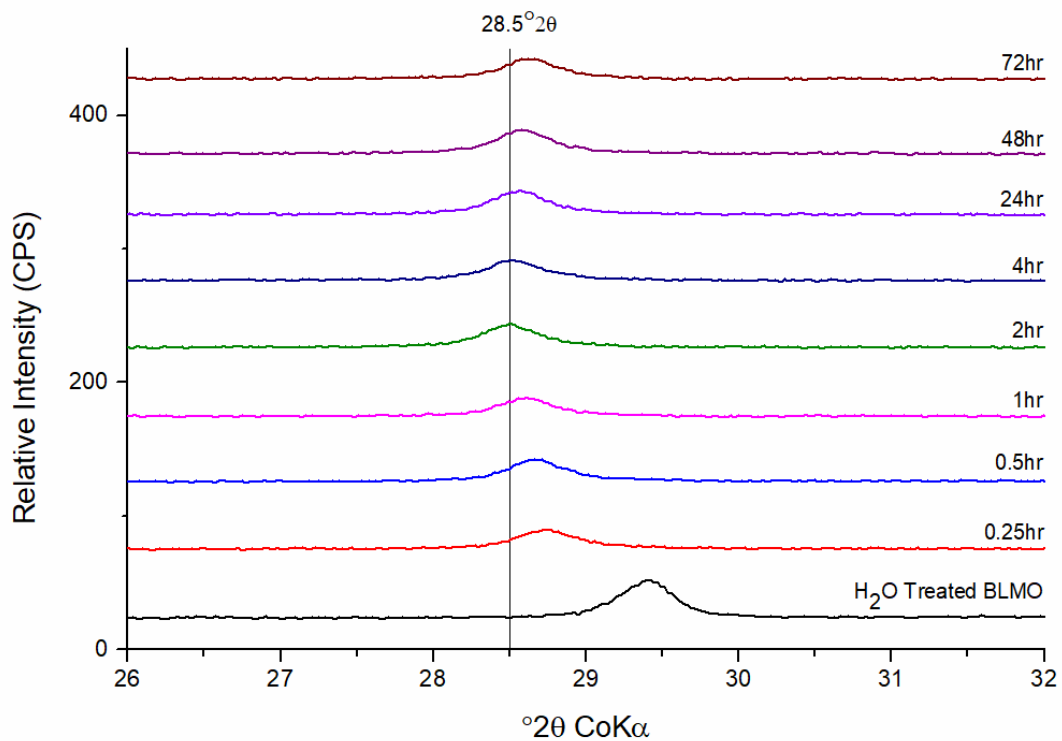
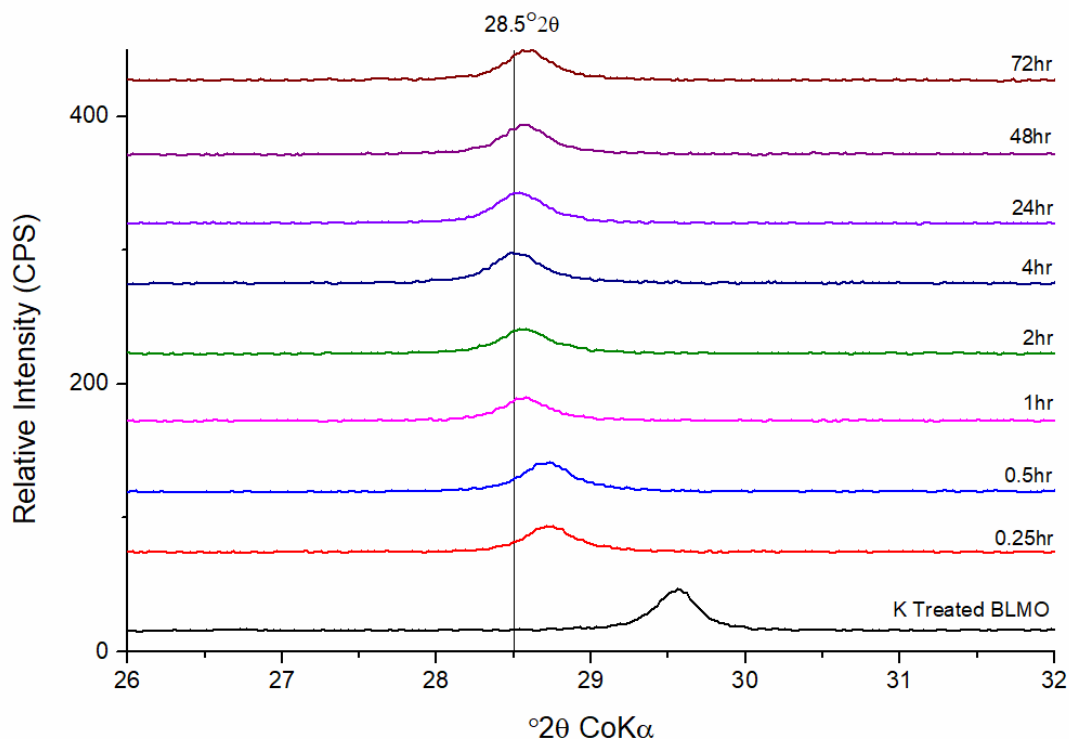


Figure 4-17:  $\text{CoK}\alpha$  diffraction patterns of the water treated BLMOs exposed to an acidic saline solution for various time intervals, showing 26-32  $^\circ 2\theta$ .



**Figure 4-18: CoK $\alpha$  diffraction patterns of the K treated BLMOs exposed to an acidic saline solution for various time intervals, showing 26-32  $^{\circ}2\theta$ .**

#### 4.3.4 Confirming the role of potassium

To further investigate the effect of potassium in the BLMO structure on the reactivity, Raman spectra were collected for six BLMO materials and two Raman spectra for standards of Na-BLMO and K-BLMO (Figure 4-19). Raman spectroscopy has been found to distinguish between K-BLMO and Na-BLMO due to different Raman shifts at  $97\text{ cm}^{-1}$  and  $150\text{ cm}^{-1}$  for K-BLMO and  $132\text{ cm}^{-1}$  for Na-BLMO. Two of the BLMOs tested (Figure 4-19-KBr and 1hr KCl) were found to be purely K-BLMO, whereas three of the samples tested were either purely Na-BLMO (Figure 4-19-NaCl), contained a mixture of Na and K-BLMO (Figure 4-19-24hr KCl and KCl) or in the case of Li-BLMO had Na like peak positions. When comparing these cation data with the reactivity data collected for these materials (Figure 4-20) we see that the two that contain only potassium are lower, and the samples that contain sodium cluster in a wide range that is distinct from the potassium samples. These results further indicate that  $\text{K}^+$  interlayer cations

have a stabilization effect on the conversion to hexagonal BLMOs and reduce the reactivity towards V under the conditions studied.

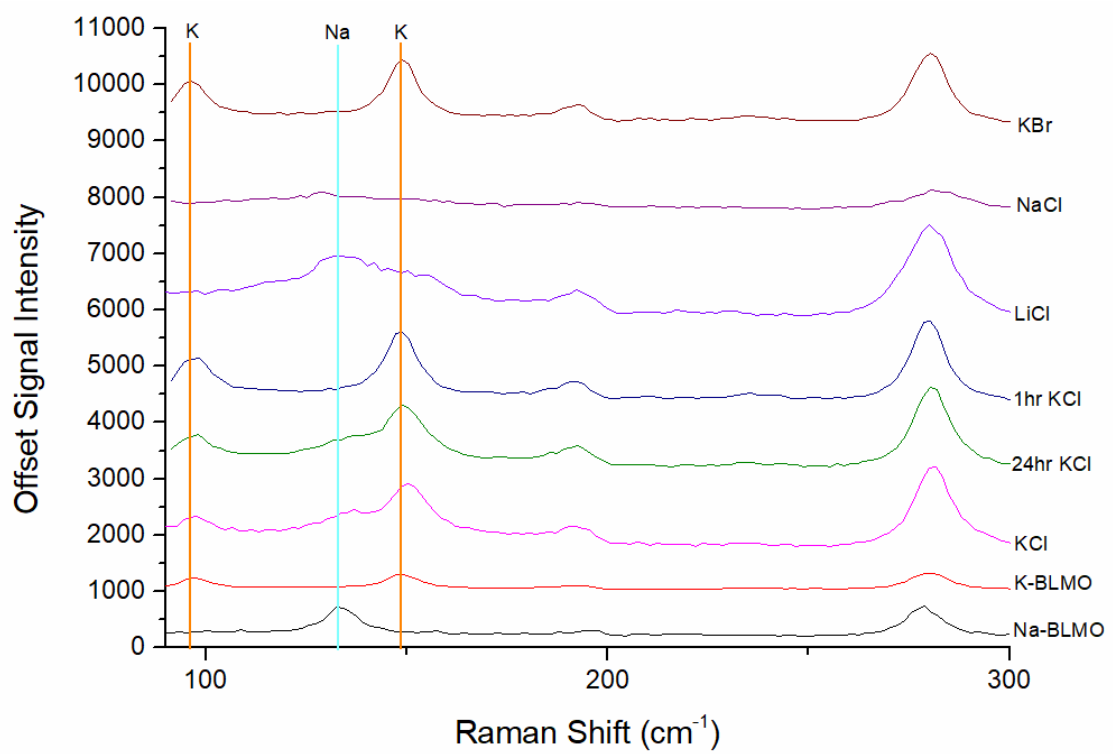


Figure 4-19: Raman spectra of standards of Na-BLMO, K-BLMO and six BLMO materials.

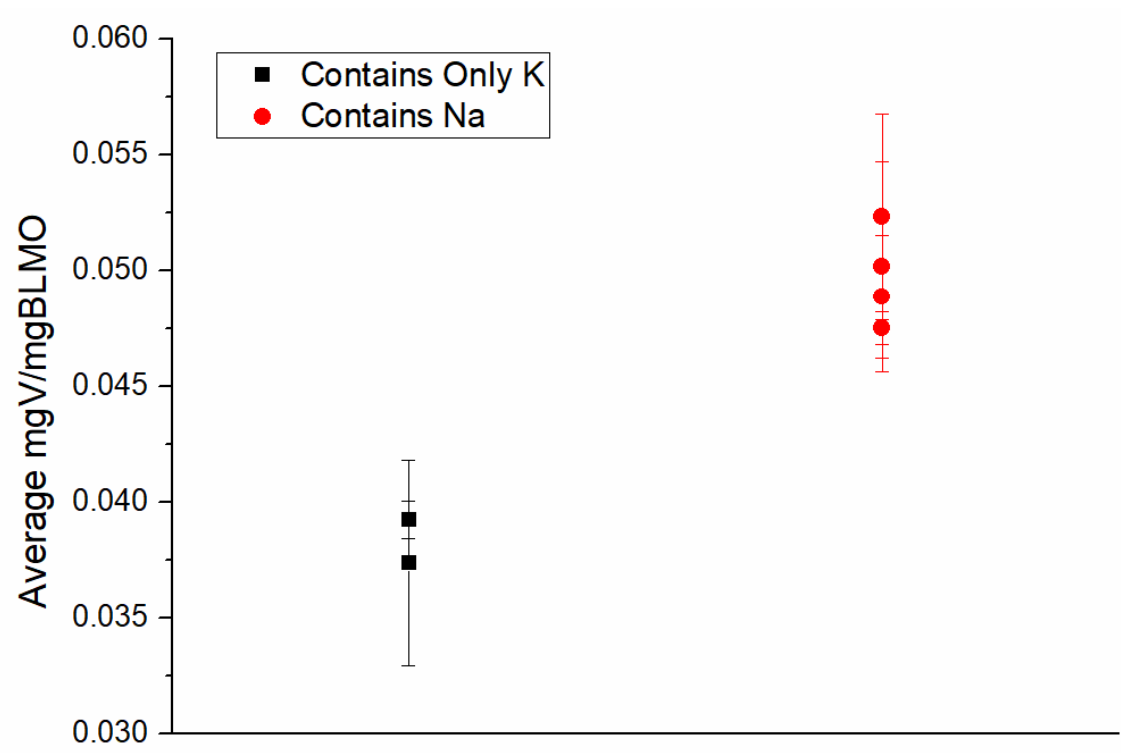


Figure 4-20: Comparison plot showing the reactivity of six BLMO materials separated by the presence of sodium in the crystal structure determined by Raman spectroscopy. Error bars represent one standard deviation  $n=3$ .

Lopano *et al.*<sup>225</sup>, reported that the exchange rates for converting Na-BLMO to K-BLMO, Ba-BLMO and Ca-BLMO were explained by the enthalpies of hydration. The greater negative value for enthalpy of hydration of the cations increases the affinity of the hydrated cation to remain in the aqueous solution (instead of losing their hydration water to fit into the interlayer space of BLMOs), thus slowing the exchange. Thus, the reactivity of triclinic BLMOs for the oxidation of vanadium metal under the conditions studied, is likely to be dependent on the cation in solution and its enthalpy of hydration. This, in turn, effects the rate that the triclinic form loses its cation and converts to the more reactive hexagonal form.

#### 4.3.5 Effect of Interlayer Cation

To confirm the effect of interlayer cation on the ability of BLMO materials to oxidize vanadium, several different cation BLMOs were prepared by post synthesis treatments with various cation salt solutions. The BLMOs prepared were: H-BLMO, Li-BLMO, Na-BLMO, K-BLMO, Mg-BLMO and Ca-BLMO. These materials were reacted with V as described earlier and were observed to oxidize various amounts of V (Figure 4-21), with the values ranging from 0.039 mgV/mgBLMO to 0.069 mgV/mgBLMO (39 to 70% of the original amount of V). The BLMO modified with H<sup>+</sup> was determined to have hexagonal BLMO structure and was found to oxidize the most V. The remaining materials were determined to have triclinic BLMO structures and were lower in reactivity. The K-BLMO exchanged using KBr was found to dissolve the least V, while the other samples were all statistically similar with Ca-BLMO and Mg-BLMO dissolving more V. The reactivity of the different cation triclinic BLMO materials follow the inverse trend observed in the enthalpy of hydrations,  $Mg^{2+} < Ca^{2+} < Li^{+} < Na^{+} < K^{+}$ <sup>226</sup>. These results support the hypothesis that the interlayer cation is the main driving force behind the variation in the reactivity of triclinic BLMOs observed in this paper. To further

confirm the stabilization effect of  $K^+$ , a sample of  $H^+$  treated BLMO was treated with 1 M KCl, and subsequently reacted with  $V(0)$ . The reincorporation of  $K^+$  into the structure resulted in a decrease in the amount of V dissolved (red-Figure 9), providing further evidence to the stabilizing effect of  $K^+$ .

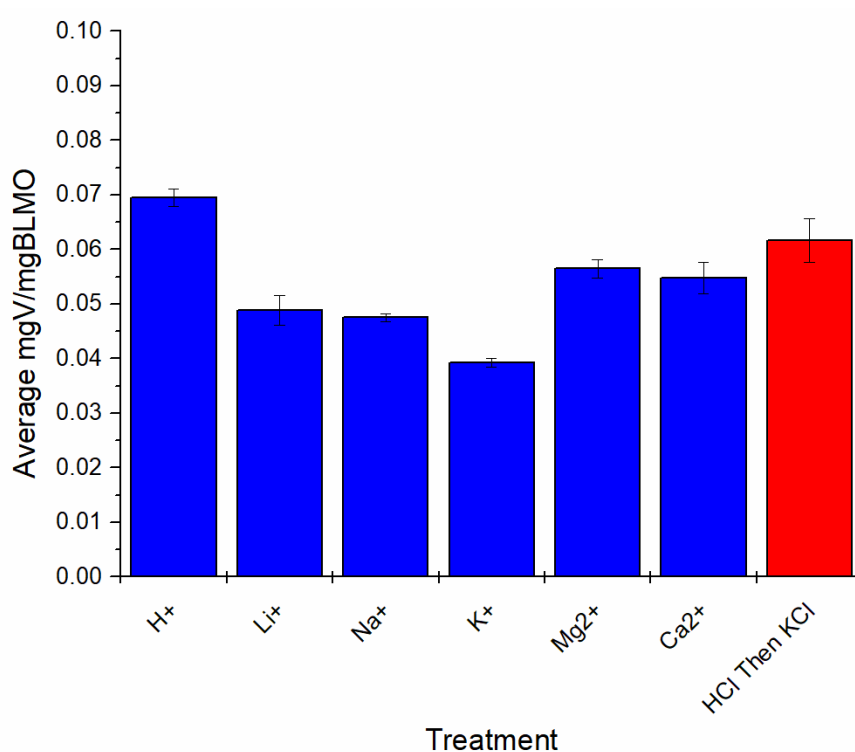


**Figure 4-21: Effect of the interlayer cation present in BLMO materials on the oxidation of vanadium powder. Error bars represent one standard deviation  $n=3$ .**

#### 4.3.6 Changes to BLMO material

Research by other groups has modified the structure and composition of BLMO materials by doping other transition metals such as  $Al^{47}$ ,  $Ni^{47, 227}$ ,  $Fe^{228}$ ,  $Co^{47, 227}$  and  $V^{206, 227}$  into the BLMO structure in place of both interlayer cations<sup>227-228</sup> and Mn in the octahedral layer<sup>47, 227-228</sup>. This raises the question of whether the oxidised vanadium produced during the reactions studied here is being incorporated into the BLMO structure. To test this, BLMO material was collected via filtration after undergoing reaction with  $V(0)$ , and subsequently analysed via XRD. The resulting pattern was then compared to the XRD patterns of the original BLMO and a BLMO material that was exposed to an acidic saline solution for the same amount of time (Figure

4-22). As shown, the BLMO begins as triclinic (Figure 4-22a). Once exposed to the solutions, both are converted to hexagonal BLMO. However, the two first diffraction peaks for the BLMO from the solution containing V were shifted to smaller d-spacings when compared to the BLMO from the acidic saline solution. These two peaks are indicative of the interlayer spacing, and suggest that the material exposed to the V(0) reaction has a slightly smaller interlayer space than the material exposed to just acidic saline solution. This observation is supported by the subsequent Rietveld refinements conducted on these diffraction patterns (Figure 4-23 and Table 4-6), where it was seen that the c parameter is smaller for the BLMO from V(0) oxidation test (7.1604 Å) than the BLMO exposed to acidic saline without V(0) (7.2616 Å). This is consistent with results of Yin *et al.*<sup>206</sup> who observed that doping hexagonal BLMO with V results in a shift in the XRD pattern to smaller d spacing values. They also showed that as the concentration of V incorporated into the material increases, it was found the XRD peaks begin to broaden and collapse. This could be due to the incorporation of V into the interlayer space reducing the packing order of the layers. Previously in 2015, Liu *et al.*<sup>229</sup> suggested that the V doped into the crystal structure not only replaced some Mn<sup>4+</sup>, but also replaced K<sup>+</sup> as the interlayer cation. However, a recent paper in 2020 by the same authors suggests that the V is present on the edges of the layer structure instead but make no mention of why they changed their theory<sup>227</sup>. The compacting of the interlayer space observed with the V exposed BLMO, is likely due to the incorporation of V cations into the interlayer space, due to a lack of a change in the other cell parameters observed in the Rietveld refinements.

SEM showed that the morphology of the BLMO material from the vanadium test was found to have changed from the micaceous sheets observed previously to thinner and more flaky material (Figure 4-24), however, there was observed to be two morphologies present, one that was more flaky (Figure 4-24a) and one that was more aggregated compared to the

starting material (Figure 4-24b). The presence of a flakier BLMO after V treatment was consistent with the acid saline treated BLMO, however there was no evidence of a clumpy BLMO in the acid saline treatment. EDXS analysis on these two morphologies show a difference in the amount of vanadium present, with the flaky material containing slightly less V (Figure 4-25) than the other (Figure 4-26). The small amount of V found in the EDXS, combined with the minimal peak collapsing of the BLMO material in the XRD, suggests that only a small amount of V has been incorporated into the structure. Vacancies in the BLMO starting crystal structure could affect levels of V uptake into BLMO, however, it is unlikely that this level of V would significantly influence the ability of the material to oxidise V. Prior work has shown that V doping was found to have minimal effect on the ability of BLMO materials to oxidise  $\text{Cr}^{3+}$  to  $\text{Cr}^{6+}$  <sup>227</sup>. Thus, the differences observed between the different BLMO oxidation experiments should not be due to differences in the incorporation of V.

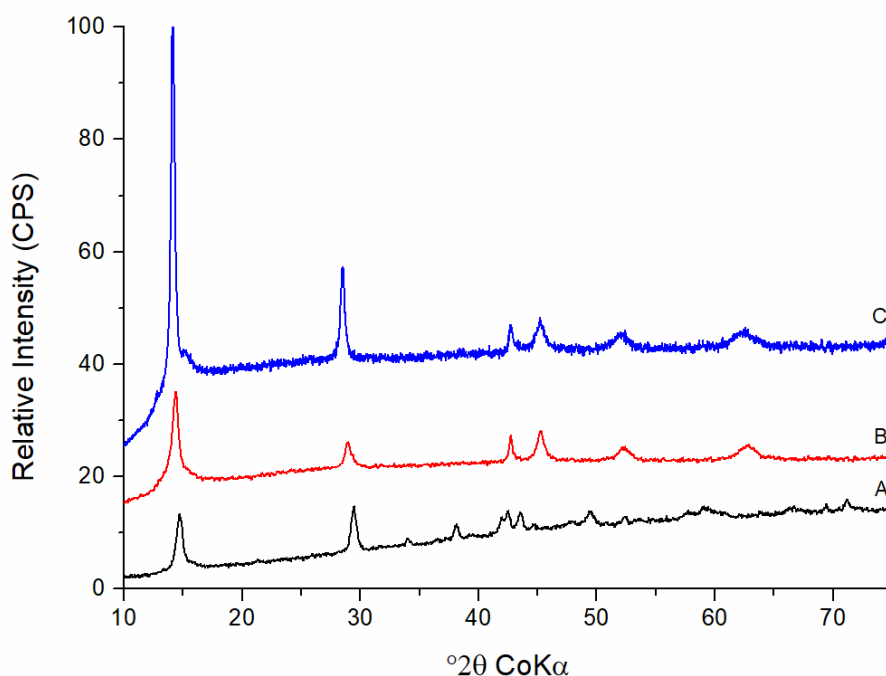
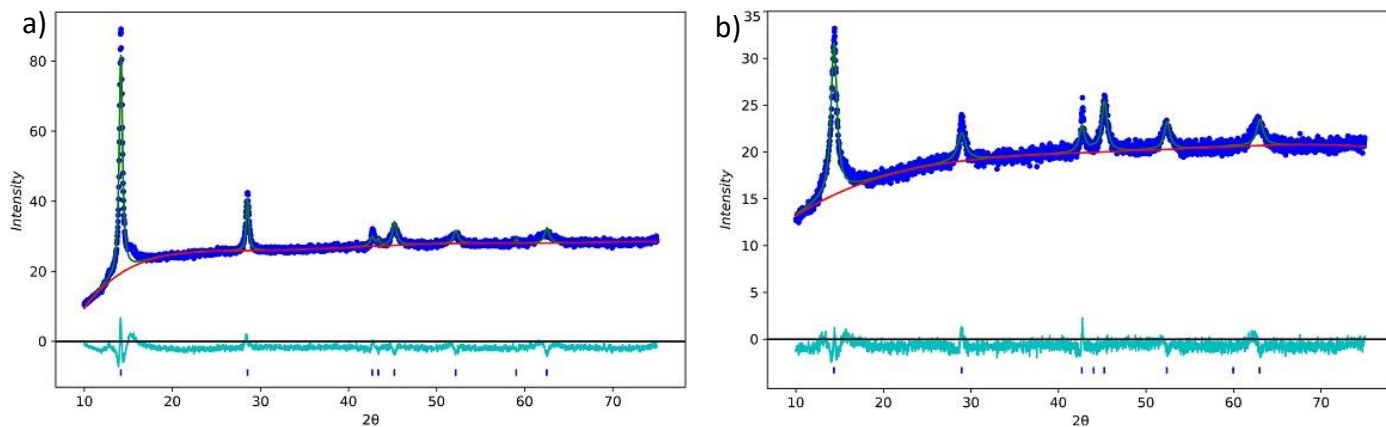


Figure 4-22: CoK $\alpha$  diffraction patterns of BLMO materials, a) BLMO material before exposure, b) BLMO material after utilisation of V(0) oxidation for 3 days, and c) BLMO material after exposure in acidic saline solution without V(0) for 3 days.



**Figure 4-23:** Rietveld refinement and difference plots for the BLMOs formed after exposure to different reaction solutions a) acidic saline solution without V(0) for 3 days , b) an acidic saline reaction solution utilised for the oxidation of V(0) . The refinements were conducted on diffraction patterns collected via CoK $\alpha$ .

**Table 4-6:** Rietveld refinement results for different cation treatments, shown are the final refined cell parameters, the R(F<sup>2</sup>) and R<sub>wp</sub> values.

	3 Days acidic saline	3 Days reaction solution
Space Group	<i>P</i> -3	<i>P</i> -3
Radiation Source	Co	Co
Unit Cell		
a (Å)	2.8375(10)	2.8392(8)
b (Å)	2.8375(10)	2.8392(8)
c (Å)	7.2616(6)	7.1604(15)
$\alpha$ (°)	90	90
$\beta$ (°)	90	90
$\gamma$ (°)	120	120
Vol (Å <sup>3</sup> )	50.632(22)	49.989(18)
Refinement		
No. of Observations	2985	2985
No. of Reflections	11	11
Diffraction Range (°2 $\theta$ )	10 - 75	10 - 75
R(F <sup>2</sup> )	0.29339	0.20254
R <sub>wp</sub>	0.03005	0.02316

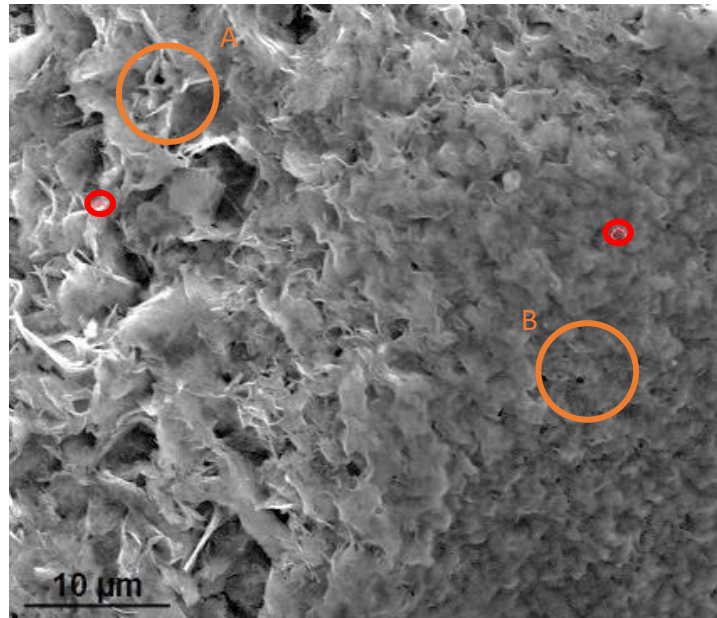


Figure 4-24: SEM image of the BLMO material after utilisation for the oxidation of V(0), showing two different morphologies and the locations analysed via EDXS.

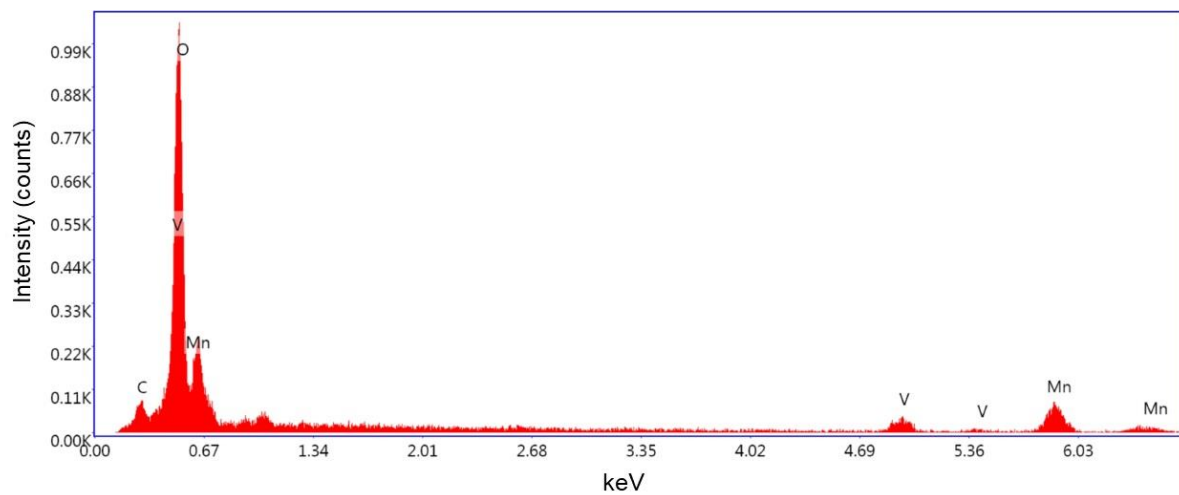


Figure 4-25: EDXS spectra of the left hand EDXS spot on Figure 4-24 of the BLMO material utilised to oxidise V(0), showing the presence of V and Mn present in the BLMO.

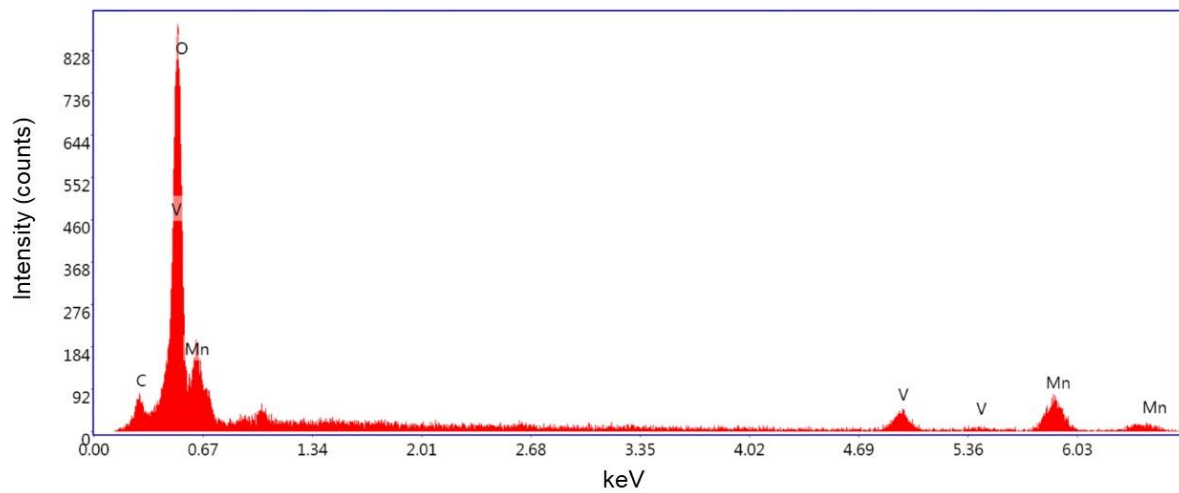


Figure 4-26: EDXS spectra of the right hand EDXS spot on Figure 4-24 of the BLMO material utilised to oxidise V(0), showing the presence of V and Mn present in the BLMO.

#### 4.3.7 Long term reaction

A series of vanadium oxidation reactions were allowed to proceed at room temperature for a period of at least three months. After that time, red spindle like crystals had begun to form (Figure 4-27). The crystals were collected, dried and analysed via XRD (Figure 4-28), and were determined to be the manganese vanadate mineral ansermetite ( $\text{MnV}_2\text{O}_6 \cdot 4\text{H}_2\text{O}$ )<sup>230</sup> (Figure 4-29). This is consistent with the laboratory synthesis of ansermetite which typically involves the combination of  $\text{Mn}^{2+}$  and  $\text{V}^{5+}$  solutions. However in these cases, the reactions are usually undertaken using forcing conditions such as high pressure and high temperatures<sup>231-232</sup> and microwave radiation<sup>233</sup>. Alternately ansermetite can be synthesised by solid-state metathesis reactions using milling<sup>234-235</sup>. The formation of ansermetite in these reaction solutions could be occurring via two pathways, i) the incorporation of V into the vacancies formed in the octahedral layer as the mineral oxidises V and a subsequent rearrangement once the layer is sufficiently exchanged, or ii) the generated  $\text{Mn}^{2+}$  and  $\text{V}^{5+}$  slowly coprecipitate over time under the conditions of the reaction solution. This gentle method for the formation of these crystals could give insight into how manganese vanadate minerals form in the environment.

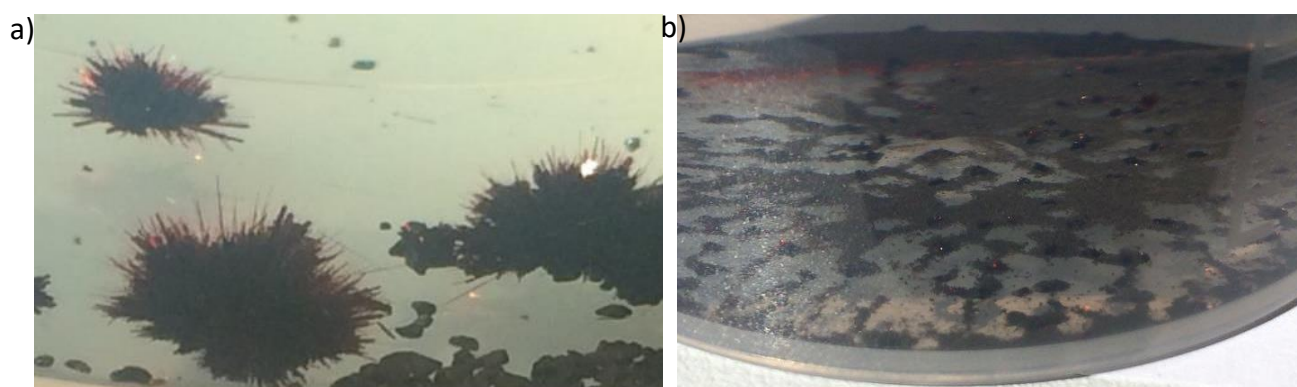


Figure 4-27: a) spindle clusters of red crystals found in the resulting reaction solution after storage for several months, b) multiple small crystals forming.

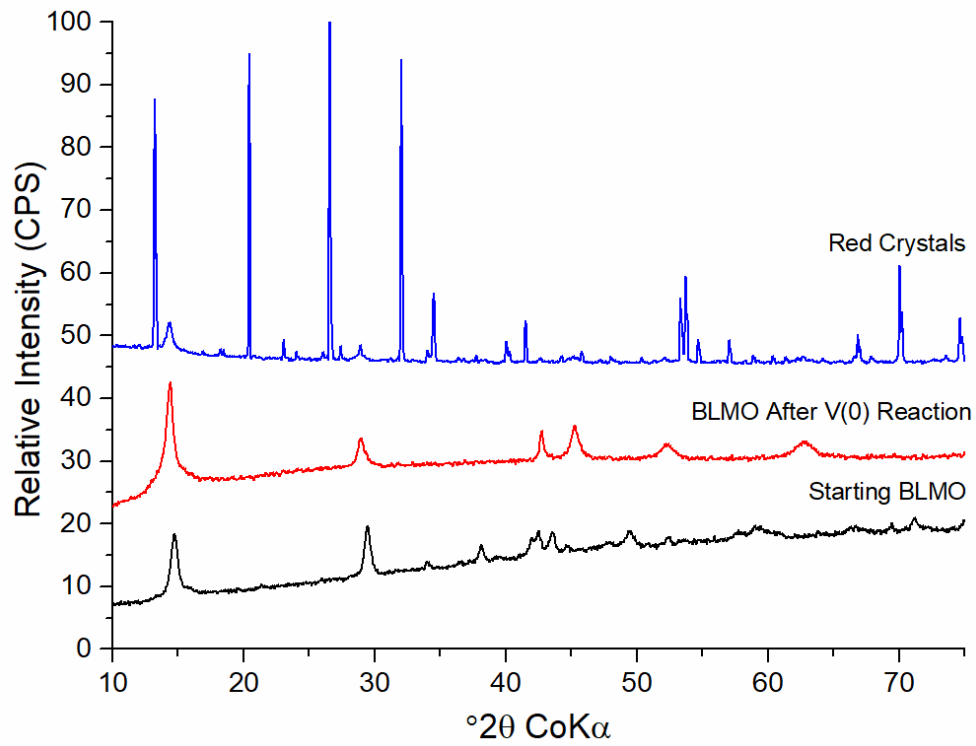


Figure 4-28: CoKα diffraction patterns of the red crystals found in the reaction solution after several months and the starting BLMO material for comparison

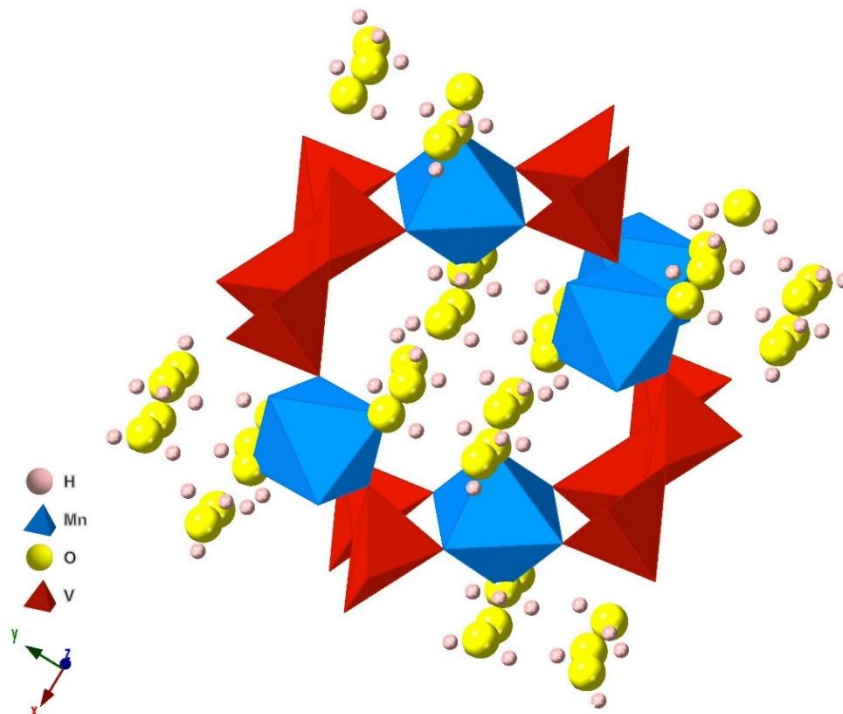


Figure 4-29: Crystal structure of ansermetite, a manganese vanadate mineral, structure created using CrystalMaker and the structure file provided with Brugger *et al.*<sup>230</sup>.

## 4.4 Conclusion

In this chapter we have shown that synthesis method has a significant impact on the reactivity of BLMO materials and that the structural order does not drive the reactivity of the materials towards the oxidation of V(0). During the course of this study we observed that hexagonal BLMOs are the more reactive form of BLMOs for the oxidation of vanadium and that the reactivity of triclinic BLMO is extremely variable. This variability is not dependent on the unit cell structure and average manganese oxidation state. The triclinic BLMO variability can be best explained best by the interlayer cation present and its ability to be removed from the interlayer space during the conversion of triclinic to hexagonal BLMO that occurs in this reaction system. It was found that some of the oxidised vanadium is incorporated into the BLMO structures and that over time, the reaction solutions allow for the formation of the manganese vanadate mineral ansermetite.

## Chapter 5 Tunnel Structured Manganese Oxide Materials

### 5.1 Introduction

Layered manganese oxides are not the only form of manganese oxide materials that have garnered the interest of the scientific community for their oxidative properties and potential applications. Tunnel structured manganese oxide materials (TSMOs) are another common structural form investigated. Like BLMOs, these structures are comprised of chains of edge sharing  $\text{MnO}_6$  octahedra, however in this case neighbouring chains are linked at the corners to form square cross-sections, which form 'tunnels'. The number of octahedra joined in this manner can vary, with common combinations including 1x1 (pyrolusite), 1x2 (ramsdellite), 2x2 (hollandite-type), and 3x3 structures (todorokite) (Figure 5-1)<sup>1</sup>, (where 1 represents 1 octahedra in the chain). Much like layered manganese oxides, these tunnel spaces can contain cations, water molecule or remain empty. The most common type of TSMO utilised are cryptomelane structures (2x2 tunnels containing  $\text{K}^+$ ).

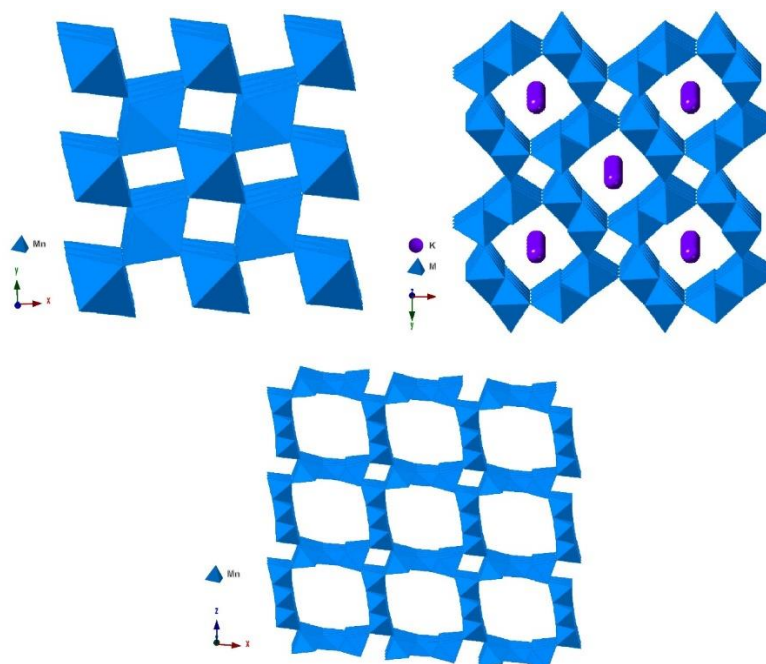


Figure 5-1: Diagrams showing the crystal structure of pyrolusite (top left), cryptomelane (top right) and todorokite (bottom). Structures were recreated using CrystalMaker from CIF structure files from structure determination papers<sup>86-88</sup>.

Research utilising TSMOs primarily focuses on the oxidation and degradation of organic compounds. In these cases, the manganese oxide typically acts as a catalyst rather than a direct oxidant. For example, Opembe *et al.*<sup>92</sup> utilised cryptomelane materials to selectively oxidise vaporised benzyl alcohol to benzaldehyde, while Genuino *et al.*<sup>93</sup> used similar conditions to achieve the oxidation of benzene, toluene, and xylenes to CO<sub>2</sub> and H<sub>2</sub>O. Son *et al.*<sup>94</sup> achieved the conversion of various benzylic and allylic alcohols in a toluene liquid phase with cryptomelane. TSMOs have been also been combined with peroxymonosulfate in aqueous solutions to achieved the degradation of organic dyes such as acid orange, methylene blue and rhodamine B<sup>95</sup>. Unlike layered manganese oxides, the use of TSMOs to oxidise metals has not been as extensively researched with two papers found showing the oxidation of As<sup>3+</sup> to As<sup>6+</sup><sup>96-97</sup> by TSMOs. Due to this lack of research on the ability of TSMOs to oxidise metals, a preliminary investigation was undertaken using three common TSMOs, pyrolusite, cryptomelane, and todorokite.

## 5.2 Materials and Methods

All reagents were reagent grade or higher and purchased from Chem-Supply, Australia unless otherwise stated below, including Pyrolusite as commercial MnO<sub>2</sub>. Manganese acetate tetrahydrate and potassium permanganate were purchased from Sigma Aldrich, USA as reagent grade chemicals. Hydrochloric acid was sourced from Sharlau, Spain, glacial acetic acid was sourced from RCI Labscan, and manganese chloride was obtained from Merck, USA as analytical reagent grade. Sodium oxalate was purchased as reagent grade from BDH Chemicals, USA and potassium acetate was sourced from M&B Ltd. as a laboratory grade chemical. High purity water (MilliQ, 18.2 MΩ) was used throughout.

### 5.2.1 Synthesis of Cryptomelane (2x2 TSMO)

Five methods were utilised for the synthesis of cryptomelane structures, as outlined below.

**Method A-1** follows the preparation outlined by Burhanuddin *et al.*<sup>236</sup>. Aqueous solutions of  $\text{KMnO}_4$  (7.11 g, 150 mL) and citric acid (2.88 g, 150 mL) were combined slowly with stirring at room temperature. The resulting mixture was left until precipitate formed and was filtered (Whatman, cellulose, 11  $\mu\text{m}$ ), washed with MilliQ water then ethanol and air-dried at room temperature. Once dried the material was ground with a mortar and pestle and calcined at 500 °C for three hours.

**Method A-2** follows the same preparation method outlined for A-1, however the reactants were combined dropwise with a rate of 4 mL/min. The resulting mixture was left stirring for five hours until the precipitate formed and was subsequently filtered (Whatman, cellulose, 11  $\mu\text{m}$ ), washed with MilliQ water then ethanol and air-dried at room temperature. Once dried the material was ground with a mortar and pestle and calcined at 500 °C for three hours.

**Method A-3** follows the same preparation method outlined for A-1, however the reactants were combined at once. The resulting mixture was left stirring for 24 hours until the precipitate formed and was subsequently filtered (Whatman, cellulose, 11  $\mu\text{m}$ ), washed with MilliQ water then ethanol and air-dried at room temperature. Once dried the material was ground with a mortar and pestle and calcined at 500 °C for three hours.

**Method B** was according to Liu *et al.*<sup>237</sup>. Solid  $\text{KMnO}_4$  (1 g) was added to a stirring solution of manganese acetate (4 g, 24 mL 60% acetic acid solution) and then heated to 60 °C for 10 minutes. The resulting solution was then air dried at room temperature for two days, after which the precipitate was added to a saturated ethanolic sodium hydroxide solution (25 mL) and stirred at room temperature for two hours. This precipitate was then filtered (Whatman,

cellulose, 11  $\mu\text{m}$ ), washed with MilliQ water, ethanol then acetone, and air-dried at room temperature. The final dried product was then calcined at 600  $^{\circ}\text{C}$  for five hours.

**Method C** followed a similar procedure outlined by Luo *et al.*<sup>238</sup>, where an aqueous solution of  $\text{KMnO}_4$  (6.5 g, 150 mL) was added dropwise to a solution of buffered manganese acetate (11 g manganese acetate, buffer consisted of 5 g potassium acetate and 5 mL acetic acid, made up to 40 mL with MilliQ water). This reaction mixture was refluxed at 100  $^{\circ}\text{C}$  for 24 hours, the resulting precipitate was then filtered (Whatman, cellulose, 11  $\mu\text{m}$ ), washed with MilliQ water and air-dried at room temperature. The final dried product was then calcined at 450  $^{\circ}\text{C}$  for four and half hours.

#### *Synthesis of Todorokite (3 x 3 TSMO)*

**Todorokite** follows the preparation method outlined by Feng *et al.*<sup>239</sup>, where BLMO was dispersed in  $\text{MgCl}_2$  for 12 hours, then filtered (Whatman, cellulose, 11  $\mu\text{m}$ ), washed with MilliQ water and air-dried at room temperature. The dried precipitate was then resuspended in water and refluxed at 100  $^{\circ}\text{C}$  for 24 hours, then collected via filtration (Whatman, cellulose, 11  $\mu\text{m}$ ) and air-dried at room temperature.

#### 5.2.2 Reactivity of Other Manganese Oxide Materials

These oxidation experiments were conducted according to the method outlined in section 2.6 utilising vanadium powder (laboratory grade, Hopkins & Williams Limited, Wales) or gold powder (3.0-3.5  $\mu\text{m}$ , Alfa Aesar, USA). These samples were left to react for four days before ICP-MS analysis using the methodology described in section 2.7.1 for V and section 2.7.2 for Au.

## 5.3 Results and Discussion

### 5.3.1 Structural analysis of tunnel structured manganese oxide materials

Cryptomelane materials were synthesised by three literature methods, with alterations made to the addition rate of reactants for method A. This resulted in the preparation of five different materials. XRD analysis shows that the five methods produced cryptomelane materials that were pure and had various levels of structural order (Figure 5-2), due to the presence of diffraction peaks corresponding to d-spacings of 6.9, 4.9, 3.4, 3.1, 2.4, 2.2, 2.16, 1.8, 1.6, and 1.5 Å<sup>87</sup>. Method A-1 produced the most crystalline material while method C produced the least crystalline sample based on the peak sharpness in the XRD patterns. The preparation of synthetic todorokite resulted in a pure and ordered material (Figure 5-3), as confirmed by major diffraction peaks corresponding to d-spacings of 9.5, 4.8, 3.2, 2.7, and 2.4 Å<sup>86</sup>. The commercial MnO<sub>2</sub> was verified to have the pyrolusite structure due to peaks corresponding to d-spacings of 3.1, 2.4, 2.2, 2.1, 1.9, 1.6, and 1.55 Å<sup>88</sup> (Figure 5-3) and was found to contain an unidentified phase corresponding to peaks at 3.4 and 2.8 Å. Subsequent EDX analysis of the pyrolusite sample showed only Mn and O present in the sample, which suggests that the phase seen in the XRD is either a minor impurity unobservable by EDX or is another manganese oxide phase. The average manganese oxidation state of the five cryptomelane materials were found to vary between 3.80 and 4.1 (Table 5-1), these values are on the higher end of the expected range of 3.48-3.83<sup>240</sup>. This suggests different synthesis methods produce cryptomelane materials with differing ratios of Mn<sup>3+</sup> to Mn<sup>4+</sup> in the crystal structures, which corresponds to different levels of K<sup>+</sup> incorporation into the tunnels<sup>241</sup>. It was shown in chapter 4 that K<sup>+</sup> had a stabilising effect on the crystal structure, which subsequently reduced the reactivity of BLMO materials towards vanadium oxidation. The pyrolusite sample was found to have an average manganese oxidation state lower than the expected value of

4, with the oxidation state found to be  $3.78 \pm 0.18$ , which could be due to the presence of some impurities in the sample. Synthetic todorokite was found to have an oxidation state of  $3.21 \pm 0.06$ , this suggests that  $Mn^{3+}$  is the more common oxidation state in this material.

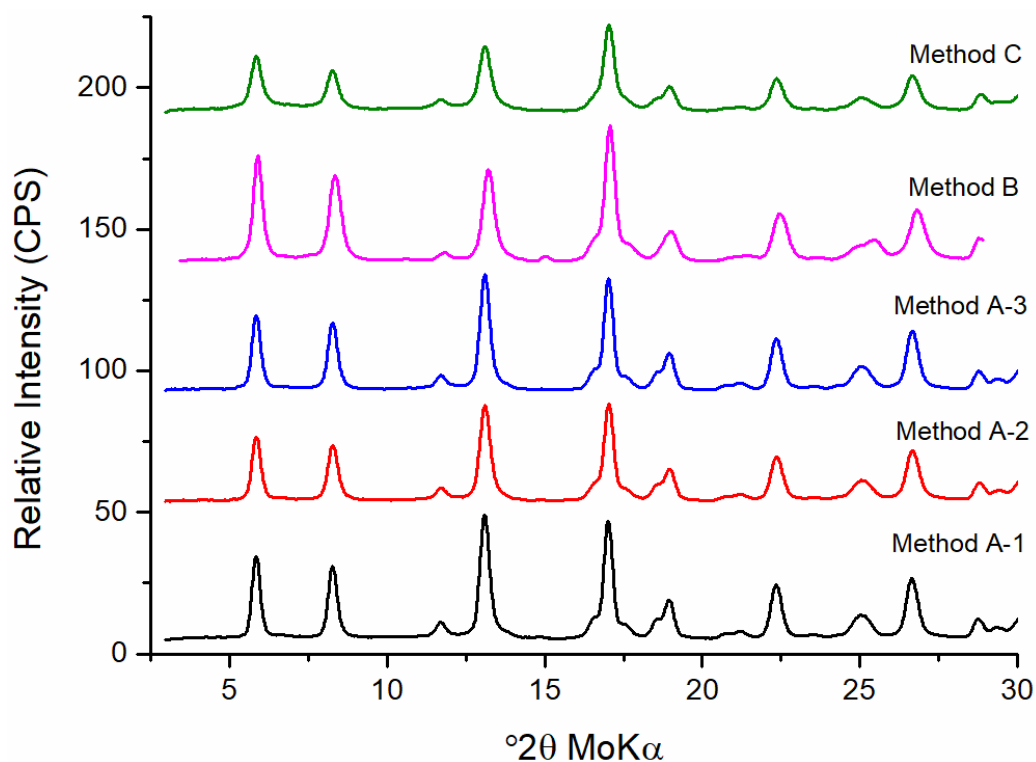


Figure 5-2: MoK $\alpha$  diffraction patterns of five synthetic cryptomelane samples.

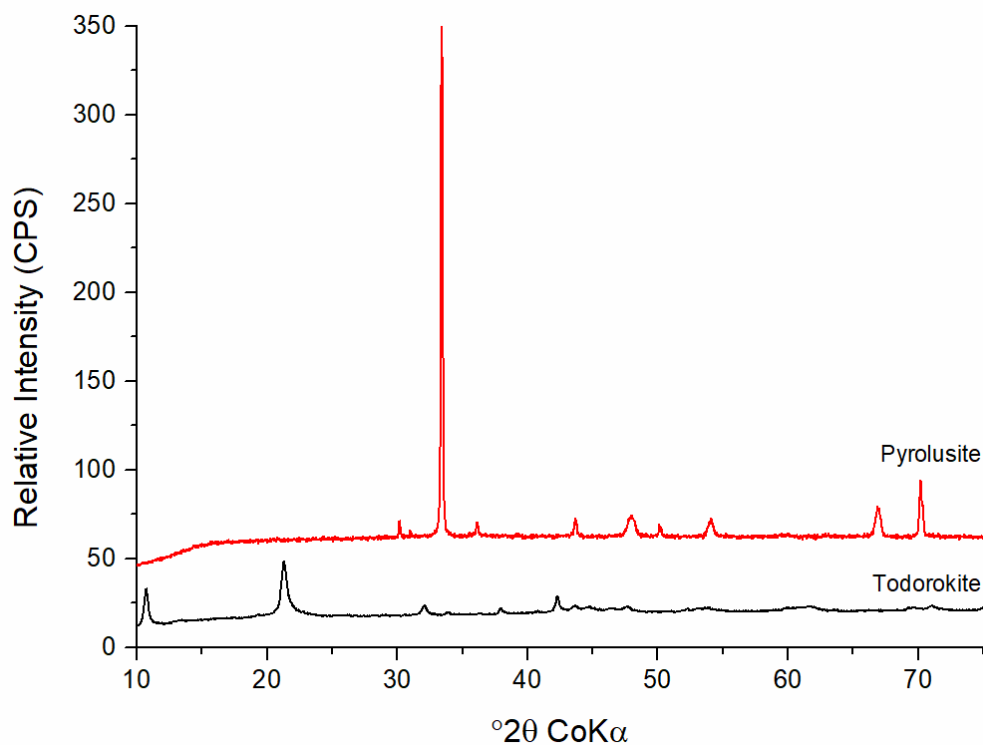


Figure 5-3: CoK $\alpha$  diffraction patterns of synthetic todorokite and commercial pyrolusite.

**Table 5-1: Average manganese oxidation state for TSMO materials. Errors are standard deviation of triplicate analysis ( $n=3$ ).**

Mineral	Average Manganese Oxidation State
Cryptomelane Method A-1	$3.97 \pm 0.34$
Cryptomelane Method A-2	$3.94 \pm 0.11$
Cryptomelane Method A-3	$3.80 \pm 0.05$
Cryptomelane Method B	$4.12 \pm 0.11$
Cryptomelane Method C	$3.79 \pm 0.09$
Todorokite	$3.21 \pm 0.06$
Pyrolusite	$3.78 \pm 0.18$

The morphology of pyrolusite, todorokite and two cryptomelane samples was determined by SEM (Figure 5-4). The todorokite and cryptomelane samples were found to have very fine fibrous morphology, whereas pyrolusite was found to have larger and more defined fibral structures. Rietveld refinements (Figure 5-5, Table 5-2) of the cryptomelane samples showed that these materials have a tetragonal crystal structure with space group  $I 4/m$ , and have similar unit cell parameters across all five samples. The cell parameters, however, are consistently lower than literature values for tetragonal cryptomelane reported by Vicat *et al.*<sup>87</sup>. This difference can be attributed to the synthesis method as the material prepared by Vicat *et al.*<sup>87</sup> contained  $H_3O^+$  instead of  $K^+$  in some of the tunnel spaces resulting in larger unit cell values. The pyrolusite was found to be the expected tetragonal crystal structure with space group  $P 4_2/mnm$  and the unit cell parameters refined were close to the expected values<sup>88</sup>. Todorokite was found to have the expected monoclinic crystal structure with space group  $P 2/m$ , however the refined parameters were lower than literature values<sup>86</sup>. This difference in parameters could be due to the literature refinements being conducted on natural todorokite containing a combination of cations ( $Na^+$ ,  $Ca^{2+}$ ,  $K^+$ ,  $Mg^{2+}$ ) whereas the sample produced here would have majority of  $Mg^{2+}$  with minor inclusions of  $K^+$ .

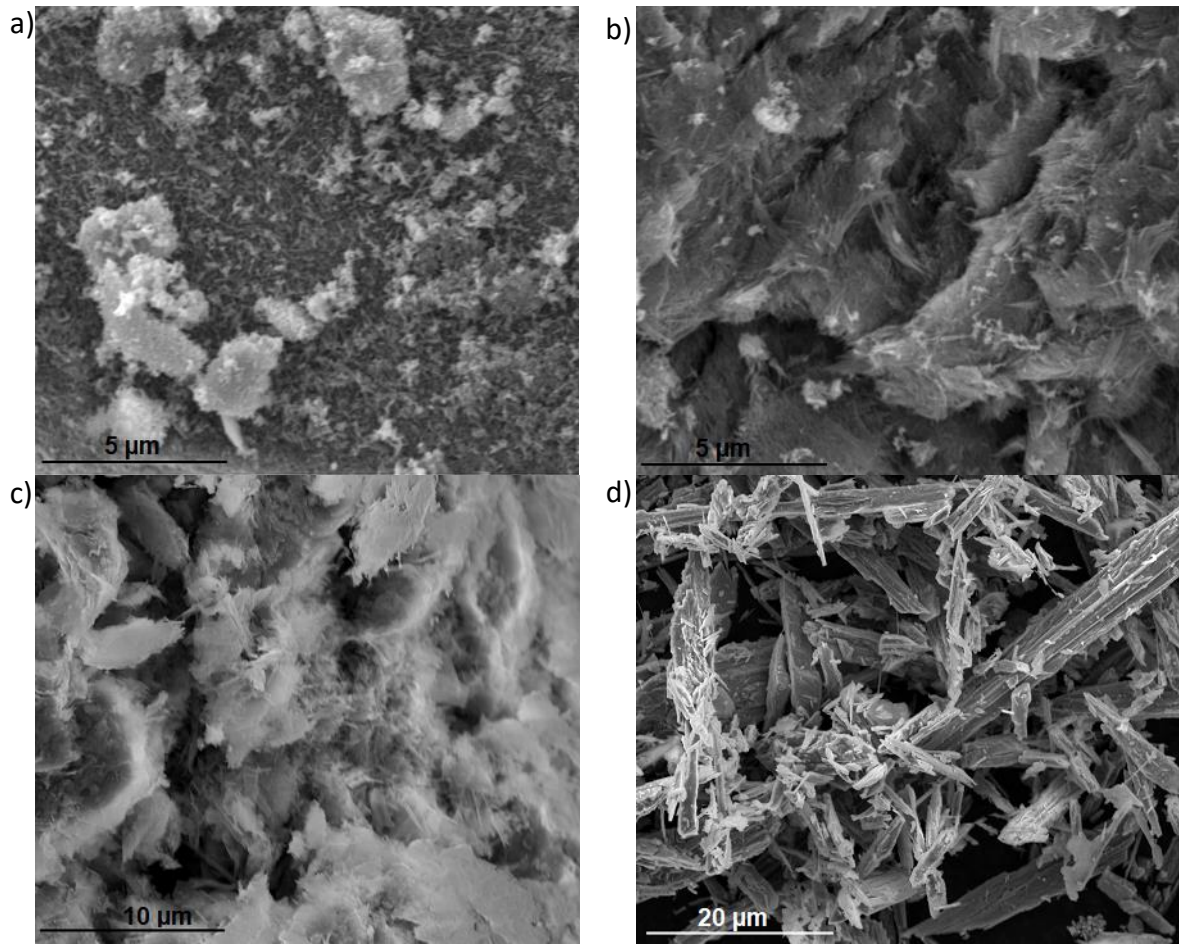


Figure 5-4: SEM images of four TSMO materials , a) cryptomelane method A-3, b) cryptomelane method C, c) todorokite, and d) pyrolusite.

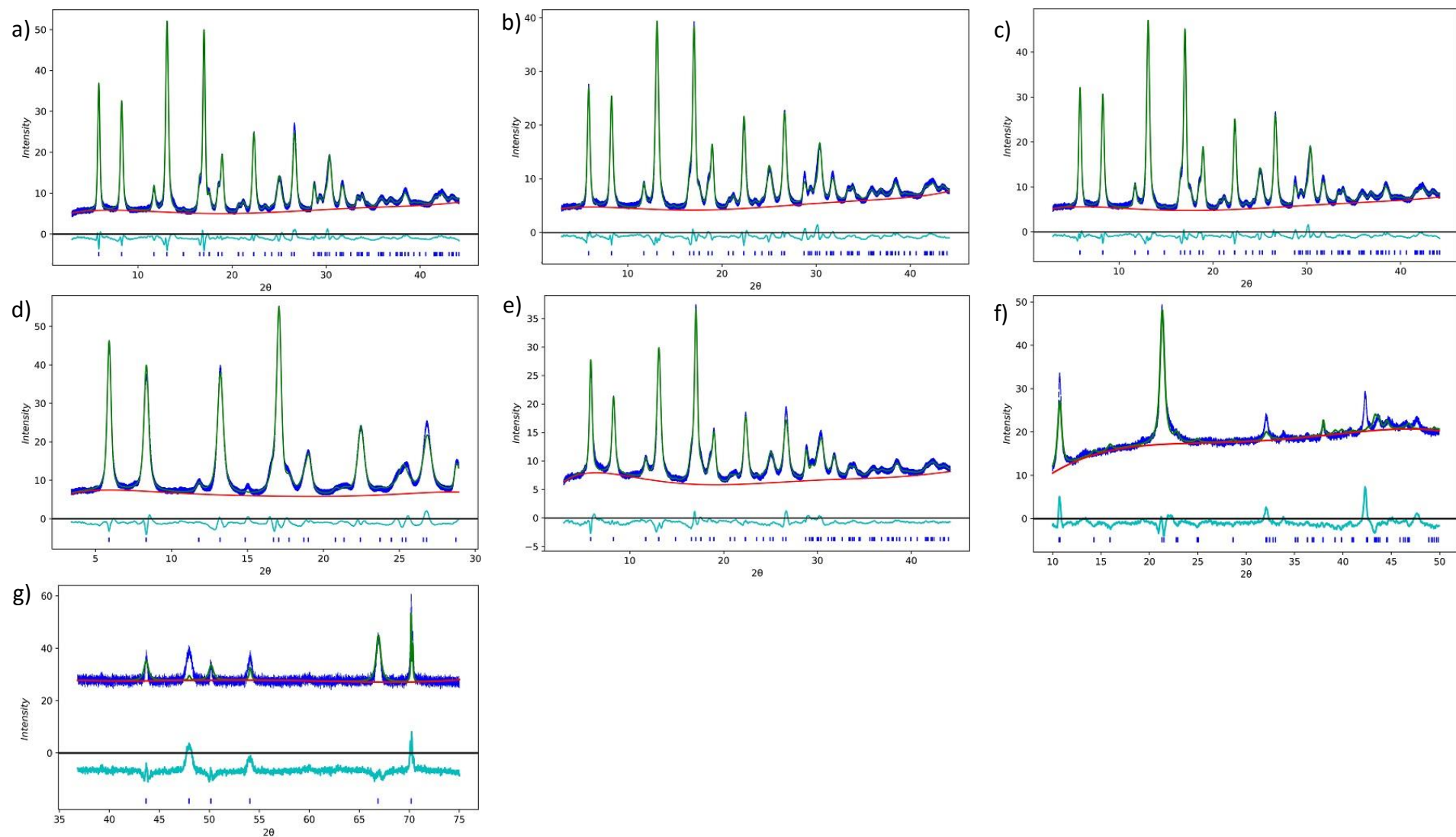


Figure 5-5: Rietveld refinement and difference plots for the TSMO materials presented. a) cryptomelane A-1, b) cryptomelane A-2, c) cryptomelane A-3, d) cryptomelane B, e) cryptomelane C, f) todorokite, and g) pyrolusite.

**Table 5-2: Rietveld refinement results for the TSMO materials prepared, shown are the final refined cell parameters , the R(F)<sup>2</sup> and R<sub>wp</sub> values.**

	Cryptomelane A-1	Cryptomelane A-2	Cryptomelane A-3	Cryptomelane B	Cryptomelane C	Todorokite	Pyrolusite
Space Group	<i>I</i> 4/ <i>m</i>	<i>P</i> 2/ <i>m</i>	<i>P</i> 4 <sub>2</sub> / <i>mnm</i>				
Radiation Source	Mo	Mo	Mo	Mo	Mo	Co	Co
Unit Cell							
a (Å)	9.8495(11)	9.8434(14)	9.8451(12)	9.7594(24)	9.8474(20)	9.699(15)	4.39984(27)
b (Å)	9.8495(11)	9.8434(14)	9.8451(12)	9.7594(24)	9.8474(20)	2.8767(13)	4.39984(27)
c (Å)	2.86216(18)	2.85932(24)	2.86076(21)	2.8602(24)	2.85575(27)	9.784(13)	2.8711(8)
α (°)	90	90	90	90	90	90	90
β (°)	90	90	90	90	90	96.31(10)	90
γ (°)	90	90	90	90	90	90	90
Vol (Å <sup>3</sup> )	277.66(6)	277.05(7)	277.28(6)	272.42(12)	276.93(11)	271.3(4)	55.579(15)
Refinement							
No. of Observations	2060	2060	2060	1275	2060	1836	1960
No. of Reflections	109	107	109	31	107	49	6
Diffraction Range (°2θ)	3 - 44	3 - 44	3 - 44	3.5 - 29	3 - 44	10 - 75	6 - 75
R(F <sup>2</sup> )	0.05421	0.06551	0.05211	0.03006	0.0818	0.19937	0.47354
R <sub>wp</sub>	0.04485	0.04641	0.04368	0.05142	0.03868	0.04728	0.05646

### 5.3.2 Oxidation of V(0) with TSMOs

With the success of BLMOs at oxidising vanadium, investigations into the ability of TSMOs to oxidise vanadium was undertaken. The reactivity of these TSMOs was determined in the same manner as the layer structures in Chapter 4. It was found that pyrolusite was able to oxidise the most vanadium at 0.067 mgV/mgTSMO (68% of the original V), which is similar to the amount oxidised by hexagonal BLMOs (Figure 5-6). In contrast, the todorokite sample oxidised the lowest amount of V with 0.006 mgV/mgTSMO (6% of the original), which makes it the lowest performing material tested. The cryptomelane samples were found to oxidise V(0) in a range from 0.050 mgV/mgTSMO to 0.064 mgV/mgTSMO, this equates to oxidising 52% to 66% of the original amount of vanadium. As was seen for BLMOs, the synthesis method was found to influence the reactivity of cryptomelane materials towards vanadium oxidation, as the three samples prepared using the same base method (A1-3), had similar reactivity, whereas the other two synthesis methods resulted in less reactive cryptomelanes. The reactivity of TSMOs towards V(0) oxidation follows the trend of  $1x1 > 2x2 > 3x3$ , this suggests that the more ordered and larger the tunnel structures are less reactive. In an attempt to determine a structural correlation for this trend, the amount of vanadium dissolved by the materials was plotted against unit cell parameters and shown in Figure 5-7 a-c. Here, we observed that the  $c$ ,  $\alpha$ ,  $\gamma$  unit cell parameters, and AOS did not correlate to the reactivity observed; however, it was found that the reactivity correlates to the  $a$  unit cell parameter, unit cell volume and inversely correlates to the average Mn-O bond length (Figure 5-7d-f). The Mn-O bond length was found to increase as the size of the tunnels increased; this suggests the presence of  $Mn^{2+}$ . This increase in bond length should have resulted in an increase in reactivity due to the destabilisation of the structure by Jahn-Teller

distortions<sup>218, 242-243</sup>. However, the opposite was found, suggesting that the larger tunnel structures are compact and rigid enough to offset this destabilisation.

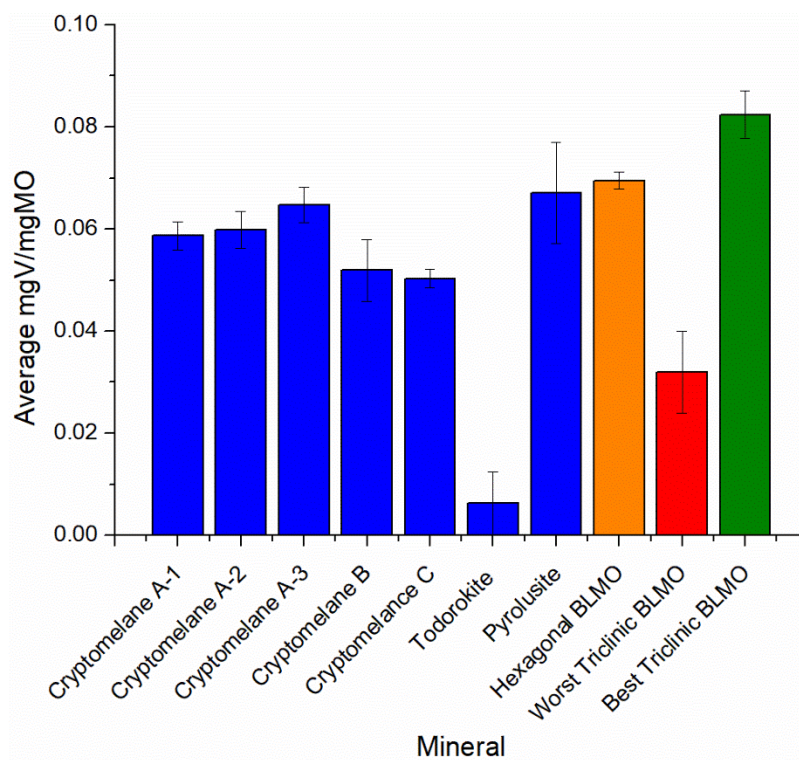


**Figure 5-6: Reactivity plots for other manganese oxide materials, with a hexagonal and the best and worst triclinic BLMO as a reference comparison. Error bars represent one standard deviation  $n=3$ .**

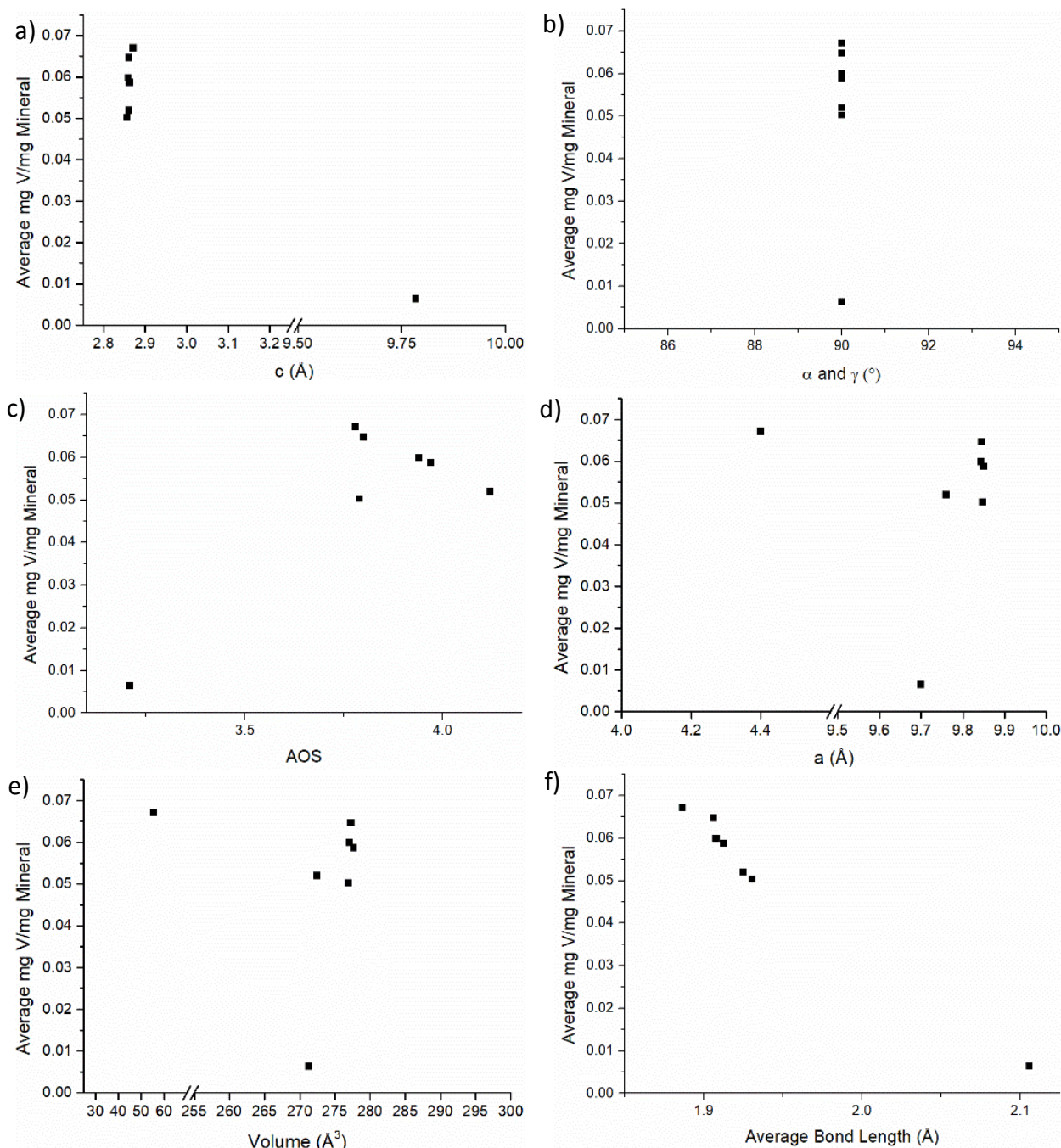


**Figure 5-7: Variability plots showing different refined parameters for the tunnel structure manganese oxide minerals, a) c unit cell parameter, b)  $\alpha$  and  $\gamma$  unit cell parameter, c) average manganese oxidation state, d) a unit cell parameter, e) unit cell volume and f) the average Mn-O bond length.**

On average, cryptomelane materials oxidised 58% of the vanadium, which is comparable to the 60% oxidation achieved on average by the seven BLMOs under identical conditions. The cryptomelane structures had varying amounts of  $K^+$  incorporated into the tunnels, which has previously been found to stabilise the tunnel structure of cryptomelanes<sup>244</sup>. In this study an increase in  $K^+$  content correlated with a small increase in the amount of V(0) oxidised by the

cryptomelanes (Figure 5-8). This is in contrast to the results found for layered structures in chapter 4, where  $K^+$  stabilisation resulted in a decrease in the oxidation of V(0). Normally at temperatures of  $\sim 550-600$  °C, cryptomelane tunnels collapse into the framework structured manganese oxide bixbyite ( $Mn_2O_3$ )<sup>195, 245</sup>, which is subsequently converted to hausmannite ( $Mn_3O_4$ ) at  $825$  °C<sup>245</sup> (Figure 5-9). However, Gao *et al.*<sup>244</sup> found that  $K^+$  stabilised cryptomelanes partially collapse into bixbyite at a higher temperature range ( $600-900$  °C), form a layered manganese oxide phase that persisted from  $800-1000$  °C and also preserved the tunnel structure up to  $800$  °C<sup>244</sup>. In our work it was seen that the increase in  $K^+$  content correlated to a small increase in the amount of V(0) oxidised by the cryptomelanes (Figure 5-8), this is in contrast to the results found for layered structures in chapter 4, where  $K^+$  stabilisation resulted in a decrease in the oxidation of V(0). XRD analysis of the remaining cryptomelane sample after storage in the oxidation reaction solution for two years shows that some of the tunnel structure had collapsed into layered BLMO (Figure 5-10). The variation in the reactivity of cryptomelanes could be due the more stabilised materials forming a layered structure BLMO instead of bixbyite, which could affect the amount of V(0) dissolved. However, the transformations occurring during the reaction are unknown and the ability of bixbyite and hausmannite to oxidise V(0) are also unknown and were not studied in this research. Therefore, further work is required to gain an understanding of the stability and phase conversion of cryptomelanes in our reaction system and their potential effect on the amount of metal dissolved.

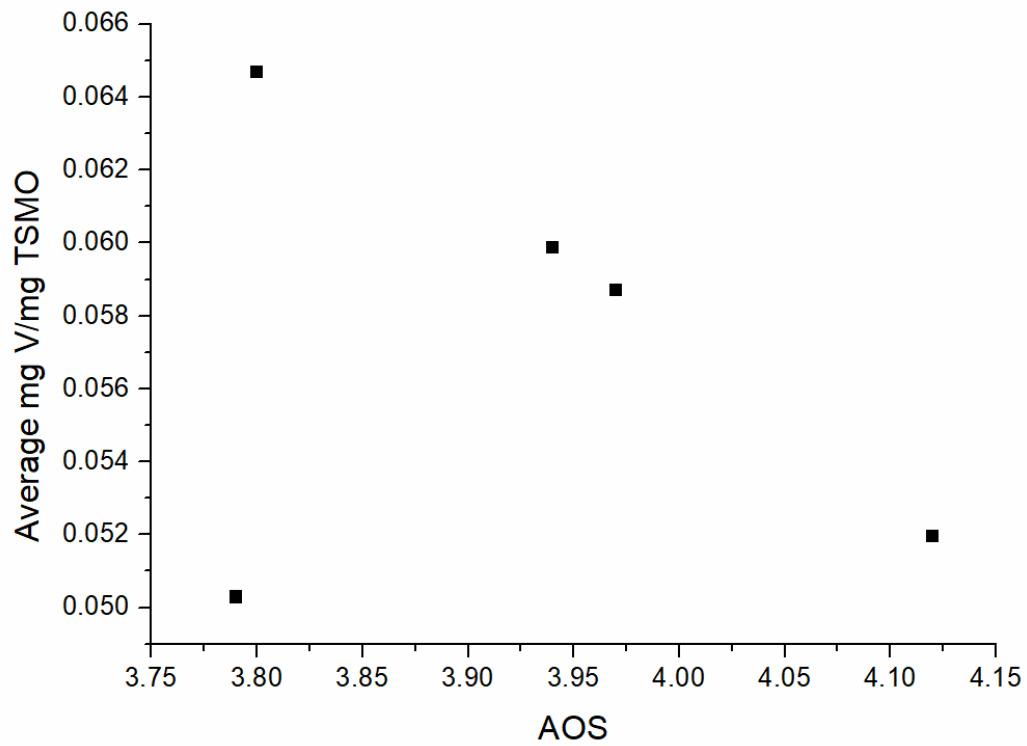


Figure 5-8: Comparison of the average manganese oxidation state and the amount of V oxidised by the five cryptomelane samples.

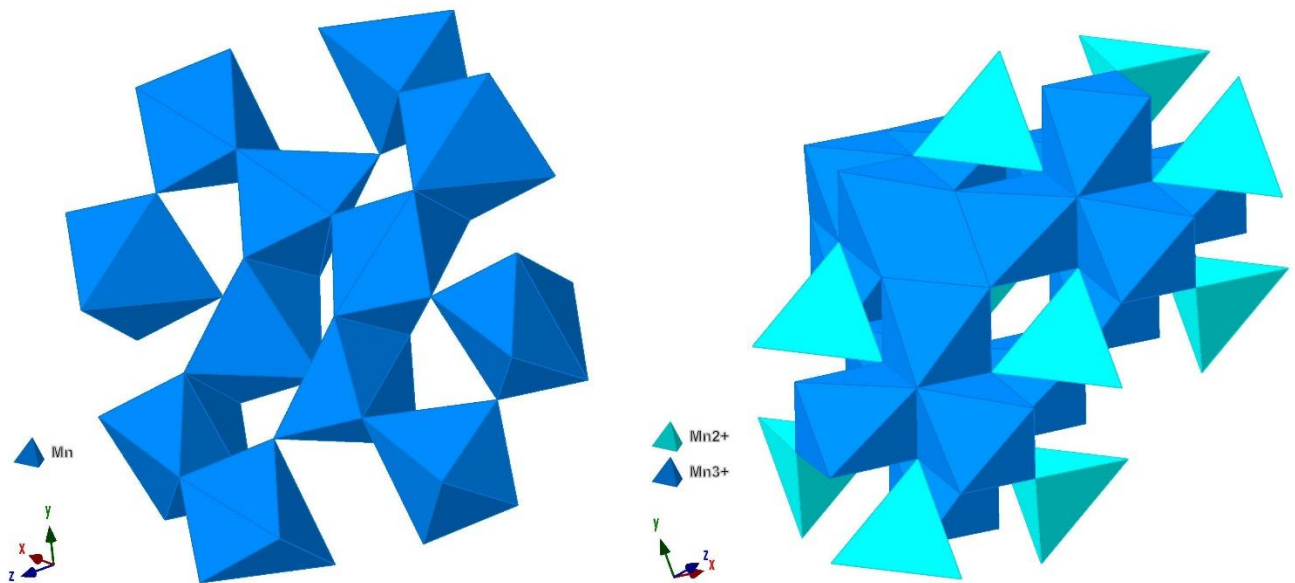


Figure 5-9: Crystal structure of bixbyite (left) showing the random point-sharing and edge-sharing  $\text{MnO}_6$  octahedra, and hausmannite (right).

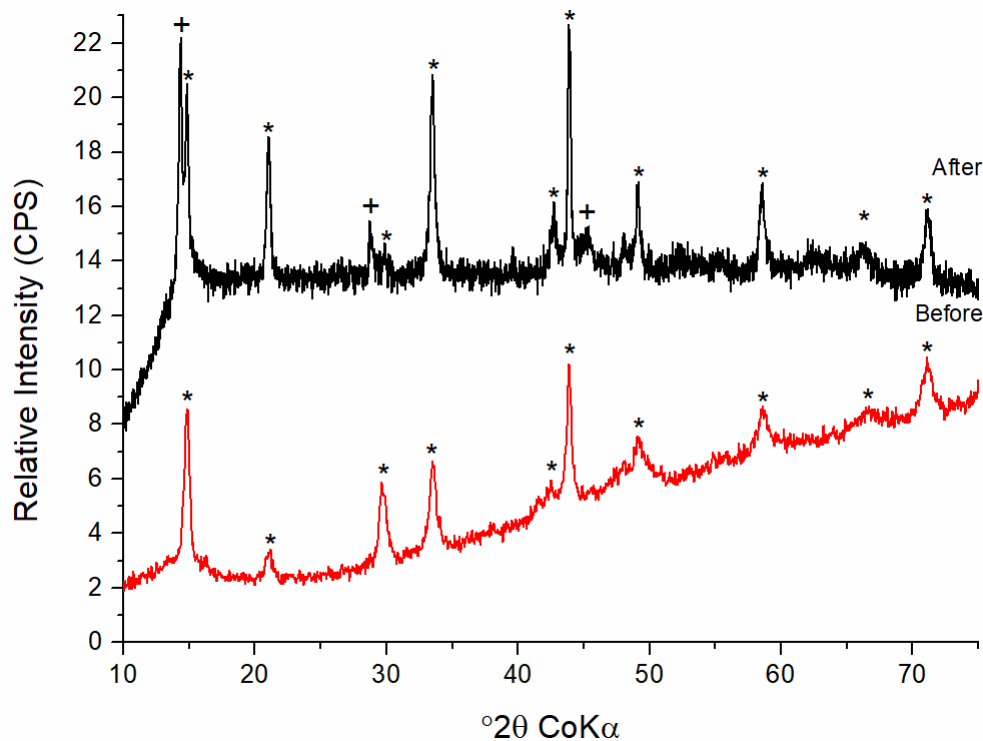


Figure 5-10: CoK $\alpha$  diffraction patterns of cryptomelane method A-2 before and after oxidising vanadium and stored in the reaction solution for two years. \*cryptomelane, +BLMO

### 5.3.3 Comparison of Manganese Oxide Reactivity for Vanadium and Gold

As noted in chapter 4, prior work by Yin *et al.*<sup>206</sup> and Liu *et al.*<sup>229</sup> has indicated that V may replace one or both of a Mn<sup>3+</sup> from the MnO layer in hexagonal BLMO or a K<sup>+</sup> from within the interlayer space. This brings about some questions as to whether this replacement may also be influencing the oxidation reaction and the cause of some of the variation observed. Therefore, reactions of BLMOs and TSMOs were undertaken under identical conditions using Au(0) in place of V(0). A selection of nine manganese oxide materials comprising the two worst performing materials (BLMO Method A and todorokite), two of the best materials (pyrolusite and cryptomelane method A-3) and five medium materials (BLMO methods B, C, and C-M, along with CaBLMO and cryptomelane method C) were tested. Hexagonal BLMOs were not investigated here as insufficient quantities of the hexagonal samples remained after the vanadium and AOS tests. It was found that the manganese oxides ability to oxidise gold was highly variable. The amount of gold in solution was slightly lower than that of V, and

ranged from 0.001 mgAu/mgMO to 0.03 mgAu/mgMO which corresponds to a range of 1-31% (Figure 5-11). The amount of gold oxidised is lower than those found for vanadium (18-68%) due to the differences in oxidation potential ( $E^\circ/V$  V= -1.175, Au=1.401). However, there is a greater variation in the oxidation results for Au(0) than those observed for V(0), which could be due to differences in gold particle size used for each individual replicate as the particle size was found to vary from 1  $\mu\text{m}$  to  $\sim 7.5 \mu\text{m}$ . In general, the reactivities of manganese oxides towards Au(0) were similar to the reactivity to V(0), whereby a material that produced high levels of oxidised vanadium also resulted in higher levels of oxidised gold (Figure 5-11). However, BLMO A and pyrolusite were exceptions to this trend. BLMO A was found to oxidise similar amounts of gold and vanadium. This level of gold is higher than expected given the amount of V oxidised, which could be due to discrepancies in the levels of vanadium in solution vs amount of V oxidised. This would result from the greater incorporation of V in the structure of the amorphous BLMO. Contrastingly, pyrolusite was found to be the worst material for gold oxidation although it was one of the best for vanadium. It was thought that this could be the potential passivation of the material. Very little is reported in the literature regarding the passivation of pyrolusite; Chen *et al.*<sup>246</sup> managed to deposit gold nanoparticles into etched pockets on the surface of cryptomelanes and Bodoardo *et al.*<sup>247</sup> reported the passivation of MnO<sub>2</sub> electrodes; however, neither used conditions similar to those used here. A preliminary test was conducted where 200 mg of pyrolusite was soaked in 100 ppm Au<sup>3+</sup><sub>(aq)</sub> solution at pH 2 (acidified with HCl) for 3 days. The pyrolusite was subsequently recovered via filtration, washed, and subjected to SEM, EDXS and XRD. The SEM and EDAX results (Figure 5-12, Figure 5-13) showed no evidence of Au binding to the pyrolusite and there was no observed shifting of the diffraction peaks (Figure 5-14). This suggests that passivation of the pyrolusite surface is not the primary mechanism that is driving the lower reactivity

observed under these conditions. However, the limits of detection achievable by EDAX and SEM are poor and further work is required to verify this.

Further investigations into the general trend observed with tunnel structured manganese oxides are required due to the increased oxidation variability found in the gold experiments and the presence of anomalies in BLMO A and pyrolusite.

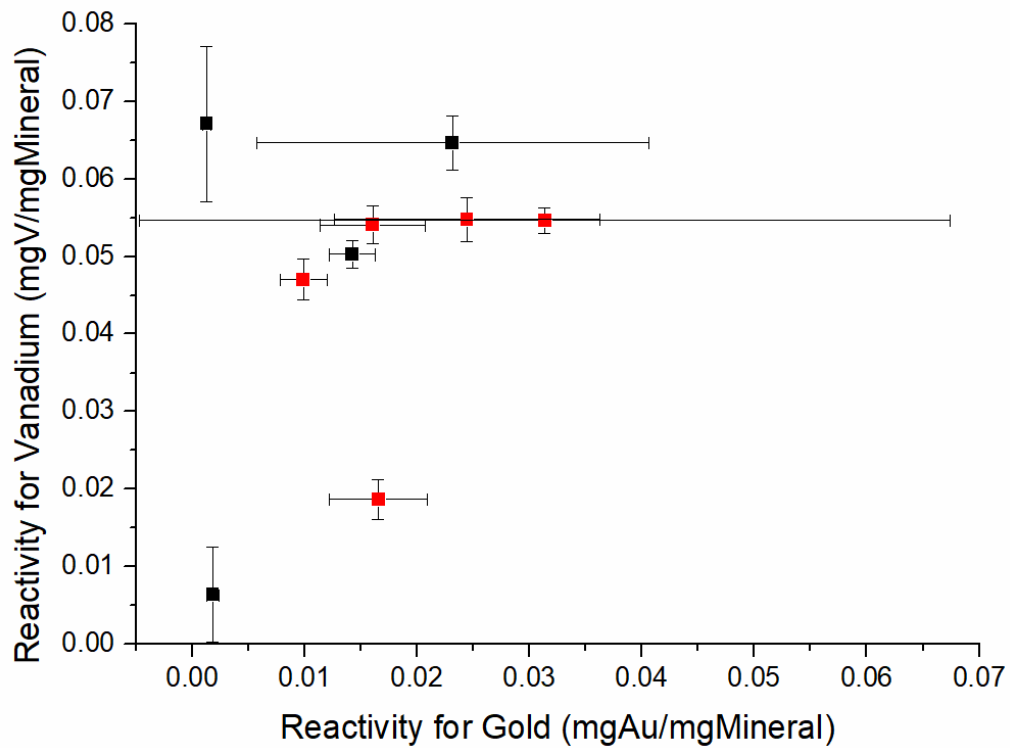


Figure 5-11: Comparison plot of the reactivities of nine manganese oxide materials for the oxidation of gold and vanadium. Red-BLMO, Black-TSMO. Error bars represent one standard deviation  $n=3$ .

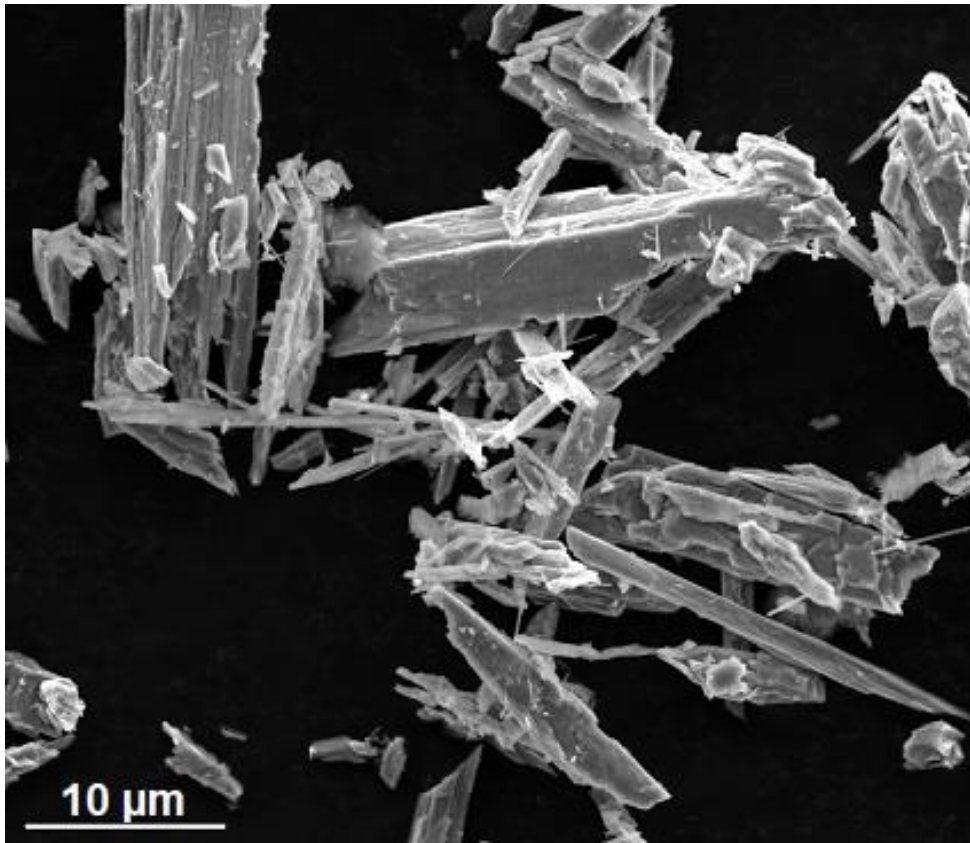


Figure 5-12: SEM image of the pyrolusite powder after submersion in 100 ppm  $\text{Au}^{3+}$  for three days.

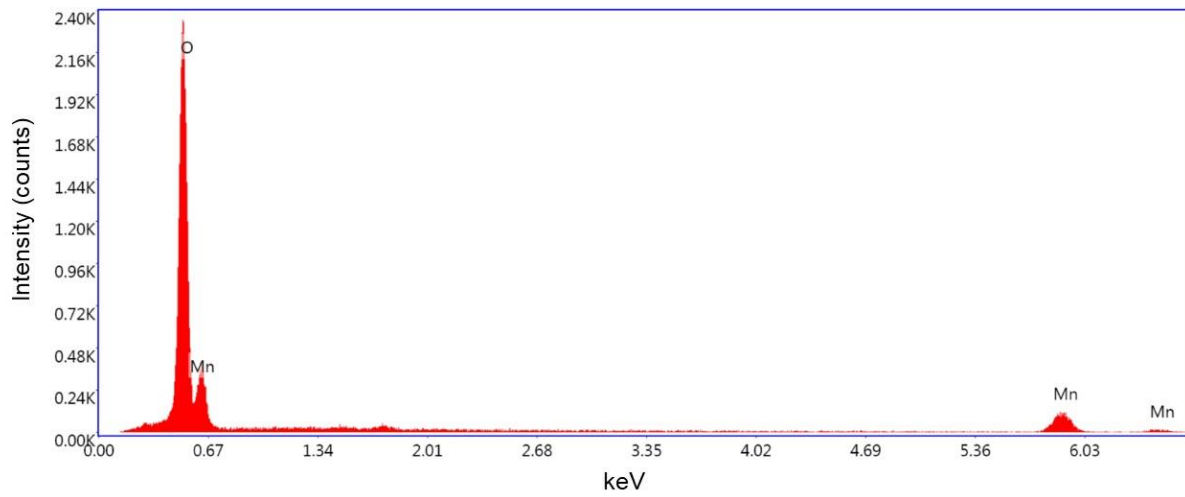
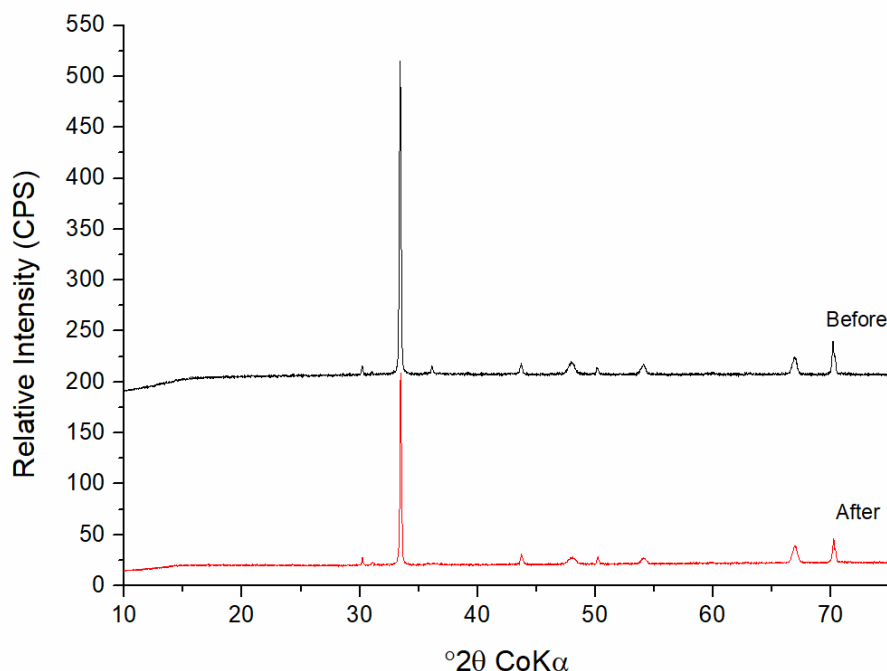


Figure 5-13: EDXS spectra of pyrolusite powder collected after submersion in 100 ppm  $\text{Au}^{3+}$  solution for 3 days.



**Figure 5-14: CoK $\alpha$  diffraction patterns collected for the pyrolusite powder before and after submersion in a 100 ppm Au<sup>3+</sup> solution for 3 days.**

## 5.4 Conclusion

In this chapter we showed that the reactivity of TSMOs for vanadium oxidation follows the trend of  $1 \times 1 > 2 \times 2 > 3 \times 3$ . Furthermore, the reaction of cryptomelane ( $2 \times 2$ ) materials towards vanadium oxidation was variable and affected by its preparation method. Those with more K<sup>+</sup> content oxidised slightly more V(0), which could be due to the K<sup>+</sup> stabilisation of the tunnel structure preventing the formation of a less reactive material. However, further exploration into the effect of this stabilisation is needed. When comparing the ability of various BLMO and TSMO materials to oxidise V(0) and Au(0), we observe a general trend in the amount of metal oxidise that suggests that a material good for V(0) oxidation is typically a good material for Au(0) oxidation. However, further investigations into the anomalies observed here and an investigation into different manganese oxide materials are need, including the testing of hexagonal BLMOs.

## Chapter 6 Electronic Waste Applications

### 6.1 Introduction

The rapid advancement of technology over the past two decades has increased the amount of electronic waste produced globally. Electronic waste is a term that covers a broad range of items from monitors and IT equipment to larger equipment such as washing machines and solar panels<sup>155</sup>. In 2010, 33.8 million tonnes<sup>156</sup> of electronic waste was generated worldwide, while only 6 years later this value increased to 44.7 million tonnes<sup>155</sup> and current projections have the e-waste production for 2020 at ~51 million tonnes<sup>155</sup>. As of 2016, only 20% of e-waste generated was recycled<sup>155</sup>, with the rest either incinerated or dumped into landfills. A specific component of e-waste is printed circuit boards (PCBs), found in computers, phones and other electronics. PCBs have a high metal content, which ranges from including common metals such as Cu, Sn, Pb, and Ni<sup>157</sup>, to precious metals such as Au, Ag and Pd<sup>158</sup>. Interest in the recovery of metals from PCBs has increased due to the economic value of recovering precious metals from secondary sources and the cost of mining diminishing ore deposits<sup>159-160</sup>.

Current industrial recycling processes generally involve a grinding pre-treatment of the PCBs, followed by pyrometallurgical processes<sup>161</sup>. The pyrometallurgical process employed at Aurubis uses the Kayser Recycling System to separate the Cu from the Fe, Zn, Sn and Pb present in the PCBs<sup>162</sup>. This 95% pure copper smelt is then cast into anodes and electrowinned to separate the precious metals such as gold and silver, and remove nickel as a byproduct<sup>162</sup>. Research into the development of metal extraction from PCBs is focused on improving the separation stage of metal recovery, this stage is split into three methodologies: 1) pyrometallurgical, 2) hydrometallurgical, and 3) biometallurgical. Discussions on these

techniques can be found in Chapter 1, here the focus will be on hydrometallurgical processes. Hydrometallurgical extraction processes typically employ acidic or alkaline medium to achieve the dissolution of metals from pre-treated PCBs. Pre-treatments typically involve a physical treatment followed by a chemical treatment. The physical pre-treatments consist of the removal of external components<sup>248</sup> and the grinding/milling<sup>166</sup> of the PCBs. Chemical pre-treatments are used to remove the laminating layer and solder joints present on PCBs, these treatments involve soaking in NaOH<sup>163</sup>, dilute HNO<sub>3</sub><sup>249</sup>, DMSO<sup>250</sup>, DMF<sup>251</sup>, or HCl + Sn<sup>4+</sup><sup>252</sup>. Once pre-treatments are completed the PCBs are subjected to the hydrometallurgical process of choice. Traditional hydrometallurgical processes utilise either mineral acids<sup>166, 253-255</sup>, mineral acids in conjunction with an oxidant<sup>256-259</sup> or cyanide processes<sup>260-261</sup>. Current hydrometallurgical research is focus on the development of greener, more sustainable oxidation techniques such as ionic liquids<sup>167-168</sup>, glycine<sup>169-170</sup> and supercritical CO<sub>2</sub><sup>171-172</sup>. Another avenue of research is looking for more effective pre-treatments<sup>166, 173</sup> and the addition of multistep processes<sup>174</sup>.

BLMO materials in combination with an acidic saline solution have been shown in the earlier work detailed in Chapters 4 and 5 to have the ability to oxidise elemental vanadium and gold. Their ability to oxidise and subsequently dissolve metals provides a potential application for utilising BLMOs as an oxidant addition in the hydrometallurgical extraction of metals from electronic waste. To investigate this, small e-waste components from computers (CPUs and RAM pins) were collected for a preliminary investigation into the feasibility of BLMOs for metal recovery from e-waste.

## 6.2 Materials and Methods

### 6.2.1 Preliminary Metal Oxidations

Various elemental metals (20 mg, Fe, Ni, V, Pb, Pd, Rh, Au, Cu and Pt) were combined with 200 mg of triclinic BLMO in an aqueous acidic saline solution (0.05 M NaCl, pH 2). Experimental blanks for each metal were prepared in the same manner with the absence of BLMO material. These reactions were then allowed to react for 7 days at 35 °C with an agitation rate of 150 rpm (Labec Shaking Incubator, Australia). Aliquots (500 µL) of the reaction solutions were taken at 0 and 7 days, diluted with 4.5 mL of 2% hydrochloric acid, BLMO particulate was removed via syringe filtering (0.45 µm PDVF, Kinesis Australia) and kept at -20 °C until analysis. Before analysis samples were diluted by a factor of 200 and then the dissolved concentration of each metal was determined using ICP-MS as outlined in Section 2.7.3.

### 6.2.2 First Electronic Waste Oxidations

Electronic waste in the form of CPUs and RAM pins were combined with 250 mg of triclinic BLMO, in an acidic saline solution (0.5 M NaCl, pH 2, 100 mL) and left to react for six days at 30 °C and 155 rpm in an orbital incubator (Ratek OM15C, Ratek Australia). The BLMO oxidation of each computer part was conducted in duplicate, with a saline acid control (0.5 M NaCl, pH 2, 100 mL) containing no BLMO. The dissolved concentration of each metal was determined using ICP-MS as outlined in Section 2.7.3.

### 6.2.3 Second Electronic Waste Oxidations

The same CPUs and RAM pins from the first oxidation were combined with 500 mg of triclinic BLMO, in an acidic saline solution (0.5 M NaCl, pH 1, 100 mL) and left to react for four days at 30 °C and 155 rpm in an orbital incubator (Ratek OM15C, Ratek Australia). The BLMO oxidation of each computer part was conducted in duplicate, with a saline acid control

containing no BLMO. Before analysis samples were diluted by a factor of 200 and then the dissolved concentration of each metal was determined using ICP-MS as outlined in Section 2.7.3. The dissolved concentration of each metal was determined using ICP-MS as outlined in Section 2.7.3.

#### 6.2.4 Aqua Regia Digest Controls

CPUs were oxidised in triplicate in a 66% v/v 3HCl:1 HNO<sub>3</sub> aqua regia solution for two hours. Whereas RAM pins were split into two types of pins and oxidised in duplicate in a 27% v/v 3HCl:1HNO<sub>3</sub> aqua regia solution for two days. Both oxidation solutions were frozen at -20°C until ICP-MS analysis was conducted as described in section 2.7.3.

### 6.3 Results and Discussion

#### 6.3.1 Preliminary Metal Oxidations

It has been shown in chapter 4 and 5 that the combination of an acidic saline solution and manganese dioxide materials results in the oxidation and subsequent dissolution of vanadium and gold powders. Preliminary testing was conducted using a combination of common and precious transition metals to investigate the potential of BLMOs to oxidise other metals, such as those typically found in e-waste. Metal powders were reacted with BLMO in acidic saline solution as described earlier, with the exception that they were allowed to react for seven days. Analysis of the reaction solutions after seven days via ICP-MS demonstrated that this reaction system is able to oxidise significantly more palladium (47 ppm) along with vanadium (95 ppm) and gold (3.4 ppm) than the acidic saline controls (Pd: 0.9 ppm, V: 10.3 ppm, Au: 0 ppm) (Figure 6-1). In contrast, it was also demonstrated that copper (130 ppm), iron (149 ppm), nickel (206 ppm) and lead (160 ppm) were oxidised at greater levels in the saline acid controls than in the presence of BLMO (Cu: 59 ppm, Fe: 11 ppm, Ni: 173 ppm and Pb: 3.5 ppm). This suggests that BLMO materials have an inhibitory effect on the dissolution of these

metals. The cause of this inhibition could be due to absorption of these cations to the BLMO materials after oxidation, which has been proposed for heavy metal elements such as lead and cadmium<sup>31</sup>. Alternatively, the oxidised metals could be precipitating onto the surface of the remaining metal and causing passivation to occur, which would reduce further oxidation by the BLMO system. The precious metals of Rh and Pt were unable to be oxidised by either the BLMO test or the acid control. These results are consistent with the solubility of the resulting metal chloride salts in water. Chloride salts of gold, vanadium and palladium chlorides have a higher solubility in water<sup>262</sup>, whereas the chlorides of lead, iron, nickel and copper have lower solubility than other salts and generally the chloride salts of rhodium and platinum are insoluble in water<sup>262</sup>. This suggests that the ability of BLMO materials to oxidise metals could be dependent on the solubility of the final solubilised form of the metal.

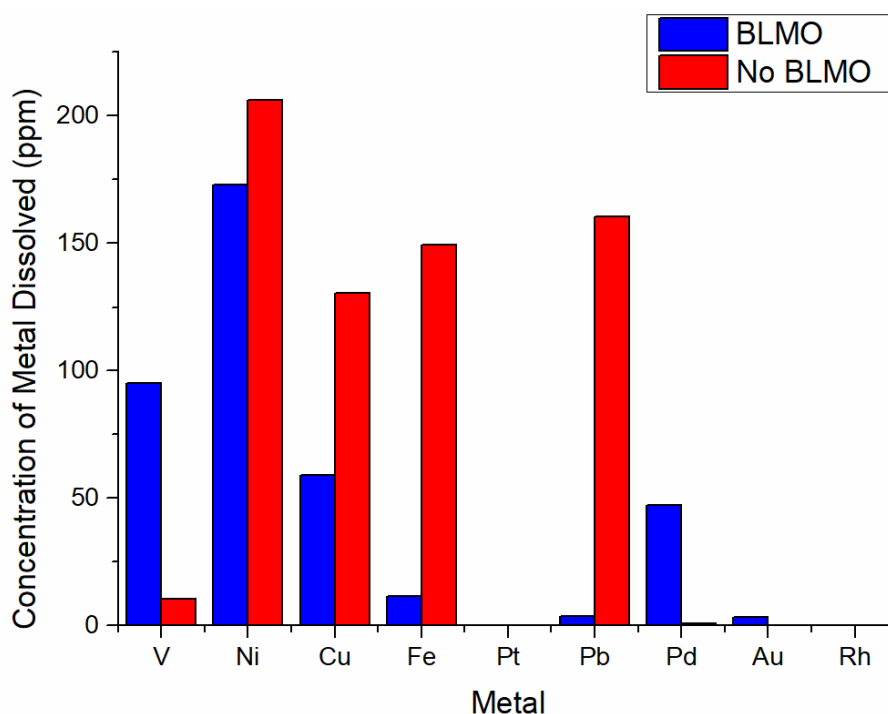


**Figure 6-1: Preliminary trials for BLMO oxidation of nine transition metals**

The controlling effect of metal salt solubility on the ability of the BLMO reaction system to oxidise metals was investigated by changing the ligand present in the reaction solution. Copper bromides are more soluble in water than copper chlorides<sup>262</sup>, therefore copper metal

was combined with a bromide-based system (NaBr and HBr) instead of a chloride system (NaCl and HCl) and reacted under identical conditions as above. It was observed that switching the halide system from chloride to bromide resulted an increased concentration of copper generated by BLMO system (Figure 6-2), with the bromide system oxidising twice as much copper as the chloride system (Cl system Cu: 59 ppm and Br system Cu: 121 ppm). Switching Cl for Br was also found to reduce the amount of copper oxidised in the acidic control sample, with only a small amount of copper oxidised in the bromide control (Cl system Cu: 130 ppm and Br system Cu: 0.7 ppm). This reduction of Cu from the bromide control is likely due to the hydrobromic acid being unable to oxidise copper unlike hydrochloric acid<sup>263</sup> and therefore less able to solubilise copper without the aid of BLMO materials. These results show that our reaction system has the potential to be modified to enable the oxidation of different metals. For example, utilising different salts could increase the selectivity for particular metals due to differences in product solubilities, as well as modifying the pH of the reaction system to effect the efficiency of the oxidation of metals, these alterations could decrease the levels of unwanted metals extracted.

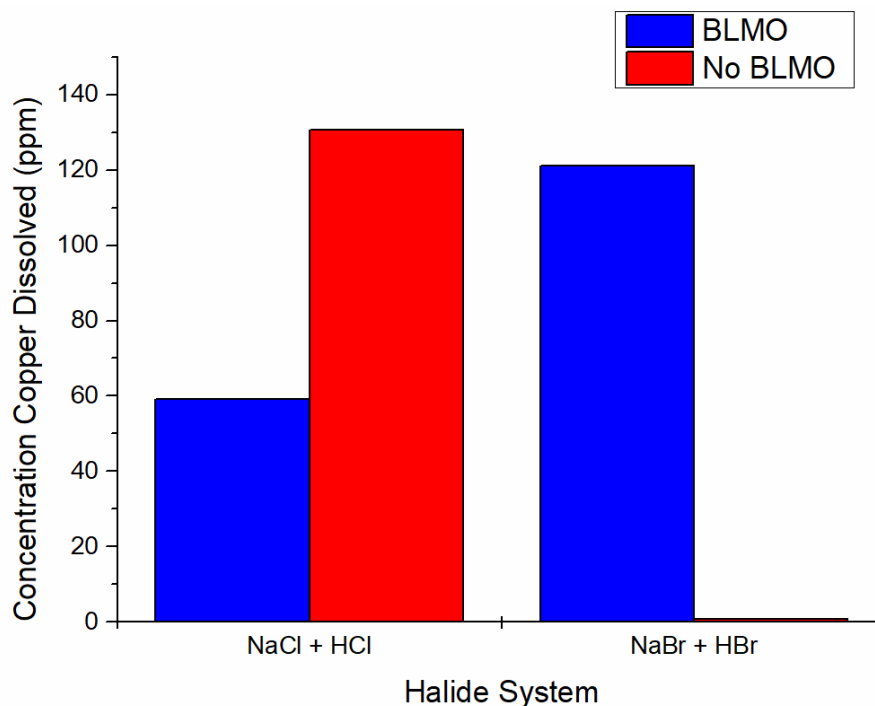


**Figure 6-2: Reaction of copper metal with different combinations of halide salts and acids**

### 6.3.2 Electronic Waste Applications

Given that the BLMOs were shown to oxidise precious metals such as Au, and Pd, it was decided to test the system for the dissolution of metals from electronic waste as this waste stream is known to contain high levels of metals such as Au. Preliminary experiments were conducted to investigate the feasibility of this application for the dissolution of metal using two types of computer parts (CPUs and RAM pins). The e-waste was combined with 250 mg of triclinic BLMO and acidic saline solutions (0.5 M NaCl, pH 2, 100 mL) and were left to react for six days in an orbital incubator (30 °C and 155 rpm). After the reaction time elapsed the concentration of Ag, Al, As, Au, B, Ba, Ca, Cd, Co, Cr, K, Mg, Mo, Ni, Pb, Sb, Se, Sr, Ti, Tl, V, Zn dissolved by this system were determined using ICP-MS analysis. Results for Fe and Sn had very high relative standard deviations and as such the levels of Sn and Fe were re-analysed after storage of the reaction solution in the dark at room temperature for one month. The levels of Cu, omitted from the first analysis, were also measured after for this sample. It was found that BLMOs were able to extract higher quantities of Ag, Al, Ba, Co, Cu, Ni, Sb, Ti, and

Zn from CPUs than the control saline acid treatment (Figure 6-3). In contrast, Pb and Sr oxidation was found to be inhibited by the BLMO, this result is expected as BLMO materials are known to adsorb metal cations of Pb, Cd, Zn, and Cu<sup>31, 264</sup>. Similarly, BLMOs were also able to extract metals from RAM pins (Figure 6-4), with the BLMO system extracting higher quantities of Ag, Ba, Ni, Sn, and Zn present from the RAM cards. Al, B, Cu, and Pb dissolution from the RAM was lower in the BLMO system, whilst the levels of Sr and Cr being roughly even in both the BLMO tests and the control test. The differences observed in the metals oxidised from the CPUs and RAM pins could be due to the quantity of metals present, as the easier to oxidise metals would outcompete metals such as Ag and Au due to differences in reduction potentials. This is supported by an observed increase in pH over time for the CPUs, whereas the pH in the RAM tests had a limited increase in pH. It was observed that there was more carbon material in the RAM tests than the CPU, suggesting that some coating remained on the RAM pins before the oxidation experiments took place, which may have interfered with the resulting levels of metals extracted into solution. Potassium values determined for the oxidation tests are not reliable due to the BLMOs containing potassium as the interlayer cation, and the magnesium values are also unreliable due to the presence of Mg as impurities in the NaCl used<sup>265</sup>.

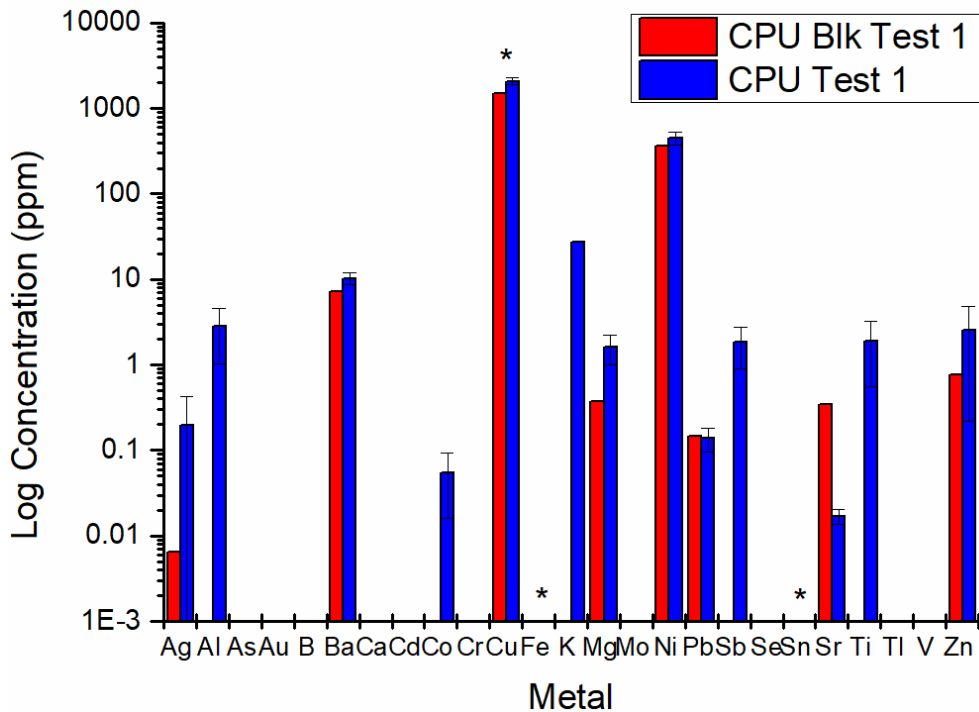


Figure 6-3: Preliminary concentration results from the first attempt to oxidise the metals in CPUs with our reaction system. \*concentrations were determined from the solutions at a later date than the other elements. Error bars represent one standard deviation n=2.

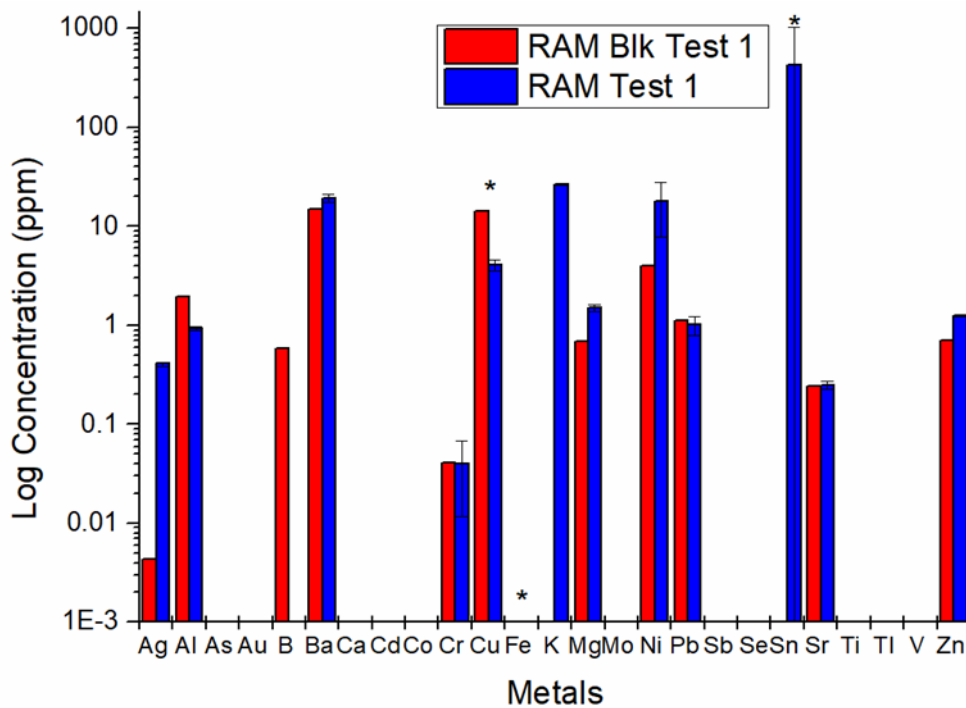


Figure 6-4: Preliminary concentration results from the first attempt to oxidise the metals in RAM pins with our reaction system. \* concentration were determined from the solutions at a later date than the other elements. Error bars represent one standard deviation n=2.

The large concentrations of elements recovered from the e-waste and the lack of any gold being found in solution, implies that gold is being outcompeted by the easier to oxidise elements ( $E^{\circ}/V$  values Au= 1.498, Cu=0.3419, Ni=-0.257 and Pb= -0.1262)<sup>263</sup>. To counteract this, the computer parts were oxidised again with a stronger set of conditions. The acidity of the solution was decreased to pH 1, the amount of BLMO material was doubled and the pH was adjusted twice a day to ensure a constant replenishment of  $H^+$ . This second BLMO oxidation of the CPUs were found to oxidise the same elements as the first oxidation, with the additional oxidation of Au, Pb, Sr and V (Figure 6-5). However, the more acidic conditions resulted in the acid control oxidising more Cr and Sn than the BLMO tests. A second oxidation of the RAM pins resulted in a higher amount of elements oxidised (Figure 6-6), suggesting that the coating present on the pins was removed by the first oxidation treatment. It was observed that there was a reduction in the effectiveness of BLMO to oxidise Ni and Sn when compared to the acid controls, but these stronger conditions were able to oxidise Au and Co. The final concentration of Cu in the RAM tests was found to be even; however, a green precipitate was formed in the BLMO RAM tests as time progressed (replicate 1 = 0.7647 g, replicate 2 = 1.8367 g). This green precipitate was identified by X-ray Diffraction (Figure 6-7) as the copper hydroxychloride materials atacamite ( $Cu_2(OH)_3Cl$ ) and paratacamite ( $Cu_3(Cu,Zn)(OH)_6Cl_2$ ). This shows that the BLMO tests were more effective than the acid control at oxidising Cu and provides evidence to support the hypothesis of the metals being oxidised by BLMO and then precipitating.

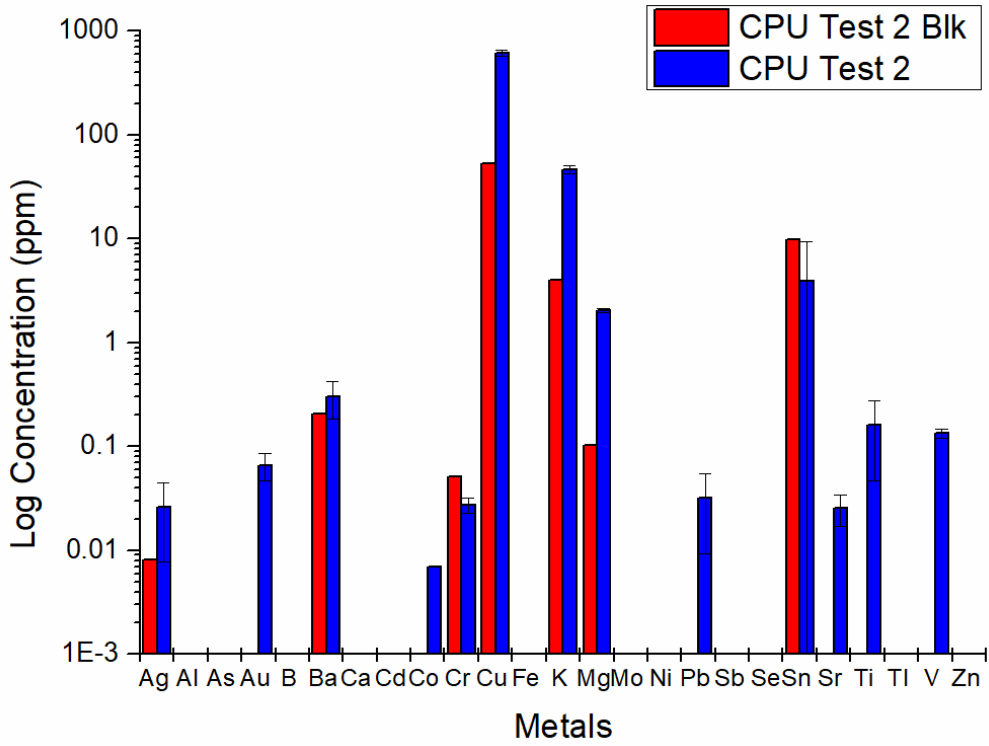


Figure 6-5: Concentration results from a second attempt at oxidising the metals in CPUs with our reaction system. Error bars represent one standard deviation  $n=2$ .

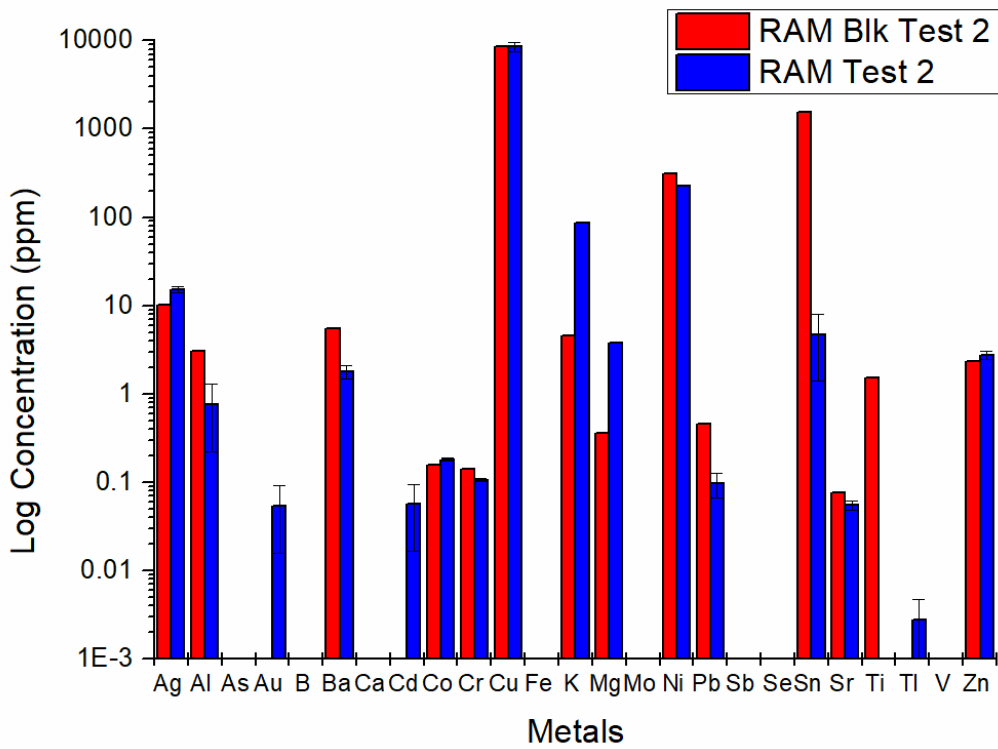


Figure 6-6: Concentration results from a second attempt at oxidising the metals in RAM pins with our reaction system. Error bars represent one standard deviation  $n=2$ .

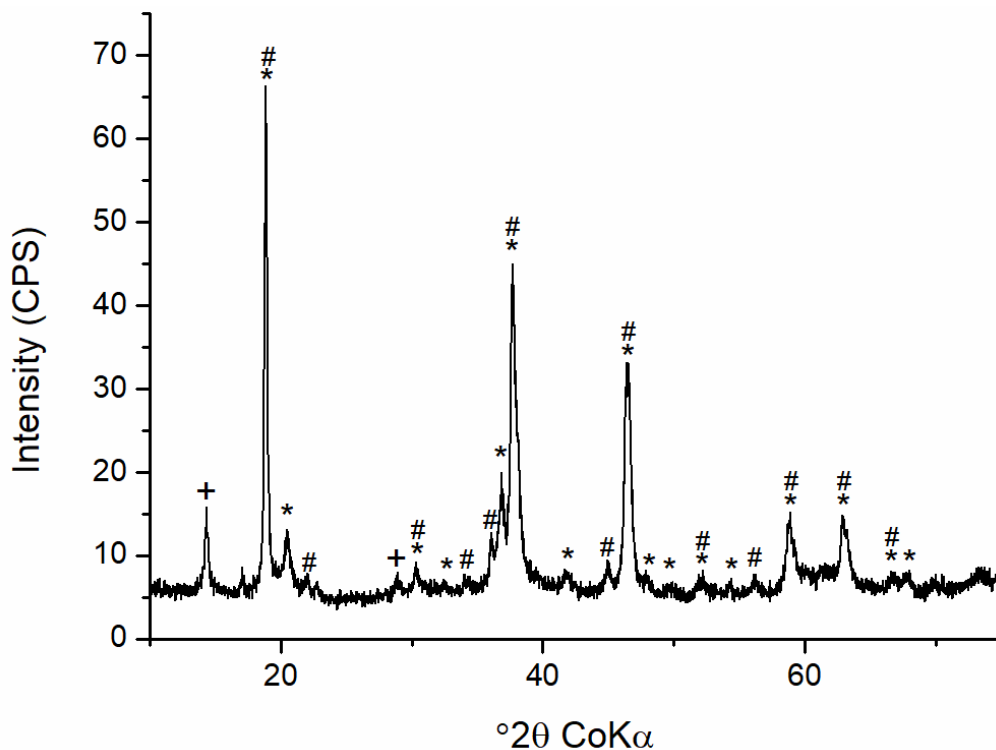


Figure 6-7: CoK $\alpha$  diffraction pattern of green precipitate found in RAM card samples after the second oxidation trial. +BLMO, \*atacamite, #paratacamite

Aqua regia digests of CPUs and RAM pins, were conducted to collect reference data for the concentration of elements present in the computer parts. While a direct comparison can be taken between the BLMO tests and control digests for the CPUs, identical RAM pins were unable to be sourced. To counter this, two different types of RAM pins were used to get a better understanding of the difference between the pins and to get a rough idea of how effective the BLMO tests were. Efficiency comparisons between the BLMO oxidations and the aqua regia digests for the CPUs (Figure 6-8) show that the BLMO system ranges in efficiency. BLMO tests for the elements Ag, Ba and Cu have ~40% efficiency when compared to aqua regia digestion, whereas BLMOs are more effective than the aqua regia digest for Al, Cr, Sr and Zn. In contrast, the BLMO efficiencies for the elements oxidised from RAM pins (Figure 6-9), are ~75% for most elements except Cr, Cu, Sr and Zn which were more effective with BLMO. The BLMO oxidations were found to be not as effective for Au and Sn, which could be due to the sheer amount of metals present in the computer parts outcompeting for the

oxidative ability of the BLMO system. However, the oxidative power of the BLMO system can be improved by increasing the concentration of NaCl, acid and BLMO. The introduction of pre-treatments to remove the easier to oxidise elements such as NaOH or HCl could also be implemented to improve the effectiveness of the BLMO system for gold oxidation.

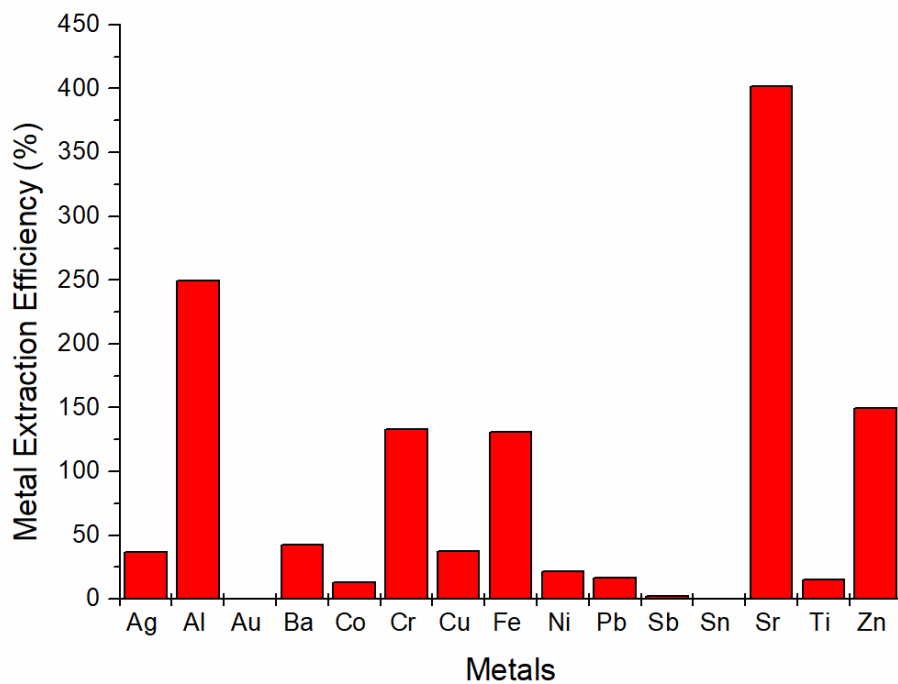


Figure 6-8: Efficiency plots for the metals extracted from CPUs from both BLMO trials.

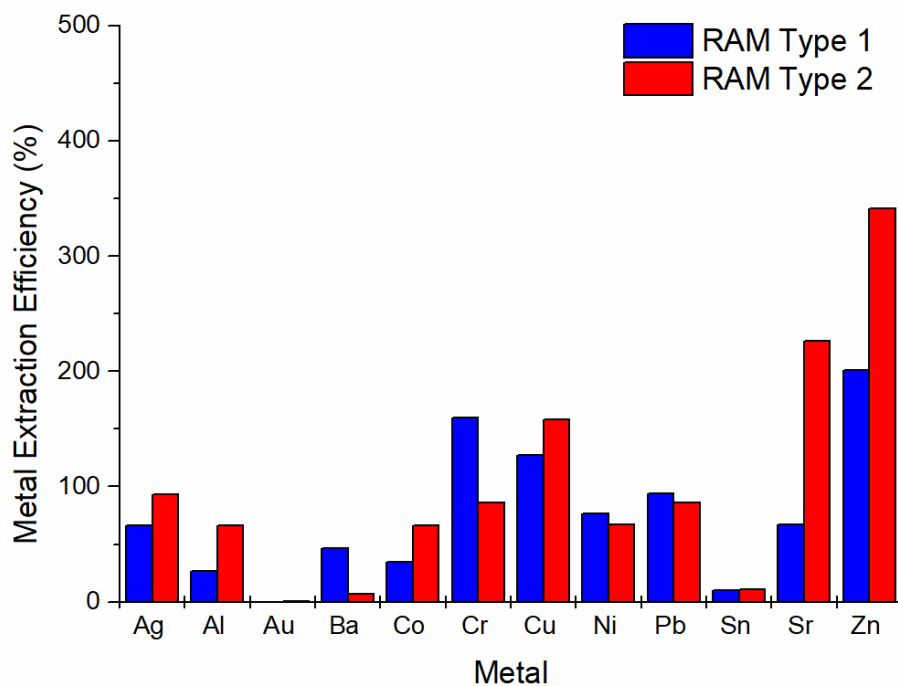


Figure 6-9: Efficiency plots for the metals extracted from RAM pins from both BLMO trials.

## 6.4 Conclusion

In this chapter we have demonstrated that BLMO materials in acidic saline solutions are able to oxidise palladium metal as well as gold and vanadium. Contrastingly, copper, lead, nickel and iron were generated at higher amounts in acidic controls than the BLMO test, suggesting that the BLMO materials inhibits the oxidation of these metals. The precious metals of platinum and rhodium were unable to be oxidised by either the BLMO test or the acidic control. These results were found to follow the trend observed by the corresponding metal chloride salt solubility, with a more soluble chloride salt resulting in more metal oxidised. To investigate this, copper was taken and treated to an alternative BLMO reaction system using a bromine system (NaBr and HBr). It was observed that switching to a bromine-based system doubled the amount of copper dissolved in the BLMO test and reduced the amount of copper oxidised in the acidic control. This reaction system was then extended to a preliminary study investigating the ability of BLMOs to oxidise metals from electronic waste. This study showed that the BLMO reaction system can oxidise metals from e-waste; however, further investigations are necessary to increase its effectiveness towards the recovery of gold from e-waste.

## Chapter 7 Conclusion and Future Work

### 7.1 Conclusions

The aim of this research was to gain an understanding of the effect that the varying crystal structures of birnessite-like manganese oxides have on their ability to oxidise metals. To achieve this thirty-five BLMO materials were synthesised using a combination of different synthesis methods and post synthesis modifications. Chapter 3 describes the synthesis and characterisation of these materials by XRD, subsequent Rietveld refinement, average manganese oxidation state determination and SEM. It was found that the different synthesis methods resulted in materials with different unit cell parameters, levels of stacking order and morphologies. Deeper investigations into the alkaline BLMO synthesis method showed that changes to the aging time and length of post synthesis treatment with 1 M KCl can affect the level of order in the materials. Further investigations into the reproducibility of material synthesis between batches was undertaken showed that even when conducting the synthesis identically, slight differences in the purity and unit cell parameters occur.

Prior to this research, BLMO materials had been reported for the i) oxidation of aqueous metal cations, ii) environmental remediation of heavy metal cations and iii) use as capacitor materials. Chapter 4 presents the new application of oxidising and subsequent dissolution of elemental vanadium using BLMO materials in an acidic saline solution. The materials prepared and characterised in Chapter 3 were investigated for their ability to oxidise vanadium and it was found that BLMOs prepared using different synthesis methods had variable ability to oxidise V(0), and it was also variable between synthesis replicates. It was observed that triclinic BLMOs had the highest variability in the amount of V(0) oxidised and that hexagonal BLMO materials were more consistent and slightly more reactive. This variability in V(0)

oxidation was determined to not be caused by the level of stacking order, unit cell parameters or the average manganese oxidation state. The variability observed was best explained by the stabilising effect of  $K^+$  cations on the layered structure of triclinic BLMOs, which alters the ability of triclinic BLMOs to convert to hexagonal BLMOs in the acidic conditions utilised in this application. It was found that some of the dissolved vanadium is being incorporated into the interlayer space and octahedral sheets of BLMO, however, this should not have a major effect on the material's oxidative ability. Long term experiments over the course of three months observed the formation of the manganese vanadate mineral ansermetite, which is likely formed from the coprecipitation of the dissolved  $Mn^{2+}$  and  $V^{5+}$  generated in this reaction system.

Following on from the study of layered manganese oxide materials, a selection of tunnel structured manganese oxides were synthesised and characterised in Chapter 5. A commercial pyrolustite (1x1), five synthetic cryptomelanes (2x2) and a synthetic todorokite (3x3) were then utilised for the oxidation of V(0) in the same manner as the BLMOs in Chapter 4. It was determined that the different tunnel structure sizes resulted in different amounts of vanadium oxidised and the observe trend was  $1x1 > 2x2 > 3x3$ . The cryptomelane materials were prepared using different synthesis methods and as was seen with BLMOs, the synthesis method resulted in different levels of vanadium oxidised. This potentially could be due to the stabilising effect of incorporated  $K^+$  in the tunnels, which is known to prevent the collapsing of cryptomelane into bixbyite. However, further work is required to investigate these tunnelled materials. The variability with the oxidation of vanadium led to a preliminary investigation into the oxidation of elemental gold by a combination of layered and tunnelled manganese oxide materials. It was found that a general trend existed, where a material that achieved high levels of oxidised vanadium also resulted in high levels of oxidised gold albeit

at a lower concentration due to the difference in the reduction potentials between gold and vanadium. There were two exceptions to this trend, pyrolusite and a disordered BLMO material, which could be due to surface passivation and a greater affinity for absorption, however, further investigations into this area are required.

The ability of BLMO materials to oxidise elemental vanadium and gold in an acidic saline solution led to a preliminary investigation into other metals that can be oxidised. Common metals such as iron, nickel, copper and lead, along with precious metals such as palladium, platinum and rhodium were attempted to be oxidised using the reaction system explored in this research. It was found that BLMO in combination with an acidic saline solution was able to oxidise palladium along with vanadium and gold at higher levels than an acidic saline control. Contrastingly, copper, lead, nickel and iron were generated at higher amounts in the acidic controls than the BLMO test, suggesting that the BLMO materials inhibits the oxidation of these metals. The precious metals of platinum and rhodium were unable to be oxidised by either the BLMO test or the acidic control. The trend observed with the metals able to be oxidised by BLMOs follows the trend observed by the corresponding metal chloride salt solubility, with a more soluble chloride salt resulting in more metal oxidised. To investigate this, copper was taken and treated to an alternative BLMO reaction system using a bromine system (NaBr and HBr) as copper bromides are more soluble than copper chlorides. It was observed that switching to a bromine-based system doubled the amount of copper dissolved in the BLMO test and also reduced the amount of copper oxidised in the acidic control. These results suggest that the reaction system could be altered for the selective dissolution of metals. This work lead to a preliminary investigation into assessing the ability of BLMO materials to recover metals from electronic waste. It was found that this system can oxidise

metals from CPUs and RAM pins however further work is required to adapt this reaction system for the efficient extraction of metals.

## 7.2 Future Work

### 7.2.1 Expansion of manganese oxide materials

Future work investigating the reactivity of BLMOs is necessary to better understand the differences between the reactivity of triclinic and hexagonal BLMOs. This future work should include confirming if hexagonal BLMOs are the more reactive form of BLMOs by investigating a larger sample size of hexagonal BLMOs. Ideally, Hexagonal BLMOs prepared from a selection of different methods should be used, including synthesised by methods that don't include acid in the preparation. For example, Qin *et al.*<sup>266</sup> utilised hydrogen peroxide, whilst Yang *et al.*<sup>267</sup> utilised a reaction between  $Mn^{2+}$  and  $Mn^{7+}$  similar to the preparation of triclinic BLMO used here. It is also known that hexagonal BLMO can be produced by several bacteria, such as *Leptothrix discophora*<sup>268</sup>, which may give insight into the ability of biogenically produced manganese dioxide behaves in the environment. An investigation also needs to be conducted into the ability of other manganese oxides such as hausmannite and bixbyite to oxidise metals in this reaction system, due to the potential of these being intermediate phases present during the collapse of cryptomelane materials. Furthermore, increasing the quantity and variety of tunnelled manganese oxides investigated would aid in clarifying the trends observed for the oxidation of vanadium.

### 7.2.2 Stabilisation effect of $K^+$ on cryptomelane materials

It was determined that the  $K^+$  stabilisation present in layered manganese oxides results in a decrease in the amount of vanadium oxidised. However, the preliminary investigation into tunnelled structures suggests that  $K^+$  stabilisation may be beneficial for the reactivity of cryptomelane materials. Further studies into the phase transformations occurring in the

reaction system both for the layered structures and the tunnelled structures are required to gain a further understanding of the mechanism behind the oxidation of vanadium. Quantitative analysis of the potassium/sodium content in the manganese materials would also be useful to gain an indication as to the level of stability and its correlation to the potassium content.

### 7.2.3 Confirming the production of chlorine

It has been proposed that the reaction of manganese oxides in acidic saline solutions produces dissolved chlorine that subsequently dissociates into hypochlorous acid, and that these are the reactive agents involved in the oxidation of metals. However, the production of chlorine is difficult to prove through chemical means due to the presence of high levels of chloride ions in the solution. The speciation of chlorine molecules (chloride, chlorite and chlorate) has been achieved by Raman spectroscopy in aqueous solutions<sup>269</sup> and ion chromatography in both water<sup>270</sup> and blood matrices<sup>271</sup>. These techniques could be useful in the determination of the chlorine speciation and for potential real time analysis of the reaction system.

### 7.2.4 Determinations of reaction rates for different metals

The successful oxidation of gold, vanadium and palladium with a chloride-based reaction system and the oxidation of copper with the bromide-based system shows the variety in the metals able to be oxidised and dissolved. The expansion of this work to electronic waste showed that there is variability in the amount of each metal oxidised, therefore further work investigating the kinetic rates of dissolution for several metals needs to be conducted. It would also be worthwhile investigating the differences in reaction rates for the different reaction systems that are possible to gain an understanding of what procedures should be used for specific metals.

### 7.2.5 Further exploration into metal recovery from electronic waste

Preliminary extractions of metals from CPU and RAM pins has been achieved with the BLMO reaction system, however further investigations are required to increase the efficiency of extracting metals from these computer parts. Deeper investigations will also need to be conducted on the extraction from other electronic waste, such as phone circuits, monitor circuitry and motherboards from larger e-waste. Once the efficient and potentially selective extraction of metals from these sources of electronic waste has been achieved, studies will be required to investigate the separation and recovery of the metals from the reaction solutions.

## Chapter 8 References

1. Post, J. E., Manganese oxide minerals: Crystal structures and economic and environmental significance. *Proceedings of the National Academy of Sciences* **1999**, *96* (7), 3447-3454.
2. Taylor, R., The association of manganese and cobalt in soils—further observations. *Journal of Soil Science* **1968**, *19* (1), 77-80.
3. Jones, L.; Milne, A. A., Birnessite, a new manganese oxide mineral from Aberdeenshire, Scotland. *Mineralogical Magazine and Journal of the Mineralogical Society* **1956**, *31* (235), 283-288.
4. Weaver, R. M.; Hochella Jr, M. F., The reactivity of seven Mn-oxides with Cr<sup>3+</sup> aq: A comparative analysis of a complex, environmentally important redox reaction. *American Mineralogist* **2003**, *88* (11-12), 2016-2027.
5. Post, J. E.; Veblen, D. R., Crystal structure determinations of synthetic sodium, magnesium, and potassium birnessite using TEM and the Rietveld method. *American Mineralogist* **1990**, *75* (5-6), 477-489.
6. Post, J. E.; Heaney, P. J.; Hanson, J., Rietveld refinement of a triclinic structure for synthetic Na-birnessite using synchrotron powder diffraction data. *Powder Diffraction* **2002**, *17* (3), 218-221.
7. Post, J. E.; Heaney, P. J.; Ertl, A., Rietveld refinement of the ranciéite structure using synchrotron powder diffraction data. *Powder Diffraction* **2008**, *23* (1), 10-14.
8. Fleeger, C. R.; Heaney, P. J.; Post, J. E., A time-resolved X-ray diffraction study of Cs exchange into hexagonal H-birnessite. *American Mineralogist* **2013**, *98* (4), 671-679.
9. Li, Y. R.; Marschilok, A. C.; Takeuchi, E. S.; Takeuchi, K. J., Synthesis of Copper Birnessite, CuxMnOy·nH<sub>2</sub>O with Crystallite Size Control: Impact of Crystallite Size on Electrochemistry. *Journal of The Electrochemical Society* **2016**, *163* (2), A281-A285.
10. Zhu, M.; Ginder-Vogel, M.; Sparks, D. L., Ni (II) sorption on biogenic Mn-oxides with varying Mn octahedral layer structure. *Environmental science & technology* **2010**, *44* (12), 4472-4478.
11. Lucht, K. P.; Mendoza-Cortes, J. L., Birnessite: A Layered Manganese Oxide to Capture Sunlight for Water-Splitting Catalysis. *Journal of Physical Chemistry C* **2015**, *119* (40), 22838-22846.
12. McKenzie, R., The synthesis of birnessite, cryptomelane, and some other oxides and hydroxides of manganese. *Mineralogical Magazine* **1971**, *38* (296), 493-502.
13. Chen, R.; Zavalij, P.; Whittingham, M. S., Hydrothermal Synthesis and Characterization of KxMnO<sub>2</sub>·yH<sub>2</sub>O. *Chemistry of Materials* **1996**, *8* (6), 1275-1280.
14. Ching, S.; Petrovay, D. J.; Jorgensen, M. L.; Suib, S. L., Sol-gel synthesis of layered birnessite-type manganese oxides. *Inorganic Chemistry* **1997**, *36* (5), 883-890.
15. Zhang, X.; Yu, P.; Zhang, H.; Zhang, D.; Sun, X.; Ma, Y., Rapid hydrothermal synthesis of hierarchical nanostructures assembled from ultrathin birnessite-type MnO<sub>2</sub> nanosheets for supercapacitor applications. *Electrochimica Acta* **2013**, *89*, 523-529.
16. Ming, B.; Li, J.; Kang, F.; Pang, G.; Zhang, Y.; Chen, L.; Xu, J.; Wang, X., Microwave-hydrothermal synthesis of birnessite-type MnO<sub>2</sub> nanospheres as supercapacitor electrode materials. *Journal of Power Sources* **2012**, *198*, 428-431.
17. Subramanian, V.; Zhu, H.; Wei, B., Nanostructured MnO<sub>2</sub>: Hydrothermal synthesis and electrochemical properties as a supercapacitor electrode material. *Journal of Power Sources* **2006**, *159* (1), 361-364.
18. Ziller, S.; Von Bülow, J. F.; Dahl, S.; Lindén, M., A fast sol-gel synthesis leading to highly crystalline birnessites under non-hydrothermal conditions. *Dalton Transactions* **2017**, *46* (14), 4582-4588.
19. Ma, Y.; Luo, J.; Suib, S. L., Syntheses of birnessites using alcohols as reducing reagents: Effects of synthesis parameters on the formation of birnessites. *Chemistry of Materials* **1999**, *11* (8), 1972-1979.
20. Händel, M.; Rennert, T.; Totsche, K. U., A simple method to synthesize birnessite at ambient pressure and temperature. *Geoderma* **2013**, *193-194*, 117-121.
21. Shen, X. F.; Ding, Y. S.; Liu, J.; Cai, J.; Laubernds, K.; Zenger, R. P.; Vasiliev, A.; Aindow, M.; Suib, S. L., Control of Nanometer-Scale Tunnel Sizes of Porous Manganese Oxide Octahedral Molecular Sieve Nanomaterials. *Advanced Materials* **2005**, *17* (7), 805-809.
22. Bach, S.; Pereira-Ramos, J. P.; Baffier, N.; Messina, R., Birnessite manganese dioxide synthesized via a sol-gel process: a new rechargeable cathodic material for lithium batteries. *Electrochimica Acta* **1991**, *36* (10), 1595-1603.
23. Sabri, M.; King, H. J.; Gummow, R. J.; Lu, X.; Zhao, C.; Oelgemöller, M.; Chang, S. L.; Hocking, R. K., Oxidant or Catalyst for Oxidation? A Study of How Structure and Disorder Change the Selectivity for Direct versus Catalytic Oxidation Mediated by Manganese (III, IV) Oxides. *Chemistry of Materials* **2018**, *30* (22), 8244-8256.

24. Gaillot, A.-C.; Lanson, B.; Drits, V. A., Structure of Birnessite Obtained from Decomposition of Permanganate under Soft Hydrothermal Conditions. 1. Chemical and Structural Evolution as a Function of Temperature. *Chemistry of Materials* **2005**, *17* (11), 2959-2975.
25. Fleischer, M.; Richmond, W. E., The manganese oxide minerals, a preliminary report. *Economic Geology* **1943**, *38* (4), 269-286.
26. Bricker, O., Some stability relations in the system Mn-O<sub>2</sub>-H<sub>2</sub>O at 25 and one atmosphere total pressure. *American Mineralogist: Journal of Earth and Planetary Materials* **1965**, *50* (9), 1296-1354.
27. Feng, X.; Tan, W.; Liu, F.; Huang, Q.; Liu, X., Pathways of birnessite formation in alkali medium. *Science in China Series D: Earth Sciences* **2005**, *48* (9), 1438-1451.
28. Yang, D. S.; Wang, M. K., Syntheses and Characterization of Well-Crystallized Birnessite. *Chemistry of Materials* **2001**, *13* (8), 2589-2594.
29. Villalobos, M.; Escobar-Quiroz, I. N.; Salazar-Camacho, C., The influence of particle size and structure on the sorption and oxidation behavior of birnessite: I. Adsorption of As(V) and oxidation of As(III). *Geochimica et Cosmochimica Acta* **2014**, *125*, 564-581.
30. Lu, H.; Zhang, W.; Tao, L.; Liu, F.; Zhang, J., Enhanced removal of antimony by acid birnessite with doped iron ions: Accompanied by the structural transformation. *Chemosphere* **2019**, *226*, 834-840.
31. Della Puppa, L.; Komárek, M.; Bordas, F.; Bollinger, J.-C.; Joussein, E., Adsorption of copper, cadmium, lead and zinc onto a synthetic manganese oxide. *Journal of Colloid and Interface Science* **2013**, *399*, 99-106.
32. Hou, J.; Xiang, Y.; Zheng, D.; Li, Y.; Xue, S.; Wu, C.; Hartley, W.; Tan, W., Morphology-dependent enhancement of arsenite oxidation to arsenate on birnessite-type manganese oxide. *Chemical Engineering Journal* **2017**, *327*, 235-243.
33. Ling, F. T.; Post, J. E.; Heaney, P. J.; Ilton, E. S., The relationship between Mn oxidation state and structure in triclinic and hexagonal birnessites. *Chemical Geology* **2018**, *479*, 216-227.
34. Zhu, Y.; Liang, X.; Zhao, H.; Yin, H.; Liu, M.; Liu, F.; Feng, X., Rapid determination of the Mn average oxidation state of Mn oxides with a novel two-step colorimetric method. *Analytical Methods* **2017**, *9* (1), 103-109.
35. Chalmin, E.; Farges, F.; Brown, G. E., A pre-edge analysis of Mn K-edge XANES spectra to help determine the speciation of manganese in minerals and glasses. *Contributions to Mineralogy and Petrology* **2009**, *157* (1), 111-126.
36. Kovács, K. A.; Gróf, P.; Burai, L.; Riedel, M., Revising the Mechanism of the Permanganate/Oxalate Reaction. *The Journal of Physical Chemistry A* **2004**, *108* (50), 11026-11031.
37. Ilton, E. S.; Post, J. E.; Heaney, P. J.; Ling, F. T.; Kerisit, S. N., XPS determination of Mn oxidation states in Mn (hydr)oxides. *Applied Surface Science* **2016**, *366*, 475-485.
38. Manceau, A.; Marcus, M. A.; Grangeon, S., Determination of Mn valence states in mixed-valent manganates by XANES spectroscopy. *American Mineralogist* **2012**, *97* (5-6), 816-827.
39. Atkins, P. W.; De Paula, J., *Atkins' physical chemistry*. 7th ed.; Oxford university press: USA, 2002.
40. Bianconi, A., Surface X-ray absorption spectroscopy: Surface EXAFS and surface XANES. *Applications of Surface Science* **1980**, *6* (3), 392-418.
41. Xiao, W.; Wang, D.; Lou, X. W., Shape-controlled synthesis of MnO<sub>2</sub> nanostructures with enhanced electrocatalytic activity for oxygen reduction. *The Journal of Physical Chemistry C* **2009**, *114* (3), 1694-1700.
42. Luo, J.; Huang, A.; Park, S. H.; Suib, S. L.; O'Young, C.-L., Crystallization of Sodium- Birnessite and Accompanied Phase Transformation. *Chemistry of materials* **1998**, *10* (6), 1561-1568.
43. Liu, S.; Fan, C.-Z.; Zhang, Y.; Li, C.-H.; You, X.-Z., Low-temperature synthesis of Na<sub>2</sub>Mn<sub>5</sub>O<sub>10</sub> for supercapacitor applications. *Journal of Power Sources* **2011**, *196* (23), 10502-10506.
44. Sakai, N.; Ebina, Y.; Takada, K.; Sasaki, T., Photocurrent generation from semiconducting manganese oxide nanosheets in response to visible light. *The Journal of Physical Chemistry B* **2005**, *109* (19), 9651-9655.
45. Nakayama, M.; Kanaya, T.; Lee, J.-W.; Popov, B. N., Electrochemical synthesis of birnessite-type layered manganese oxides for rechargeable lithium batteries. *Journal of Power Sources* **2008**, *179* (1), 361-366.
46. Nam, K. W.; Kim, S.; Lee, S.; Salama, M.; Shterenberg, I.; Gofer, Y.; Kim, J. S.; Yang, E.; Park, C. S.; Kim, J. S.; Lee, S. S.; Chang, W. S.; Doo, S. G.; Jo, Y. N.; Jung, Y.; Aurbach, D.; Choi, J. W., The High Performance of Crystal Water Containing Manganese Birnessite Cathodes for Magnesium Batteries. *Nano Letters* **2015**, *15* (6), 4071-4079.
47. Ogata, A.; Komaba, S.; Baddour-Hadjean, R.; Pereira-Ramos, J. P.; Kumagai, N., Doping effects on structure and electrode performance of K-birnessite-type manganese dioxides for rechargeable lithium battery. *Electrochimica Acta* **2008**, *53* (7), 3084-3093.
48. Yin, H.; Feng, X.; Qiu, G.; Tan, W.; Liu, F., Characterization of Co-doped birnessites and application for removal of lead and arsenite. *Journal of Hazardous Materials* **2011**, *188* (1-3), 341-349.

49. Feng, L. L.; Wang, J.; Han, X.; Wang, H. B., Oxidation of formaldehyde over birnessite-type manganese oxides at room-temperature. *Materials Science Forum* **2016**, *852*, 547-550.
50. Lin, H.; Chen, D.; Liu, H.; Zou, X.; Chen, T., Effect of MnO<sub>2</sub> crystalline structure on the catalytic oxidation of formaldehyde. *Aerosol and Air Quality Research* **2017**, *17* (4), 1011-1020.
51. Liu, L.; Tian, H.; He, J.; Wang, D.; Yang, Q., Preparation of birnessite-supported Pt nanoparticles and their application in catalytic oxidation of formaldehyde. *Journal of Environmental Sciences (China)* **2012**, *24* (6), 1117-1124.
52. Pei, J.; Han, X.; Lu, Y., Performance and kinetics of catalytic oxidation of formaldehyde over copper manganese oxide catalyst. *Building and Environment* **2015**, *84*, 134-141.
53. Tian, H.; He, J., Research progress in catalytic oxidation of formaldehyde by manganese oxides. *Chemistry Bulletin / Huaxue Tongbao* **2013**, *76* (2), 100-106.
54. Tian, H.; He, J.; Liu, L.; Wang, D.; Hao, Z.; Ma, C., Highly active manganese oxide catalysts for low-temperature oxidation of formaldehyde. *Microporous and Mesoporous Materials* **2012**, *151*, 397-402.
55. Wang, J.; Li, D.; Li, P.; Zhang, P.; Xu, Q.; Yu, J., Layered manganese oxides for formaldehyde-oxidation at room temperature: The effect of interlayer cations. *RSC Advances* **2015**, *5* (122), 100434-100442.
56. Wang, J.; Li, J.; Jiang, C.; Zhou, P.; Zhang, P.; Yu, J., The effect of manganese vacancy in birnessite-type MnO<sub>2</sub> on room-temperature oxidation of formaldehyde in air. *Applied Catalysis B: Environmental* **2017**, *204*, 147-155.
57. Wang, J.; Zhang, G.; Zhang, P., Layered birnessite-type MnO<sub>2</sub> with surface pits for enhanced catalytic formaldehyde oxidation activity. *Journal of Materials Chemistry A* **2017**, *5* (12), 5719-5725.
58. Wang, J.; Zhang, P.; Li, J.; Jiang, C.; Yunus, R.; Kim, J., Room-Temperature Oxidation of Formaldehyde by Layered Manganese Oxide: Effect of Water. *Environmental Science and Technology* **2015**, *49* (20), 12372-12379.
59. Zhu, L.; Wang, J.; Rong, S.; Wang, H.; Zhang, P., Cerium modified birnessite-type MnO<sub>2</sub> for gaseous formaldehyde oxidation at low temperature. *Applied Catalysis B: Environmental* **2017**, *211*, 212-221.
60. Fu, Z.; Liu, L.; Song, Y.; Ye, Q.; Cheng, S.; Kang, T.; Dai, H., Catalytic oxidation of carbon monoxide, toluene, and ethyl acetate over the xPd/OMS-2 catalysts: Effect of Pd loading. *Frontiers of Chemical Science and Engineering* **2017**, *11* (2), 185-196.
61. Fu, Z. D.; Zang, J. X.; Ye, Q.; Cheng, S. Y.; Kang, T. F., Cu-doped octahedral layered birnessites catalysts for the catalytic oxidation of CO and ethyl acetate. *Wuli Huaxue Xuebao/ Acta Physico - Chimica Sinica* **2017**, *33* (9), 1855-1864.
62. Gandhe, A. R.; Rebello, J. S.; Figueiredo, J. L.; Fernandes, J. B., Manganese oxide OMS-2 as an effective catalyst for total oxidation of ethyl acetate. *Applied Catalysis B: Environmental* **2007**, *72* (1-2), 129-135.
63. Santos, V. P.; Pereira, M. F. R.; Órfao, J. J. M.; Figueiredo, J. L., Synthesis and characterization of manganese oxide catalysts for the total oxidation of ethyl acetate. *Topics in Catalysis* **2009**, *52* (5), 470-481.
64. De Luna, M. D.; Millanar, J. M.; Yodsa-Nga, A.; Wantala, K., Gas phase catalytic oxidation of VOCS using hydrothermally synthesized nest-like K-OMS 2 catalyst. *Sains Malaysiana* **2017**, *46* (2), 275-283.
65. Einaga, H.; Ogata, A., Benzene oxidation with ozone over supported manganese oxide catalysts: Effect of catalyst support and reaction conditions. *Journal of Hazardous Materials* **2009**, *164* (2-3), 1236-1241.
66. Genuino, H. C.; Dharmarathna, S.; Njagi, E. C.; Mei, M. C.; Suib, S. L., Gas-phase total oxidation of benzene, toluene, ethylbenzene, and xylenes using shape-selective manganese oxide and copper manganese oxide catalysts. *Journal of Physical Chemistry C* **2012**, *116* (22), 12066-12078.
67. Li, D. Y.; Liu, H. D.; Chen, Y. F., Synthesis of manganese oxide octahedral molecular sieve and their application in catalytic oxidation of benzene. *Huanjing Kexue/Environmental Science* **2011**, *32* (12), 3657-3661.
68. Li, J.; Li, L.; Cheng, W.; Wu, F.; Lu, X.; Li, Z., Controlled synthesis of diverse manganese oxide-based catalysts for complete oxidation of toluene and carbon monoxide. *Chemical Engineering Journal* **2014**, *244*, 59-67.
69. Li, X. Q.; Yang, L. F., Liquid-phase oxidation of toluene to benzoic acid over manganese oxide catalyst. *Advanced Materials Research* **2013**, *750-752*, 1822-1825.
70. Sihaib, Z.; Puleo, F.; Garcia-Vargas, J. M.; Retailleau, L.; Descorme, C.; Liotta, L. F.; Valverde, J. L.; Gil, S.; Giroir-Fendler, A., Manganese oxide-based catalysts for toluene oxidation. *Applied Catalysis B: Environmental* **2017**, *209*, 689-700.
71. Sun, H.; Chen, S.; Wang, P.; Quan, X., Catalytic oxidation of toluene over manganese oxide octahedral molecular sieves (OMS-2) synthesized by different methods. *Chemical Engineering Journal* **2011**, *178*, 191-196.
72. Xie, J.; Chen, L.; Zhou, W. F.; Au, C. T.; Yin, S. F., Selective oxidation of p-chlorotoluene to p-chlorobenzaldehyde over metal-modified OMS-2 molecular sieves. *Journal of Molecular Catalysis A: Chemical* **2016**, *425*, 110-115.

73. Ye, Q.; Lu, H.; Zhao, J.; Cheng, S.; Kang, T.; Wang, D.; Dai, H., A comparative investigation on catalytic oxidation of CO, benzene, and toluene over birnessites derived from different routes. *Applied Surface Science* **2014**, *317*, 892-901.
74. Zhang, T.; Deng, Y. Q.; Zhou, W. F.; Au, C. T.; Yin, S. F., Selective oxidation of p-chlorotoluene to p-chlorobenzaldehyde with molecular oxygen over zirconium-doped manganese oxide materials. *Chemical Engineering Journal* **2014**, *240*, 509-515.
75. Banerjee, D.; Nesbitt, H. W., Oxidation of aqueous Cr(III) at birnessite surfaces: Constraints on reaction mechanism. *Geochimica et Cosmochimica Acta* **1999**, *63* (11-12), 1671-1687.
76. Zhong, L.; Yang, J.; Liu, L.; Xing, B., Oxidation of Cr(III) on birnessite surfaces: The effect of goethite and kaolinite. *Journal of Environmental Sciences (China)* **2015**, *37*, 8-14.
77. Kim, J. G.; Dixon, J. B.; Chusuei, C. C.; Deng, Y., Oxidation of chromium (III) to (VI) by manganese oxides. *Soil Science Society of America Journal* **2002**, *66* (1), 306-315.
78. Feng, X. H.; Zhai, L. M.; Tan, W. F.; Zhao, W.; Liu, F.; He, J. Z., The controlling effect of pH on oxidation of Cr(III) by manganese oxide minerals. *Journal of Colloid and Interface Science* **2006**, *298* (1), 258-266.
79. Feng, X. H.; Zu, Y. Q.; Tan, W. F.; Liu, F., Arsenite oxidation by three types of manganese oxides. *Journal of Environmental Sciences* **2006**, *18* (2), 292-298.
80. Lafferty, B. J.; Ginder-Vogel, M.; Sparks, D. L., Arsenite oxidation by a poorly crystalline manganese-oxide 1. stirred-flow experiments. *Environmental Science and Technology* **2010**, *44* (22), 8460-8466.
81. Wang, N.; Liang, C.; Du, L.; Cui, H., Arsenite sorption and oxidation by synthetic birnessite. *Journal of Water Supply: Research and Technology - AQUA* **2013**, *62* (4), 245-253.
82. Ta, C.; Brugger, J.; Pring, A.; Hocking, R. K.; Lenehan, C. E.; Reith, F., Effect of manganese oxide minerals and complexes on gold mobilization and speciation. *Chemical Geology* **2015**, *407-408*, 10-20.
83. Bartle, J. Investigating the Modes of Solubilisation of Au(0) in the Environment Honours, Flinders University, Adelaide, 2016.
84. Emmons, W. H., The agency of manganese in the superficial alteration and secondary enrichment of gold deposits. *The Journal of Geology* **1911**, *19* (1), 15-46.
85. Boyle, R. W., *The geochemistry of gold and its deposits (together with a chapter on geochemical prospecting for the element)*. Unipub: 1979.
86. Post, J. E.; Bish, D. L., Rietveld refinement of the todorokite structure. *American Mineralogist* **1988**, *73* (7-8), 861-869.
87. Vicat, J.; Fanchon, E.; Strobel, P.; Tran Qui, D., The structure of K1. 33Mn8O16 and cation ordering in hollandite-type structures. *Acta Crystallographica Section B: Structural Science* **1986**, *42* (2), 162-167.
88. Wyckoff, R., *Crystal Structures*. 2nd ed.; 1963; Vol. 1.
89. Baur, W. H., Rutile-type compounds. V. Refinement of MnO<sub>2</sub> and MgF<sub>2</sub>. *Acta Crystallographica Section B: Structural Crystallography and Crystal Chemistry* **1976**, *32* (7), 2200-2204.
90. Rossouw, M.; Liles, D.; Thackeray, M.; David, W.; Hull, S., Alpha manganese dioxide for lithium batteries: A structural and electrochemical study. *Materials research bulletin* **1992**, *27* (2), 221-230.
91. Frondel, C.; Marvin, U.; Ito, J., New occurrences of todorokite. *American Mineralogist: Journal of Earth and Planetary Materials* **1960**, *45* (11-12), 1167-1173.
92. Opembe, N. N.; Guild, C.; King'Ondu, C.; Nelson, N. C.; Slowing, I. I.; Suib, S. L., Vapor-phase oxidation of benzyl alcohol using manganese oxide octahedral molecular sieves (OMS-2). *Industrial and Engineering Chemistry Research* **2014**, *53* (49), 19044-19051.
93. Genuino, H. C.; Dharmarathna, S.; Njagi, E. C.; Mei, M. C.; Suib, S. L., Gas-phase total oxidation of benzene, toluene, ethylbenzene, and xylenes using shape-selective manganese oxide and copper manganese oxide catalysts. *The Journal of Physical Chemistry C* **2012**, *116* (22), 12066-12078.
94. Son, Y. C.; Makwana, V. D.; Howell, A. R.; Suib, S. L., Efficient, catalytic, aerobic oxidation of alcohols with octahedral molecular sieves. *Angewandte Chemie International Edition* **2001**, *40* (22), 4280-4283.
95. Luo, S.; Duan, L.; Sun, B.; Wei, M.; Li, X.; Xu, A., Manganese oxide octahedral molecular sieve (OMS-2) as an effective catalyst for degradation of organic dyes in aqueous solutions in the presence of peroxymonosulfate. *Applied Catalysis B: Environmental* **2015**, *164*, 92-99.
96. Hou, J.; Luo, J.; Hu, Z.; Li, Y.; Mao, M.; Song, S.; Liao, Q.; Li, Q., Tremendous effect of oxygen vacancy defects on the oxidation of arsenite to arsenate on cryptomelane-type manganese oxide. *Chemical Engineering Journal* **2016**, *306*, 506-606.
97. Liu, Y.; Zhang, F.; Hou, J.; Hartley, W., Peroxymonosulfate Improves the Activity and Stability of Manganese Oxide for Oxidation of Arsenite to Arsenate. *CLEAN – Soil, Air, Water* **2020**, *48* (2), 1900195.
98. Cotton, A. F.; Wilkinson, G.; Bochmann, M.; Murillo, C. A., *Advanced Inorganic Chemistry*. Wiley: 1999.

99. Greenwood, N. N.; Earnshaw, A., *Chemistry of the Elements*. A. Wheaton and Co. Ltd: Great Britain, 1984.
100. Emsley, J., *Nature's building blocks: an AZ guide to the elements*. Oxford University Press: 2011.
101. Jung, M. C., Contamination by Cd, Cu, Pb, and Zn in mine wastes from abandoned metal mines classified as mineralization types in Korea. *Environmental Geochemistry and Health* **2008**, *30* (3), 205-217.
102. Peacey, J. G.; Davenport, W. G., *The iron blast furnace: theory and practice*. Elsevier: 2016.
103. Hind, A. R.; Bhargava, S. K.; Grocott, S. C., The surface chemistry of Bayer process solids: a review. *Colloids and Surfaces A: Physicochemical and Engineering Aspects* **1999**, *146* (1), 359-374.
104. Palmer, F. M., Process and apparatus for smelting aluminum. Google Patents: 2005.
105. Mellor, J. W., *A comprehensive treatise on inorganic and theoretical chemistry-Cu, Ag, Au, Ca, Sr and Ba*. Longmans, Green and Company: 1923; Vol. 3.
106. Aylmore, M. G.; Muir, D. M., Thiosulfate leaching of gold—a review. *Minerals engineering* **2001**, *14* (2), 135-174.
107. Grosse, A. C.; Dicoski, G. W.; Shaw, M. J.; Haddad, P. R., Leaching and recovery of gold using ammoniacal thiosulfate leach liquors (a review). *Hydrometallurgy* **2003**, *69* (1), 1-21.
108. Li, J.; Miller, J. D., A review of gold leaching in acid thiourea solutions. *Mineral Processing and Extractive Metallurgy Review* **2006**, *27* (3), 177-214.
109. Mpinga, C.; Eksteen, J.; Aldrich, C.; Dyer, L., Direct leach approaches to Platinum Group Metal (PGM) ores and concentrates: A review. *Minerals Engineering* **2015**, *78*, 93-113.
110. Syed, S., Recovery of gold from secondary sources—a review. *Hydrometallurgy* **2012**, *115*, 30-51.
111. Sparrow, G. J.; Woodcock, J. T., Cyanide and other lixiviant leaching systems for gold with some practical applications. *Mineral Processing and Extractive Metallurgy Review* **1995**, *14* (3-4), 193-247.
112. De Lacerda, L. D.; Salomons, W., *Mercury from gold and silver mining: a chemical time bomb?* Springer Science & Business Media: 2012.
113. Veiga, M. M.; Maxson, P. A.; Hylander, L. D., Origin and consumption of mercury in small-scale gold mining. *Journal of Cleaner Production* **2006**, *14* (3), 436-447.
114. Assessment, U. G. M., Sources, Emissions, Releases and Environmental Transport. *UNEP Chemicals Branch, Geneva, Switzerland* **2013**, 42.
115. Langford, N.; Ferner, R., Toxicity of mercury. *Journal of human hypertension* **1999**, *13* (10).
116. Williams, G., The cyanides of gold. *Gold Bulletin* **1978**, *11* (2), 56-59.
117. John MacArthur; Robert Forrest; William Forrest Process of Obtaining Gold and Silver from Ores. US403202, 1887.
118. Marsden, J.; House, I., *The chemistry of gold extraction*. SME: 2006.
119. Wright, I. H.; Vesey, C. J., Acute poisoning with gold cyanide. *Anaesthesia* **1986**, *41* (9), 936-939.
120. Organization, W. H., Hydrogen cyanide and cyanides: Human health aspects. *Concise international chemical assessment document* **2004**, 61.
121. Kondos, P.; Deschenes, G.; Morrison, R., Process optimization studies in gold cyanidation. *Hydrometallurgy* **1995**, *39* (1-3), 235-250.
122. Deschenes, G., Advances in the cyanidation of gold. *Developments in Mineral Processing* **2005**, *15*, 479-500.
123. Deschenes, G.; Lastra, R.; Brown, J.; Jin, S.; May, O.; Ghali, E., Effect of lead nitrate on cyanidation of gold ores: progress on the study of the mechanisms. *Minerals Engineering* **2000**, *13* (12), 1263-1279.
124. Nunan, T. O.; Viana, I. L.; Peixoto, G. C.; Ernesto, H.; Verster, D. M.; Pereira, J. H.; Bonfatti, J. M.; Cesar Teixeira, L. A., Improvements in gold ore cyanidation by pre-oxidation with hydrogen peroxide. *Minerals Engineering* **2017**, *108*, 67-70.
125. Mubarok, M. Z.; Winarko, R.; Chaerun, S. K.; Rizki, I. N.; Ichlas, Z. T., Improving gold recovery from refractory gold ores through biooxidation using iron-sulfur-oxidizing/sulfur-oxidizing mixotrophic bacteria. *Hydrometallurgy* **2017**, *168*, 69-75.
126. McInnes, C.; Sparrow, G.; Woodcock, J., Extraction of platinum, palladium and gold by cyanidation of Coronation Hill ore. *Hydrometallurgy* **1994**, *35* (2), 141-159.
127. Kappes, D., Heap leaching of gold and silver ores. *Developments in Mineral Processing* **2005**, *15*, 456-478.
128. Akcil, A.; Mudder, T., Microbial destruction of cyanide wastes in gold mining: process review. *Biotechnology Letters* **2003**, *25* (6), 445-450.
129. McNulty, T., Cyanide substitutes. *Mining Magazine* 2001, 2001, p 256.
130. White, H. A., The solubility of gold in thiosulphates and thiocyanates. *South African Journal of Science* **1905**, *1* (1), 211-215.

131. Berezowsky, R. M. G. S.; Sefton, V. B. In *Recovery of gold and silver from oxidation leach residues by ammoniacal thiosulphate leaching*, 108th AIME Annual Meeting New Orleans, New Orleans, 1979; pp 17-34.
132. Brent Hiskey, J.; Atluri, V., Dissolution chemistry of gold and silver in different lixivants. *Mineral Processing and Extractive Metallurgy Review* **1988**, 4 (1-2), 95-134.
133. Ter-Arakelyan, K., On technological expediency of sodium thiosulphate usage for gold extraction from raw material. *Izv. V. U. Z. Tsvetn. Metall.* **1984**, (5), 72-76.
134. Tripathi, A.; Kumar, M.; Sau, D.; Agrawal, A.; Chakravarty, S.; Mankhand, T., Leaching of gold from the waste mobile phone printed circuit boards (PCBs) with ammonium thiosulphate. *International Journal of Metallurgical Engineering* **2012**, 1 (2), 17-21.
135. Feng, D.; van Deventer, J. S. J., Ammoniacal thiosulphate leaching of gold in the presence of pyrite. *Hydrometallurgy* **2006**, 82 (3-4), 126-132.
136. Adams, M., Liddell, K.S., Smith, L.A. In *The KellGold hydrometallurgical process for cyanide-free extraction of gold from refractory concentrates and feedstocks—a preliminary assessment*, World Gold 2015, Johannesburg, South Africa, The Southern African Institute of Mining and Metallurgy: Johannesburg, South Africa, 2015.
137. Clark, D., The Chlorination of Gold Ores. In *The Varsity Engineer*, 1911; pp 8-22.
138. Baghalha, M., Leaching of an oxide gold ore with chloride/hypochlorite solutions. *International Journal of Mineral Processing* **2007**, 82 (4), 178-186.
139. Nicol, M. J., The anodic behaviour of gold. *Gold Bulletin* **1980**, 13 (2), 46-55.
140. Nam, K. S.; Jung, B. H.; An, J. W.; Ha, T. J.; Tran, T.; Kim, M. J., Use of chloride–hypochlorite leachants to recover gold from tailing. *International Journal of Mineral Processing* **2008**, 86 (1-4), 131-140.
141. Tiburcio Munive, G.; Encinas Romero, M. A.; Vazquez, V. M.; Valenzuela García, J. L.; Valenzuela Soto, A.; Coronado Lopez, J. H., Dissolution of Gold and Silver with Ammonium Thiosulfate from Manganese-Argentiferous Ores Treated in Acid-Reductive Conditions. *JOM* **2017**, 1-8.
142. Jeffrey, M. I.; Breuer, P. L.; Choo, W. L., A kinetic study that compares the leaching of gold in the cyanide, thiosulfate, and chloride systems. *Metallurgical and Materials Transactions B* **2001**, 32 (6), 979-986.
143. Viñals, J.; Juan, E.; Ruiz, M.; Ferrando, E.; Cruells, M.; Roca, A.; Casado, J., Leaching of gold and palladium with aqueous ozone in dilute chloride media. *Hydrometallurgy* **2006**, 81 (2), 142-151.
144. Hojo, M.; Iwasaki, S.; Okamura, K., Pure gold dissolution with hydrogen peroxide as the oxidizer in HBr or HI solution. *Journal of Molecular Liquids* **2017**.
145. Senanayake, G., Gold leaching in non-cyanide lixiviant systems: critical issues on fundamentals and applications. *Minerals Engineering* **2004**, 17 (6), 785-801.
146. Mellor, J. W., *A comprehensive treatise on inorganic and theoretical chemistry-As, Sb, Bi, V, Cb and Ta*. Longmans, Green and Company: 1923; Vol. 9.
147. Moskalyk, R. R.; Alfantazi, A. M., Processing of vanadium: a review. *Minerals Engineering* **2003**, 16 (9), 793-805.
148. Li, M.; Wei, C.; Qiu, S.; Zhou, X.; Li, C.; Deng, Z., Kinetics of vanadium dissolution from black shale in pressure acid leaching. *Hydrometallurgy* **2010**, 104 (2), 193-200.
149. Luo, D.; Huang, J.; Zhang, Y.; Liu, H.; Hu, P., Efficient and environment-friendly vanadium (V) extraction from vanadium shale leachate using tri-n-octylmethylammonium chloride. *Separation and Purification Technology* **2020**, 237, 116482.
150. Li, W.; Zhang, Y.; Liu, T.; Huang, J.; Wang, Y., Comparison of ion exchange and solvent extraction in recovering vanadium from sulfuric acid leach solutions of stone coal. *Hydrometallurgy* **2013**, 131-132, 1-7.
151. Zeng, L.; Li, Q.; Xiao, L., Extraction of vanadium from the leach solution of stone coal using ion exchange resin. *Hydrometallurgy* **2009**, 97 (3), 194-197.
152. Zeng, L.; Li, Q.; Xiao, L.; Zhang, Q., A study of the vanadium species in an acid leach solution of stone coal using ion exchange resin. *Hydrometallurgy* **2010**, 105 (1), 176-178.
153. Ye, G.; Hu, Y.; Tong, X.; Lu, L., Extraction of vanadium from direct acid leaching solution of clay vanadium ore using solvent extraction with N235. *Hydrometallurgy* **2018**, 177, 27-33.
154. Zhang, G.; Chen, D.; Zhao, W.; Zhao, H.; Wang, L.; Li, D.; Qi, T., A novel synergistic extraction method for recovering vanadium (V) from high-acidity chloride leaching liquor. *Separation and Purification Technology* **2016**, 165, 166-172.
155. Baldé, C. P., Forti V., Gray, V., Kuehr, R., Stegmann, P. *The Global E-waste Monitor – 2017*; International Telecommunication Union (ITU) & International Solid Waste Association (ISWA): Bonn/Geneva/Vienna, 2017.
156. Baldé, C. P., Wang, F., Kuehr, R., Huisman, J. *The global e-waste monitor – 2014*; United Nations University, IAS – SCYCLE: Bonn, Germany, 2015.
157. Chen, M.; Wang, J.; Chen, H.; Ogunseitan, O. A.; Zhang, M.; Zang, H.; Hu, J., Electronic Waste Disassembly with Industrial Waste Heat. *Environmental Science & Technology* **2013**, 47 (21), 12409-12416.

158. Chehade, Y.; Siddique, A.; Alayan, H.; Sadasivam, N.; Nusri, S.; Ibrahim, T. In *Recovery of gold, silver, palladium, and copper from waste printed circuit boards*, Proceedings of the international conference on chemical, civil and environment engineering (ICCEE), Dubai, United Arab Emirates, 2012; pp 24-25.
159. Cucchiella, F.; D'Adamo, I.; Lenny Koh, S. C.; Rosa, P., Recycling of WEEEs: An economic assessment of present and future e-waste streams. *Renewable and Sustainable Energy Reviews* **2015**, *51*, 263-272.
160. Wang, X.; Gaustad, G., Prioritizing material recovery for end-of-life printed circuit boards. *Waste Management* **2012**, *32* (10), 1903-1913.
161. Cui, H.; Anderson, C., Literature review of hydrometallurgical recycling of printed circuit boards (PCBs). *Journal of Advanced Chemical Engineering* **2016**, *6* (1), 1-11.
162. Aurubis Global Recycling Technology. <https://www.aurubis.com/en/products/recycling/technology> (accessed 10th February).
163. Ghosh, B.; Ghosh, M. K.; Parhi, P.; Mukherjee, P. S.; Mishra, B. K., Waste Printed Circuit Boards recycling: an extensive assessment of current status. *Journal of Cleaner Production* **2015**, *94*, 5-19.
164. Dumitrescu, D. V.; Soare, V.; Constantin, I.; Burada, M.; Dumitru, M.; Olaru, M. T.; Carlan, B. A.; Milea, L.; Dragoescu, F. M.; Dumitru, D.; Carcea, I., Waste electric and electronic equipment (WEEE) melting and resulting gases processing in microwave field. *IOP Conference Series: Materials Science and Engineering* **2018**, *400*, 022023.
165. Flandinet, L.; Tedjar, F.; Ghetta, V.; Fouletier, J., Metals recovering from waste printed circuit boards (WPCBs) using molten salts. *Journal of Hazardous Materials* **2012**, *213-214*, 485-490.
166. Jadhav, U.; Hocheng, H., Hydrometallurgical recovery of metals from large printed circuit board pieces. *Scientific reports* **2015**, *5*, 14574.
167. Schaeffer, N.; Passos, H.; Billard, I.; Papaiconomou, N.; Coutinho, J. A. P., Recovery of metals from waste electrical and electronic equipment (WEEE) using unconventional solvents based on ionic liquids. *Critical Reviews in Environmental Science and Technology* **2018**, *48* (13-15), 859-922.
168. Chen, M.; Huang, J.; Ogunseitan, O. A.; Zhu, N.; Wang, Y.-m., Comparative study on copper leaching from waste printed circuit boards by typical ionic liquid acids. *Waste Management* **2015**, *41*, 142-147.
169. Oraby, E. A.; Eksteen, J. J.; Tanda, B. C., Gold and copper leaching from gold-copper ores and concentrates using a synergistic lixiviant mixture of glycine and cyanide. *Hydrometallurgy* **2017**, *169*, 339-345.
170. Oraby, E. A.; Eksteen, J. J., The selective leaching of copper from a gold-copper concentrate in glycine solutions. *Hydrometallurgy* **2014**, *150*, 14-19.
171. Calgaro, C. O.; Schlemmer, D. F.; da Silva, M. D. C. R.; Maziero, E. V.; Tanabe, E. H.; Bertuol, D. A., Fast copper extraction from printed circuit boards using supercritical carbon dioxide. *Waste Management* **2015**, *45*, 289-297.
172. Liu, K.; Zhang, Z.; Zhang, F.-S., Direct extraction of palladium and silver from waste printed circuit boards powder by supercritical fluids oxidation-extraction process. *Journal of Hazardous Materials* **2016**, *318*, 216-223.
173. Moyo, T.; Chirume, B. H.; Petersen, J., Assessing alternative pre-treatment methods to promote metal recovery in the leaching of printed circuit boards. *Resources, Conservation and Recycling* **2020**, *152*, 104545.
174. Somasundaram, M.; Saravanathamizhan, R.; Ahmed Basha, C.; Nandakumar, V.; Nathira Begum, S.; Kannadasan, T., Recovery of copper from scrap printed circuit board: modelling and optimization using response surface methodology. *Powder Technology* **2014**, *266*, 1-6.
175. Barbara Dutrow; Christine Clark X-ray Powder Diffraction (XRD). [http://serc.carleton.edu/research\\_education/geochemsheets/techniques/XRD.html](http://serc.carleton.edu/research_education/geochemsheets/techniques/XRD.html).
176. Darrell Henry; Nelson Eby; John Goodge; David Mogk X-ray reflection in accordance with Bragg's Law. [http://serc.carleton.edu/research\\_education/geochemsheets/BraggsLaw.html](http://serc.carleton.edu/research_education/geochemsheets/BraggsLaw.html).
177. Mittemeijer, E. J.; Welzel, U., *Modern Diffraction Methods*. John Wiley & Sons, Incorporated: Weinheim, GERMANY, 2012.
178. NIST, X-ray Transition Energies Database. Physical Measurement Laboratory, Ed. 2011.
179. Binghamton University X-Ray Diffraction (XRD) System. [http://www.binghamton.edu/adl/equipment/x-ray\\_analysis/xrd.html](http://www.binghamton.edu/adl/equipment/x-ray_analysis/xrd.html).
180. Kriegner, D.; Matěj, Z.; Kužel, R.; Holý, V., Powder diffraction in Bragg-Brentano geometry with straight linear detectors. *Journal of applied crystallography* **2015**, *48* (Pt 2), 613-618.
181. Rietveld, H. M., A profile refinement method for nuclear and magnetic structures. *Journal of applied Crystallography* **1969**, *2* (2), 65-71.
182. Knoll, M., Aufladepotential und sekundäremission elektronenbestrahlter körper. *Zeitschrift für technische Physik* **1935**, *16*, 467-475.
183. Von Ardenne, M., Das elektronen-rastermikroskop. *Zeitschrift für Physik* **1938**, *109* (9-10), 553-572.

184. Oatley, C., The early history of the scanning electron microscope. *Journal of Applied Physics* **1982**, *53* (2), R1-R13.
185. Reimer, L., *Scanning Electron Microscopy: Physics of Image Formation and Microanalysis: Ludwig Reimer*. Springer: 1985.
186. Australian Microscopy and Microanalysis Research Facility <http://www.ammrf.org.au/myscope/sem/background/concepts/interactions.php>.
187. Goldstein, J.; Newbury, D. E.; Echlin, P.; Joy, D. C.; Romig Jr, A. D.; Lyman, C. E.; Fiori, C.; Lifshin, E., *Scanning electron microscopy and X-ray microanalysis: a text for biologists, materials scientists, and geologists*. Springer Science & Business Media: 2012.
188. Muso, Principle of EDX. In *Wikimedia Commons*, EDX-scheme, Ed. Wikipedia, 2007.
189. Sepúlveda, M.; Gutiérrez, S.; Vallette, M. C.; Standen, V. G.; Arriaza, B. T.; Cárcamo-Vega, J. J., Micro-Raman spectral identification of manganese oxides black pigments in an archaeological context in Northern Chile. *Heritage Science* **2015**, *3* (1), 32.
190. Julien, C.; Massot, M.; Baddour-Hadjean, R.; Franger, S.; Bach, S.; Pereira-Ramos, J. P., Raman spectra of birnessite manganese dioxides. *Solid State Ionics* **2003**, *159* (3), 345-356.
191. Post, J., Personal Communication Discussing Raman Spectroscopy of Manganese Dioxides. Bartle, J., Ed. Washington D.C., 2019.
192. Beauchemin, D., Inductively coupled plasma mass spectrometry. *Analytical chemistry* **2010**, *82* (12), 4786-4810.
193. Washington University in St. Louis Instrumentation - ICPMS. <http://eecelabs.seas.wustl.edu/ICP-MS.aspx>.
194. Toby, B. H.; Von Dreele, R. B., GSAS-II: the genesis of a modern open-source all purpose crystallography software package. *Journal of Applied Crystallography* **2013**, *46* (2), 544-549.
195. Kijima, N.; Yasuda, H.; Sato, T.; Yoshimura, Y., Preparation and Characterization of Open Tunnel Oxide  $\alpha$ -MnO<sub>2</sub> Precipitated by Ozone Oxidation. *Journal of Solid State Chemistry* **2001**, *159* (1), 94-102.
196. Burle, E.; Kirby-Smith, W. W., Application of formaldoxime colorimetric method for the determination of manganese in the pore water of anoxic estuarine sediments. *Estuaries* **1979**, *2* (3), 198-201.
197. Driehaus, W.; Seith, R.; Jekel, M., Oxidation of arsenate(III) with manganese oxides in water treatment. *Water Research* **1995**, *29* (1), 297-305.
198. Ghodbane, O.; Pascal, J.-L.; Favier, F., Microstructural effects on charge-storage properties in MnO<sub>2</sub>-based electrochemical supercapacitors. *ACS applied materials & interfaces* **2009**, *1* (5), 1130-1139.
199. Selvakumar, S.; Nuns, N.; Trentesaux, M.; Batra, V. S.; Giraudon, J. M.; Lamonier, J. F., Reaction of formaldehyde over birnessite catalyst: A combined XPS and ToF-SIMS study. *Applied Catalysis B: Environmental* **2016**.
200. Escande, V.; Lam, C. H.; Coish, P.; Anastas, P. T., Heterogeneous Sodium-Manganese Oxide Catalyzed Aerobic Oxidative Cleavage of 1,2-Diols. *Angewandte Chemie - International Edition* **2017**, *56* (32), 9561-9565.
201. Li, L.; Wei, D.; Wei, G.; Du, Y., Product identification and the mechanisms involved in the transformation of cefazolin by birnessite ( $\Delta$ -MnO<sub>2</sub>). *Chemical Engineering Journal* **2017**, *320*, 116-123.
202. Lafferty, B. J.; Ginder-Vogel, M.; Sparks, D. L., Arsenite oxidation by a poorly-crystalline manganese oxide. 3. Arsenic and manganese desorption. *Environmental Science and Technology* **2011**, *45* (21), 9218-9223.
203. Li, Z.; Wang, J.; Wang, Z.; Ran, H.; Li, Y.; Han, X.; Yang, S., Synthesis of a porous birnessite manganese dioxide hierarchical structure using thermally reduced graphene oxide paper as a sacrificing template for supercapacitor application. *New Journal of Chemistry* **2012**, *36* (7), 1490-1495.
204. Nam, K. W.; Kim, S.; Yang, E.; Jung, Y.; Levi, E.; Aurbach, D.; Choi, J. W., Critical Role of Crystal Water for a Layered Cathode Material in Sodium Ion Batteries. *Chemistry of Materials* **2015**, *27* (10), 3721-3725.
205. Peacock, C. L.; Moon, E. M., Oxidative scavenging of thallium by birnessite: Explanation for thallium enrichment and stable isotope fractionation in marine ferromanganese precipitates. *Geochimica et Cosmochimica Acta* **2012**, *84*, 297-313.
206. Yin, H.; Feng, X.; Tan, W.; Koopal, L. K.; Hu, T.; Zhu, M.; Liu, F., Structure and properties of vanadium(V)-doped hexagonal turbostratic birnessite and its enhanced scavenging of Pb<sup>2+</sup> from solutions. *Journal of Hazardous Materials* **2015**, *288*, 80-88.
207. Golden, D.; Chen, C.; Dixon, J., Transformation of birnessite to buserite, todorokite, and manganite under mild hydrothermal treatment. *Clays and Clay Minerals* **1987**, *35* (4), 271-280.
208. Villalobos, M.; Carrillo-Cárdenas, M.; Gibson, R.; López-Santiago, N. R.; Morales, J. A., The influence of particle size and structure on the sorption and oxidation behaviour of birnessite: II. Adsorption and oxidation of four polycyclic aromatic hydrocarbons. *Environmental Chemistry* **2014**, *11* (3), 279-288.

209. Zhou, J.; Yu, L.; Sun, M.; Yang, S.; Ye, F.; He, J.; Hao, Z., Novel Synthesis of Birnessite-Type MnO<sub>2</sub> Nanostructure for Water Treatment and Electrochemical Capacitor. *Industrial & Engineering Chemistry Research* **2013**, *52* (28), 9586-9593.
210. Lopano, C. L.; Heaney, P. J.; Post, J. E.; Hanson, J.; Komarneni, S., Time-resolved structural analysis of K- and Ba-exchange reactions with synthetic Na-birnessite using synchrotron X-ray diffraction. *American Mineralogist* **2007**, *92* (2-3), 380-387.
211. Bernardini, S.; Bellatreccia, F.; Della Ventura, G.; Ballirano, P.; Sodo, A., Raman spectroscopy and laser-induced degradation of groutellite and ramsdellite, two cathode materials of technological interest. *RSC Advances* **2020**, *10* (2), 923-929.
212. Luo, Y.; Tan, W.; Suib, S. L.; Qiu, G.; Liu, F., Dissolution and phase transformation processes of hausmannite in acidic aqueous systems under anoxic conditions. *Chemical Geology* **2018**, *487*, 54-62.
213. Yin, H.; Liu, F.; Feng, X.; Hu, T.; Zheng, L.; Qiu, G.; Koopal, L. K.; Tan, W., Effects of Fe doping on the structures and properties of hexagonal birnessites - Comparison with Co and Ni doping. *Geochimica et Cosmochimica Acta* **2013**, *117*, 1-15.
214. Kamimura, A.; Nozaki, Y.; Ishikawa, S.; Inoue, R.; Nakayama, M., K-birnessite MnO<sub>2</sub>: a new selective oxidant for benzylic and allylic alcohols. *Tetrahedron Letters* **2011**, *52* (4), 538-540.
215. Yang, L.; Tian, X.; Qian, L.; Liu, Y.; Guo, Y.; Xiao, D., Facile Synthesis of Birnessite-type MnO<sub>2</sub> and its application as a supercapacitor. *Nanoscience and Nanotechnology Letters* **2015**, *7* (9), 749-753.
216. Gude, J. C. J.; Rietveld, L. C.; van Halem, D., As(III) oxidation by MnO<sub>2</sub> during groundwater treatment. *Water Research* **2017**, *111*, 41-51.
217. Fischel, M. H. H.; Fischel, J. S.; Lafferty, B. J.; Sparks, D. L., The influence of environmental conditions on kinetics of arsenite oxidation by manganese-oxides. *Geochemical Transactions* **2015**, *16* (1).
218. Kong, K. P.; Fischer, T. B.; Heaney, P. J.; Post, J. E.; Stubbs, J. E.; Eng, P. J., Mineralogical and geochemical constraints on chromium oxidation induced by birnessite. *Applied Geochemistry* **2019**, *108*, 104365.
219. Landrot, G.; Ginder-Vogel, M.; Livi, K.; Fitts, J. P.; Sparks, D. L., Chromium(III) Oxidation by Three Poorly-Crystalline Manganese(IV) Oxides. 1. Chromium(III)-Oxidizing Capacity. *Environmental Science & Technology* **2012**, *46* (21), 11594-11600.
220. Crowther, D. L.; Dillard, J. G.; Murray, J. W., The mechanisms of Co (II) oxidation on synthetic birnessite. *Geochimica et Cosmochimica Acta* **1983**, *47* (8), 1399-1403.
221. Manceau, A.; Silvester, E.; Bartoli, C.; Lanson, B.; Drits, V. A., Structural mechanism of Co<sup>2+</sup> oxidation by the phyllo-manganate buserite. *American mineralogist* **1997**, *82* (11-12), 1150-1175.
222. Simanova, A. A.; Peña, J., Time-Resolved Investigation of Cobalt Oxidation by Mn(III)-Rich δ-MnO<sub>2</sub> Using Quick X-ray Absorption Spectroscopy. *Environmental Science & Technology* **2015**, *49* (18), 10867-10876.
223. Manning, B. A.; Kanel, S. R.; Guzman, E.; Brittle, S. W.; Pavel, I. E., Oxidative dissolution of silver nanoparticles by synthetic manganese dioxide investigated by synchrotron X-ray absorption spectroscopy. *Journal of Nanoparticle Research* **2019**, *21* (10), 213.
224. Yang, P.; Post, J. E.; Wang, Q.; Xu, W.; Geiss, R.; McCurdy, P. R.; Zhu, M., Metal Adsorption Controls Stability of Layered Manganese Oxides. *Environmental Science & Technology* **2019**, *53* (13), 7453-7462.
225. Lopano, C. L.; Heaney, P. J.; Bandstra, J. Z.; Post, J. E.; Brantley, S. L., Kinetic analysis of cation exchange in birnessite using time-resolved synchrotron X-ray diffraction. *Geochimica et Cosmochimica Acta* **2011**, *75* (14), 3973-3981.
226. Smith, D. W., Ionic hydration enthalpies. *Journal of Chemical Education* **1977**, *54* (9), 540.
227. Yin, H.; Sun, J.; Yan, X.; Yang, X.; Feng, X.; Tan, W.; Qiu, G.; Zhang, J.; Ginder-Vogel, M.; Liu, F., Effects of Co(II) ion exchange, Ni(II)- and V(V)-doping on the transformation behaviors of Cr(III) on hexagonal turbostratic birnessite-water interfaces. *Environmental Pollution* **2020**, *256*, 113462.
228. Yin, H.; Liu, F.; Feng, X.; Hu, T.; Zheng, L.; Qiu, G.; Koopal, L. K.; Tan, W., Effects of Fe doping on the structures and properties of hexagonal birnessites – Comparison with Co and Ni doping. *Geochimica et Cosmochimica Acta* **2013**, *117*, 1-15.
229. Liu, L.; Min, M.; Liu, F.; Yin, H.; Zhang, Y.; Qiu, G., Influence of vanadium doping on the supercapacitance performance of hexagonal birnessite. *Journal of Power Sources* **2015**, *277*, 26-35.
230. Brugger, J.; Berlepsch, P.; Meisser, N.; Armbruster, T., Ansermetite, MnV<sub>2</sub>O<sub>6</sub>·4H<sub>2</sub>O, a new mineral species with V<sup>5+</sup> in five-fold coordination from Val Ferrera, Eastern Swiss Alps. *The Canadian Mineralogist* **2003**, *41* (6), 1423-1431.
231. Zhang, S.; Hu, R.; Liu, L.; Wang, D., Hydrothermal synthesis of MnV<sub>2</sub>O<sub>6</sub> nanobelts and its application in lithium-ion battery. *Materials Letters* **2014**, *124*, 57-60.
232. Huang, W.; Gao, S.; Ding, X.; Jiang, L.; Wei, M., Crystalline MnV<sub>2</sub>O<sub>6</sub> nanobelts: Synthesis and electrochemical properties. *Journal of Alloys and Compounds* **2010**, *495* (1), 185-188.

233. Viegas, J. I.; Moreira, R. L.; Dias, A., Polymorphism and Optical–Vibration Properties of MnV<sub>2</sub>O<sub>6</sub>·nH<sub>2</sub>O (n = 0, 2, 4) Prepared by Microwave Irradiation. *Crystal Growth & Design* **2019**, *19* (6), 3233-3243.
234. Manivannan, V.; Parhi, P.; Howard, J., Mechanochemical metathesis synthesis and characterization of nano-structured MnV<sub>2</sub>O<sub>6</sub>·xH<sub>2</sub>O (x=2, 4). *Journal of Crystal Growth* **2008**, *310* (11), 2793-2799.
235. Wu, X.; Wu, W.; Cui, X.; Liao, S., Selective self-assembly synthesis of MnV<sub>2</sub>O<sub>6</sub>·4H<sub>2</sub>O with controlled morphologies and study on its thermal decomposition. *Journal of Thermal Analysis and Calorimetry* **2012**, *109* (1), 163-169.
236. Burhanuddin, S.; Yarmo, A.; Yamin, B. M. In *Synthesis and characterisation of manganese oxides from potassium permanganate and citric acid mixtures*, AIP Conference Proceedings, AIP: 2013; pp 932-937.
237. Liu, S.; Fan, C.-Z.; Zhang, Y.; Li, C.-H.; You, X.-Z., Low-temperature synthesis of Na<sub>2</sub>Mn<sub>5</sub>O<sub>10</sub> for supercapacitor applications. *Journal of Power Sources* **2011**, *196* (23), 10502-10506.
238. Luo, J.; Zhang, Q.; Huang, A.; Suib, S. L., Total oxidation of volatile organic compounds with hydrophobic cryptomelane-type octahedral molecular sieves. *Microporous and Mesoporous Materials* **2000**, *35-36*, 209-217.
239. Feng, X. H.; Tan, W. F.; Liu, F.; Wang, J. B.; Ruan, H. D., Synthesis of todorokite at atmospheric pressure. *Chemistry of Materials* **2004**, *16* (22), 4330-4336.
240. Birkner, N.; Navrotsky, A., Thermodynamics of manganese oxides: Sodium, potassium, and calcium birnessite and cryptomelane. *Proceedings of the National Academy of Sciences of the United States of America* **2017**, *114* (7), E1046-E1053.
241. Poyraz, A. S.; Huang, J.; Pelliccione, C. J.; Tong, X.; Cheng, S.; Wu, L.; Zhu, Y.; Marschilok, A. C.; Takeuchi, K. J.; Takeuchi, E. S., Synthesis of cryptomelane type α-MnO<sub>2</sub> (K<sub>x</sub>Mn<sub>8</sub>O<sub>16</sub>) cathode materials with tunable K<sup>+</sup> content: the role of tunnel cation concentration on electrochemistry. *Journal of Materials Chemistry A* **2017**, *5* (32), 16914-16928.
242. Drits, V. A.; Silvester, E.; Gorshkov, A. I.; Manceau, A., Structure of synthetic monoclinic Na-rich birnessite and hexagonal birnessite: I. Results from X-ray diffraction and selected-area electron diffraction. *American Mineralogist* **1997**, *82* (9-10), 946-961.
243. Silvester, E.; Manceau, A.; Drits, V. A., Structure of synthetic monoclinic Na-rich birnessite and hexagonal birnessite: II. Results from chemical studies and EXAFS spectroscopy. *American Mineralogist* **1997**, *82* (9-10), 962-978.
244. Gao, T.; Norby, P., Frame Stability of Tunnel-Structured Cryptomelane Nanofibers: The Role of Tunnel Cations. *European Journal of Inorganic Chemistry* **2013**, *2013* (28), 4948-4957.
245. Faulring, G. M.; Zwicker, W. K.; Forgeng, W. D., Thermal transformations and properties of cryptomelane. *American Mineralogist* **1960**, *45* (9-10), 946-959.
246. Chen, J.; Yan, D.; Xu, Z.; Chen, X.; Chen, X.; Xu, W.; Jia, H.; Chen, J., A Novel Redox Precipitation to Synthesize Au-Doped α-MnO<sub>2</sub> with High Dispersion toward Low-Temperature Oxidation of Formaldehyde. *Environmental Science & Technology* **2018**, *52* (8), 4728-4737.
247. Bodoardo, S.; Brenet, J.; Maja, M.; Spinelli, P., Electrochemical behaviour of MnO<sub>2</sub> electrodes in sulphuric acid solutions. *Electrochimica acta* **1994**, *39* (13), 1999-2004.
248. Yoo, J.-M.; Jeong, J.; Yoo, K.; Lee, J.-c.; Kim, W., Enrichment of the metallic components from waste printed circuit boards by a mechanical separation process using a stamp mill. *Waste Management* **2009**, *29* (3), 1132-1137.
249. Yang, H.; Liu, J.; Yang, J., Leaching copper from shredded particles of waste printed circuit boards. *Journal of Hazardous Materials* **2011**, *187* (1), 393-400.
250. Zhu, P.; Chen, Y.; Wang, L. Y.; Zhou, M.; Zhou, J., The separation of waste printed circuit board by dissolving bromine epoxy resin using organic solvent. *Waste Management* **2013**, *33* (2), 484-488.
251. Verma, H. R.; Singh, K. K.; Mankhand, T. R., Dissolution and separation of brominated epoxy resin of waste printed circuit boards by using di-methyl formamide. *Journal of Cleaner Production* **2016**, *139*, 586-596.
252. Jung, M.; Yoo, K.; Alorro, R. D., Dismantling of Electric and Electronic Components from Waste Printed Circuit Boards by Hydrochloric Acid Leaching with Stannic Ions. *Materials Transactions* **2017**, *58* (7), 1076-1080.
253. Sheng, P. P.; Etsell, T. H., Recovery of gold from computer circuit board scrap using aqua regia. *Waste management & research* **2007**, *25* (4), 380-383.
254. Park, Y. J.; Fray, D. J., Recovery of high purity precious metals from printed circuit boards. *Journal of Hazardous Materials* **2009**, *164* (2), 1152-1158.
255. Bas, A. D.; Deveci, H.; Yazici, E. Y., Treatment of manufacturing scrap TV boards by nitric acid leaching. *Separation and Purification Technology* **2014**, *130*, 151-159.
256. Yazici, E. Y.; Deveci, H., Extraction of metals from waste printed circuit boards (WPCBs) in H<sub>2</sub>SO<sub>4</sub>–CuSO<sub>4</sub>–NaCl solutions. *Hydrometallurgy* **2013**, *139*, 30-38.

257. Silvas, F. P. C.; Jiménez Correa, M. M.; Caldas, M. P. K.; de Moraes, V. T.; Espinosa, D. C. R.; Tenório, J. A. S., Printed circuit board recycling: Physical processing and copper extraction by selective leaching. *Waste Management* **2015**, *46*, 503-510.
258. Birloaga, I.; Coman, V.; Kopacek, B.; Vegliò, F., An advanced study on the hydrometallurgical processing of waste computer printed circuit boards to extract their valuable content of metals. *Waste Management* **2014**, *34* (12), 2581-2586.
259. Birloaga, I.; De Michelis, I.; Ferella, F.; Buzatu, M.; Vegliò, F., Study on the influence of various factors in the hydrometallurgical processing of waste printed circuit boards for copper and gold recovery. *Waste Management* **2013**, *33* (4), 935-941.
260. Behnamfard, A.; Salarirad, M. M.; Veglio, F., Process development for recovery of copper and precious metals from waste printed circuit boards with emphasize on palladium and gold leaching and precipitation. *Waste Management* **2013**, *33* (11), 2354-2363.
261. Montero, R.; Guevara, A.; dela Torre, E., Recovery of gold, silver, copper and niobium from printed circuit boards using leaching column technique. *Journal of earth science and engineering* **2012**, *2* (10), 590.
262. Haynes, W.; Lide, D.; Bruno, T., CRC Handbook of Chemistry and Physics, 97th edn, Vol. 2016–2017. CRC Press: 2017.
263. Vanysek, P., Electrochemical series. *CRC handbook of chemistry and physics* **2000**, *8*.
264. Feng, X. H.; Zhai, L. M.; Tan, W. F.; Liu, F.; He, J. Z., Adsorption and redox reactions of heavy metals on synthesized Mn oxide minerals. *Environmental Pollution* **2007**, *147* (2), 366-373.
265. Koch, K., Certificate of Analysis fo Sodium Chloride of HPLC LiChropur Batch Number K48327332. Merck: 2016.
266. Qin, Z.; Chen, X.; Ouyang, N.; Lan, S.; Jiang, G.; Zhang, J.; Zhang, Q., Characterisation of hexagonal birnessite with a new and rapid synthesis method—comparison with traditional synthesis. *RSC Advances* **2019**, *9* (45), 25951-25956.
267. Yang, P.; Lee, S.; Post, J. E.; Xu, H.; Wang, Q.; Xu, W.; Zhu, M., Trivalent manganese on vacancies triggers rapid transformation of layered to tunneled manganese oxides (TMOs): Implications for occurrence of TMOs in low-temperature environment. *Geochimica et Cosmochimica Acta* **2018**, *240*, 173-190.
268. Jürgensen, A.; Widmeyer, J. R.; Gordon, R. A.; Bendell-Young, L. I.; Moore, M. M.; Crozier, E. D., The structure of the manganese oxide on the sheath of the bacterium *Leptothrix discophora*: An XAFS study. *American Mineralogist* **2004**, *89* (7), 1110-1118.
269. Cherney, D. P.; Duirk, S. E.; Tarr, J. C.; Collette, T. W., Monitoring the Speciation of Aqueous Free Chlorine from pH 1 to 12 with Raman Spectroscopy to Determine the Identity of the Potent Low-pH Oxidant. *Applied Spectroscopy* **2006**, *60* (7), 764-772.
270. Hafeez Fatunmbi; Fatunmbi, B., Determination of Chloride, Chlorite and Chlorate in Drinking Water Samples by High Performance Ion Chromatography. *Separation Methods Technologies Separation Journals* **2018**, *2*.
271. Schwan, A. M.; Martin, R.; Goessler, W., Chlorine speciation analysis in blood by ion chromatography-inductively coupled plasma mass spectrometry. *Analytical Methods* **2015**, *7* (21), 9198-9205.